

# **Characterisation of Mechanically Alloyed Feedstock for Selective Laser Melting: Titanium Silicon Carbide Metal Matrix Composite.**

IAIN LYALL (BEng.)

A thesis has been submitted in partial fulfilment of the requirements of the  
University of Wolverhampton for the award of Doctor of Philosophy

January 2020

## **Declaration:**

This work or any part thereof has not previously been presented in any form to the University or to any other body whether for assessment, publication or for any other purpose (unless otherwise indicated). Save for any express acknowledgements, references and/or bibliographies cited in the work, I confirm that the intellectual content of the work is the result of my own efforts and of no other person.

The rights Iain Lyall to be identified as the author of this work is asserted in accordance with ss.77 and 78 of the copyright, Designs and Patents act 1988. At this date, copyright is owned by the author.

Signature.....

Date.....

# Acknowledgements

The author would like to express gratitude to my supervisors Professor Mark Stanford and Professor Kevin Kibble for their patience and guidance throughout this period of study. My sincere thanks to the staff within the Faculty of Science and Engineering at the University of Wolverhampton and specifically to those within the School of Engineering who have advised and guided me.

The author would also like to thank the industrial manufacturers of the equipment used during this research. Many items were new not only to me but also the manufacturers and I appreciate their patience while we found innovative solutions to challenging questions. I look forward to continuing this relationship in expanding the limits of the technology.

The author would also like to thank the technical staff within the Faculty of Science and Engineering and specifically to those within the School of Engineering who have advised guided and supported me.

# Abstract

The research presented investigates the characterisation of new materials for the additive manufacturing industry. Herein, a metal matrix composite (MMC) with a titanium (Ti6Al4V) matrix reinforced with silicon carbide (SiC) is characterised from the use of an innovative feedstock production process involving mechanical alloying through to the systematic evaluation of process parameters including laser power, scan speed and hatch spacing.

The experimental route is discussed, and detailed findings are presented with a methodology for elemental feedstock production in small batch sizes and process parameter characterisation for in-situ alloying during laser bed fusion.

Evidence showed that acceptable parameters could be found for mechanical alloying with a rotational speed of 500 rev/min and an alloying time of twenty-four minutes that showed acceptable changes in size and morphology, therefore enabling the feedstock to be used within the SLM process.

New knowledge is presented in the form of experimental methodologies, namely the evaluation and comparison of single beads, the use of mini-chambers to experiment with reduced levels of feedstock, the two-rail system to accurately deliver powder for single layer experimentation and equations developed to calculate energy density for single beads and the maximum volume of reinforcement material achievable from particle size data.

MMC material was successfully synthesised due to the use of the methodologies described, with silicon carbide (SiC), silicon oxide (SiO<sub>2</sub>) and titanium silicide (Ti<sub>5</sub>Si<sub>4</sub>) detected as chemical compositions within the sample.

# Table of contents

|                                                                                                                                              |              |
|----------------------------------------------------------------------------------------------------------------------------------------------|--------------|
| <b>CHARACTERISATION OF MECHANICALLY ALLOYED FEEDSTOCK FOR SELECTIVE LASER MELTING: TITANIUM SILICON CARBIDE METAL MATRIX COMPOSITE. ....</b> | <b>I</b>     |
| <b>DECLARATION: .....</b>                                                                                                                    | <b>II</b>    |
| <b>ACKNOWLEDGEMENTS .....</b>                                                                                                                | <b>III</b>   |
| <b>ABSTRACT .....</b>                                                                                                                        | <b>IV</b>    |
| <b>TABLE OF CONTENTS.....</b>                                                                                                                | <b>V</b>     |
| <b>LIST OF FIGURES.....</b>                                                                                                                  | <b>XI</b>    |
| <b>LIST OF TABLES.....</b>                                                                                                                   | <b>XV</b>    |
| <b>NOMENCLATURE .....</b>                                                                                                                    | <b>XVII</b>  |
| <b>GLOSSARY OF ACRONYMS. ....</b>                                                                                                            | <b>XVIII</b> |
| <b>PAPERS AND CONFERENCES .....</b>                                                                                                          | <b>XIX</b>   |
| <b>CHAPTER ONE .....</b>                                                                                                                     | <b>1</b>     |
| <b>1.0 INTRODUCTION.....</b>                                                                                                                 | <b>1</b>     |
| 1.1 RESEARCH JUSTIFICATION.....                                                                                                              | 2            |
| 1.2 AIM AND OBJECTIVES.....                                                                                                                  | 6            |
| 1.2.1 <i>Aim</i> .....                                                                                                                       | 6            |
| 1.2.2 <i>Objectives</i> .....                                                                                                                | 6            |
| <b>CHAPTER TWO .....</b>                                                                                                                     | <b>7</b>     |
| <b>2.0 LITERATURE REVIEW .....</b>                                                                                                           | <b>7</b>     |
| 2.1 SCOPE OF THE LITERATURE REVIEW. ....                                                                                                     | 7            |
| 2.2 MATERIALS .....                                                                                                                          | 9            |
| 2.2.1 <i>Titanium Alloy (Ti6Al4V)</i> .....                                                                                                  | 9            |
| 2.2.2 <i>Mechanical Properties for Ti6Al4V Key to This Research.</i> .....                                                                   | 11           |
| 2.2.3 <i>Alloy Types</i> .....                                                                                                               | 12           |
| 2.2.4 <i>Crystallographic Forms of Titanium</i> .....                                                                                        | 12           |
| 2.2.5 <i>Alpha Stabilisers</i> .....                                                                                                         | 13           |
| 2.3 SILICON CARBIDE .....                                                                                                                    | 13           |
| 2.3.1 <i>Mechanical Properties for Sic Key to This Research.</i> .....                                                                       | 14           |
| 2.3.2 <i>Crystallographic Forms of Silicon Carbide</i> .....                                                                                 | 15           |
| 2.4 METAL MATRIX COMPOSITES (MMCs) .....                                                                                                     | 16           |
| 2.4.1 <i>MMC Systems</i> .....                                                                                                               | 16           |
| 2.4.2 <i>Matrix Materials</i> .....                                                                                                          | 16           |
| 2.4.3 <i>Reinforcement Materials</i> .....                                                                                                   | 16           |

|                                      |                                                                                   |           |
|--------------------------------------|-----------------------------------------------------------------------------------|-----------|
| 2.5                                  | THE SLM PROCESSES.....                                                            | 19        |
| 2.5.1                                | <i>Process Parameters</i> .....                                                   | 19        |
| 2.5.2                                | <i>Laser Power</i> .....                                                          | 19        |
| 2.5.3                                | <i>Layer Thickness</i> .....                                                      | 19        |
| 2.5.4                                | <i>Scan Speed</i> .....                                                           | 20        |
| 2.5.5                                | <i>Hatch Distance</i> .....                                                       | 20        |
| 2.5.6                                | <i>Scan Strategy</i> .....                                                        | 20        |
| 2.5.7                                | <i>Environmental Conditions</i> .....                                             | 21        |
| 2.5.7.1                              | <i>Build Platform and Substrate Temperature</i> .....                             | 21        |
| 2.5.7.2                              | <i>Environmental Atmosphere (Gas)</i> .....                                       | 23        |
| 2.5.7.3                              | <i>Gas Flow and Recoat Speed</i> .....                                            | 23        |
| 2.5.7.4                              | <i>Filtration and condensate removal</i> .....                                    | 24        |
| 2.5.8                                | <i>Surface Tension and Wettability</i> .....                                      | 24        |
| 2.6                                  | CONVENTIONAL FEEDSTOCK PRODUCTION FOR SLM.....                                    | 27        |
| 2.6.1                                | <i>Strategies for Mixing Dissimilar Powders</i> .....                             | 31        |
| 2.6.1.1                              | <i>Manual Mixing</i> .....                                                        | 31        |
| 2.6.1.2                              | <i>Gas Atomisation</i> .....                                                      | 32        |
| 2.6.1.3                              | <i>Mechanical Alloying (MA)</i> .....                                             | 33        |
| 2.6.2                                | <i>Mechanical Alloying (MA) For Selective Laser Melting (SLM)</i> .....           | 34        |
| 2.6.2.1                              | <i>Changes to Particle Size and Size Distribution During the MA Process</i> ..... | 35        |
| 2.6.2.2                              | <i>Changes in Morphology During the MA Process</i> .....                          | 36        |
| 2.6.2.3                              | <i>Maximum Surface Coverage of The Matrix Material Possible Through MA</i> .....  | 36        |
| 2.6.2.4                              | <i>Excess Reinforcement Material Post MA</i> .....                                | 36        |
| 2.6.2.5                              | <i>Contamination Risks During the MA Process</i> .....                            | 36        |
| 2.6.3                                | <i>Process Preparation – Mechanical Alloying (MA)</i> .....                       | 37        |
| <b>CHAPTER THREE.....</b>            |                                                                                   | <b>38</b> |
| <b>3.0 BACKGROUND.....</b>           |                                                                                   | <b>38</b> |
| 3.1                                  | INITIAL EXPERIMENTATION.....                                                      | 38        |
| 3.1.1                                | <i>Feedstock Preparation</i> .....                                                | 38        |
| 3.1.2                                | <i>Data Preparation</i> .....                                                     | 39        |
| 3.2                                  | OBSERVATIONS FROM INITIAL EXPERIMENTATION.....                                    | 40        |
| <b>CHAPTER FOUR.....</b>             |                                                                                   | <b>44</b> |
| <b>4.0 RESEARCH METHODOLOGY.....</b> |                                                                                   | <b>44</b> |
| 4.1                                  | INTRODUCTION.....                                                                 | 44        |
| 4.2                                  | PHASE 1A: BASELINE ASSESSMENT OF RAW MATERIALS.....                               | 46        |
| 4.2.1                                | <i>Overview of The Experimental Design</i> .....                                  | 46        |
| 4.2.2                                | <i>Sample Sizes</i> .....                                                         | 46        |
| 4.2.3                                | <i>Restrictions and limitations</i> .....                                         | 46        |

|           |                                                                                                                      |    |
|-----------|----------------------------------------------------------------------------------------------------------------------|----|
| 4.2.3.1   | <i>Moisture Content, Restrictions and Limitations</i> .....                                                          | 46 |
| 4.2.3.2   | <i>Particle Size and Morphological, Restrictions and Limitations</i> .....                                           | 47 |
| 4.2.3.3   | <i>Rheological Restrictions and Limitations</i> .....                                                                | 47 |
| 4.2.4     | <i>Equipment</i> .....                                                                                               | 47 |
| 4.2.4.1   | <i>Moisture Content</i> .....                                                                                        | 47 |
| 4.2.4.2   | <i>Particle Size and Morphological Characteristics</i> .....                                                         | 48 |
| 4.2.4.4   | <i>Rheological Characteristics</i> .....                                                                             | 48 |
| 4.2.4.3.1 | <i>Apparent Density</i> .....                                                                                        | 49 |
| 4.2.4.3.3 | <i>Angle of Repose</i> .....                                                                                         | 50 |
| 4.2.5     | <i>Procedures and variables</i> .....                                                                                | 50 |
| 4.2.5.1   | <i>Moisture Content Analysis Procedure and Variables</i> .....                                                       | 50 |
| 4.2.5.2   | <i>Particle Size and Morphological Analysis Procedure and Variable</i> .....                                         | 51 |
| 4.2.5.3   | <i>Rheological Procedure and Variables for Apparent Density and Angle of Repose</i>                                  | 51 |
| 4.2.6     | <i>Statistical Treatment</i> .....                                                                                   | 52 |
| 4.2.6.1   | <i>Moisture Content</i> .....                                                                                        | 52 |
| 4.2.6.2   | <i>Particle Size and Morphological Analysis</i> .....                                                                | 52 |
| 4.3       | PHASE 1B: BASELINE ASSESSMENT OF Ti6Al4V SINGLE BEADS EVALUATED AGAINST ENERGY DENSITY.                              |    |
|           | 53                                                                                                                   |    |
| 4.3.1     | <i>Overview of The Experiment/Design</i> .....                                                                       | 53 |
| 4.3.2     | <i>Sample Size</i> .....                                                                                             | 54 |
| 4.3.3     | <i>Restrictions and limitations</i> .....                                                                            | 54 |
| 4.3.3.1   | <i>Feedstock Availability</i> .....                                                                                  | 54 |
| 4.3.3.2   | <i>Energy Density Calculations Without Hatch Distance</i> .....                                                      | 55 |
| 4.3.3.3   | <i>Laser Power Range</i> .....                                                                                       | 55 |
| 4.3.4     | <i>Equipment</i> .....                                                                                               | 55 |
| 4.3.5     | <i>Procedures</i> .....                                                                                              | 56 |
| 4.3.5.1   | <i>Digital Files</i> .....                                                                                           | 56 |
| 4.3.5.2   | <i>Process Chamber Preparation</i> .....                                                                             | 57 |
| 4.3.5.3   | <i>Build Platform Preparation</i> .....                                                                              | 57 |
| 4.3.6     | <i>Variables</i> .....                                                                                               | 58 |
| 4.3.6.1   | <i>Phase 3a Variables (Single Bead Evaluation Against Energy Density)</i> .....                                      | 58 |
| 4.3.6.2   | <i>Phase 3a Attributes</i> .....                                                                                     | 58 |
| 4.4       | PHASE 2A: DEVELOPMENT OF MECHANICAL ALLOYING PROCESS AS A HOMOGENOUS TRANSPORTATION MECHANISM FOR MMC FEEDSTOCK..... | 59 |
| 4.4.1     | <i>Overview of The Mechanical Alloying Experiment / Design</i> .....                                                 | 59 |
| 4.4.2     | <i>Mechanical Alloying Experimental Sample Size</i> .....                                                            | 59 |
| 4.4.3     | <i>Restrictions and limitations</i> .....                                                                            | 59 |
| 4.4.4     | <i>Mechanical Alloying Equipment</i> .....                                                                           | 60 |
| 4.4.5     | <i>Procedures</i> .....                                                                                              | 62 |

|                     |                                                                                                                              |           |
|---------------------|------------------------------------------------------------------------------------------------------------------------------|-----------|
| 4.4.6               | <i>Mechanical Alloying Variables for Surface Coverage by Reinforcement.</i>                                                  | 62        |
| 4.4.6.1             | <i>Conversion from Volume Fraction to Weight Fraction of Reinforcement</i>                                                   | 64        |
| 4.5                 | PHASE 2B: MMC FEEDSTOCK ANALYSIS FOR MOISTURE, SIZE, MORPHOLOGY AND RHEOLOGY IN COMPARISON TO BASELINE ASSESSMENT, PHASE 1A. | 66        |
| 4.5.1               | <i>MMC Feedstock Analysis Overview of Experiment/Design</i>                                                                  | 66        |
| 4.5.2               | <i>Sample Size</i>                                                                                                           | 66        |
| 4.5.1.2             | <i>MMC Feedstock Moisture and Rheological Analysis.</i>                                                                      | 66        |
| 4.6                 | PHASE 3A: ASSESSMENT OF MMC SINGLE BEADS EVALUATED AGAINST ENERGY DENSITY IN COMPARISON TO Ti6Al4V BASELINE.                 | 66        |
| 4.6.1               | <i>Overview of The Experiment/Design</i>                                                                                     | 66        |
| 4.7                 | PHASE 3B: HATCH SPACING EVALUATION OF MULTIPLE BEADS.                                                                        | 66        |
| 4.7.1               | <i>Overview of The Experiment/Design</i>                                                                                     | 66        |
| 4.7.2               | <i>Phase 3b Variables</i>                                                                                                    | 67        |
| 4.7.2               | <i>Phase 3b Attributes</i>                                                                                                   | 67        |
| 4.8                 | PHASE 3C: MULTIPLE-LAYER EVALUATION OF DENSITY AND HOMOGENEITY OF REINFORCEMENT.                                             | 68        |
| 4.8.1               | <i>Overview of the Experiment/Design</i>                                                                                     | 68        |
| 4.8.2               | <i>Phase 3c Variables.</i>                                                                                                   | 68        |
| 4.8.3               | <i>Phase 3c Attributes (Multiple Layer Evaluation of Density and Homogeneity of Reinforcement)</i>                           | 68        |
| 4.8.4               | <i>Phase 3c Statistical Treatment</i>                                                                                        | 69        |
| 4.9                 | PHASE 3D: CRYSTALLOGRAPHIC AND CHEMICAL ANALYSIS OF MMC MATERIAL.                                                            | 69        |
| 4.9.1               | <i>Overview of The Experiment / Design</i>                                                                                   | 69        |
| 4.9.2               | <i>Phase 3d Variables</i>                                                                                                    | 69        |
| 4.9.2.1             | <i>Chemical etching Variables.</i>                                                                                           | 69        |
| 4.9.2.2             | <i>X-Ray Spectroscopy (EDS) Variables</i>                                                                                    | 70        |
| 4.9.2.3             | <i>X-Ray Diffraction (EDX) Variables</i>                                                                                     | 70        |
| 4.9.3               | <i>Phase 3d Attributes</i>                                                                                                   | 71        |
| 4.9.3.1             | <i>Chemical etching Attributes.</i>                                                                                          | 71        |
| <b>CHAPTER FIVE</b> |                                                                                                                              | <b>72</b> |
| <b>5.0</b>          | <b>RESULTS AND DISCUSSION.</b>                                                                                               | <b>72</b> |
| 5.1                 | INTRODUCTION.                                                                                                                | 72        |
| 5.2                 | PHASE 1A: BASELINE ASSESSMENT OF RAW MATERIALS.                                                                              | 72        |
| 5.2.1               | <i>Phase 1a Baseline Assessment of Moisture Content.</i>                                                                     | 72        |
| 5.2.2               | <i>Phase 1a Baseline Assessment of Rheological Characteristics.</i>                                                          | 73        |
| 5.2.3               | <i>Phase 1a Baseline Assessment of Particle Size, Size Distribution.</i>                                                     | 74        |
| 5.2.3.1             | <i>Ti6Al4V Particle Size and Size Distribution Baseline Assessment.</i>                                                      | 74        |
| 5.2.3.2             | <i>SiC Particle Size and Size Distribution Baseline Assessment.</i>                                                          | 81        |
| 5.2.4               | <i>Phase 1a Baseline Assessment of Ti6Al4V Particle Morphology.</i>                                                          | 87        |
| 5.2.4.1             | <i>Scanning Electron Microscopy of Ti6Al4V Powder.</i>                                                                       | 88        |



|                        |                                                                                                                        |            |
|------------------------|------------------------------------------------------------------------------------------------------------------------|------------|
| 5.2.5                  | <i>Phase 1a Baseline Assessment of SiC Particle Morphology</i> .....                                                   | 89         |
| 5.2.5.1                | <i>Scanning Electron Microscopy of SiC Powder</i> .....                                                                | 90         |
| 5.3                    | PHASE 1B: BASELINE ASSESSMENT OF Ti6Al4V SINGLE BEADS EVALUATED AGAINST ENERGY DENSITY.                                | 92         |
| 5.4                    | PHASE 2A: MECHANICALLY ALLOYED MMC FEEDSTOCK. ....                                                                     | 111        |
| 5.4.1                  | <i>Reinforcement Material Embed onto the Surface of the Matrix Material</i> .....                                      | 111        |
| 5.4.1.1                | <i>Rounded Particles</i> .....                                                                                         | 115        |
| 5.4.1.2                | <i>Non-rounded particles</i> .....                                                                                     | 116        |
| 5.4.1.3                | <i>Cylindrical Particles</i> .....                                                                                     | 116        |
| 5.4.1.4                | <i>Flattened Particles</i> .....                                                                                       | 117        |
| 5.4.1.5                | <i>Agglomerated Particles</i> .....                                                                                    | 117        |
| 5.4.1.6                | <i>Cleaved Agglomerated Particles</i> .....                                                                            | 118        |
| 5.4.1.7                | <i>Flattened Agglomerated Particles</i> .....                                                                          | 118        |
| 5.4.2                  | <i>Minimise Increase in Particle Size</i> .....                                                                        | 119        |
| 5.4.3                  | <i>Minimise Change in Particles Morphology</i> .....                                                                   | 122        |
| 5.4.4                  | <i>Homogeneously Mix the Reinforcement Material Throughout the Feedstock</i> .....                                     | 125        |
| 5.4.5                  | <i>Avoid Contamination</i> .....                                                                                       | 125        |
| 5.5                    | PHASE 2B: MMC FEEDSTOCK ANALYSIS FOR MOISTURE, SIZE, MORPHOLOGY AND RHEOLOGY IN COMPARISON TO BASELINE ASSESSMENT..... | 132        |
| 5.5.1                  | <i>Assessment of MMC Feedstock Moisture Content</i> .....                                                              | 132        |
| 5.5.2                  | <i>Assessment of MMC Feedstock Size and Morphology</i> .....                                                           | 132        |
| 5.5.2.1                | <i>MMC feedstock Particle Size and Size Distribution Comparison</i> .....                                              | 134        |
| 5.5.3                  | <i>MMC Feedstock Rheology comparison against Ti6Al4V</i> .....                                                         | 140        |
| 5.6                    | PHASE 3A: MMC SINGLE BEAD EVALUATION AGAINST ENERGY DENSITY COMPARED TO BASELINE RESULTS.....                          | 140        |
| 5.7                    | PHASE 3B: HATCH SPACING EVALUATION OF MULTIPLE BEADS.....                                                              | 157        |
| 5.8                    | PHASE 3C: MULTIPLE LAYER EVALUATION OF DENSITY AND HOMOGENEITY OF REINFORCEMENT.....                                   | 164        |
| 5.9                    | PHASE 3D: CRYSTALLOGRAPHIC AND CHEMICAL ANALYSIS OF MMC MATERIAL.....                                                  | 165        |
| <b>CHAPTER SIX</b>     | .....                                                                                                                  | <b>167</b> |
| <b>6.0 CONCLUSIONS</b> | .....                                                                                                                  | <b>167</b> |
| 6.1                    | BASELINE ASSESSMENT OF RAW MATERIALS (Ti6Al4V).....                                                                    | 167        |
| 6.2                    | BASELINE ASSESSMENT OF RAW MATERIALS (SiC).....                                                                        | 167        |
| 6.3                    | BASELINE ASSESSMENT OF Ti6Al4V SINGLE BEADS.....                                                                       | 168        |
| 6.4                    | MECHANICAL ALLOYING (MA) OF METAL MATRIX COMPOSITE (MMC) MATERIALS.....                                                | 168        |
| 6.5                    | MMC FEEDSTOCK ANALYSIS FOR MOISTURE, SIZE, MORPHOLOGY AND RHEOLOGY IN COMPARISON TO BASELINE ASSESSMENT.....           | 169        |
| 6.6                    | ASSESSMENT OF MMC SINGLE BEADS EVALUATED AGAINST ENERGY DENSITY IN COMPARISON TO Ti6Al4V BASELINE.....                 | 169        |
| 6.7                    | HATCH SPACING EVALUATION OF MMC MATERIAL, MULTIPLE BEADS.....                                                          | 169        |

|                           |                                                                          |            |
|---------------------------|--------------------------------------------------------------------------|------------|
| 6.8                       | MULTI-LAYER EVALUATION OF DENSITY AND HOMOGENEITY OF REINFORCEMENT. .... | 170        |
| 6.9                       | CRYSTALLOGRAPHIC AND CHEMICAL ANALYSIS OF MMC MATERIAL. ....             | 170        |
| <b>CHAPTER SEVEN.....</b> |                                                                          | <b>171</b> |
| 7.0                       | RECOMMENDATIONS FOR FUTURE WORK.....                                     | 171        |
| <b>CHAPTER EIGHT.....</b> |                                                                          | <b>172</b> |
| 8.0                       | CONTRIBUTION TO KNOWLEDGE .....                                          | 172        |
| <b>CHAPTER NINE .....</b> |                                                                          | <b>173</b> |
| 9.0                       | REFERENCES .....                                                         | 173        |
| <b>CHAPTER TEN.....</b>   |                                                                          | <b>187</b> |
| 10.0                      | APPENDICES .....                                                         | 187        |
|                           | APPENDIX 1, ZOZ MALTOZ 3.2.1 SOFTWARE CONFIGURATION. ....                | 187        |
|                           | APPENDIX 2, STRUERS, TITANIUM ALLOYS (DIAPRO, APPLICATION NOTES) .....   | 188        |
|                           | APPENDIX 3, XRD ANALYSIS RESULTS .....                                   | 189        |

# List of Figures

|            |                                                                                                                   |    |
|------------|-------------------------------------------------------------------------------------------------------------------|----|
| Figure 1   | Number of AM systems for metal parts sold, according to Wohler’s report 2017 (Algardh, et al., 2017).....         | 2  |
| Figure 2   | Available alloys for the SLM process (EPMA European Powder Metallurgy Association 2018).....                      | 9  |
| Figure 3   | Effect of alpha-stabilising elements on titanium (AZo Metals 2001). ....                                          | 13 |
| Figure 4   | SiC Structures (Eriksson, J. 2010).....                                                                           | 15 |
| Figure 5   | Reinforcement (Kainer, 2006).....                                                                                 | 17 |
| Figure 6   | Wettability Contact Angle $\theta$ (Banerjee, 2008).....                                                          | 25 |
| Figure 7   | Evidence of Gas Entrapment in Feedstock (Lyll, 2017). ....                                                        | 26 |
| Figure 8   | Dimensioned cross sectioned 316L stainless steel single beads (Yadroitsev, et al., 2012).....                     | 27 |
| Figure 9   | Typical Powder Characterisation Parameters (Benson, and Snyders, 2015).....                                       | 28 |
| Figure 10  | Inter-Relationships of Characteristics on Powder Behaviour (Benson and Snyders, 2015).....                        | 28 |
| Figure 11  | SLM Powder Production Methods (Murray, Sandvik Osprey 2015) .....                                                 | 30 |
| Figure 12  | EOS DM20 - Tungsten Powder Mixed by Hand (Lyll, 2009) .....                                                       | 32 |
| Figure 13  | Mechanical Alloying Systems, (ZoZ GmbH 2018).....                                                                 | 33 |
| Figure 14  | High Energy Mill Cross Sectional View (Zoz, H. Ren, H. 2008).....                                                 | 34 |
| Figure 15  | SiC Reinforcement Material Embedded onto Ti6Al4V Matrix Material by MA (Lyll, 2012).....                          | 35 |
| Figure 17a | Flake or Plate Like Structures Produced by Excessive MA (Lyll, 2012) .....                                        | 36 |
| Figure 17b | Tube or Cylindrical Like Structures Produced by Excessive MA (Lyll, 2012) .....                                   | 36 |
| Figure 18  | Initial Test Samples. Aborted after approx. 1.5mm.....                                                            | 38 |
| Figure 19  | PSW version 3.4 (EOS GmbH).....                                                                                   | 39 |
| Figure 20  | EOS M270 Process Setup Flow .....                                                                                 | 40 |
| Figure 21  | In-Process Fractures.....                                                                                         | 41 |
| Figure 22  | MMC Fracture Surface. ....                                                                                        | 42 |
| Figure 23  | Ti Fracture Surface (Yin et al., 2015).....                                                                       | 42 |
| Figure 24  | MMC Fracture Surface (50 x magnification).....                                                                    | 43 |
| Figure 25  | Methodology Workflow.....                                                                                         | 45 |
| Figure 26  | Energy Density ( $J/mm^3$ ) Over Scan Speed (V) (mm/s).....                                                       | 54 |
| Figure 27  | Mini Platforms with Reduced Build Area for Limited Feedstock, Recoated Using 45 – 50 $\mu m$ Two Rail System..... | 56 |
| Figure 28  | EOSPrint 1.5, Layout for Ti6Al4V Phase 3b.....                                                                    | 57 |
| Figure 29  | Primes laser power Pocket Monitor PMT 05P.....                                                                    | 57 |
| Figure 30  | MA (Mechanical Alloying) Equipment .....                                                                          | 60 |
| Figure 31  | Symoloyer CM01 Detailed View .....                                                                                | 61 |
| Figure 32  | Haake Phoenix ii Chiller Unit .....                                                                               | 62 |

|           |                                                                                                                                                                 |     |
|-----------|-----------------------------------------------------------------------------------------------------------------------------------------------------------------|-----|
| Figure 33 | MVR (Maximum Volume Reinforcement) (%).....                                                                                                                     | 64  |
| Figure 34 | Powder Mixing Calculations.....                                                                                                                                 | 65  |
| Figure 35 | EDS Cobalt Calibration Sample.....                                                                                                                              | 70  |
| Figure 36 | Panalytical Empyrean EDX apparatus.....                                                                                                                         | 71  |
| Figure 37 | Ti6Al4V Size Distribution Baseline $X_{c \text{ Min}}$ .....                                                                                                    | 76  |
| Figure 38 | Ti6Al4V Size Distribution Baseline $X_{\text{area}}$ .....                                                                                                      | 77  |
| Figure 39 | Volume Based Distribution Curve Results for Ti6Al4V Baseline $X_{c \text{ Min}}$ .....                                                                          | 78  |
| Figure 40 | Volume Based Distribution Curve for Ti6Al4V Baseline $X_{\text{area}}$ .....                                                                                    | 79  |
| Figure 41 | Volume Based Distribution Curve for Ti6Al4V Baseline $b/l$ .....                                                                                                | 80  |
| Figure 42 | SiC Size Distribution baseline $x_{c \text{ min}}$ .....                                                                                                        | 83  |
| Figure 43 | SiC Size Distribution Baseline $X_{\text{area}}$ .....                                                                                                          | 84  |
| Figure 44 | Volume Based Distribution Curve for SiC Baseline $X_{c \text{ Min}}$ .....                                                                                      | 85  |
| Figure 45 | Volume Based Distribution Curve for SiC Baseline $X_{\text{area}}$ .....                                                                                        | 86  |
| Figure 46 | Retsch Camsizer X2 Database Images of Nonrounded Ti6Al4V Particles ( $B/L \leq 0.850$ ).....                                                                    | 87  |
| Figure 47 | Retsch Camsizer X2 Database Images of Rounded Ti6Al4V Particles ( $B/L \geq 0.850$ ).....                                                                       | 88  |
| Figure 48 | Scanning Electron Microscopy of Ti6Al4V Powder (A) 1000 X Magnification (B) 2000 X Magnification.....                                                           | 89  |
| Figure 49 | Scanning Electron Microscopy Of Ti6Al4V Powder 8,000 X Magnification. ....                                                                                      | 89  |
| Figure 50 | Retsch Camsizer X2 Database Images of Nonrounded SiC Particles ( $B/L \leq 0.600$ ).....                                                                        | 90  |
| Figure 51 | Scanning Electron Microscopy of SiC Powder 30,000 X Magnification.....                                                                                          | 91  |
| Figure 52 | Scanning Electron Microscopy of SiC Powder 70,000 X Magnification.....                                                                                          | 91  |
| Figure 53 | Scanning Electron Microscopy of SiC Powder 90,000 X Magnification.....                                                                                          | 92  |
| Figure 54 | Comparison Between Ti6Al4V Bead Widths ( $w1$ ) at 150 W, 250 W and 350 W Versus Energy Density.....                                                            | 105 |
| Figure 55 | Comparison Between Ti6Al4V Bead Heights ( $h1$ ) at 150 W, 250 W and 350 W Versus Energy Density.....                                                           | 107 |
| Figure 56 | Comparison Between Ti6Al4V Substrate Penetration ( $h2$ ) at 150 W, 250 W and 350 W Versus Energy Density.....                                                  | 108 |
| Figure 57 | Comparison Between Ti6Al4V Substrate Penetration Width ( $W2$ ) at 150 W, 250 W and 350 W Versus Energy Density.....                                            | 109 |
| Figure 58 | Comparison between Ti6Al4V Powder (a, c, e) and MA Feedstock (b, d, f) After 5 Minutes at 1,000 X (a, b), 2,000 X (c, d) and 16,000 X Magnification (e, f)..... | 112 |
| Figure 59 | MA Feedstock After 8 Minutes at 2,000 X Magnification (a) and at 16,000 X Magnification (b).....                                                                | 113 |
| Figure 60 | MA Feedstock After 16 Minutes Compared at 2,000 X Magnification (a) and 16,000 X Magnification (b). ....                                                        | 113 |
| Figure 61 | MA Feedstock After 24 Minutes at 1,000 X Magnification (a) and at 2,000 X Magnification (b).....                                                                | 114 |

|           |                                                                                                                                       |     |
|-----------|---------------------------------------------------------------------------------------------------------------------------------------|-----|
| Figure 62 | MA Feedstock After 32 Minutes at 1,000 X Magnification (a) and at 2,000 X Magnification (b).....                                      | 114 |
| Figure 63 | MA Feedstock After 40 Minutes at 1,000 X Magnification (a) and at 2,000 X Magnification (b).....                                      | 115 |
| Figure 64 | Rounded Powder Particle (SEM 1,000 X Magnification, Thirty-Two Minutes Processing).....                                               | 116 |
| Figure 65 | Single Impact on Powder Particle (SEM 1,000 X Magnification, Thirty-Two Minutes Processing).....                                      | 116 |
| Figure 66 | Cylindrical Ti6Al4V Powder Particle (SEM 1,000 X Magnification, Thirty-Two Minutes Processing).....                                   | 116 |
| Figure 67 | Flattened Powder Particle (SEM 1,000 X Magnification, Thirty-Two Minutes Processing).....                                             | 117 |
| Figure 68 | Agglomerated Powder Particles (SEM 1,000 X Magnification, Thirty-Two Minutes Processing).....                                         | 118 |
| Figure 69 | Cleaved Agglomerated Powder Particle (SEM 1,000 X Magnification, Thirty-Two Minutes Processing).....                                  | 118 |
| Figure 70 | Flattened Agglomerated Ti6Al4V Powder Particle (SEM 1,000 X Magnification, Thirty-Two Minutes Processing).....                        | 119 |
| Figure 71 | Volume Based Distribution Analysis for $X_c$ Min, MA Feedstock.....                                                                   | 120 |
| Figure 72 | Volume Based Comparison of Aspect Ratio (b/l) For Mechanically Alloyed Feedstock.....                                                 | 121 |
| Figure 73 | Mechanical Alloying Ti6Al4V - SiC (5 Min).....                                                                                        | 122 |
| Figure 74 | Mechanical Alloying Ti6Al4V - SiC (8 Min).....                                                                                        | 123 |
| Figure 75 | Mechanical Alloying Ti6Al4V - SiC (16 Min).....                                                                                       | 123 |
| Figure 76 | Mechanical Alloying Ti6Al4V - SiC (24 Min).....                                                                                       | 124 |
| Figure 77 | Mechanical Alloying Ti6Al4V - SiC (32 Min).....                                                                                       | 124 |
| Figure 78 | Mechanical Alloying Ti6Al4V - SiC (40 Min).....                                                                                       | 125 |
| Figure 79 | EDS Area Analysis of Ti6Al4V Sample 1, Sectioned Horizontally.....                                                                    | 126 |
| Figure 80 | EDS Area Analysis of Ti6Al4V Sample 2, Sectioned Vertically.....                                                                      | 127 |
| Figure 81 | EDS Area 1 Analysis of MMC Sample 3, Sectioned Horizontally.....                                                                      | 128 |
| Figure 82 | EDS Area 2 Analysis of MMC Sample 3, Sectioned Horizontally.....                                                                      | 129 |
| Figure 83 | EDS Area 3 Analysis of MMC Sample 3, Sectioned Horizontally.....                                                                      | 129 |
| Figure 84 | EDS Spot 1 Analysis of MMC Sample 3, Sectioned Horizontally.....                                                                      | 130 |
| Figure 85 | EDS Spot 2 Analysis of MMC Sample 3, Sectioned Horizontally.....                                                                      | 131 |
| Figure 86 | EDS Spot 3 Analysis of MMC Sample 3, Sectioned Horizontally.....                                                                      | 131 |
| Figure 87 | $X_{c \text{ Min}}$ Comparison Between Ti6Al4V Baseline and MMC Feedstock Alloyed for 24 Minutes.....                                 | 133 |
| Figure 88 | $X_{\text{area}}$ Comparison Between Ti6Al4V Baseline and MMC Feedstock Alloyed for 24 Minutes.....                                   | 136 |
| Figure 89 | $X_{c \text{ Min}}$ Volume Based Distribution Curve Comparison Between Ti6Al4V Baseline and MMC Feedstock Alloyed for 24 Minutes..... | 137 |

|            |                                                                                                                                  |     |
|------------|----------------------------------------------------------------------------------------------------------------------------------|-----|
| Figure 90  | $X_{area}$ Volume Based Distribution Curve Comparison Between Ti6Al4V Baseline and MMC Feedstock Alloyed for 24 Minutes. ....    | 138 |
| Figure 91  | b/l Volume Based Distribution Curve Comparison Between Ti6Al4V Baseline and MMC Feedstock Alloyed for 24 Minutes .....           | 139 |
| Figure 92  | Comparison Between MMC and Ti6Al4V Bead Widths ( $w_1$ ) at 150 W, 250 W and 350 W Versus Energy Density. ....                   | 152 |
| Figure 93  | Linear Trend Line Comparison Between MMC and Ti6Al4V Bead Widths ( $w_1$ ) at 150 W, 250 W and 350 W Versus Energy Density. .... | 153 |
| Figure 94  | Comparison Between MMC and Ti6Al4V Bead Height ( $h_1$ ) at 150 W, 250 W and 350 W Versus Energy Density .....                   | 154 |
| Figure 95  | Comparison Between MMC and Ti6Al4V Substrate Penetration ( $h_2$ ) at 150 W, 250 W and 350 W Versus Energy Density. ....         | 155 |
| Figure 96  | Comparison Between MMC and Ti6Al4V Substrate Penetration Width ( $w_2$ ) at 150 W, 250 W and 350 W Versus Energy Density. ....   | 156 |
| Figure 97  | Multiple Layer Evaluation of Density and Homogeneity of Reinforcement. ....                                                      | 164 |
| Figure 98  | Optical microscopic view of MMC material (2K x magnification) .....                                                              | 165 |
| Figure 99  | XRD Stick Pattern (98-002-8341 $C_1Si_1$ , 00-023-1079 $Ti_5Si_4$ , 98-003-9830 $O_2Si_1$ ) .....                                | 166 |
| Figure 100 | XRD Diffractogram ( $C_1Si_1$ green, $Ti_5Si_4$ Blue, $O_2Si_1$ Grey) .....                                                      | 166 |

# List of Tables

|          |                                                                                                                       |     |
|----------|-----------------------------------------------------------------------------------------------------------------------|-----|
| Table 1  | Powders available for SLM manufacturing (Algardh, et al., 2017) .....                                                 | 3   |
| Table 2  | Ti6Al4V Material Composition (EOS GmbH 2018).....                                                                     | 10  |
| Table 3  | Typical Physical Properties of Ti6Al4V (AZo metals 2019).....                                                         | 11  |
| Table 4  | SiC Material Properties (AZo Metals 2019) .....                                                                       | 14  |
| Table 5  | Environmental Atmosphere (Gas) EOS GmbH (2018) .....                                                                  | 23  |
| Table 6  | International Standards for Powder Characterisation (ISO 17296-3 2014).....                                           | 29  |
| Table 7  | SLM Powder Manufactures Worldwide (2018) .....                                                                        | 30  |
| Table 8  | Initial Test Samples.....                                                                                             | 38  |
| Table 9  | EOS M270, Ti6Al4V Standard Parameters (EOS GmbH) .....                                                                | 39  |
| Table 10 | Powder Analysis Sample Sizes.....                                                                                     | 46  |
| Table 11 | Rheological Experimentation with Respect to This Research.....                                                        | 49  |
| Table 12 | Moisture Analysis Process Variables (Adam, 2018) .....                                                                | 51  |
| Table 13 | Variables for Particle Size and Morphological Analysis (Retsch, 2018).....                                            | 51  |
| Table 14 | Variable for Rheological Analysis (LPW Technologies 2017).....                                                        | 52  |
| Table 15 | Variables for Particle Size and Morphological Analysis (Retsch, 2018).....                                            | 52  |
| Table 16 | Energy Density Matrix (J/mm <sup>3</sup> ).....                                                                       | 53  |
| Table 17 | Build Variables for Single Bead Experiment .....                                                                      | 58  |
| Table 18 | Build Attributes for Single Bead Experiment.....                                                                      | 58  |
| Table 19 | Hatch Spacing Calculation Form. ....                                                                                  | 67  |
| Table 20 | Build Attributes for Hatch Spacing Experiment.....                                                                    | 68  |
| Table 21 | Build Attributes for Multiple Layer Experiment .....                                                                  | 69  |
| Table 22 | Moisture Content Results (Initial Analysis) .....                                                                     | 72  |
| Table 23 | Moisture Content Results After Moisture Removal Process.....                                                          | 73  |
| Table 24 | Rheological Characteristics for Ti6Al4V And Sic Powders Prior To MA .....                                             | 73  |
| Table 25 | Statistical Results for Ti6Al4V Particle Size and Distribution ( $X_{c\ Min}$ ) Baseline Results.....                 | 74  |
| Table 26 | Statistical Results for Ti6Al4V Particle Size and Distribution, $X_{c\ Min}$ Versus $X_{area}$ Baseline Results ..... | 75  |
| Table 27 | Statistical Results for SiC Particle Size and Distribution ( $X_{c\ Min}$ ) Baseline Results .....                    | 81  |
| Table 28 | Statistical Results for SiC Particle Size and Distribution, $X_{c\ Min}$ Versus $X_{c\ Area}$ Baseline Results. ....  | 81  |
| Table 29 | Phase 1b, Baseline Assessment of Ti6Al4V Single Beads Evaluated Against Energy Density At 150 W.....                  | 94  |
| Table 30 | Phase 1b, Baseline Assessment of Ti6Al4V Single Beads Evaluated Against Energy Density at 250 W.....                  | 97  |
| Table 31 | Phase 1b, Baseline Assessment of Ti6Al4V Single Beads Evaluated Against Energy Density at 350 W.....                  | 101 |
| Table 32 | Volume Based Distribution Analysis Comparison for MA Feedstock.....                                                   | 119 |

|          |                                                                                                                               |     |
|----------|-------------------------------------------------------------------------------------------------------------------------------|-----|
| Table 33 | Moisture Content Results for MA Feedstock in Comparison to baseline Assessments.                                              | 132 |
| Table 34 | Statistical Results for Ti6Al4V Particle Size and Distribution ( $X_{c \text{ Min}}$ ) Baseline Results.                      | 134 |
| Table 35 | Statistical Results for Ti6Al4V Particle Size and Distribution, $X_{c \text{ Min}}$ Versus $X_{\text{area}}$ Baseline Results | 135 |
| Table 36 | Comparison of Rheological Characteristics for Ti6Al4V And MMC Feedstock.                                                      | 140 |
| Table 37 | Phase 3a; MMC Single Bead Evaluation Against Energy Density Compared to Baseline Results At 150 W                             | 141 |
| Table 38 | Phase 3a; MMC Single Bead Evaluation Against Energy Density Compared to Baseline Results At 250 W                             | 145 |
| Table 39 | Phase 3a; MMC Single Bead Evaluation Against Energy Density Compared to Baseline Results At 350 W                             | 148 |
| Table 40 | Hatch Spacing Calculation.                                                                                                    | 157 |
| Table 41 | Cross-sectional Views of Hatch Spacing, 150 (W), 1000 mm/s (v) 0.030 mm (t).                                                  | 159 |
| Table 42 | Cross-sectional Views of Hatch Spacing, 250 (W), 1000 mm/s (v) 0.030 mm (t).                                                  | 160 |
| Table 43 | Cross-sectional Views of Hatch Spacing, 250 (W), 667 mm/s (v) 0.030 mm (t).                                                   | 160 |
| Table 44 | Cross-sectional Views of Hatch Spacing, 250 (W), 500 mm/s (v) 0.030 mm (t).                                                   | 161 |
| Table 45 | Cross-sectional Views of Hatch Spacing, 250 (W), 333 mm/s (v) 0.030 mm (t).                                                   | 162 |
| Table 46 | Cross-sectional Views of Hatch Spacing, 350 (W), 1000 mm/s (v) 0.030 mm (t).                                                  | 163 |
| Table 47 | Cross-sectional Views of Hatch Spacing, 350 (W), 667 mm/s (v) 0.030 mm (t).                                                   | 163 |
| Table 48 | Phase 3c Build Parameters                                                                                                     | 164 |
| Table 49 | Selected Build Parameters from Phase 3b.                                                                                      | 170 |



# Nomenclature

|                      |                                                                                               |
|----------------------|-----------------------------------------------------------------------------------------------|
| 1-Q3 (b/l = 0.850)   | Volume percentage of round particles                                                          |
| $\alpha$             | Alpha, used to describe a metallic phase                                                      |
| $\alpha_1$           | First contact angle                                                                           |
| $\alpha_2$           | Second contact angle                                                                          |
| $\beta$              | Beta, used to describe a metallic phase                                                       |
| b/l                  | Aspect ration                                                                                 |
| b/l <sub>3</sub>     | Mean aspect ration                                                                            |
| $c$                  | Specific heat capacity (j/Kg°C)                                                               |
| $\cos \theta$        | cosign of the contact angle (Deg)                                                             |
| D10                  | 10 Percentiles                                                                                |
| D50                  | 50 Percentiles                                                                                |
| D90                  | 90 Percentiles                                                                                |
| $D_m$                | Average particle size ( $X_{c \text{ min}}$ ) of the matrix material ( $\mu\text{m}$ )        |
| $D_r$                | Average particle size ( $X_{c \text{ min}}$ ) of the reinforcement material ( $\mu\text{m}$ ) |
| Ed                   | Energy density                                                                                |
| F                    | Volume fraction of reinforcement material (%)                                                 |
| $g$                  | Grams                                                                                         |
| $h$                  | Hatch spacing                                                                                 |
| $h_1$                | Bead height                                                                                   |
| $h_2$                | Substrate penetration                                                                         |
| $m$                  | Mass (Kg)                                                                                     |
| min                  | Minutes                                                                                       |
| MVR                  | Maximum volume of reinforcement material (%)                                                  |
| $Mv_3(\bar{x})$      | Sample mean size                                                                              |
| P                    | Density of the MMC ( $\text{g}/\text{Cm}^3$ )                                                 |
| $P$                  | Laser power                                                                                   |
| $P_m$                | Density of the matrix material ( $\text{g}/\text{Cm}^3$ )                                     |
| $P_r$                | Density of the reinforcement material ( $\text{g}/\text{Cm}^3$ )                              |
| Q3                   | Volume based distribution                                                                     |
| S                    | Spreading coefficient                                                                         |
| $s$                  | Spot size                                                                                     |
| sec                  | Seconds                                                                                       |
| $t$                  | Layer thickness                                                                               |
| $v$                  | Scan speed                                                                                    |
| W                    | Watts                                                                                         |
| $w_1$                | Width of bead                                                                                 |
| $w_2$                | Width of dilution area                                                                        |
| $X_{\text{area}}$    | Width of circumferential particle boundary                                                    |
| $x_{c \text{ min}}$  | Shortest particle length                                                                      |
| $X_{\text{Fe Max}}$  | Longest particle length                                                                       |
| $\gamma$             | Gamma, Free surface energy of solids and liquids                                              |
| $\gamma_{\text{sl}}$ | Solid-liquid interface                                                                        |
| $\gamma_{\text{sv}}$ | Solid- vapour interface                                                                       |
| $\gamma_{\text{lv}}$ | Liquid-vapour interface                                                                       |
| $\Delta E_t$         | Change in thermal energy (J)                                                                  |
| $\Delta \emptyset$   | Temperature Change (°C)                                                                       |

# Glossary of Acronyms.

|                 |                                                                                                |
|-----------------|------------------------------------------------------------------------------------------------|
| 3D.....         | Three Dimensional                                                                              |
| Al.....         | Aluminium                                                                                      |
| AM.....         | Additive Manufacturing                                                                         |
| AS.....         | As Built                                                                                       |
| Ar.....         | Argon                                                                                          |
| <i>A</i> R..... | Aspect Ratio                                                                                   |
| BCC.....        | Body Centred Cubic                                                                             |
| BPR.....        | Ball to Powder Ratio                                                                           |
| BSE.....        | Back Scatter Electron Microscopy                                                               |
| B/W.....        | By Weight                                                                                      |
| B/V.....        | By Volume                                                                                      |
| CAD.....        | Computer Aided Design                                                                          |
| C.....          | Carbon                                                                                         |
| DMLS.....       | Direct Metal Laser Sintering                                                                   |
| ED.....         | Energy Density                                                                                 |
| Fe.....         | Iron                                                                                           |
| FCC.....        | Face Centred Cubic                                                                             |
| HAZ.....        | Heat Effected Zone                                                                             |
| HCP.....        | Hexagonal Close Packed                                                                         |
| H.....          | Hydrogen                                                                                       |
| LM.....         | Laser Melting                                                                                  |
| MA.....         | Mechanical Alloying                                                                            |
| MMC.....        | Metal Matrix Composite                                                                         |
| N.....          | Nitrogen                                                                                       |
| Nd: YAG.....    | Neodymium-doped Yttrium Aluminium Garnet (Nd: Y <sub>3</sub> Al <sub>5</sub> O <sub>12</sub> ) |
| O.....          | Oxygen                                                                                         |
| PM.....         | Powder Metallurgy                                                                              |
| RD.....         | Relative Density                                                                               |
| SiC.....        | Silicone Carbide                                                                               |
| SEM.....        | Scanning Electron Microscope                                                                   |
| SPHT.....       | Sphericity                                                                                     |
| SLM.....        | Selective Laser Melting                                                                        |
| STL.....        | Standard Triangulation Language or Standard Tessellation Language                              |
| Ti.....         | Titanium                                                                                       |
| Trans.....      | Transparency                                                                                   |
| V.....          | Vanadium                                                                                       |
| Wt.%.....       | Weight Percentage                                                                              |
| XDR.....        | X-Ray Diffraction                                                                              |
| Y.....          | Yttrium                                                                                        |

## Papers and Conferences

Olowofela O. H., Stanford, M., Zhang, L., Oduoza, C., Kibble, K. and Lyall, I. Mechanical Alloying of Additive Layer Manufacturing. Presented at ICCE-21 in Tenerife, Spain, 21<sup>st</sup> – 27<sup>th</sup> July 2013.

Lyall, I., Stanford, M., Kibble, K., and Lister, P A., Reliable manufacture of Additive Layer Manufacturing feed-stock for the Selective Laser Melting process via Mechanical Alloying. Presented at FAIM, Flexible Automation and Intelligent Manufacturing, Wolverhampton, UK, 23<sup>rd</sup> – 26<sup>th</sup> June 2015

# Chapter One

## 1.0 Introduction

The adoption of Selective Laser Melting (SLM) for metal parts is becoming more prevalent. Whilst this is a small proportion of the global 3D printing industry, it stands at the pinnacle of the 3D industry due to the technological level, engineering expertise and infrastructure required (Algardh, et al., 2017). Technological advances over the last ten years have seen the technology transformed from prototype / rapid visualisation to one of fabricating fully functional parts with additional functionality (Gupta 2017, Negi 2013). Current users of the technology have reached a position of confidence with the process, confident that parts manufactured through this manufacturing route will offer, functionality, accuracy, reliability and will be fit for purpose. As the industry expands with new companies joining each year bringing fresh ideas and innovation, the industry has recognised that moving forward there are three key areas of development namely:

- Process,
- Applications,
- Materials (Chalabyan, 2017; Sculpto, 2017).

The process is advancing with new machines being developed by multiple manufacturers including EOS GmbH, Renishaw Plc, Concept Laser GmbH, and SLM Solutions GmbH. Quality, accuracy, and repeatability are the key areas of concern for the customer and manufacturers have developed better in-process monitoring and feedback systems that assist in accurately setting the build process and monitoring it to produce parts with fewer defects and in process build failures. Areas of process development include the development of laser technology, larger build volumes, layer thicknesses, and improved scanning strategies. (Sevcik, 2017)

Applications are being presented by a range of industrial sectors such as aerospace, space, medical, jewellery, automotive, toolmaking and electronics. However, many sectors wrongly believe that materials used in their industry will translate across to the SLM process. As more research is undertaken into how materials behave during SLM processing, it is becoming evident that simply converting metals to powders and building with them does not work. Materials when processed as powders exhibit qualities unlike their wrought or cast counterparts. Post-processing has also demonstrated that established regimes for wrought and cast materials do not translate directly, hence new regimes are needed to be developed. (Renishaw PLC. 2016)

Materials that are suitable for the SLM process have traditionally been slow to be introduced to the marketplace due to the extensive and time-consuming development process required for

characterisation. Current materials such as titanium alloys (Ti6Al4V), aluminium alloys (Al), maraging steel, cobalt chrome steel, Inconel 718 and stainless steel have been available for some time now (Eos GmbH, 2018). Research into new materials such as gold, silver, and copper (University of Wolverhampton) and Waspaloy and zirconia (Mumtaz, and Hopkinson, 2007) exemplifies that the industry requires complex materials for specific applications and therefore by association a robust method of characterising materials adequately for further “end user optimisation” is needed. (Locker, 2018)

**1.1 Research Justification**

This research investigates the characterisation of titanium-based Metal Matrix Composites (MMCs) with silicone carbide (SiC) reinforcement, employing Selective Laser Melting (SLM) techniques and the theoretical feasibility of processing such materials. MMC’s are difficult to process using conventional material-removal techniques; material-removal is normally kept to a minimum while processing, as this requires specialised tooling or grinding processes to achieve satisfactory components (Kainer, 2006). This can be cost prohibitive and time-consuming (3T RPD, 2018). Through the additive route, however, the manufacture of components is achieved by the fabrication of near net shape parts in individual layers requiring minimal finishing to only the critical surfaces, an allowance of around 0.2 mm to 0.4 mm is added to the CAD model at the design stage. (Vrancken, et al., 2014)

Currently, the additive manufacturing industry is experiencing high confidence in manufacturers and their equipment. Sales of equipment have been steadily increasing year on year. (Figure 1)

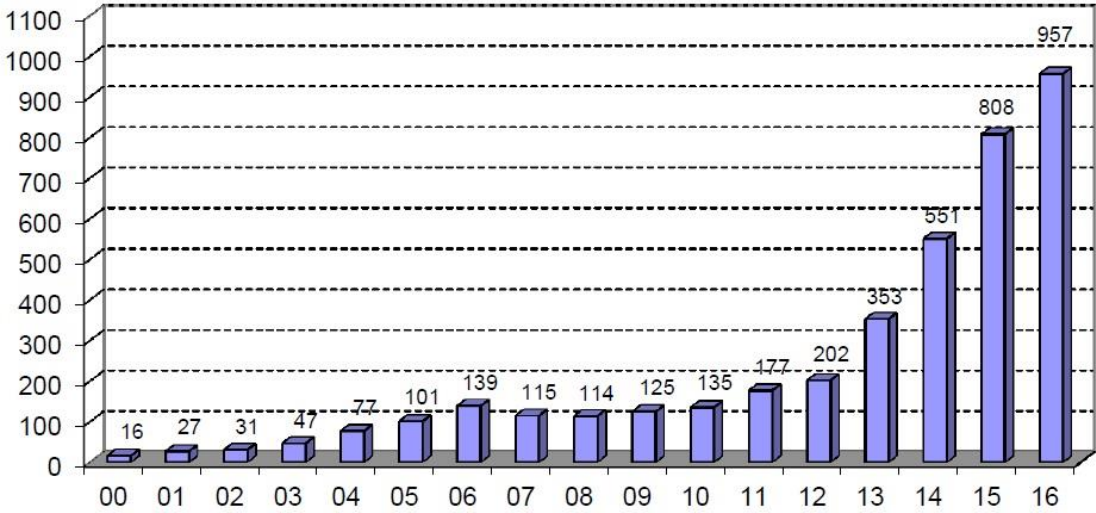


Figure 1 Number of AM systems for metal parts sold, according to Wohler’s report 2017 (Algarth, et al., 2017)

However, the development of materials (Feedstock) for the process has been slow in comparison.

Algarth (2017) wrote about the number of alloys available, voicing concerns over, what he called “a tedious and expensive process with trial and error” the overriding conclusion from his work was that if SLM is more widely adopted, a larger number of materials and materials suppliers were required.

Table 1 shows current powders available to the SLM process (Algarth, et al., 2017).

**Table 1 Powders available for SLM manufacturing (Algarth, et al., 2017)**

| Stainless                          | Fe-base and Tool steel       | Titanium             | Aluminium         | Hard metals | Nickel-based                             | Cobalt-based       | Precious |
|------------------------------------|------------------------------|----------------------|-------------------|-------------|------------------------------------------|--------------------|----------|
| 304L<br>S30403<br>1.4307           | H13<br>T20813<br>1.2344      | Pure<br>Titanium     | AlSi12            |             | 625<br>N06625<br>2.4856                  | CoCr F75<br>R31537 | Gold     |
| 316L<br>S31603<br>1.4404           | X40Cr14<br>-<br>1.2083       | Ti6Al4V              | AlSi25            |             | 718<br>N07718<br>2.4668                  |                    | Silver   |
| 420<br>S42000<br>1.4034            | 4140<br>G41400<br>1.7225     | Ti5Al2.5Sn           | AlMg3             |             | 738                                      |                    | 99,9% Cu |
| ?<br>J94224<br>1.4848              | M300<br>(K93120)<br>1.2709   | Ti6Al2.5Sn<br>4Zr2Mo | AlSi10Mg          |             | 939                                      |                    | CuSn     |
| 15-5PH<br>S15500<br>1.4545         | INVAR 36<br>K93601<br>1.3912 | Ti5Al5Mo<br>5V3Cr    | AlSi7Mg           |             | 230<br>N06230<br>2.4733                  |                    |          |
| 17-4PH<br>S17400<br>1.4542         |                              | Ti6Al7Nb             | AlSi9Cu3          |             | Waspaloy<br>N07001<br>2.4654             |                    |          |
| 347<br>S34700<br>1.4550            |                              |                      | AlMg4.5Mn<br>n0.4 |             | HX<br>N06002<br>2.4665                   |                    |          |
| Duplex<br>2205<br>S32205<br>1.4462 |                              |                      |                   |             | C-276<br>(N10276<br>?)<br>(Ni 6276<br>?) |                    |          |
| 2507<br>S32750<br>1.4410           |                              |                      |                   |             | (C-1023?)                                |                    |          |

Looking at the state of the 3D printing industry in the UK, Dickens and Minshall (2015) commented on what they considered were the fundamental barriers to the adoption of SLM, namely:

- materials,
- design, skills and education,
- costs and investment,
- standards and regulations,
- measurement and testing, and
- IP and protection.

Regarding materials, they considered that a better understanding of materials properties was required going forward, but also how the SLM machines affected the material characteristics within the process (Dickens and Minshall 2015).

Powder manufacturers have offered enhancements to existing materials, optimised for the additive process such as “Ancor TiTM” by Hoeganaes Corporation and Micro-Melt® powders by Carpenter Powder Products (US), but only a small percentage offer new material. This is due to several factors including; development cost, equipment, reliability, insurance, and industry confidence in the technology. Mostly it is due to no one having clearly defined a material characterisation methodology that works for all materials. Developers are realising that simply taking an existing material, making powder and fabricating parts is naive and simplistic. A more mature manufacturing approach is needed where Additive Manufacturing (AM) engineers will be able to:

- Design the process as they would design parts.
- Exploit sophisticated process monitoring and controls.
- Vary microstructure and properties within parts.
- Choose from a wide variety of powders (Beuth, 2017)

Historically, composite materials have offered engineers advanced material solutions for thousands of years, combining compatible materials such as metals alloys, polymer blends and so on. Combining materials from dissimilar groups does present additional challenges in the form of chemical compatibility in bonding, but at the same time offers benefits that utilise the best properties from the material types employed. MMC components exhibit improved properties such as wear resistance chemical and corrosion resistance, improved fatigue life, compressive strength, and could maintain their mechanical properties at elevated temperatures whilst resisting heat damage (Beuth, 2017).

However, due to the complex process for MMC production it can be challenging to achieve characteristics within the component and care must be taken to ensure that the reinforcement is homogeneously distributed throughout the part, often achieved through constant stirring of the molten material, referred to as Stir Casting (SC). This is also a concern in the additive process, as consecutive layers must achieve identical properties to the previously manufactured layers. The challenge here is to deliver the reinforcement evenly throughout the build and use the build process parameters to optimise the materials unique characteristics.

The benefits of making titanium based MMC over standard monolithic titanium alloys has been extensively explored. Authors such as Singerman and Jackson (1996) considered the many applications for the aerospace industry and the practicalities of production against prohibitively high production costs. They said that aerospace engineers were constantly seeking lighter weight, higher strength materials to improve performance, claiming that Titanium Metal Matrix Composites (Ti MMC) had offered the promise of significant weight saving since the 1960’s but the high cost of production and poor quality had prevented their introduction into

mainstream production (Singerman and Jackson, 1996). This highlights the requirement for high-quality cost-effective production of components for this material. Alman, and Hawk, (1999) further expand on the need for reducing the cost of MMCs. They advocated the use of particulates rather than fibres, pointing out that for many years titanium alloys and composites were only considered aerospace materials and that they were now being considered for non-aerospace applications including automotive and consumer products. They attributed this to the material's superior properties related to:

- Strength/density,
- Stiffness/density, and modulus/density,
- Creep and corrosion resistance

They proposed that these properties could be augmented by composite strengthening. However, pointing out that continuous filament reinforced titanium-matrix composites were expensive, limited by formability and highly anisotropic. They advocated the use of particulates or discontinuous reinforcement due to low cost and near isotropic properties (Alman, and Hawk, 1999). Gu et al., (2008) whilst considering Cu particulate reinforced MMCs also highlighted the benefits of particulate reinforced MMCs but stressed the unique contribution of Direct Metal Laser Sintering (DMLS), stating that the process exhibited great potential for net-shape fabrication of complex shaped particulate reinforced Cu matrix composites.

Whilst titanium has been used predominately for its light weight and strength. Titanium is nonmagnetic and corrosion resistant, relatively inert which this makes it a good choice for medical applications. Key disadvantages such as; poor wear resistance and being difficult to shape and machine means that there is considerable scope to improve its properties by using it as a matrix in an MMC condition. (Liu, 2015)

In addition, there are some unique research opportunities related to MMCs, specifically in the areas of:

- Small volume feedstock production,
- In-situ MMC fabrication through Selective Laser Melting (SLM),
- Reliable in-process reinforcement delivery method,
- Innovative process parameter development for new process materials,



## 1.2 Aim and Objectives

To fully realise the manufacture of MMC material by SLM, the underlying metallurgy and manufacturing characteristics must be understood, therefore the following aim and objectives have been set for the research.

### 1.2.1 Aim

The aim of this research is to characterise MMC feedstock production through a mechanical alloying route and evaluate the materials characteristics with regard to the SLM process.

### 1.2.2 Objectives

#### *Objective one, MMC feedstock production and characterisation.*

The processing of suitable feedstock is essential to ensure in-process reliability and stability, (Wegner and Witt, 2012). Inconsistencies in the feedstock such as particle size shape and other rheological characteristics will lead to an unsuccessful build or part failure, (Sustarsic *et al.*, 2005). Hence, objective one, is to devise a suitable MA processing regime and characterise MMC feedstock in accordance with the requirements of the SLM process.

#### *Objective two, SLM process parameter characterisation for processing MMC.*

It has been established, (Kruth, 2007), that the behaviour of materials within the SLM process is markedly different from other manufacturing methods such as casting or material removal. Materials processed by SLM must first possess an ability to change state from solid (feedstock), to liquid (melt pool) and solidify back to a solid (part) in a controllable and predictable and repeatable manner. Unlike traditional manufacturing methods where few parameters are required to process parts, the SLM process can be influenced by many complex parameters that affect the above stages and in-process conditions, (Kurzynowski, et al., 2012), many of which are still not fully understood for the currently available materials. Objective two is to characterise the material in-process. Whilst it is accepted that there are many process parameters and apparatus that cannot be modified, it is the objective to process the material by modifying a basic range of parameters and benchmarked against the characteristics of Ti6Al4V.

# Chapter two

## 2.0 Literature Review

### 2.1 Scope of the literature review.

This review focusses on the literature within the following areas:

1. Titanium and silicon carbide materials,
2. Metal matrix composites,
3. The SLM process,
4. Feedstock production for SLM.

Titanium is a highly valued material for the SLM process. It is reliably processed with consistent results, having a relatively wide processing window, it can be used for the manufacture of finely detailed structures and can be post processed through heat treatment and post machining (Negi et al., 2013). Processing with titanium powder, however, has its challenges. It is chemically reactive with oxygen and nitrogen and produces highly flammable and in some cases explosive, very fine particulates whilst being processed. This material is commonly referred to as a condensate as it is liberated during the SLM process. Titanium also suffers from the effects of internal stresses developed during processing. Research to date has informed and allowed mitigation against these challenges and over recent years the process has become safer and easier to manage.

Silicon carbide (SiC) has been selected as the reinforcement material. SiC has been used to improve strength and wear characteristics of Titanium metal matrix composites with success (Nelson et al., 2017 and Lu et al., 2006) however, it is unknown how such materials react when processed by SLM. SiC is a relatively common ceramic material, commercially produced from carbon and silicone. Its uses are varied, from abrasives to jewellery. Industrial applications find silicon carbide used in automotive and aerospace applications due to its high wear resistance and endurance to temperatures above 1800° C (Yamada and Mohri. 1991).

Metal matrix composites are far from a recent engineering development; their use has been widespread for many years, offering an opportunity to experience the properties of combined materials unachievable by a single material alone. Combining properties such as wear resistance with ductility or strength while offering weight reduction and temperature resistance has made them desirable. Metal matrix composites comprise a matrix material and a reinforcement element. MMCs promise potential within engineering but can also pose significant challenges to manufacture namely regards the homogeneity of reinforcement throughout the part, cost, batch-size and post processability (Anish et al., 2012). MMCs are most commonly used within

high strength and / or high temperature applications where the stability of the product can be more reliable over conventionally manufactured components (Singerman, and Jackson, 1996).

The SLM process has in recent years established a reputation within the advanced manufacturing sector as a reliable and repeatable process to produce complex and intricate parts that cannot be produced using traditional manufacturing routes. Complex freeform structures both internally and externally can be fabricated from a modest range of alloys from materials such as aluminium, steel and titanium.

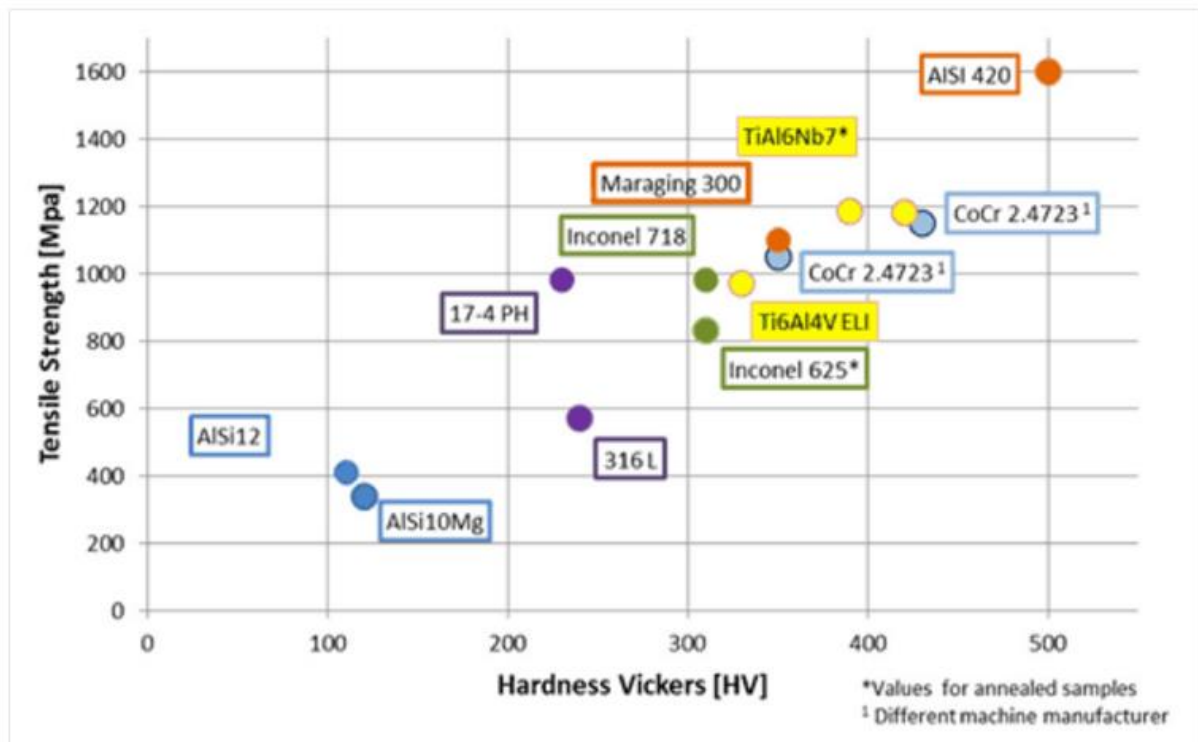
Despite this, the raw material for the SLM process, that of metal powder feedstock, is a significant controlling element. Successful downstream processing is reliant on reliable feedstock that is consistent and predictable. To this end several powder characteristics have been established as being essential to ensure process success; these are reported as chemical composition, rheology, particle size, size distribution, particle shape and layer packing density amongst others (Berretta et al., 2013). The SLM process interaction with feedstock has been shown to have a direct influence on the produced materials mechanical properties. The processing window varies from material to material but must be understood in order to select optimal process parameters for serial part production (Berretta et al., 2013).

## 2.2 Materials

### 2.2.1 Titanium Alloy (Ti6Al4V)

Ti6Al4V has become a common and highly valued material used in SLM, despite it being a costly material to produce. Two grades of titanium are commonly used: Ti6Al4V ELI (extra low inter-stitials) (grade 23) and Ti6Al4V (grade 5), grade 23 is comparable to grade 5 except that it has reduced levels of oxygen, nitrogen, carbon and iron providing increased ductility and fracture toughness (www.Arcam.com 2018). Figure 2 compares Ti6Al4V ELI (extra low inter-stitials) with other available alloys for the SLM process, tensile strength over Vickers hardness.

Figure 2 Available alloys for the SLM process (EPMA European Powder Metallurgy Association 2018)



Within this research Ti6Al4V (grade 5) has been used as this is readily available and its build characteristics are well understood, providing the research with a reliable base line from which to work. From the early days of Additive Manufacturing, Ti6Al4V has been a stock material for all feedstock suppliers and is a mainstay for machine manufacturers and users. Whilst Ti6Al4V presents some challenges for machining, having a machinability rating of 54% compared to B-1112 Steel (100%) (American Iron and Steel Industry AISI 2019) it has lent itself well to the additive industry having a reliably wide processing window, thus reducing the risk of build failure.

In Table 2, the typical chemical composition of Ti6Al4V (EOS GmbH 2018).

**Table 2 Ti6Al4V Material Composition (EOS GmbH 2018)**

| <b>Technical Data</b>              |                         |            |            |
|------------------------------------|-------------------------|------------|------------|
| <b>Powder properties</b>           |                         |            |            |
| <b>Material composition [wt.%]</b> | <b>Element</b>          | <b>Min</b> | <b>Max</b> |
|                                    | Al                      | 5.50       | 6.50       |
|                                    | V                       | 3.50       | 4.50       |
|                                    | O                       | -          | 0.150      |
|                                    | N                       | -          | 0.040      |
|                                    | C                       | -          | 0.080      |
|                                    | H                       | -          | 0.012      |
|                                    | Fe                      | -          | 0.250      |
|                                    | Y                       | -          | 0.005      |
|                                    | Other elemets,<br>each  | -          | 0.10       |
|                                    | Other elemets,<br>total | -          | 0.40       |
|                                    | Ti                      |            | bal.       |

Table 3 shows a comprehensive list of physical properties for Ti6Al4V giving maximum and minimum values.

**Table 3 Typical Physical Properties of Ti6Al4V (AZo metals 2019)**

| Property                         | Minimum Value (S.I.) | Maximum Value (S.I.) | Units (S.I.)         |
|----------------------------------|----------------------|----------------------|----------------------|
| Atomic Volume (average)          | 0.01                 | 0.011                | m <sup>3</sup> /kmol |
| Density                          | 4.429                | 4.512                | g/cm <sup>3</sup>    |
| Energy Content                   | 750                  | 1250                 | MJ/kg                |
| Bulk Modulus                     | 96.8                 | 153                  | GPa                  |
| Compressive Strength             | 848                  | 1080                 | MPa                  |
| Ductility                        | 0.05                 | 0.18                 |                      |
| Elastic Limit                    | 786                  | 910                  | MPa                  |
| Endurance Limit                  | 529                  | 566                  | MPa                  |
| Fracture Toughness               | 84                   | 107                  | MPa.m <sup>1/2</sup> |
| Elongation at break              | 14                   | 14                   | %                    |
| Hardness (Vickers)               | 349                  | 349                  |                      |
| Modulus of Rupture               | 786                  | 1080                 | MPa                  |
| Poisson's Ratio                  | 0.31                 | 0.37                 |                      |
| Shear Modulus                    | 40                   | 45                   | GPa                  |
| Tensile Strength                 | 862                  | 1200                 | MPa                  |
| Young's Modulus                  | 110                  | 119                  | GPa                  |
| Latent Heat of Fusion            | 360                  | 370                  | kJ/kg                |
| Maximum Service Temperature      | 346                  | 417                  | °C                   |
| Melting Point                    | 1604                 | 1660                 | °C                   |
| Specific Heat                    | 526                  | 526                  | J/kg- °C             |
| Thermal Conductivity             | 6.7                  | 6.7                  | W/m.K                |
| Coefficient of Thermal Expansion | 8.9                  | 8.9                  | 10 <sup>-6</sup> /°C |
| Volume Resistivity               | 168x10 <sup>-8</sup> | 170x10 <sup>-8</sup> | ohm.m                |

Whilst these physical properties are important, many are of low significance.

### 2.2.2 Mechanical Properties for Ti6Al4V Key to This Research.

Within this research, the mechanical properties of most significance for Ti6Al4V are:

- Hardness, (Vickers) 349
- Density 4.47 g/cm<sup>3</sup>
- Tensile strength 1031 MPa
- Melting point 1604 – 1660 °C
- Expansion coefficient 8.9 10<sup>-6</sup>/°C (Hidnert, 1943)

These characteristics make Ti6Al4V an ideal choice for lightweight structures requiring strength, stability and corrosion resistance at elevated temperatures, Ti6Al4V is however, susceptible to wear and whilst it can be cold formed it can tear and gall if not lubricated sufficiently. Due to its high tensile strength it is well suited to applications involving tensile load such as structural fasteners; this however, contrasts with its low elongation (14%) and

ductility (0.53) in its annealed state, leading to failure if forces exceed its tensile strength (AZo metals 2019).

### **2.2.3 Alloy Types**

In order to understand the melting characteristics during the SLM process the metallurgy of Ti6Al4V needs to be considered. The alloys of Ti6Al4V can be classified into three main groups (AZo metals, 2019).

- Alpha alloys
- Alpha-Beta alloys
- Beta alloys

Alpha alloys are non-heat treatable and are generally very weldable. They have high specific strength, good notch toughness, reasonably good ductility and have excellent properties at cryogenic temperatures. Alpha or near alpha alloys offer the highest strength and oxidation resistance at high temperature hence their use in aerospace and petrochemical applications (Zhao, et al., 2015). Alpha alloys have a Hexagonal Close Packed (HCP) crystallography (AZo metals, 2019).

Alpha-Beta alloys such as Ti6Al4V are heat treatable to varying extents and most are weldable with the risk of some loss of ductility in the weld area. These high strength alloys exhibit excellent combinations of ductility, strength and fracture toughness (Qu et al., 2012). Hot forming qualities are good but cold forming often presents difficulties (Andrade et al., 2010). Creep strength is not usually as good as in most alpha alloys (AZo metals, 2019).

Beta alloys, Beta or near beta alloys such as VT-22 and Ti-1023 are readily heat treatable, generally weldable, and offer high strength up to intermediate temperature levels. In the solution treated condition, cold formability is generally excellent due to the beta phases increased ductility. Beta alloys have a Body Centred Cubic (BCC) crystallography and are becoming used more often for aircraft landing gear, examples being the Boeing 787 and Airbus A380 (Deshpande et al., 2018). Silicone, vanadium and molybdenum stabilise the beta phase of the alloys to improve strength when solution treated (Ranju, 2015).

### **2.2.4 Crystallographic Forms of Titanium**

The metallurgy of titanium is dominated by the crystallographic transformation which takes place in the pure metal at 882°C. Below this temperature, pure titanium has a Hexagonal Close Packed structure (HCP). Above it, the structure is Body Centred Cubic (BCC) and termed beta ( $\beta$ ) (Deshpande, et al., 2018). The fundamental effect of alloying additions to titanium is the alteration of the transformation temperature and production of a two-phase field in which both alpha and beta phases are present. Elements having extensive solubility in the alpha-phase characteristically raise the transformation temperature and are called alpha stabilisers (AZo metals, 2019).

### 2.2.5 Alpha Stabilisers

Figure 3 shows the binary phase diagram formed by the addition of an alpha stabiliser (such as aluminium, oxygen, nitrogen or carbon) to titanium (AZo metals, 2019). Oxygen is added to pure titanium to produce a range of grades having increasing strength as the oxygen level is raised. Aluminium is the only other alpha stabiliser used commercially and is a major constituent of most commercial alloys (Liu and Welsch 1988).

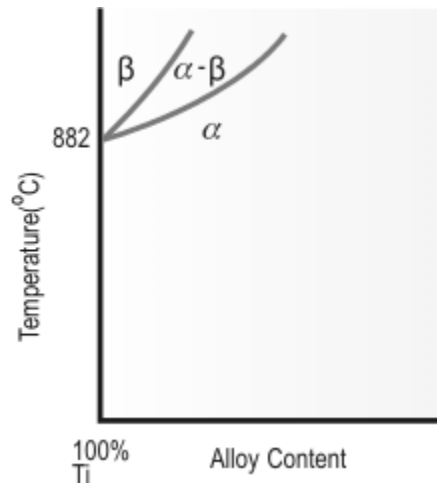


Figure 3 Effect of alpha-stabilising elements on titanium (AZo Metals 2001).

### 2.3 Silicon Carbide

Silicon Carbide (SiC) is the only compound of Silicon and Carbon atoms. Silicon carbide occurs naturally as a mineral (Moissanite), but this is very rare. In powder form, it has been produced for abrasives for over one hundred years since 1893 as its hardness (9 – 9.5 Mohs) is only a little less than natural Diamond (10 Mohs) and was discovered by Edward Acheson whilst attempting to create artificial Diamond. Whilst SiC is highly suited for devices working at high frequency, high temperature and high power (Eriksson, 2010), it is SiC superior ability to resist wear and its high fracture toughness that is primarily of interest within this research, where it is used as a reinforcement material within a metal matrix.



Table 4 shows a comprehensive list of physical properties for SiC giving maximum and minimum values

**Table 4 SiC Material Properties (AZo Metals 2019)**

| Property                         | Minimum Value (S.I.) | Maximum Value (S.I.) | Units (S.I.)                        |
|----------------------------------|----------------------|----------------------|-------------------------------------|
| Atomic Volume (average)          | 0.01                 | 0.011                | m <sup>3</sup> /kmol                |
| Density                          | 3.1                  | 3.15                 | g/cm <sup>3</sup>                   |
| Energy Content                   | 750                  | 1250                 | MJ/kg                               |
| Bulk Modulus                     | 100                  | 176                  | GPa                                 |
| Compressive Strength             | 1000                 | 1700                 | MPa                                 |
| Ductility                        | 0.01                 | 0.4                  |                                     |
| Elastic Limit                    | 172                  | 1245                 | MPa                                 |
| Endurance Limit                  | 175                  | 705                  | MPa                                 |
| Fracture Toughness               | 4.6                  | 4.6                  | MPa.m <sup>1/2</sup>                |
| Hardness (Vickers)               | 2039                 | 3059                 |                                     |
| Modulus of Rupture               | 130                  | 1300                 | MPa                                 |
| Poisson's Ratio                  | 0.35                 | 0.37                 |                                     |
| Shear Modulus                    | 210                  | 380                  | MPa                                 |
| Tensile Strength                 | 400                  | 400                  | MPa                                 |
| Young's Modulus                  | 90                   | 137                  | GPa                                 |
| Latent Heat of Fusion            | 360                  | 370                  | kJ/kg                               |
| Maximum Service Temperature      | 1500                 | 1650                 | °C                                  |
| Melting Point                    | 2650                 | 2950                 | °C                                  |
| Specific Heat                    | 670                  | 710                  | J/k <sup>-1</sup> .Kg <sup>-1</sup> |
| Thermal Conductivity             | 90                   | 160                  | W.m <sup>-1</sup> .K <sup>-1</sup>  |
| Coefficient of Thermal Expansion | 4.5                  | 4.5                  | 10 <sup>-6</sup> /°C                |
| Volume Resistivity               | 10 <sup>3</sup>      | 10 <sup>5</sup>      | ohm.cm                              |

### 2.3.1 Mechanical Properties for Sic Key to This Research.

Within this research, the mechanical properties of most significance for SiC are:

- Hardness (Vickers) 2039-3059
- Density 3.11 g/cm<sup>3</sup>
- Tensile strength 400 MPa
- Melting point 2650 – 2950 °C
- Expansion coefficient 4.5 10<sup>-6</sup>/°C

These characteristics make SiC an ideal choice for applications requiring strength, stability, corrosion and wear resistance at elevated temperatures, SiC is however, susceptible to impact when in large sections having a minimum fracture toughness as low as 14 (MPa.m<sup>1/2</sup>) in comparison with 84 (MPa.m<sup>1/2</sup>) for Ti6Al4V. as small particles, SiC functions impressively as an abrasive resisting high compressive forces (1350 MPa) and shear stress (295 MPa) making it an ideal candidate as a reinforcement material (AZo metals 2019).

### 2.3.2 Crystallographic Forms of Silicon Carbide

Silicon Carbide is formed in a strong 88% covalent 12% ionic bonded (Figure 4) tetrahedral structure (Izhevskiy, et al., 2000) that enables SiC to form other strong cryptographic structures or polytypes (Schneer, 1955) such as cubic and hexagonal.

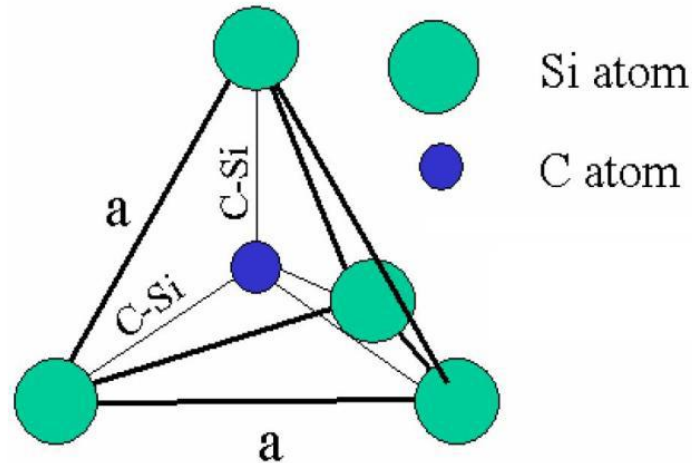


Figure 4 SiC Structures (Eriksson, J. 2010)

In granular form, the commercially available SiC particles were angular in shape due to being manufactured by crushing they presented a strong tendency to agglomerate due to high surface energy resulting from the particles large surface area. Particle sizes used for initial experimentation was  $\approx 10.0 \mu\text{m}$ , reduced by planetary ball milling to  $\approx 2.0 \mu\text{m}$ . Further experimentation saw particle sizes further reduced, typically to around  $0.5 \mu\text{m}$  as measured with a Zeiss scanning electron microscope.

Silicon when combined with titanium at relatively low quantities (below 8 Wt.%) form active eutectoid systems where below the eutectoid temperature the beta phase decomposes to alpha and intermetallic compounds such as  $\alpha + \text{Ti}_3\text{Si}$  and  $\alpha + \text{Ti}_5\text{Si}_3$ , above the eutectoid temperature  $\beta + \text{Ti}_3\text{Si}$  and  $\beta + \text{Ti}_5\text{Si}_3$  compounds are found (Fiore, et al., 2016). As a result, controlled precipitation of the intermetallic compounds can be utilised to enhance the strength of titanium alloys. Sivakumar (2016), offered more detail and considers the Orowan strengthening mechanism (dispersion strengthening) as the main reason for increased strength of the material. This work involved 5%, 10% and 15% SiC reinforcement in Ti6Al4V, with the best results achieved at 5% reinforcement using a  $20 \mu\text{m}$  particle size, SiC reinforcement.

This mechanism of dispersion strengthening using nano particulates (Orowan strengthening mechanism) is the expected strengthening methodology for this research. In the case of this work a maximum achievable reinforcement volume of  $\approx 3.81\%$  was calculated (see Section 4.4.6) and used.

## **2.4 Metal Matrix Composites (MMCs)**

### **2.4.1 MMC Systems**

Composite materials have been around for thousands of years and the idea of combining metallics with non-metallics is well established (Kainer, 2006). The aim in combining different categories of materials is to benefit from the best mechanical properties from each material including hardness conductivity, strength or wear-resistance. MMC materials produced by SLM is relatively new and novel. Care is needed in selecting the choice of matrix material and reinforcement for the SLM process, as this is significantly different to the traditional manufacturing routes. Traditionally MMC materials are processed in a liquid state using stir casting, or in a solid state, processed by hot isostatic pressing. There are commonly three main categories of materials combined to produce MMCs:

- Metallic materials
- Non-metallic materials
- Ceramic materials (Kainer, 2006).

Metallic materials in the main take the form of metallic bonded crystalline structures with good conductivity and ductility but are chemically unstable. Non-metallic materials have, for the better part dipolar bonds, amorphous structures, poor conductivity, are ductile at high temperatures and are chemically stable (Miracle, 2005). For example, ceramic materials are predominately crystalline or amorphous structures with poor conductivity and ductility. These materials are generally chemically stable (Miracle, 2005). MMC systems can potentially use any combination of these materials but always have a metal matrix, using ceramics or non-metallics as reinforcement to enhance the matrix (Holt, 1996). Where three or more materials are present it is described as a hybrid composite material (Anish, et al., 2012).

### **2.4.2 Matrix Materials**

Matrix materials are classified into three general groups:

- Conventional cast alloys
- Conventional wrought alloys
- Special alloys (Kainer, 2006).

Conventional cast alloys consist of aluminium or magnesium alloys. Wrought alloys consist of aluminium or titanium and special alloys consist of aluminium or magnesium. This has little bearing on the final product but is more specifically related to the manufacturing process (Kainer, 2006).

### **2.4.3 Reinforcement Materials**

Whilst the metallic material constitutes the bulk of the MMC, the reinforcement, either non-metallic or ceramic, makes up the rest. This is commonly a percentage by volume fraction in one of three common forms:

- Mono Filaments
- Whisker or Short fibres
- Equiaxed Particles (Kainer, 2006).

It is important that the volume of reinforcement is precisely balanced to achieve optimal mechanical properties. Figure 5 diagrammatically shows the three common forms of reinforcement. In all three uses, the volume of reinforcement should not be increased past the super-saturation point at which the matrix will become discontinuous and therefore structurally compromised.

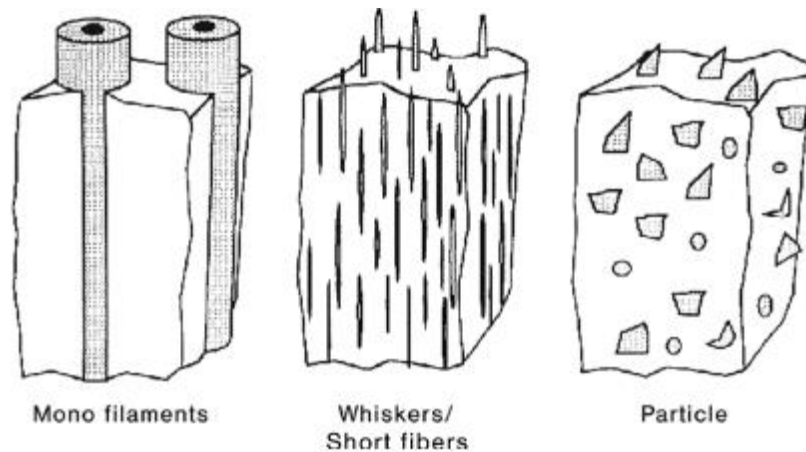


Figure 5 Reinforcement (Kainer, 2006)

Manufacture using of all three modes of reinforcement is not possible using the SLM process. Due to the nature of the feedstock delivery for SLM it is essential that a form of reinforcement is used that can be homogeneously distributed throughout the recoat and hence the powder bed. Filaments, whiskers and short fibres provide better mechanical properties in terms of strength in the direction of alignment for a component produced using conventional MMC manufacturing techniques. However, due to the nature of the SLM build process it is not possible to pre-determine or influence this alignment. Authors have used short fibre reinforcement (Salazar, et al., 2014) with fibre lengths of up to 200  $\mu\text{m}$  but only for SLS (selective laser sintering) where layer thicknesses are up to 500  $\mu\text{m}$  allowing fibres to freely align naturally within the layer. This is not the case for SLM where layer thickness is much smaller i.e. 20  $\mu\text{m}$ , preventing random fibre alignment. Therefore, the only option is to choose particulates as reinforcement, but homogeneous distribution still poses significant challenges (Chang, et al., 2015).

Authors Slipenyuk, et al., (2006) and Wang, et al., (2011) working with extruded MMCs have conducted work considering the effect of size and volume of reinforcement on the mechanical properties of the MMC. The work concludes that excessive reinforcement size and volume contributed significantly to structural failure of the matrix. Furthermore, the authors were able to demonstrate that at 4.7  $\mu\text{m}$  SiC particle size for the reinforcement would achieve critical content at 6.0 Wt.% and in addition a 77.0  $\mu\text{m}$  SiC particle size for the reinforcement would achieve critical content at 17.8 Wt.%

It is therefore evident that with a reinforcement size of 5.0  $\mu\text{m}$ , and %/W of 20% used for the initial experimentation in this work, it would suggest that the critical content percentage for the SiC reinforcement was exceeded.

Hence there are three key considerations to be focussed on:

1. Smaller reinforcement particulates ( $< 0.001 \text{ mm}$ ).
2. More accurate volume fraction based on maximum possible surface coverage of the matrix particles.
3. Homogeneous distribution of the reinforcement material (Chang, et al., 2015).

## **2.5 The SLM Processes**

### **2.5.1 Process Parameters**

EOS M270 and M290 metal melting machines were used for the experimentation throughout the work presented. The key process parameters for the SLM process are:

- Layer thickness
- Laser power
- Scan speed
- Hatch distance
- Scan strategy
- Environmental conditions (Tucho. et al., 2018)

In combination these process parameters produce what is referred to as volume energy density (Neilson, 1993). Within a range of correctly optimised energy densities, feedstock is melted in a controlled, accurate and repeatable manor to produce a part of known mechanical properties. The energy densities translate into an operating range for laser power, layer thickness, scan speed and hatch distance. This gives an operating window in which the resulting mechanical properties are stable. There is a processing window for all available materials, within this range of parameters, a part produced at the top of the range, i.e. highest laser scan speed and wider hatch distance are typically faster to manufacture and thus more economical to produce, however they are generally of a lower quality standard, having a higher percentage of porosity and shorter fatigue life. Parts produced at the bottom of the range i.e. slow laser scan speed and closer hatch distance, are typically slower to process thus more expensive but tend to exhibit reduced porosity improved mechanical properties and superior quality but have increased internal stress levels. Most production parts are produced using parameters to the middle of the range to allow for process variations (Prashanth, et al., 2017).

### **2.5.2 Laser Power**

Laser power, (W) is the amount of energy available to the process. Referenced as a maximum, most systems currently available will supply up to 400W as with the EOS M290. Older machines are limited to 200W (M270), however, machines are emerging into the market with the capability of power levels up to 1KW. Researchers have used 1.5KW systems in research processing 17-4PH Stainless steel with promising results (Yadroitsev, et al., 2010). and predictable laser power is essential to a stable and reliable process, different types of laser work better with certain materials as do specific wavelengths. The EOS M290 uses a wavelength of 1067nm, giving efficient energy delivery for most materials however; other manufactures have reported success with alternative laser sources, wavelengths and beam delivery (pulsed laser, Renishaw).

### **2.5.3 Layer Thickness**

Layer thickness refers to the depth of the individual slice layers being lased. Component CAD is digitally sliced into discreet layers for processing. On process completion, a solid part is

produced. Layer thickness is, however, critical to mechanical properties as variations in layer thicknesses during processing will result in stress concentrations within the part and unbalanced microstructures leading to part failure (Dadbakhsh, and Hao, 2014).

Whilst it is possible to produce parts with different layer thicknesses, it is with the understanding that the mechanical properties will be different and parameter sets are modified to compensate for material being lased thus maintaining the energy density. It is generally understood that thinner layer thicknesses give better surface finish but at the sacrifice of cost as thicker layered parts are faster to produce and thus more cost effective. Within commercial machines, layer thickness has traditionally been a fixed parameter, however, more system manufacturers are opening parameter sets to enable users to alter layer thickness. This should only be attempted with an understanding of the processing window. As layer thickness and laser power increase the material produced subsequently, will alter in grain structure and chemical composition, (Dadbakhsh and Hao, 2014).

#### **2.5.4 Scan Speed**

Scan speed is the speed at which the laser moves across the surface of the powder bed melting the feedstock. It is not essential to have a given scan speed for a given material, the faster the scan speed the quicker the part will build, and this will have a dramatic effect on reducing cost. What is important, however, is the energy being delivered into the feedstock, if this is increased then the scan speed must be balanced with the laser power and volume of material (feedstock) being melted. The speed at which the laser moves across the feedstock does have limits also. Excessive velocity can cause turbulent conditions that disrupt the feedstock, moving it away from the melt pool leading to a starved melt pool resulting in porosity and part failure. It has been observed from work with single tracks (Kusuma, 2014) that as the scan speed increases the bead width, height and depth of penetration decrease. This analysis is significant as scan speed is a parameter that is open to the operator and can be altered at their discretion.

#### **2.5.5 Hatch Distance**

Hatch distance refers to the distance between individual beads of processed feedstock. This distance must be optimised for the material, layer thickness, scan speed and laser power to match the weld bead size produced. Should this distance be too large, there will be an increased risk of porosity in the finished part due to unmelted powder being left between beads and layers. Similarly, if the hatch distance is too small, the melting process has insufficient feedstock to add to the process and repeatedly melts material previously lased (Yadroitsev and Smurov, 2011). This results in porosity in the finished part leading to inadequate mechanical properties. The hatch distance parameter can also be altered by the operator.

#### **2.5.6 Scan Strategy**

Scan strategy refers to the method used to cover the slice area with the laser. The most common strategy consists of stripes scanned as a raster pattern which is rotated by 67 degrees after each layer. The stripe width can be modified by the operator and this will have a direct effect on the energy delivered into the substrate due to the time the laser spends in a vicinity. Raising the

temperature of the substrate by reducing the stripe width results in less energy needed to raise the local temperature by the laser, this can result in excessive laser power being delivered and thus higher residual stresses (Kusuma, 2014). Due to the nature of each build being different, with the current level of technology, the substrate temperature is unknown, therefore, the precise level of energy required to achieve optimal melt conditions cannot be determined accurately hence the reliance on remaining within the materials operating window (Hanzel, et al., 2015).

A checkerboard strategy can help to reduce localised heating for materials that suffer detrimentally from thermal shock. By lasing random squares across the layer, the lased section has longer to reduce temperature and residual stresses. This method can also reduce processing time by increasing the scan speed for the inner volumes of the part; this can increase productivity by scanning the core areas of a part with a larger hatch distance and faster laser scan speed, however, this can influence part strength which must be taken into consideration when selecting this strategy. The skin aspect is scanned with standard parameters thus giving predictable mechanical properties in these areas.

### **2.5.7 Environmental Conditions**

For a SLM process to operate the melting must be carried out in an inert atmosphere to prevent O<sub>2</sub> contamination. The environmental conditions must be maintained throughout the build process to ensure accuracy and stability of the process. These environmental conditions can influence the melt pool significantly by influencing the crystallographic microstructure of the material in selective areas or producing unmelted areas or voids in the part, (Tucho et al., 2018).

The environmental conditions controlled include the:

- Build platform and substrate temperature,
- Environmental atmosphere (Gas and O<sub>2</sub> content),
- Filtration and condensate removal,
- Gas flow and Recoat Speed.

Changes in the environmental conditions can have a detrimental effect on the process's ability to deliver precise energy levels into the feedstock and substrate. Manufacturers devote large amounts of research time and money looking at the effects of environmental conditions within the process (Zhang, et al., 2013).

#### **2.5.7.1 Build Platform and Substrate Temperature**

Build platform and substrate temperatures are key factors when considering the reaction mechanics of the melt pool. It is well established that under specific conditions of laser power, scan speed, layer thickness and hatch distance a suitable energy density (Gu, et al., 2013) can be achieved that will melt a given volume of powder and substrate and produce reliable and predictable mechanical properties expressed by Equation (1) (Witsa, et al., 2016).



$$E_d = \frac{P}{h * v * t} \quad \text{Equation (1)} \quad (\text{Williams, et al., 1996, Savalani, et al., 2011})$$

Where:  $E_d$  is the Laser Energy Density (J/mm<sup>3</sup>)

$P$  is the Laser Power (W)

$h$  is the Hatch Spacing (mm)

$v$  is the Scan Speed (mm/s)

$t$  is the Layer Thickness (mm)

This energy density sometimes referred to as the Andrew Number, (Williams, *et al.*, 1996, and Savalani, *et al.*, 2011) is dependent on a reliable substrate temperature, when considering the thermal energy change equation (Equation 2) the energy input into the system required to reach a specific temperature is only that required to effect temperature change ( $\Delta\theta$ )

$$\Delta E_t = m * c * \Delta\theta \quad \text{Equation (2)} \quad (\text{Banerjee, 2008})$$

Where:  $\Delta E_t$  is the Change in Thermal Energy (J)

$m$  is the Mass (Kg)

$c$  is the Specific Heat Capacity (j/Kg<sup>o</sup>C)

$\Delta\theta$  is the Temperature Change (<sup>o</sup>C)

Build platform temperature is elevated prior to commencement of the build process in order to aid adhesion between the build platform and the first few layers of the build, this is typically 35 °C for Ti6Al4V on the M290 machine, providing an additional 93 J/cm<sup>3</sup>. Once the process advances beyond this point, approximately 0.3 to 0.5 mm above the platform the heat generated within the melt pool given a constant input energy can vary depending on the temperature of the substrate (Kusuma, 2014). Research with Ti6Al4V has shown that elevating the platform temperature to 100 °C can have a significant effect on the build-up of residual stress (Agius, et al., 2017) by reducing the thermal gradient.

### 2.5.7.2 Environmental Atmosphere (Gas)

The environmental atmosphere (Gas) within the build chamber is typically an inert gas supplied to reduce the oxygen levels in the build chamber. For EOS systems, oxygen levels are typically in the range of 0.1% (1000 ppm) to begin the process with a range of, 0.0% to 0.13% (0 – 1300 ppm) during operation. The M270 and M290 machines use either Argon or Nitrogen in the build chamber depending on the material being processed (Table 5).

| Material        | Ref       | Gas |
|-----------------|-----------|-----|
| Titanium        | Ti6V4Al   | Ar  |
| Aluminium       | AlSi10Mg  | Ar  |
| Maraging Steel  | MS1       | N   |
| Cobalt Chrome   | SP2 – MP1 | N   |
| Stainless Steel | GP1       | N   |
| Nickel Alloy    | IN718     | Ar  |

Table 5 Environmental Atmosphere (Gas) EOS GmbH (2018)

As new materials are developed for the SLM process along with the use of alternative laser sources, it may become necessary to combine material, laser and gas to produce the most desirable mechanical properties (Linde, Russia 2018). Further development of process atmosphere gasses may be possible but not within this work, at this stage and for this research it is recognised that this environment must be free from oxygen.

### 2.5.7.3 Gas Flow and Recoat Speed

The M270 uses a top-down fill configuration that utilises the atmospheric gas to keep the laser window free from contamination by feeding the gas in past the lens, the gas then falls to the build area. This, however, has been proven through research conducted, by EOS, to be detrimental to the build process. Due to a combination of the chamber geometry and the position of the recoater arm during lasing and the movement of gas within the chamber, multi directional gas flows are generated. This configuration disturbs the feedstock on the powder bed and prevents condensate produced by the process from evacuating the chamber resulting in the interference of the passage of the laser beam causing reduced and unpredictable levels of laser energy being delivered to the workpiece. Recent developments in gas flow delivery now used in the EOS M290 deliver the gas with a ‘gas blade’ at the rear of the build platform, the gas travels across the build platform and is extracted at the front of the machine. The gas flow is designed to be laminar in nature to minimise turbulence and remove condensate producing a clean build area. This has been proven to be a major improvement but still requires development work to avoid disruption of the powder bed and interference with the laser beam. Care must also be taken in the placement of parts within the build areas to avoid weld spatter falling in areas before lasing. Typically, parts are built from the front of the build chamber to the rear;

excessive spatter is then removed by the recoater arm on recoat between each layer's production. The recoat speed can also be influential to the build process. By increasing the speed of recoat build time can be reduced, however, this increased velocity can cause lighter particles of powder to become airborne impairing the energy levels of the laser by acting as a filter. The reduced volume of powder on the powder bed also effects bead formation by reducing the volume of available feedstock. In this instance, weld beads will be less than optimal leading to porosity in the part. Conversely, by significantly reducing the recoat speed improvements in part density can be achieved however, the build time and production cost will increase (Baitimerov, et al., 2018).

#### **2.5.7.4 Filtration and condensate removal**

Within the build area, the environmental gases are continually monitored for O<sub>2</sub> levels and filtered through a dedicated system in order to remove condensate and contamination generated by the laser melting process. Filtration flow rates can be adjusted to optimise environmental conditions providing a clear passage for the laser beam. However, care must be taken to ensure that the flow rate is not too high as particles with lower mass can travel into the filtration system. Filter clogging is monitored by the control system. Users are prompted to replace filters after 200 hours of production and filters are automatically self-cleaned (EOS GmbH 2019).

#### **2.5.8 Surface Tension and Wettability**

Wettability is one of the most important factors affecting the Laser Melting process. The process requires care in selecting parameters that will produce the desired bead geometry and this geometry can be an indicator of the process behaviour within the weld pool and the liquid–solid wetting characteristics are crucial for a successful SLM process.

The wetting of a solid by a liquid is related to the surface or boundary energy of solid–liquid  $\gamma_{sl}$ , solid–vapour  $\gamma_{sv}$  and liquid–vapour  $\gamma_{lv}$  interfaces. Wettability can be defined by the contact angle  $\theta$  (Figure 6)

$$\cos \theta = \frac{\gamma_{sv} - \gamma_{sl}}{\gamma_{lv}} \quad \text{Equation (3)} \quad (\text{Kruth, et al., 2003})$$

Where:  $\cos \theta$  is the cosine of the contact angle (Deg)

$\gamma_{sl}$  is the solid–liquid interface

$\gamma_{sv}$  is the solid– vapour interface

$\gamma_{lv}$  is the liquid–vapour interface

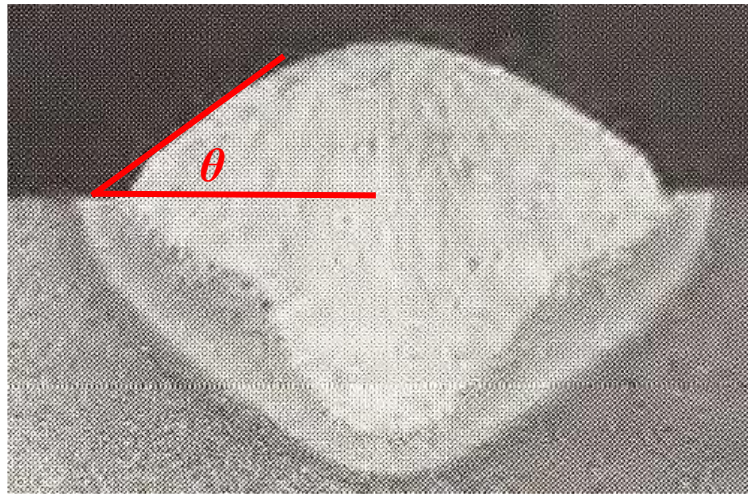


Figure 6 Wettability Contact Angle  $\theta$  (Banerjee, 2008)

The liquid wets the solid as  $\cos \theta \rightarrow 1$ . The spreading coefficient is described as:

$$S = \gamma_{sv} - \gamma_{sl} + \gamma_{lv} \quad \text{Equation (4)} \quad \text{(Young, 1805; Dupré, 1869)}$$

Where: **S** is the spreading coefficient

$\gamma_{sl}$  is the solid–liquid interface

$\gamma_{sv}$  is the solid– vapour interface

$\gamma_{lv}$  is the liquid–vapour interface

Normally, a large positive  $S$  ( $S > 0$ ) favours spreading of the liquid across a solid surface. Conversely if  $S < 0$  there is a strong possibility of the liquid spheroidising or balling rather than wetting the surface leading to incompatibility between the surface energy of the liquid melt pool and the solid substrate. The surface tension of the liquid is such that it becomes self-sustaining forming a ball that travels away from the weld pool, this is referred to as “balling”. Incompatibilities between the liquid and solid elements can be caused by:

- A. Temperature difference between the molten feedstock, and the substrate,
- B. Gas evacuation from feedstock and or weld pool,
- C. Contamination in the form of oxides,
- D. Substrate surface roughness.

### *Temperature difference between the molten feedstock, and the substrate.*

Upon lasing, the energy from the laser penetrates through the powder bed into the substrate to produce a melt pool. This melt pool is sustained through the progression of the laser as it scans across the substrate. If excessive layer thickness or a difference between the substrate temperature and the bead is experienced balling can occur due to insufficient energy in the substrate.

### *Gas evacuation from feedstock and or weld pool.*

Gasses such as Oxygen and Nitrogen can be entrapped within the feedstock (Figure 7) and can be released during the welding process causing a disruption. Similarly, at elevated laser powers typically above 1KW plasmerisation can occur, (Yadroitsev, et al., 2013) disrupting the surface tension by producing a layer of insulation between the molten powder and the substrate known as the Lidonfrost effect, leading to the balling effect.

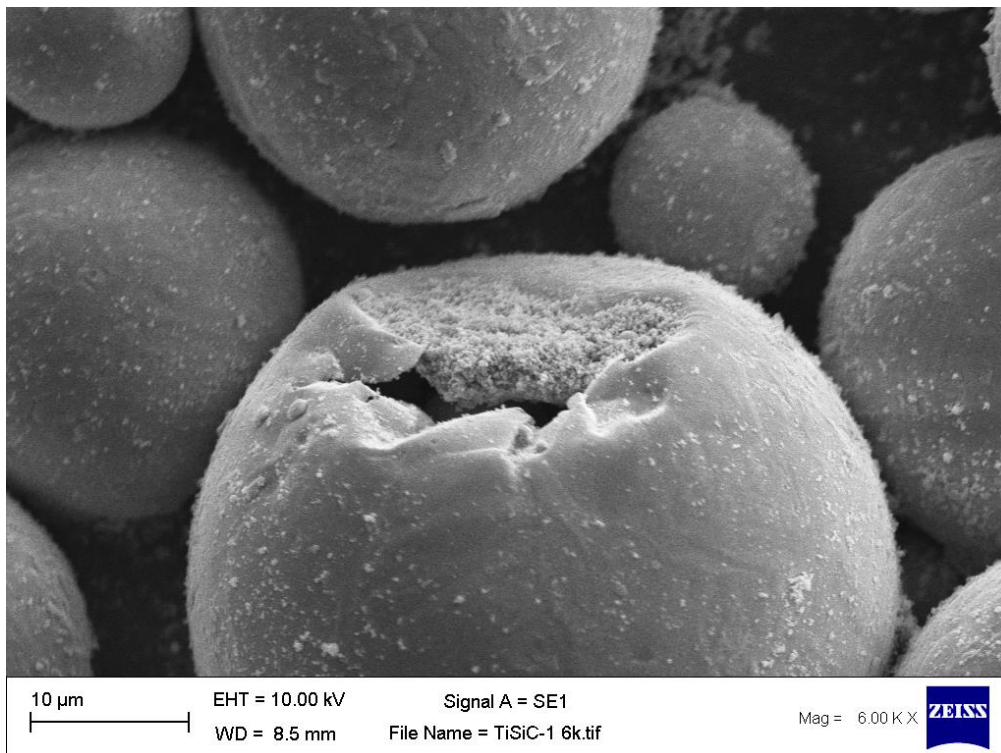


Figure 7 Evidence of Gas Entrapment in Feedstock (Lyall, 2017).

### *Contamination in the form of oxides.*

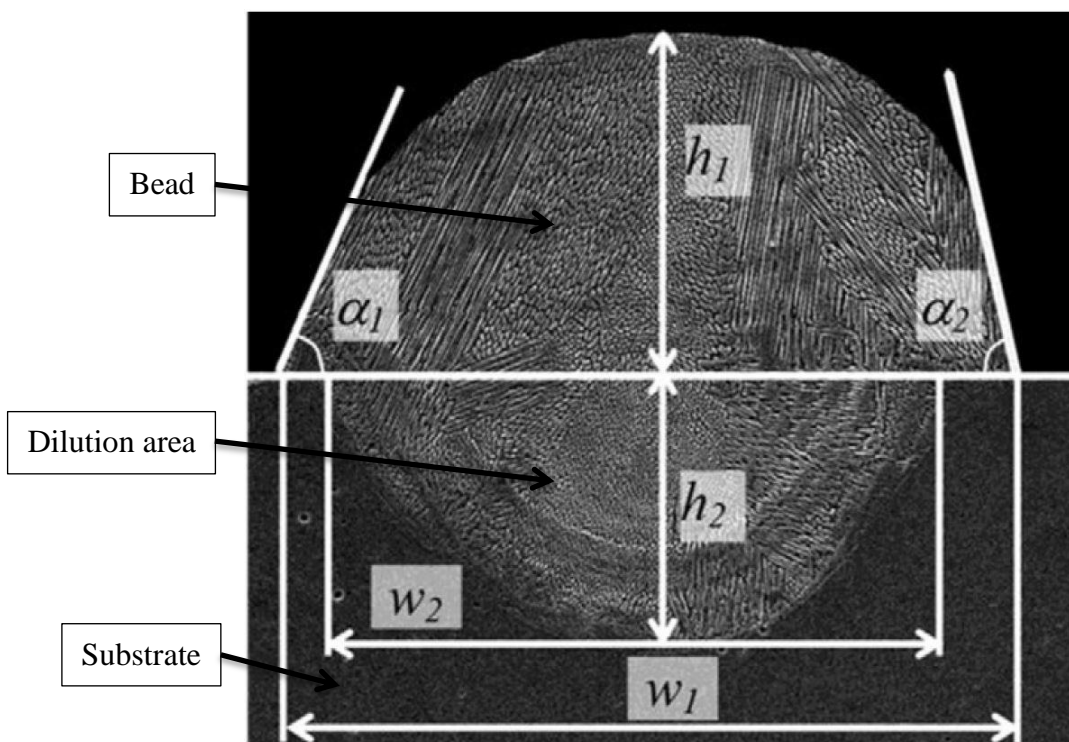
Contamination in the feedstock can be either through gas entrapment within the feedstock (Figure 7) or oxygen pickup caused by frequent use and handling in an oxygen rich atmosphere between processing (LPW 2018). Fluxing agents or in situ deoxidisers can be used to reduce the effect of oxides within the process. Additives in small quantities can either be mixed or pre-alloyed with the feedstock to aid the wetting activity and flowability. In Kruth's (2004) work, phosphides were added in the form of  $Fe_3P$ ,  $SCuP$  and  $Cu_3P$  to Fe based and Cu based powder

systems. This was effective in enhancing the wetting behaviour and the reduction of porosity of the material produced.

#### ***D – Substrate surface roughness.***

Wettability is also a function of surface roughness, the flatter a surface, the easier a liquid can wet that surface (Banerjee, 2008). Within the SLM process the roughness of the substrate is dependent on the surface finish of the previously lasered layer, As the substrate becomes rougher the possibility of balling increases leading to increased roughness, porosity and part failure.

In combination with other measurements such as bead continuity, cracking and coloration, bead height ( $h_1$ ), substrate penetration denoted by the depth of the dilution area ( $h_2$ ), width of the bead ( $w_1$ ), and width of dilution area ( $w_2$ ) (Figure 8) the optimal process parameters that promote compatibility of surface tensions and promote wettability can be determined.



**Figure 8** Dimensioned cross sectioned 316L stainless steel single beads (Yadroitsev, et al., 2012)

## **2.6 Conventional Feedstock Production for SLM**

Metal powder (Feedstock) is the key raw material of the SLM process. Poor quality powder equates to poor quality components and contamination in powders equates to contamination in components. It is therefore essential to establish what constitutes good powder and how to determine this, but more specifically powder that is “fit for purpose”. There are many powder manufacturers worldwide and the industry can produce many materials in whatever particulate size range that is required. Authors such as Benson, and Snyders, (2015) have developed criteria for feedstock acceptance and hence demonstrated direct correlation between feedstock characteristics and part defects including density, surface finish and mechanical properties.

The main considerations are:

- Powder flow behaviour for consistent feeding/spreading
- Powder packing for maximum layer density
- Thermal conductivity of the powder layer (and substrate)
- Particle porosity (affects final part density)
- Impurity levels (affect final mechanical properties).

The typical powder characteristics measured are summarised in Figure 9.

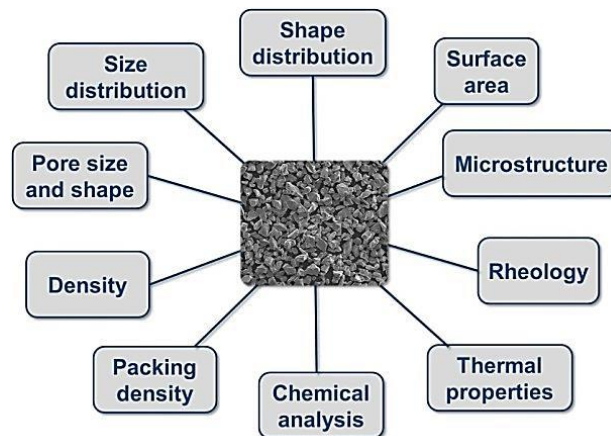


Figure 9 Typical Powder Characterisation Parameters (Benson, and Snyders, 2015)

In combination, these characteristics and their interactions impact significantly on the SLM process. This impact is complex, as indicated in Figure 10.

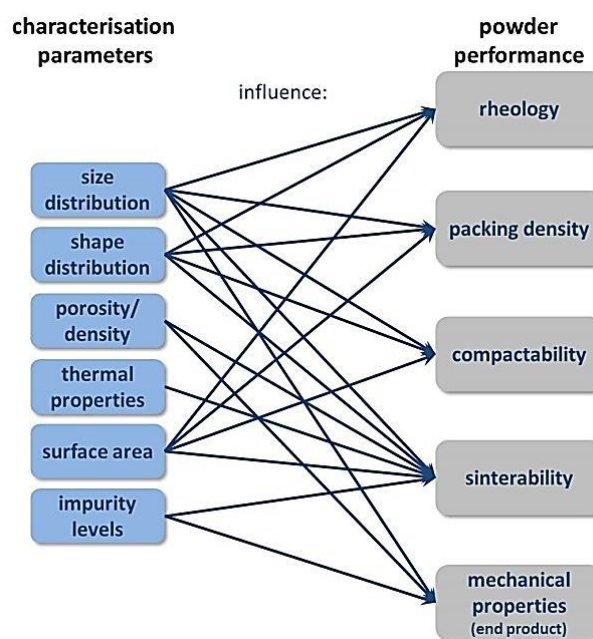


Figure 10 Inter-Relationships of Characteristics on Powder Behaviour (Benson and Snyders, 2015)

To characterise powders for SLM there are international standards available offering the requirements for bulk feedstock (Table 6).

**Table 6 International Standards for Powder Characterisation (ISO 17296-3 2014)**

| <b>Powder Characteristic</b>          | <b>International Standard</b>       | <b>Year</b> | <b>Description</b>                                                                                                                |
|---------------------------------------|-------------------------------------|-------------|-----------------------------------------------------------------------------------------------------------------------------------|
| Powder Particle Size and Distribution | ISO 24497                           | 1993        | Metallic powders. Determination of particle size by dry sieving                                                                   |
|                                       | ISO 8130-1                          | 2010        | Determination of particle size distribution by sieving                                                                            |
|                                       | ISO 13319                           | 2007        | Determination of particle size distributions. Electrical sensing zone method                                                      |
|                                       | ISO 13320                           | 2009        | Particle size analysis. Laser diffraction methods                                                                                 |
| Morphology                            | ISO 9276-6                          | 2008        | Representation of results of particle size analysis. Descriptive and quantitative representation of particle shape and morphology |
| Surface                               | ISO 9277                            | 2010        | Determination of the specific surface area of solids by gas absorption – BET method                                               |
| Density (Tap and Apparent)            | BS EN 23923-2 (Formerly ISO 3923-2) | 1993        | Metallic powders – Determination of apparent density – part 2 Scott volumeter method)                                             |
| Flowability / Pourability             | ISO 4490                            | 2014        | Determination of flow rate by means of a calibrated funnel (Hall flowmeter).                                                      |

Table 6 is taken from the international standard, ISO 17296-3: 2014 “Additive manufacturing - General principles Part 3: Main characteristics and corresponding test methods”. This document provides the basic characteristics and test methods for the relevant standards within the SLM industry. In an industry, as dynamic and fast paced as SLM, these standards continually need to be updated, therefore, Table 6 includes updates to reflect the current issue levels of standards that the document lists. Other new standards include ASTM F3049 - 14: Standard Guide for Characterising Properties of Metal Powders Used for Additive Manufacturing Processes. The



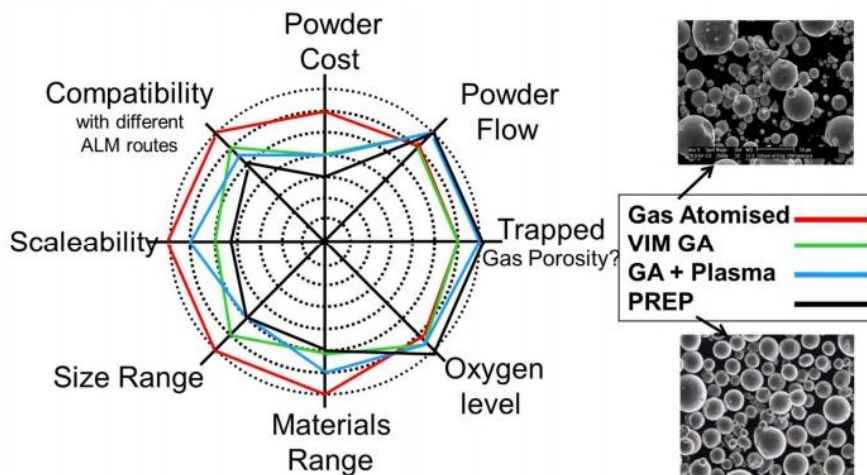
American Society for Testing and Materials (ASTM International) standard focusses not only on virgin powders but also the characterisation of used powders. This is a significant step forward for the industry as it recognises the end user’s requirement for continuous quality throughout the lifecycle of the powder.

Powder manufacturers for SLM are shown in Table 7.

**Table 7 SLM Powder Manufactures Worldwide (2018)**

| Company                          | Location  | Established | Notes                                               |
|----------------------------------|-----------|-------------|-----------------------------------------------------|
| LPW                              | (UK)      | 2007        | Currently owned by Carpenter Technology Corporation |
| Sandvik Osprey                   | (UK)      | 1974        |                                                     |
| H.C. Starck                      | (Germany) | 1920        |                                                     |
| Praxair surface technologies     | (US)      | 1904        |                                                     |
| GKN Hoeganaes                    | (Germany) | 1998        | Became industrial partners with EOS in June 2017    |
| Carpenter Technology Corporation | (US)      | 1889        | Acquired LPW in 2018                                |

Powders can be manufactured in different ways, Gas Atomisation, Plasma Atomisation, EIGA (Electrode Induction melting Gas Atomisation) or Plasma Rotating Electrode Process (PREP). Figure 11 shows comparisons between powder manufacturing methods in relation to powder characteristics and powder defects. (Sun, et al., 2017)



**Figure 11 SLM Powder Production Methods (Murray, Sandvik Osprey 2015)**

Gas Atomisation (GA) is a popular process for powder production and demonstrates good qualities in most quality categories such as size range, materials and compatibility but is limited by cost, oxygen content and trapped gasses (Figure 7). Regarding oxygen content and trapped gasses, this is problematic. In most conventional applications such as casting and powder sintering, elevated oxygen content and trapped gasses can be tolerated as they can be removed during the manufacturing process or through post processing. For SLM, oxygen or trapped gasses are detrimental to the process and have deleterious effects on the part quality. For applications where powder flowability and trapped gasses are of significance, such as SLM, the plasma atomisation or PREP process developed by PyroGenesis (Canada) offer, the ability to burn off gaseous substances to produce clean spherical particles thus improving flowability and reducing oxygen and trapped gas content during the SLM process, (Clayton, 2015, Sun, et al., 2017). In their research Ahsana, et al., 2011) found improvements in mechanical and crystallographic properties from their parts manufactured from PREP produced material in comparison to GA material-based components.

### **2.6.1 Strategies for Mixing Dissimilar Powders**

A crucial factor for the manufacture of an MMC is the homogeneous distribution of reinforcement within the product (Rosso, M. 2006). Achieving an optimal volume of reinforcement is equally as crucial. Too little reinforcement and the product will not demonstrate any benefits, with too much, the product is at risk from over saturation of reinforcement, and hence insufficient binding to hold the MMC together (Sivakumar, et al., 2016). Over saturation of the matrix varies depending on the materials used for the matrix, the reinforcement material and the form in which it is used. Two key factors thus present themselves; the amount of reinforcement and its homogeneous distribution throughout the matrix.

Within conventional MMC production, stir casting has become one of the most widely used methods employed, due to its reliability in suspending the reinforcement within the MMC. Within this research, in-situ alloying is principally employed in the formation of the MMC material, taking place continually as the melt pool advances. It is therefore necessary to develop a method to reliably deliver the correct mix of both matrix and reinforcement materials. There are currently three possible solutions:

- Manual Mixing,
- Gas Atomising,
- Mechanical alloying.

#### **2.6.1.1 Manual Mixing**

For this research the constituent powders could be prepared by manually tumbling or shaking of the powder mixture until the SiC would be distributed throughout the Ti6Al4V powder. This only remains so at the time of mixing. If the mixture is agitated during transportation, either to

the production machine or during the process of recoating, the materials will separate through granular convection. Typically, granular convection is not reliant on gravity or effected by the mass of the objects involved but more their size. If slight movement or oscillations are produced, smaller particles are encouraged to fall between the gaps of the larger ones forcing them to appear to rise to the surface. The granular convection effect is more visible when the particles have contrasting colours as seen in Figure 12 where DM20 (EOS Direct metal 20) was mixed with tungsten (W). The DM20 has a smaller particle size than the tungsten, and has fallen beneath the tungsten leaving it exposed (Lyll, 2009).

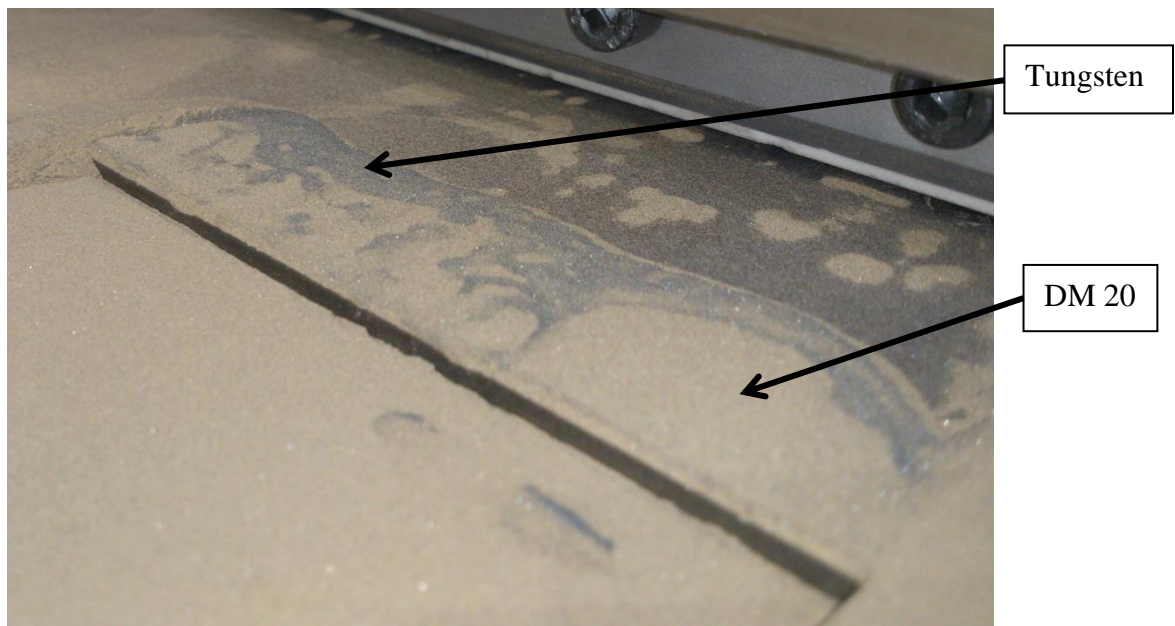


Figure 12 EOS DM20 - Tungsten Powder Mixed by Hand (Lyll, 2009)

Manual mixing is therefore an unacceptable methodology due to its inconsistency and inability to produce the desired results in terms of homogeneous powder delivery.

### 2.6.1.2 Gas Atomisation

Gas atomisation is currently the widest spread process for the manufacture of metal powders/feedstock within the additive industry. Several producers have invested significantly in new technology such as plasma atomisation, but the industry is still undecided as to whether this produces qualities that are more desirable than gas atomised powder. Furthermore, the cost of plasma atomisation is set to be significantly higher than gas atomising at this stage due to the availability of such equipment.

With respect to MMCs this is the most reliable method of producing feedstock. This method produces a range of particle sizes that are subsequently sieved to achieve the desired size distribution. This method can also achieve higher saturations of reinforcement within the feedstock if required.

Gas atomisation is a costly production process. The economics are usually amortised across large batches to produce a cost-effective method of production. Small batches of powder can

be produced in the region of 30Kg (Minimum order), however, for research this is impractical as this minimum order will only offer one version of the powder mix ratio, should the requirement be for a varied mix ratio range of the same material for testing purposes, this cost would be significant. In this instance and as for this research mechanical alloying was investigated.

### 2.6.1.3 Mechanical Alloying (MA)

Mechanical Alloying (MA) is a solid-state powder processing technique involving repeated cold working of a material, typically in powder form. Using a high energy ball mill, powder particles are fractured and re-welded to form solid agglomerates, over long periods of time. These agglomerates once formed, increase in size and fracture many times to produce a refined grain structure within the resultant powder yield (ZoZ GmbH, 2018). Originally developed to produce oxide-dispersion strengthened (ODS) nickel and iron-base super alloys for applications in the aerospace industry, MA has now been shown to be capable of synthesising a variety of equilibrium and non-equilibrium alloy phases starting from blended elemental or pre-alloyed powders.


| Device                                                            |       | Shaker Mill                                                                          | Simoloyer <sup>®</sup> | Planetary Ball Mill | Attritor <sup>®</sup> | Drum/Ball-Mill |
|-------------------------------------------------------------------|-------|--------------------------------------------------------------------------------------|------------------------|---------------------|-----------------------|----------------|
| properties                                                        | brand | (spex)                                                                               | (zoz)                  | (various)           | (union process)       | (various)      |
| Energy Impact relation                                            |       | 10                                                                                   | 08                     | 05                  | 04                    | 01             |
| Friction / Sheer relation                                         |       | low                                                                                  | low                    | medium              | medium - high         | high           |
| Collision relation                                                |       | high                                                                                 | high                   | medium              | low – medium          | low            |
| Kinetic, Processing                                               |       | very fast                                                                            | fast                   | medium              | medium                | slow           |
| Influence of gravity                                              |       | little                                                                               | very little            | little              | difficult             | needed!        |
| max. Diameter [m]                                                 |       | 0.08                                                                                 | 0.9                    | 0.2                 | 1                     | 3              |
| max. Total Volume [l]                                             |       | 0.2                                                                                  | 400                    | 8                   | 1000                  | 20000          |
| max. relat. velocity [m/s]                                        |       | 19                                                                                   | 14                     | 5                   | 4.5 - 5.1             | x - 5          |
| Specific Energy [kW/l]                                            |       | --                                                                                   | 0.55 (- 3)             | --                  | 0.1 (- 0.75)          | 0.01 - 0.03    |
| Continuous process (dry)                                          |       | impossible                                                                           | Yes, semi              | impossible          | difficult             | impossible*    |
| Scaling up                                                        |       | no                                                                                   | yes                    | no                  | yes                   | yes            |
| max. batch [kg]                                                   |       | 0.2                                                                                  | 250                    | 2                   | 250                   | 12000          |
| Contamination                                                     |       | low                                                                                  | low - high             | low                 | low - high            | low            |
| Vacuum                                                            |       | possible                                                                             | - 10 <sup>-4</sup> hPa | possible            | poor                  | poor           |
| Discharging                                                       |       | very difficult                                                                       | easy                   | very difficult      | medium                | easy           |
| Airlock                                                           |       | impossible                                                                           | yes                    | impossible          | difficult**           | impossible***  |
| Temperature control                                               |       | very difficult                                                                       | possible               | difficult           | possible              | possible       |
| Investment (costs)                                                |       | low                                                                                  | very high              | low                 | high                  | low            |
| Operation (costs)                                                 |       | very high                                                                            | high                   | low                 | high                  | very low       |
| *exception tube-mill<br>**due to gravity<br>***exception BMxx-zoz |       |  |                        |                     |                       |                |

Figure 13 Mechanical Alloying Systems, (ZoZ GmbH 2018)

Commercially available MA systems (Figure 13) vary in investment and running costs, capacity and flexibility of use. Systems such as Drum ball mills are often the largest with a capacity of up to 20,000L of powder as opposed to a planetary ball mills being able to hold a maximum of 8L. Chosen due to its fast kinetic processing, the ability for temperature and vacuum / gas control, the Zoz Simoloyer CM01 was used for this research provides an adequate chamber capacity (up to 400L) for small batch powder production.

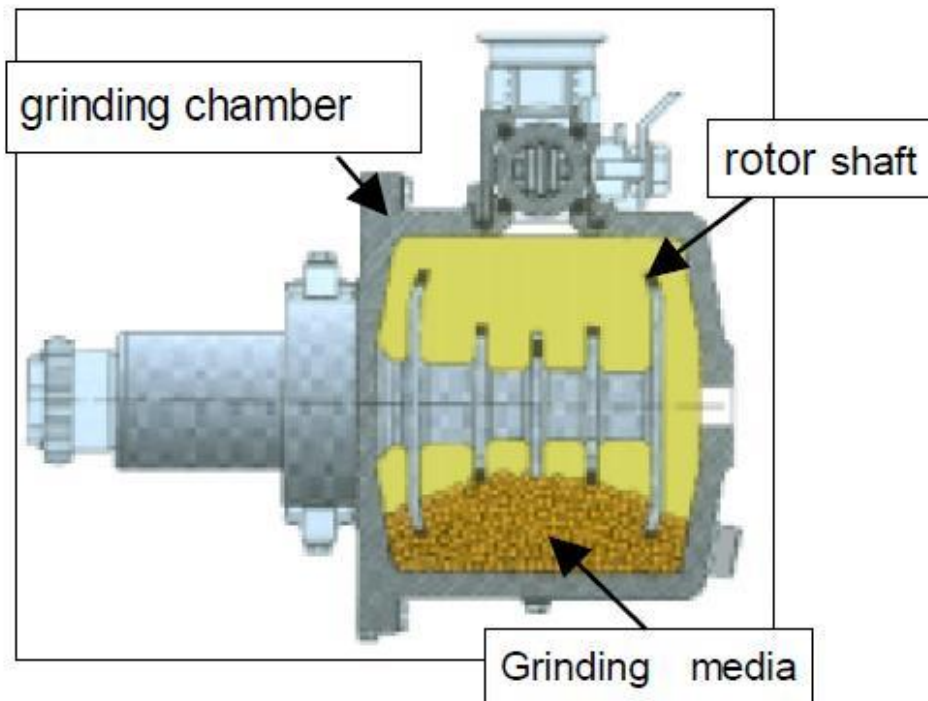


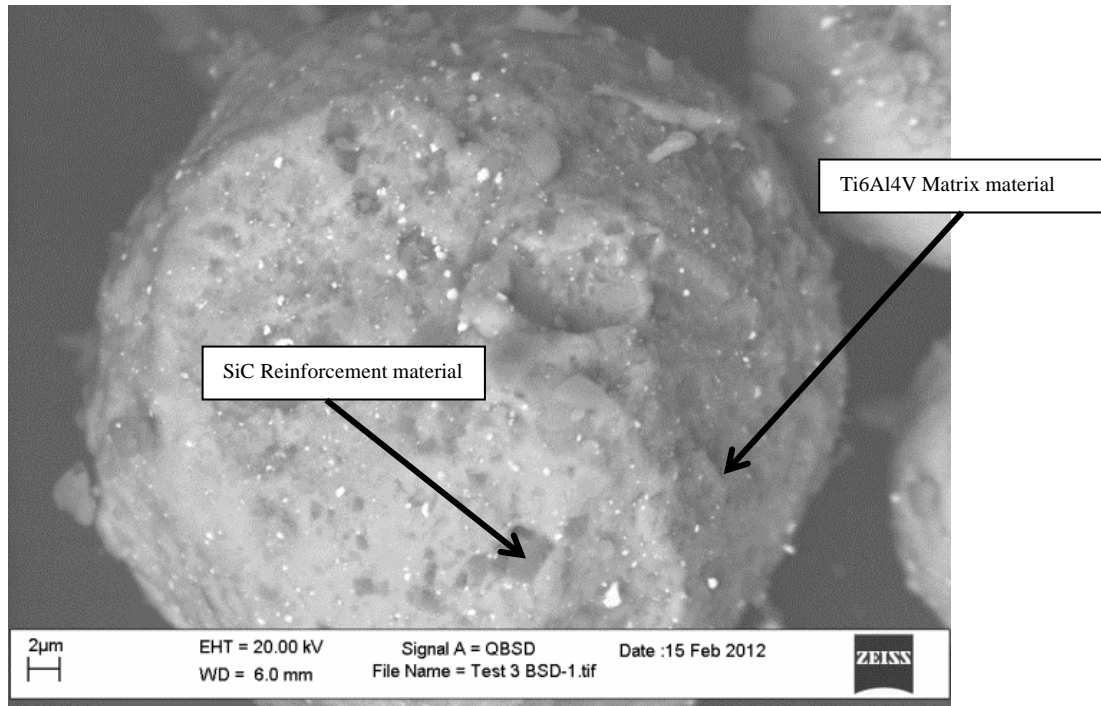
Figure 14 High Energy Mill Cross Sectional View (Zoz, H. Ren, H. 2008)

The Zoz Simoloyer, Figure 14 is an attrition ball mill having a stainless steel horizontally mounted grinding chamber with a series of steel blades on a rotor shaft in the centre forcing grinding media (stainless steel balls) to collide with the powder. The combined velocity of the rotor shaft and grinding media produce enough force and energy to both plastically deform the powder and induce cold welding to form agglomerated material (ZoZ GmbH 2018).

### 2.6.2 Mechanical Alloying (MA) For Selective Laser Melting (SLM)

MA for SLM differs significantly from commercial MA. The objective for SLM is to bind the reinforcement material to the softer matrix material for means of homogeneous transportation within the build process (Lyll, 2015) without changing the morphology of the matrix powder. There is no need for the process to refine the grain structure of the material being processed as in conventional MA, as this will be subjected to melting during the SLM process. The MA processing time can therefore be reduced significantly from that of days, (24 to 100 hours) (Zoz, 2008), down to minutes, (10 to 40 mins), the duration of the MA process is enough to embed the reinforcement particles without compromising the morphology of the matrix powder.

The MA process is therefore primarily employed to embed the smaller reinforcement particulates onto the softer surface of the matrix material (Figure 15). The matrix material then becomes a reliable delivery mechanism for those smaller particles for in-situ alloying within the SLM process.



**Figure 15** SiC Reinforcement Material Embedded onto Ti6Al4V Matrix Material by MA (Lyall, 2012)

There are therefore, five key considerations to consider during the MA process:

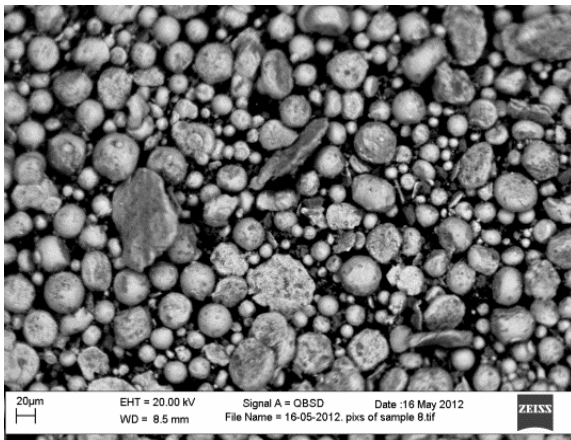
1. Changes to particle size and size distribution during the MA process.
2. Changes in morphology during the MA process.
3. Maximum surface coverage of the matrix material possible through MA.
4. Excess reinforcement material post MA.
5. Risk of contamination during the MA process.

#### **2.6.2.1 Changes to Particle Size and Size Distribution During the MA Process.**

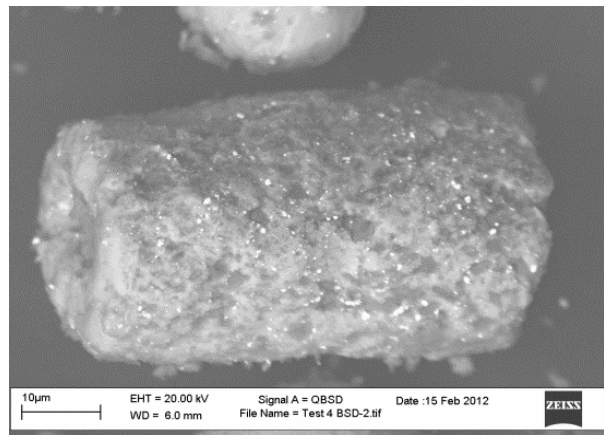
Down-stream and in-process activities such as sieving and the mechanical recoating of powder, dictate that a specific particle size range and morphology be maintained. The particle size typically being between 10 µm to 55 µm and the morphology being as close to spherical as possible for the powder bed SLM process. Sieving fully MA feedstock could remove a significant amount of the powder base due to agglomeration. For the research done for this work it was important to take a baseline measurement of the matrix powder prior to MA and at periodic stages during the process to determine at what point the process altered the particle size and morphology of the matrix powder thus establishing a satisfactory milling time.

### 2.6.2.2 Changes in Morphology During the MA Process.

Changes in morphology are found to be more significant due to the forces involved within the process and due to the processing equipment's tubular configuration (Olowofela, 2013).



**Figure 17a** Flake or Plate Like Structures Produced by Excessive MA (Lyall, 2012)



**Figure 17b** Tube or Cylindrical Like Structures Produced by Excessive MA (Lyall, 2012)

The ideal particle shape for SLM due to the need to spread the powder over the powder bed is spherical. From prolonged milling this initial spherical shape will change significantly exhibiting flake or plate like structures (Figure 17a) and tube or cylindrical like structures (Figure 17b). These particle shapes are not conducive to controlled recoating and will significantly reduce the density and predictable deposition of powder within the SLM build environment. Based on rheological evidence in section 5.2.2, the apparent density of Ti6Al4V feedstock is approximately 50.6% that of the solid material, this being a significant contributing factor in producing a satisfactory bead. hence misshapen particles can hinder the delivery of material and lead to porosity and part failure.

### 2.6.2.3 Maximum Surface Coverage of The Matrix Material Possible Through MA.

It can be estimated through particle analysis and calculation the available surface area of matrix material, to be covered by SiC, of a known size. It is therefore feasible to calculate the maximum amount of reinforcement material that the matrix material can carry. Additional amounts of reinforcement material will not adhere to the surface of the matrix material and could impinge on the process. This is resolved in section 4.4.6.

### 2.6.2.4 Excess Reinforcement Material Post MA.

Excess reinforcement material post MA is also a function of the maximum amount of reinforcement material required to coat the matrix material, exceeding this value will result in excess reinforcement material remaining unattached within the feedstock. The risk here is that it can form areas of concentrated reinforcement within the part leading to failure due to overloading or over stressing the matrix at that point.

### 2.6.2.5 Contamination Risks During the MA Process.

There are two main forms of contamination possible during the MA process:

- Foreign particles
- oxygen

### **Foreign particles:**

Whilst every effort is taken to eliminate the possibility of cross contamination between samples, it is possible to contaminate the sample with particles from the process apparatus. In Figure 15, tungsten carbide (WC) contamination is visible as small white particles, this was contamination from the planetary ball mill used to reduce the SiC in the initial experimentation. It is recommended by the manufacturer (Zoz GmbH 2018) that the milling vessels are of a harder material than the material being milled thus the choice of tungsten carbide lined vessels with tungsten carbide balls. Most of the contamination can be eliminated by purchasing SiC within the desired size range thus eliminating the attrition between the SiC and tungsten carbide equipment. Other foreign particles can be liberated from the stainless-steel paddles and the wall of the alloying chamber. Prolonged processing times increase the risk of contamination from these sources, but this is minimised when alloying for reduced cycle times as with MA for SLM.

### **Oxygen:**

Risk of oxygen contamination comes from surface oxygen on the feedstock materials and from within the MA apparatus. Submicron SiC has a large surface area and high surface energy making it susceptible to attract oxygen, similarly Ti6Al4V also has a strong affinity for oxygen. During the MA process, as particles of SiC are embedded on to the surface of the Ti6Al4V matrix material oxygen can be trapped between the interfaces, this trapped oxygen would be released during the SLM process. Therefore, during the MA process air is first removed from the chamber by vacuum and argon gas is introduced to establish an oxygen free environment, this process is repeated two to three times before alloying the materials.

### **2.6.3 Process Preparation – Mechanical Alloying (MA)**

With respect to the SLM process and the nature of the constituent materials it is known that delivery from the powder dispenser to the build platform area can be problematic and a loss of homogeneity is experienced. Mechanical alloying is therefore used to augment the delivery of smaller particles across the build area.

Hence the main objectives for the MA phase of the research are:

- Powder / particulate selection,
- Mix ratio,
- Initial powder particle size and morphology,
- post milling powder particle size and morphology,
- Homogeneity of reinforcement,
- Degree of particle embedment,
- Contamination.



# Chapter Three

## 3.0 Background

### 3.1 Initial Experimentation.

Initial exploratory experimentation into MMC consisted of manually mixing 20% (B/W) SiC with Ti6Al4V powder feedstock with a view to building several small test samples as shown in Figure 18. The intention was to establish a baseline for further experimentation and to ascertain if the materials were compatible with the SLM process.



Figure 18 Initial Test Samples. Aborted after approx. 1.5mm

The test samples (Table 8) included:

| Quantity | Description            | Size (mm)   | Test              |
|----------|------------------------|-------------|-------------------|
| 2        | XDif specimen          | 35 x 35 x 2 | X-Ray Diffraction |
| 5        | Small density specimen | Ø 10 x 5    | Porosity          |
| 5        | Density Cubes          | 12 x 12 x 5 | Porosity          |
| 3        | Large density specimen | Ø 20 x 5    | Porosity          |
| 4        | Small tensile specimen | 8 x 5 x 5   | Tensile           |

Table 8 Initial Test Samples.

#### 3.1.1 Feedstock Preparation

Feedstock was prepared by mixing 20% (B/W) SiC powder with a mean particle size of 10 µm (Dynamic Ceramic), into Ti6Al4V EOS standard powder with a mean particle size 39 µm (±3 µm), (EOS GmbH 2016) for a short period of time until the mixture appeared to be completely mixed.

### 3.1.2 Data Preparation

Slice files were prepared using PSW version 3.4 (EOS Gmbh) and files were arranged on a 120 mm x 120 mm platform, maximising the full space available (Figure 19).

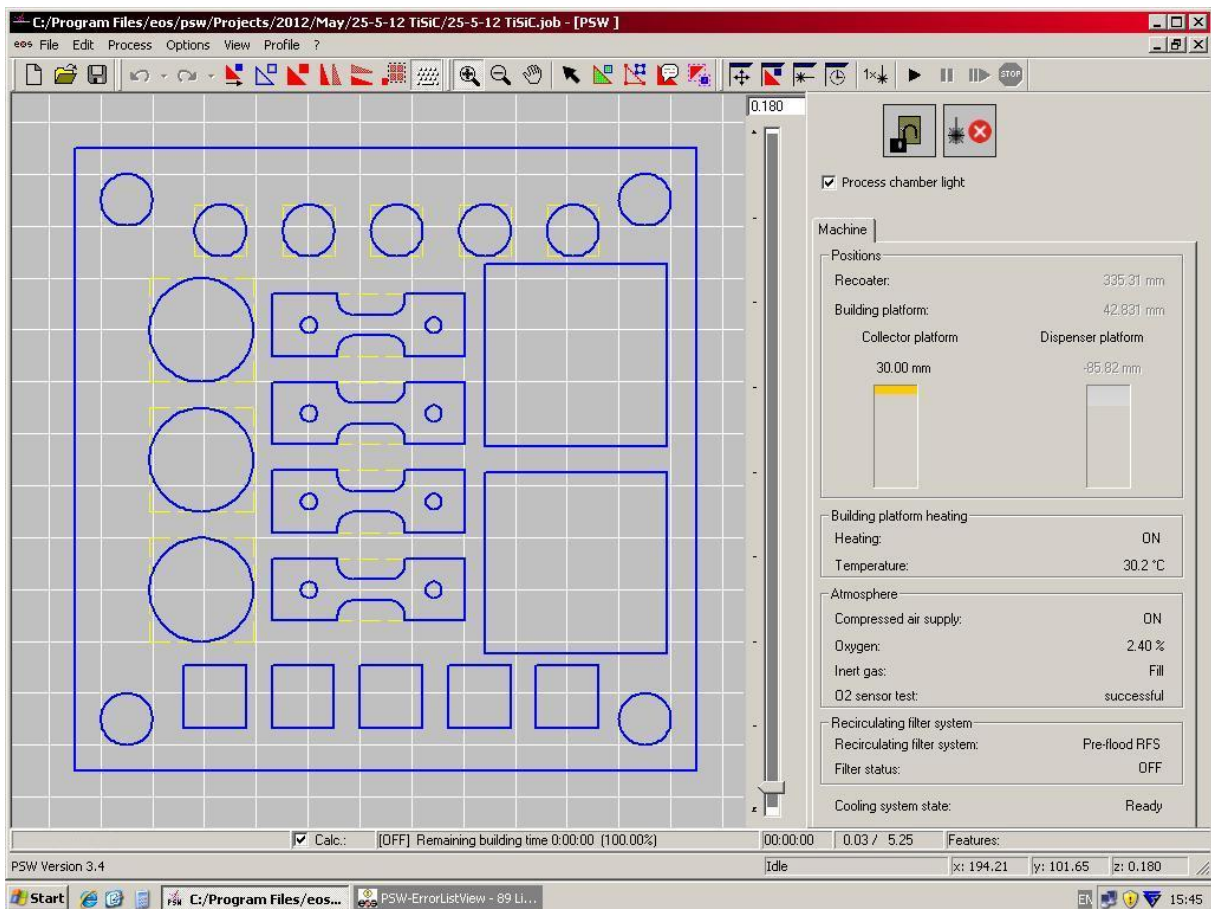


Figure 19 PSW version 3.4 (EOS GmbH)

The material was exposed with standard EOS parameters for Ti6Al4V in 30  $\mu\text{m}$  layers using an EOS M270 Machine with the following parameters (Table 9).

| Material | System | Layer Thickness  | Laser Power | Scan Speed | Hatch Distance | Oxygen concentration |
|----------|--------|------------------|-------------|------------|----------------|----------------------|
| Ti6Al4V  | M270   | 30 $\mu\text{m}$ | 175 W       | 1250 mm/s  | 0.100 mm       | 0.05% to 0.13%       |

Table 9 EOS M270, Ti6Al4V Standard Parameters (EOS GmbH)

A Ti6Al4V build platform was used and the build setup followed standard build preparation procedures (Figure 20) for Ti6Al4V material.

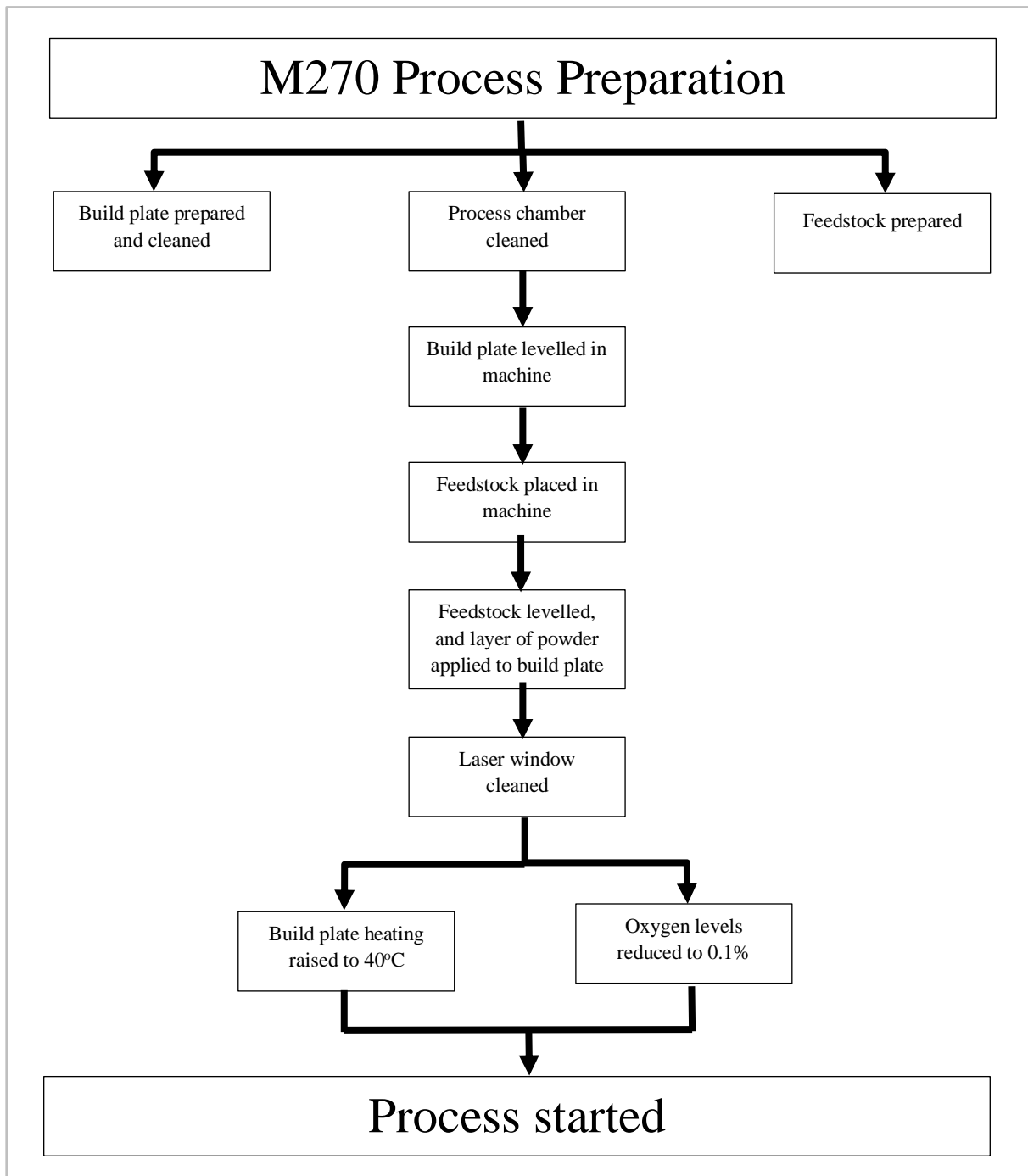


Figure 20 EOS M270 Process Setup Flow

### 3.2 Observations from Initial Experimentation

From observing the build process, it was obvious from the initial layers that the build would not complete. After approximately 0.3 mm (10 layers) of build height, the test samples began to spontaneously fracture and fail structurally. In the time it took to recoat each layer the upper surfaces fractured and detached from the body of the sample leaving large voids. The experiment was terminated in view of further investigation into the cause of the phenomena.

Investigation indicated that failure was due to internal stress build-up or shrinkage (Kumar Ghosh and Saha, 2011).

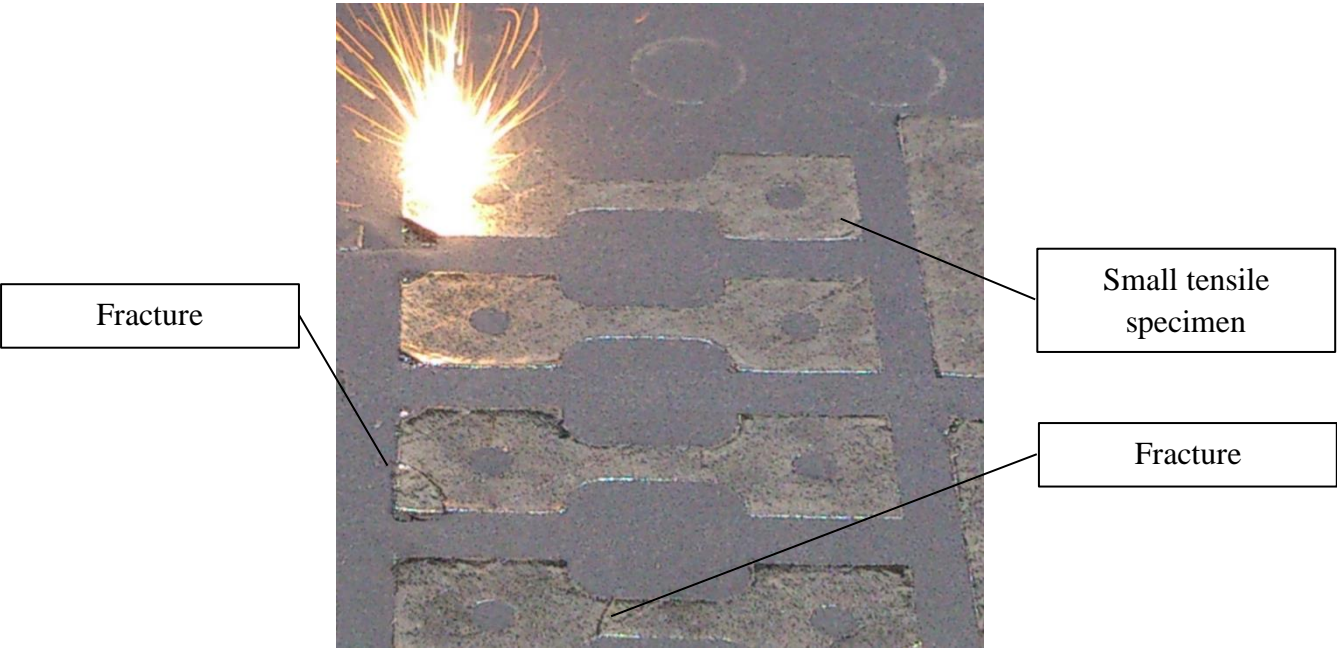


Figure 21 In-Process Fractures

Several fractures were observed across the tensile test area of the specimen sample (Figure 21). Fractures were not exclusive to geometrically weaker areas of the test samples, as they were observed across the corners of samples and between the sample and build platform. It was also noted that these fractures were not delaminations but effected multiple layers simultaneously, indicating the materials ability to build layer by layer was not in question.

It was theorised that for a part to fracture so quickly the material must be undergoing rapid contraction on solidification. It is also possible that the ductility of the matrix material (Ti6Al4V) was insufficient to accommodate the changes in expansion and contraction during laser processing.

The samples produced were analysed (Figure 22) and using a scanning electron microscope (SEM) it was found that the fracture surfaces were populated with many round particles, 3 to 8  $\mu\text{m}$  in size,

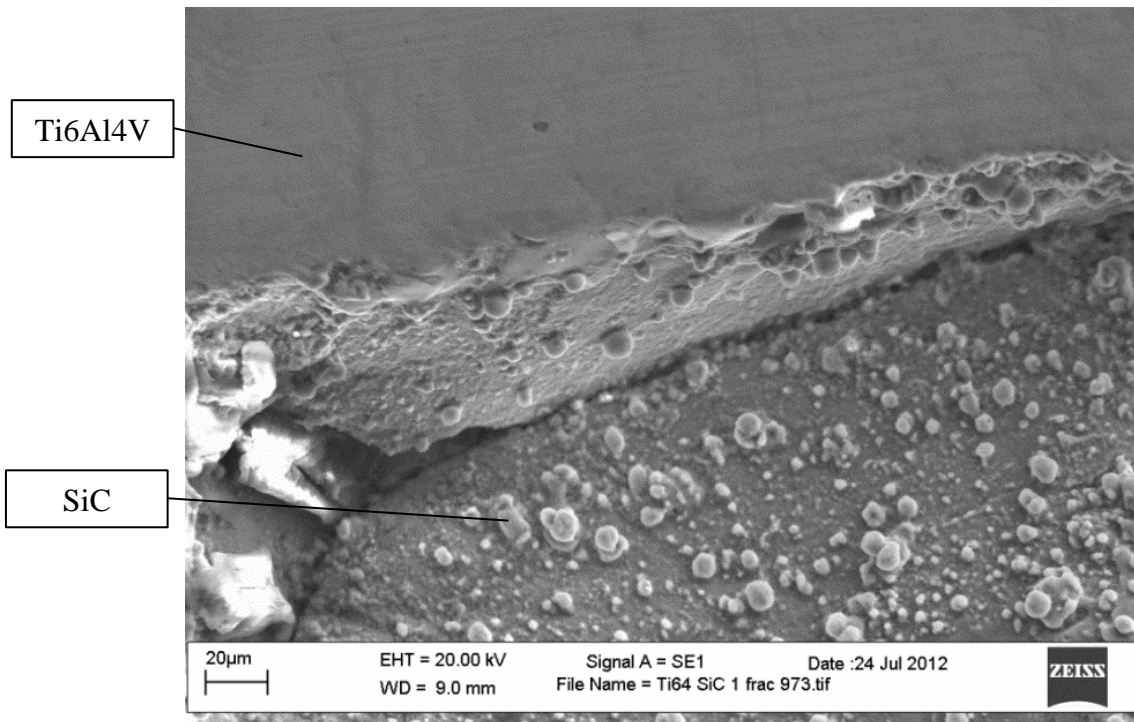


Figure 22 MMC Fracture Surface.

On analysis of the particulates around the fracture surface, SEM EDX analysis found them to be Ti6Al4V, however, they could theoretically be particles of SiC coated in Ti6Al4V. If this were the case, they would be about the correct size. It was also noted that in comparison to a typical Ti6Al4V fracture surface (Figure 23), the fracture surface differs significantly (Yin et al., 2015).

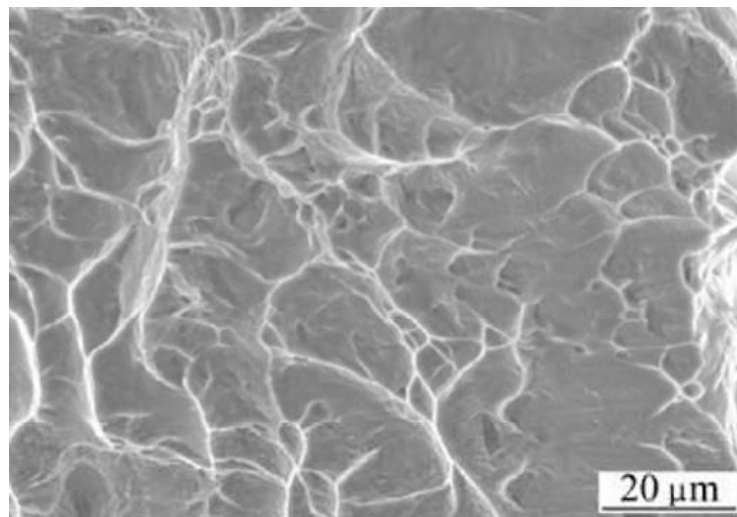
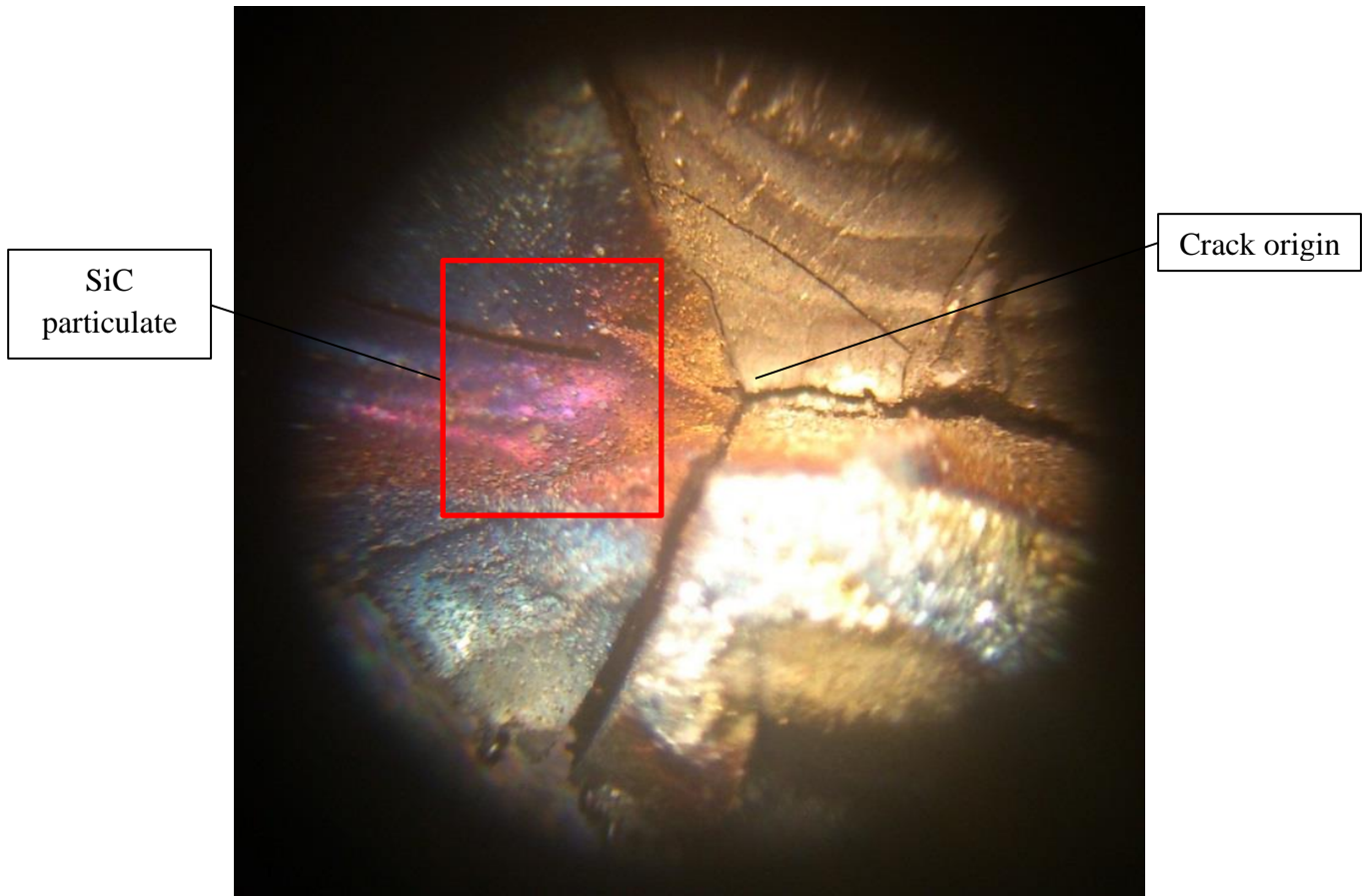


Figure 23 Ti Fracture Surface (Yin et al., 2015)

This would suggest a concentration of SiC rather than a homogeneous distribution throughout the sample. Authors such as Patterson 2017, Yadroitsev 2016, Elambasseril 2012 and Vrancken 2013 have shown that Ti64 is highly susceptible to stress concentration during the build process

and therefore it is feasible that clustered particles of SiC would act as stress raisers within the matrix by forming an area of high-saturation of SiC at this point in the matrix material (Ti6Al4V) offering a lack of continuity around the reinforcement. Figure 24 Shows the fracture surface of a fragment expelled from the test build, particulates are visible on the fracture surface. It can also be observed that the crack origin is in the centre of the sample, with a radial propagation of cracks, this would suggest that the highest concentration of stress was found at the centre of the specimen.



**Figure 24 MMC Fracture Surface (50 x magnification)**

The initial test has highlighted complex material and process interactions taking place and has highlighted the need for further investigation into the mechanics of this interaction. Furthermore, the production of feedstock is also of concern due to the evidential lack of homogeneity.

Given the initial investigations, further work focused on:

- Feedstock production and characterisation.
- Selective laser melted MMC material characterisation.

# Chapter Four

## 4.0 Research Methodology

### 4.1 Introduction

The literature review indicated that this research would benefit significantly from experimentation and analysis to determine the most appropriate and effective characteristics of feedstock and process parameters that would offer quality processed components / material. Commercially available Ti6Al4V material was used as a benchmark with which the MMC material could be compared with regards to presenting a viable effective and reliable method of validating results post the addition of SiC. It is critical that the specifications of the feedstock produced through the mechanical alloying (MA) route do not fall outside that which is processable by the SLM equipment (EOS M290). The resultant feedstock was therefore benchmarked against commercially available Ti6Al4V supplied by EOS GmbH, and SiC sourced from Dynamic Ceramic, UK for powder characteristics. The processability of the subsequently manufactured MMC material was processed using the EOS M290 SLM machine over a range of energy densities to determine a processing window for the resultant MMC material.

Figure 25 shows the methodology workflow comprising three phases. Phase one considers the baseline assessment of both raw materials (Phase 1a) and Ti6Al4V scan parameters applied to a range of energy densities (Phase 1b). Phase two investigated the MMC feedstock manufacture by MA (Phase 2a) and the benchmarking of the feedstock against Ti6Al4V material (Phase 2b). Phase three determined the scan parameters and hence the processing window for the MMC material Ti6Al4V (Phase 3).

## Characterisation of Mechanically Alloyed Feedstock for Selective Laser Melting; Titanium Silicon Carbide Metal Matrix Composite.

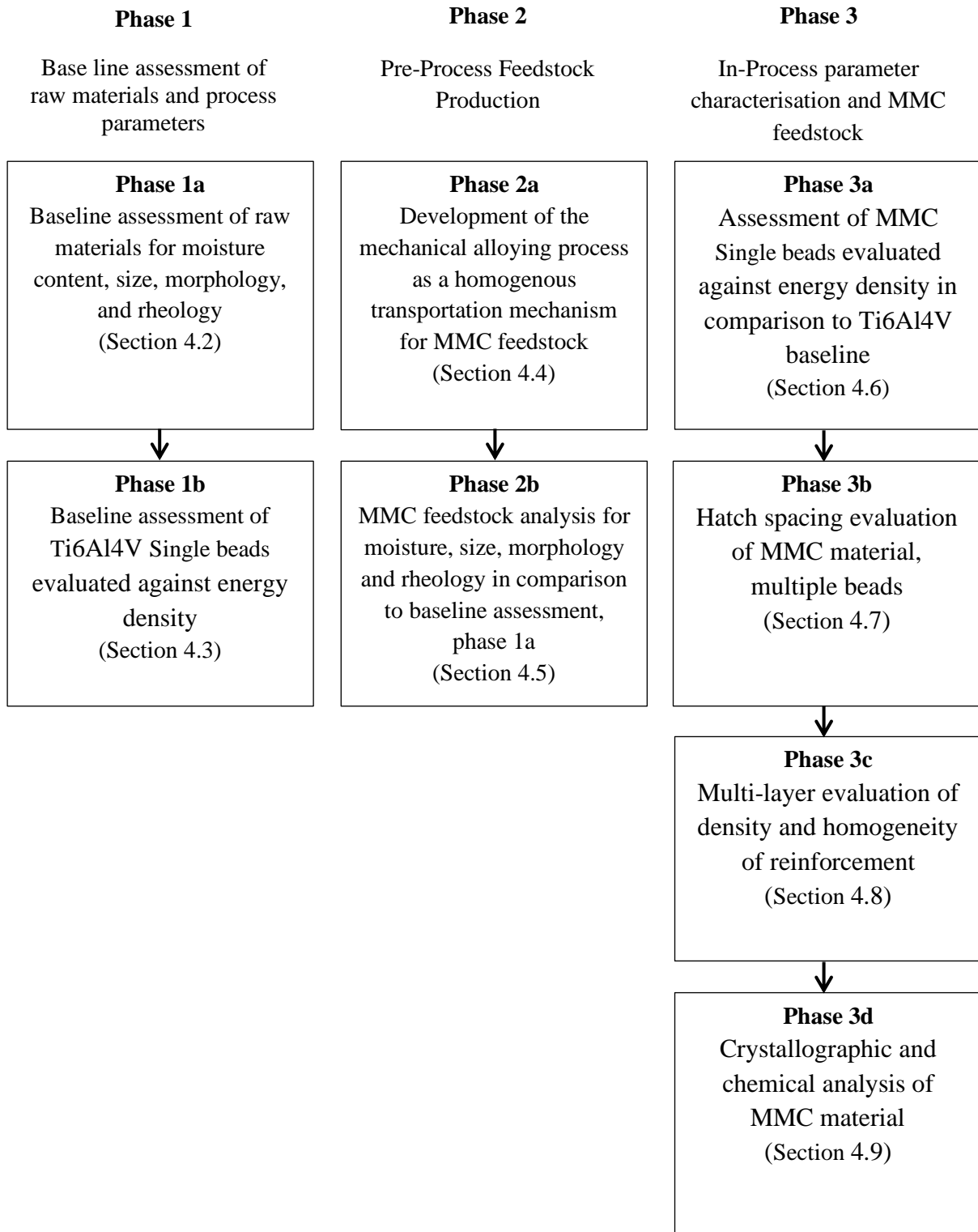


Figure 25 Methodology Workflow.



## 4.2 Phase 1a: Baseline Assessment of Raw Materials.

### 4.2.1 Overview of The Experimental Design

Powder analysis techniques were used to characterise the experimental feedstock materials to verify that they were suitable for the SLM process, in so doing they were comparable to commercially available feedstock. The objective of the MA process was to embed the reinforcement on to the surface of the matrix material without significantly altering the morphology of the matrix material and to provide a transportation mechanism for the powder spreading activity for the SLM process. The analysis provided data to benchmark the experimental results against to determine that the resultant feedstock remained comparable to the source material.

The component materials used were analysed individually as was the MMC feedstock at stages during and after MA (mechanical alloying). Data was gathered for the:

1. Moisture content
2. Particle size, size distribution, and morphology.
3. Rheological characteristics.

### 4.2.2 Sample Sizes

In all cases, a representative sample of the raw materials was collected and analysed in accordance with the test procedures as summarised in (Table 10).

Table 10 Powder Analysis Sample Sizes

| Experiment                                       | Equipment          | Sample size (g) |
|--------------------------------------------------|--------------------|-----------------|
| Moisture content                                 | Adam PMB53         | < 10            |
| Particle size, size distribution, and morphology | Retsch Camsizer X2 | 10 to 30        |
| Rheological characteristics                      | LPW Powder Flow    | 50              |

Samples were tested at a temperature of 20 °C in an environment conducive with the test being carried out and all appropriate safety precautions for the handling of powders were followed. Three samples were taken for each test to provide an arithmetic mean ( $\bar{x}$ ) to avoid the effect of anomalous results.

### 4.2.3 Restrictions and limitations

#### 4.2.3.1 Moisture Content, Restrictions and Limitations

Measurement of moisture was conducted using the ‘loss of mass’ method (Cordova, et al., 2017) wherein the measurement of all volatiles present in the sample is measured as total loss of mass, not only water present. The method chosen was conducted under laboratory conditions and a target value of < 1% was adopted for the chosen variable (Vluttert, 2016). Results were

presented as a loss of mass in the form of a percentage of the original mass (section 5.1.1 and section 5.4.1).

#### **4.2.3.2 Particle Size and Morphological, Restrictions and Limitations.**

A Camsizer X2 dynamic image analysis system was used to measure particle size, size distribution, and morphology. The specified accuracy of the equipment demonstrated an ability to measure particulates from 0.8  $\mu\text{m}$  to 8 mm. The size range for the Ti6Al4V material was specified by the manufacturer as 10  $\mu\text{m}$  to 63  $\mu\text{m}$  which was within the apparatus operating limits. However, the SiC material was specified as 0.6  $\mu\text{m}$  to 1.0  $\mu\text{m}$  which was below the operating range of the apparatus. Additional equipment in this case in the form of a Scanning Electron Microscope (SEM) was used for the measurement of particulates of 0.8  $\mu\text{m}$  and smaller. Whilst this gave accurate sizes of particles it was not possible to generate a size distribution graph. Calibration of the Camsizer X2 was conducted using a reticule provided by the equipment manufacturer and following the calibration routine. Calibration of the SEM was conducted annually by a qualified service engineer.

#### **4.2.3.3 Rheological Restrictions and Limitations.**

The methods followed were traceable to international standards where applicable (ASTM B213, ISO 4490, ASTM B964, ASTM B212 and ISO 3923-1). Angle of repose was determined using a protractor to directly measure the angle. As the same method was applied to all analysis this was not considered an issue.

The research was restricted in terms of analysis of entrapped gasses and the analysis of entrapped oxygen both on the surface and embedded within the particulate material. Every effort was made during the handling, storage, and processing of the materials to ensure that they were not exposed excessively to oxygen ensuring that the oxygen levels would remain the same throughout. Results in terms of the role that oxygen could play in the reaction process did not form part of this research.

### **4.2.4 Equipment**

#### **4.2.4.1 Moisture Content**

Moisture content measurement was carried out using an Adams PMB53 Moisture Analyser. Representative samples of the matrix material, reinforcement material, and mechanically alloyed feedstock were analysed to determine the levels of moisture that was present within the samples prior to analysis for particle size, morphology or rheology. Elevated levels of moisture within the feedstock can affect its morphology, evidenced by high levels of agglomeration within the powder; when analysed, these agglomerates can give the impression that the powder is unsatisfactory. Rheologically, elevated levels of moisture within the feedstock affect its flowability and therefore directly affect its packing density and ability to coat the entire build area homogeneously. In terms of part quality, moisture in the feedstock can lead to gas entrapment in the part and the chemical dissociation of water molecule can lead to extra oxygen and hydrogen in the process (LPW Technologies 2017).

The method employed was a volumetric measurement using the loss of mass method to measure the evaporation of water and other volatiles.

Moisture levels for Ti6Al4V were typically measured at < 1.0% for powder stored in accordance with manufacturers guidelines and used within the EOS M290 machines. This was thus taken as typical. Where levels were > 1.0% the powder was heated at 150°C for twenty minutes (Cordova, et al., 2017) and retested before conducting further analysis. Within the laboratory conditions it was accepted that environmental moisture pickup was largely unavoidable but could be minimised.

#### **4.2.4.2 Particle Size and Morphological Characteristics.**

Particle size, size distribution, and morphological characterisation was carried out using a Retsch Camsizer X2, in a dry environment suspended in an air stream. Utilising two cameras, a basic camera for large particles and a zoom camera for the smaller particles, the Retsch Camsizer X2 employs dynamic image processing (ISO 13322-2) to accurately analyse the particulate capturing on average, 300 images per second.

The Retsch Camsizer X2 was used specifically to analyse the changes taking place in terms of size and morphological aspects during the mechanical alloying stage of this research. It has been established that changes regarding the particulates shape and size distribution are key factors relating to an increase of porosity within subsequent manufactured parts (Spierings, et al., 2011, and Baitimerov, et al., 2018). The MA process was conducted until the feedstock lost these properties.

#### **4.2.4.4 Rheological Characteristics.**

Feedstock manufacture for SLM demands a range of tests to be adopted for the analysis of powders. Over recent years these have included many tests adopted from other industries such as the pharmaceutical industry, however, for the additive manufacturing industry it is becoming increasingly clear that a select few rheological tests are required. These tests apply to both the manufacturer and the end user. These include:

- Hall flow to ASTM B213 and ISO 4490 standards
- Carney flow to ASTM B964 standard
- Apparent density to ASTM B212 and ISO 3923-1 standards
- Tap density
- Angle of Repose to LPW standardized procedure.

This series of tests has been established to provide a set of standardised techniques for the characterisation of powders. The ASTM international standard was developed specifically for metal powders with the current versions being published in 1999 (B 212) and 2003 (B 213).

Table 11 summarises the rheological experimentation with respect to this research:

**Table 11 Rheological Experimentation with Respect to This Research**

| Test             | Description                                                            | Key indicator                                                                                                                | Value                                           | Research relevance                                                                                                                                                                      |
|------------------|------------------------------------------------------------------------|------------------------------------------------------------------------------------------------------------------------------|-------------------------------------------------|-----------------------------------------------------------------------------------------------------------------------------------------------------------------------------------------|
| Hall flow        | Time taken for a mass of powder to fall through an aperture of 2.54 mm | Satellites, loss of sphericity and agglomerations causing voids within the powder bed leading to porosity in the part.       | Grams per second (g/s)                          | Relevant in comparison between Ti6Al4V elemental powder and MA feedstock, an increase in time indicates an increase in surface roughness resulting in less feedstock per recoat.        |
| Carney flow      | Time taken for a mass of powder to fall through an aperture of 5.08 mm |                                                                                                                              |                                                 |                                                                                                                                                                                         |
| Apparent density | Volumetric measurement of loose powder in a standard volume            | Volume of powder deposited per layer, as this decreases less material is available within the melt pool leading to porosity. | Grams per cubic centimetre (g/cm <sup>3</sup> ) | Relevant comparison between Ti6Al4V elemental powder and MA feedstock, a decrease in apparent density indicates an increase in average particle size leading to possible part porosity. |
| Tap density      | Volumetric measurement of compacted powder in a standard volume        | Volume of powder in dispenser, powder is agitated to ensure that powder is compact to give best coverage when recoating.     | Grams per cubic centimetre (g/cm <sup>3</sup> ) | Assists in maximising packing density                                                                                                                                                   |
| Angle of repose  | Angle at which a sloping surface of loose powder is stable             | Indicator of powders ability to lock together, a low angle is preferred indicating powder will spread evenly on recoat.      | Degrees                                         | Relevant comparison between elemental powders and MA feedstock, an increase in angle indicates degradation of powder surface finish, uneven spreading may occur.                        |

Apparent density and angle of repose were used within this research as indicators of powder acceptability using commercially available Ti6Al4V as a benchmark. Hall or Carney flow was not used due to inability to obtain satisfactory results and tap density was not used as this is only an indication of the volume of compacted feedstock.

#### 4.2.4.3.1 Apparent Density

Within this research, the apparent density of mechanically alloyed feedstock was measured and compared to the same tests conducted for both the matrix material (Ti4Al6V) and the reinforcement material (SiC) to determine its suitability within the process in terms of the deliverable volume of material per layer.

The apparent density test is primarily concerned with a powders ability to occupy space, for a normal distribution within a powder sample small particle will mix freely with larger ones creating less voids between the particles and allowing more powder to occupy the same space and specifically the volume for the recoated layer. The apparent density experiment relates directly to the powder deposited during recoat. This material is mechanically positioned by the recoater with minimal force and particles can freely fall to enhance the layer density. However, as smaller fines are consumed more easily by the process the particulate size range must be monitored as more gaps form between larger particle on recoat resulting in less material per layer. This is detrimental to the formation of weld beads within the process due to the starvation of the melt-pool; this intern can lead to voids and porosity within the part. When the current layer is lased, the powder transitions from a loose mass to a solid and is added to the substrate, this process involves a loss of height as the recoated layer sinks marginally on solidification. In effect the powder is transitioning from apparent density to physical density, if the apparent

density of the powder is 50% that of the density of the solid material the resultant added material will be half that of the layer height, this will be made up on a subsequent recoat by a thicker layer of powder. This is accepted as necessary for the process however, by maintaining the maximum possible amount of material being available to the melt-pool, maintaining a high apparent density the risk of creating thicker layers and inconsistencies within the part are minimised (Baitimerov, et al., 2018).

#### **4.2.4.3.3 Angle of Repose**

Within this research, the angle of repose was measured for the mechanically alloyed feedstock and compared to both the matrix material (Ti4Al6V) and the reinforcement material (SiC) to determine its suitability within the process.

Angle of Repose was measured using the Carney flow funnel utilizing a 5.08 mm standard orifice to maintain a repeatable powder flow. A platform of known diameter (34.0 mm) is placed 25 mm beneath the funnel and powder can flow from the funnel onto the platform to form a heap. The height of the resultant heap was measured, and the angle is calculated in accordance with the manufacturer's instructions (LPW Technologies 2018).

The angle of repose is concerned primarily with the powders ability to lock together and retain position, smooth spherical particulates that flow easily demonstrate a low angle of repose. However, as the powder degrades through multiple uses, satellites form on particulates and agglomeration takes place inhibiting its ability to flow as freely, this is evidenced by an increased angle of repose. A baseline angle of repose using virgin Ti6Al4V powder was established for comparison to the optimum batch of MA feedstock to determine rheological changes that could pose challenges to the SLM process.

### **4.2.5 Procedures and variables**

#### **4.2.5.1 Moisture Content Analysis Procedure and Variables**

Aluminium weighing trays were cleaned with a solvent (isopropanol), dried and placed into the Adams PMB53 Moisture analyser and the analyser was set to zero.

Samples of <10gms of powder were distributed evenly across an aluminium weighing tray and enclosed within the Adams PMB53 Moisture Analyser. Samples were heated to 120°C for 20 minutes and the resultant percentage of moisture documented.

The sample tested was retained and the process repeated three times taking a fresh aluminium weighing tray and sample each time. This ensured that the process remained uncontaminated and that a representative sample was taken from the batch. The target moisture level was set at < 1%, samples with an average moisture level of > 1% were heated in an oven at 150 °C for twenty minutes then allowed to cool within the same environment, the moisture content analysis procedure was then repeated.

Table 12 shows the variables used across all moisture analysis experiments.

**Table 12 Moisture Analysis Process Variables (Adam, 2018)**

| Variable          | Description                           | Parameter          | Operator | Value    |
|-------------------|---------------------------------------|--------------------|----------|----------|
| Test duration     | Length of time the test was conducted | Minutes            | min      | 20       |
| Temperature range | Minimum and maximum temperatures      | Degrees centigrade | °C       | 20 - 120 |

#### 4.2.5.2 Particle Size and Morphological Analysis Procedure and Variable

Before conducting analysis, the apparatus was cleaned with a solvent (isopropanol) to remove contamination remaining from previous test samples, in accordance with the manufacturer’s instructions.

A calibrated reticule was used to calibrate the instruments optics, for both the basic and the zoom cameras in accordance with the manufacturer’s instructions (Retsch 2018).

A representative sample of raw material was taken from each batch and analysed.

Table 13 shows the variables measured across all particle size and morphological experiments.

**Table 13 Variables for Particle Size and Morphological Analysis (Retsch, 2018)**

| Variable        | Description                                                                                                                              | Parameter           | Operator                             | Value                                                        |
|-----------------|------------------------------------------------------------------------------------------------------------------------------------------|---------------------|--------------------------------------|--------------------------------------------------------------|
| Particle size   | Refers to the particle width. The shortest distance across the particles image, that which would fall through a sieve.                   | X <sub>c</sub> min  | ≥<br>(used to exclude unwanted data) | 0.010 μm<br>(used to exclude unwanted data)                  |
| Particle length | The longest measured element of a particle                                                                                               | X <sub>Fe</sub> Max | -                                    | -                                                            |
| Aspect ratio    | The ratio between width (X <sub>c</sub> min) and length (X <sub>Fe</sub> Max) an aspect ratio of 1.000 $\neq$ indicates a round particle | b/l                 | ≤<br>(used to exclude unwanted data) | 0.850<br>(to calculate number of irregular shaped particles) |
| Sphericity      | The roundness of a particle                                                                                                              | SPHT                |                                      |                                                              |
| Transparency    | Transparency of a particle high values indicate a blurred image                                                                          | Trans               | ≤<br>(used to exclude unwanted data) | 0.100<br>(used to exclude unwanted data)                     |
| Area            | The width of a circumferential boundary around a particles image, irregularities make the boundary larger.                               | X <sub>area</sub>   | μm                                   | -                                                            |

#### 4.2.5.3 Rheological Procedure and Variables for Apparent Density and Angle of Repose

Experiments were conducted on Ti6Al4V matrix material to establish baseline characteristics and SiC reinforcement material in comparison prior to mechanical alloying (Phase 1). On completion of mechanically alloying experiments, the resultant feedstock powder was analysed and compared against the results for Ti6Al4V. Before conducting analysis, the apparatus was cleaned with a solvent (isopropanol) to remove contamination remaining from previous test samples analysed by the equipment in accordance with the manufacturer’s guidelines (LPW

Technologies 2017). The apparatus was calibrated against a reference material supplied by the manufacturer and in accordance with the manufacturer’s guidelines (LPW Technologies 2017). Each test was conducted three times and an average taken to reduce errors found during the procedure. All tests were conducted in a temperature-controlled environment at 20°C. Table 14 shows variables used across all apparent density and angle of repose experiments.

**Table 14 Variable for Rheological Analysis (LPW Technologies 2017)**

| Variable         | Description                                                                               | Parameter         | Operator | Value  |
|------------------|-------------------------------------------------------------------------------------------|-------------------|----------|--------|
| Material density | Density of solid material for a fixed volume                                              | g/Cm <sup>3</sup> | =        | -      |
| Apparent density | Density of loose powder for a fixed volume, Used to calculate volume of material recoated | g/Cm <sup>3</sup> | =        | -      |
| Angle of repose  | Steepest angle of a sloping surface of loose material                                     | (x) <sup>o</sup>  | =        | 0 - 90 |

## 4.2.6 Statistical Treatment

### 4.2.6.1 Moisture Content

Three samples were analysed, an average was calculated and used to determine the batch status.

### 4.2.6.2 Particle Size and Morphological Analysis

Statistical treatments, part of the Retsch analytical software (Retsch 2017) were used in compiling data for analysis. Table 15 show the statistical operators used.

**Table 15 Variables for Particle Size and Morphological Analysis (Retsch, 2018)**

| Variable                             | Description                                                                                                            | Parameter          | Operator | Value         |
|--------------------------------------|------------------------------------------------------------------------------------------------------------------------|--------------------|----------|---------------|
| Volume based distribution            | Total volume of powder analysed against the measured particle variable                                                 | Q3                 | %        | 0 - 100       |
| Sample mean size                     | Mean size of particles in the total volume of the sample                                                               | Mv3( $\bar{x}$ )   | µm       | -             |
| 10 percentiles                       | Expected mean particle size in the first 10% of the samples total volume, 10% probability of the average particle size | D10                | µm       | -             |
| 50 percentiles                       | Expected mean particle size in the first 50% of the samples total volume, 50% probability of the average particle size | D50                | µm       | -             |
| 90 percentiles                       | Expected mean particle size in the first 90% of the samples total volume, 90% probability of the average particle size | D90                | µm       | -             |
| Mean aspect ratio                    | The mean aspect ratio is an indication of a sample’s roundness, above 0.850 $\mathcal{AR}$ would be classed as round   | b/l3               | µm       | 0.000 – 1.000 |
| volume percentage of round particles | The inverse volume of the aspect ratio at 0.850 $\mathcal{AR}$ is the percentage of particles that are rounded         | 1-Q3 (b/l = 0.850) | %        | 0 - 100       |

### 4.3 Phase 1b: Baseline Assessment of Ti6Al4V Single Beads Evaluated Against Energy Density.

#### 4.3.1 Overview of The Experiment/Design

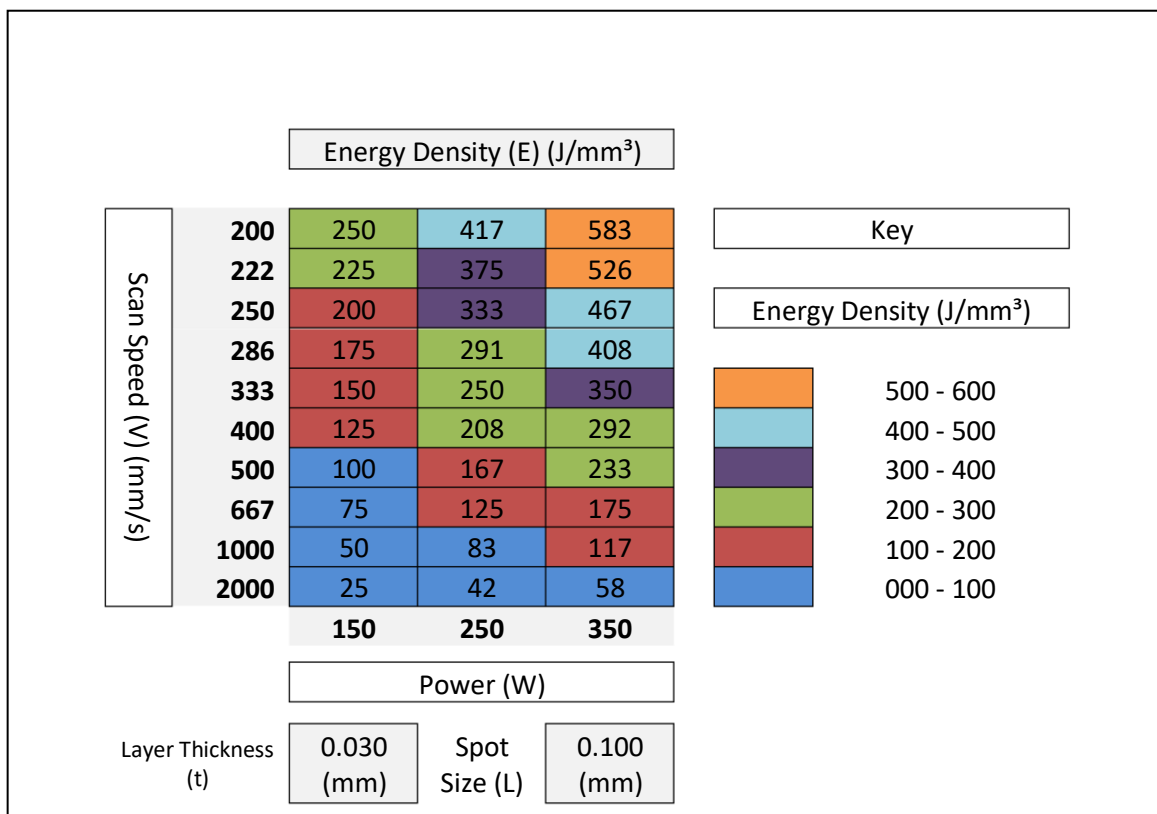
To characterise the effect of the addition of SiC reinforcement into the feedstock a series of tests were developed, and where possible, were benchmarked against Ti6Al4V to investigate the MA feedstocks processability. In view of the findings from the initial experimentation (Section 2.1), a deconstructive qualitative methodology was adopted.

The aim was to evaluate the most significant elements of the processes only, to avoid confusion and to better understand how the new material behaves in comparison to Ti6Al4V.

Where possible the operating conditions and parameters were kept the same as for Ti6Al4V, such as layer thickness, scan pattern, inert atmosphere and gas flow rate, recoat speed and recoat volume.

Beginning with single beads, Ti6Al4V was exposed to a broad range of energy densities on a single layer to evaluate the materials processability, miscibility and physical characteristics. These results were used to benchmark the MMC feedstock material in phase 2b.

Table 16 Energy Density Matrix (J/mm<sup>3</sup>)





### 4.3.2 Sample Size

An experimental population was developed to offer a matrix of energy densities across the available laser power and scan settings for the process. Table 16 shows the energy densities (E) matrix based on a spot size (L) of 0.100 mm and layer thickness (t) of 0.030 mm.

The test matrix comprises thirty single bead tests with variable scan speed and laser power. The matrix is formed of three laser power values, 150W, 250W and 350W to accommodate the full range of laser power available but also to minimise the total number of samples manufactured. Scan speeds have been calculated to linearize the energy density values for better representation of results; Figure 26 graphically illustrates the energy densities for each laser power range.

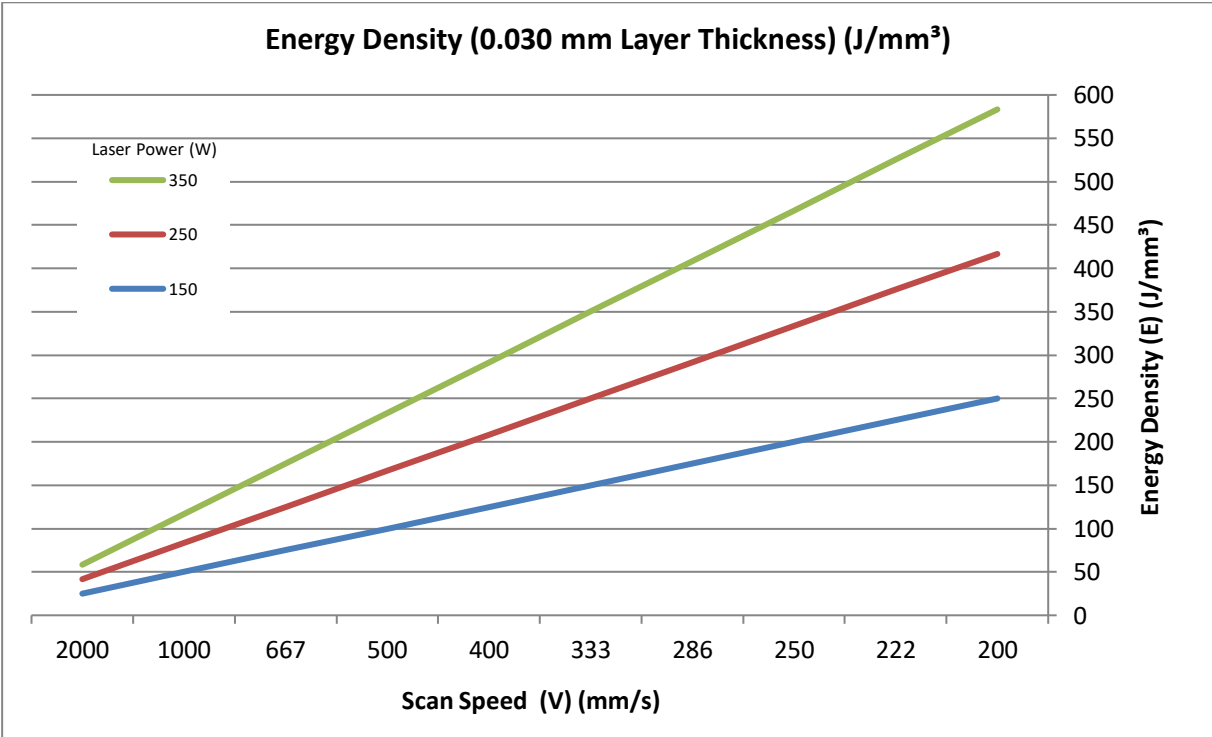


Figure 26 Energy Density (J/mm<sup>3</sup>) Over Scan Speed (V) (mm/s)

### 4.3.3 Restrictions and limitations

#### 4.3.3.1 Feedstock Availability

Due to the limited amount of feedstock produced, building sizable parts on a build platform measuring 250 mm x 250 mm was economically impractical due to the volume of powder per layer and the amount required in the dispenser. It was therefore necessary to develop a system of what became known as “mini chambers”. These mini chambers worked in conjunction with the equipment’s existing chambers but allowed for the ability to build with much less feedstock. The mini chambers build area was 120 mm x 120 mm.

#### 4.3.3.2 Energy Density Calculations Without Hatch Distance

When using energy density calculations sometimes referred to as the Andrew Number, (Williams, et al., 1996, and Savalani et al., 2011) it is common practice to calculate the affected volume of material using Equation (1):

$$Ed = \frac{P}{s * v * t} \quad \text{Equation (5)} \quad \text{(Lyall, 2018)}$$

Where:  $E_d$  is the Laser Energy Density (J/mm<sup>3</sup>)

$P$  is the Laser Power (W)

$s$  is the Spot Size (mm)

$v$  is the Scan Speed (mm/s)

$t$  is the Layer Thickness (mm)

For stage 1, single bead evaluation, the parameter of hatch distance ( $h$ ) is substituted by the laser spot size ( $s$ ) and is taken to be 0.100 mm as a constant.

#### 4.3.3.3 Laser Power Range

The apparatus used for the experiments was an EOS M290 with a manufacturer specified laser power range of 0 – 400 W, this however is not the useable range, during the calibration of the apparatus at installation the maximum laser power was fixed at 375 W to safely manage the laser equipment. In pre-test measurements a value of 372 W was measured which was within the specified tolerance of  $\pm 5\%$ . It was therefore decided not to exceed 350 W within experimentation undertaken.

#### 4.3.4 Equipment

Part experimentation was conducted using an EOS M290 selective laser melting machine.

Individual parameter setups were constructed using EOSPrint version 1.5 (2017).

Due to the limited availability of feedstock, Mini platforms and chambers were used to conduct experiments (Figure 27), comprising a build area of 120 mm by 120 mm. Counter bored holes in each corner enabled the platforms to be secured to a piston top and levelled using 5 mm grub screws in each corner, Each platform also incorporated a two-rail system as shown (Figure 27), positioned longitudinally in the direction of re-coating. The two-rail method optimised the laying of the powder bed for the single bead experiments. Under normal working conditions for most materials, the first two layers are double exposed to assist with bonding to the base plate; furthermore, the amount of feedstock on the first layer would be minimal. In the case of

the single bead experiments it was not possible to double expose as this would invalidate the results. Likewise, tests conducted with a less than normal layer thickness would also not be representative of the normal operating conditions of the process. Based on the apparent density measurements conducted in phase 1 it was observed that approximately 50.6% reduction in volume occurs through the transition from powder to solid, (section 5.1.5) each rail was therefore cut 0.045 mm to 0.050 mm high (Figure 27). By recoating the build plate until the rails were cleared of feedstock an accurate and repeatable layer thickness could be achieved, this method was used for all experiments in phases 3a and 3b. Multiple layer evaluation of density and homogeneity of reinforcement (3c) was conducted on mini build plates using standard operating procedures for preparing the build platform and environment.

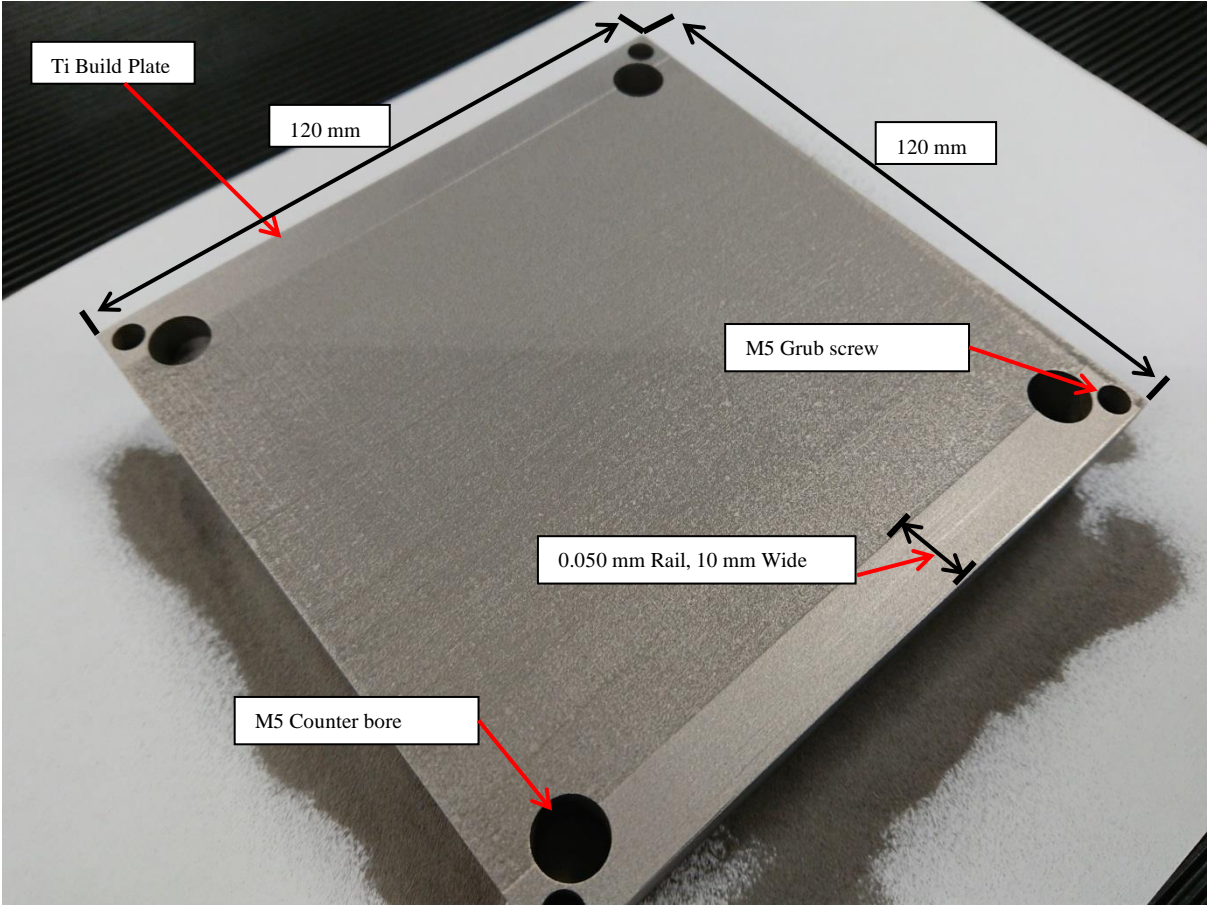


Figure 27 Mini Platforms with Reduced Build Area for Limited Feedstock, Recoated Using 45 – 50 μm Two Rail System.

### 4.3.5 Procedures

#### 4.3.5.1 Digital Files

The digital files were prepared using EOSPrint version 1.5 (Figure 28) parts were arranged as per Table 16 and labelled for future reference. The exposure order was set to expose the parts first, working from the front of the build chamber to the rear to minimise the risk of powder contamination from previous parts. Finally, the labels were exposed.

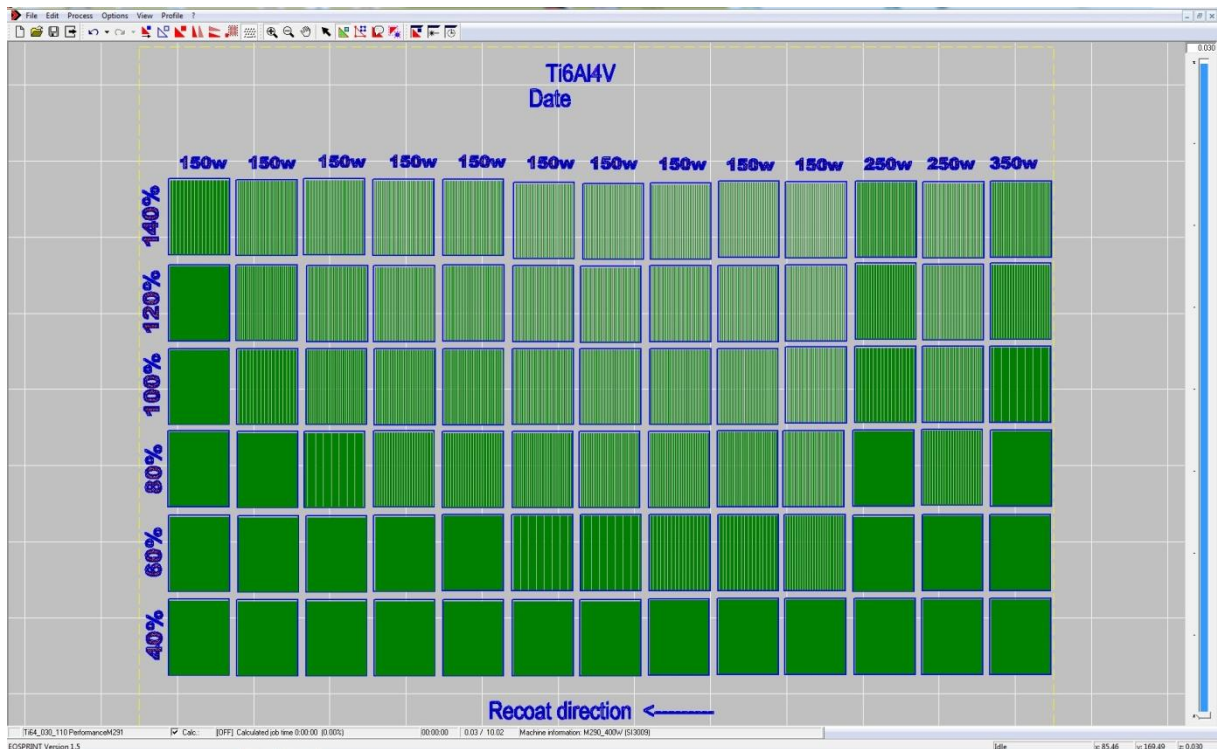


Figure 28 EOSPrint 1.5, Layout for Ti6Al4V Phase 3b

#### 4.3.5.2 Process Chamber Preparation

The process chamber was cleaned to ensure it was free from contamination, fitted with mini chambers and the laser power was checked using the laser power Pocket Monitor PMT 05P (Primes GmbH) Figure 29. The chamber was then purged of air/oxygen with Argon gas.



Figure 29 Primes laser power Pocket Monitor PMT 05P

#### 4.3.5.3 Build Platform Preparation.

The 120 mm X 120 mm square build platform was secured with M5 cap head screws (x4) in each corner and Levelled with M5 grub screws (x4) using a plunger type dial test indicator mounted to the recoater arm. For phases 3a and 3b the top surface was machined flat with 40 $\mu$ m to 50 $\mu$ m rails 10 mm wide were orientated longitudinally to the recoat direction and the build area showed no visible cutting marks or troughs such that feed stock can deposit preferentially,

phase 3c build plates were prepared flat. The surfaces were mechanically abraded to produce a uniform texture capable of retaining powder deposits uniformly across the surface and was cleaned chemically with a non-water based de-greaser (ethanol, isopropanol). A deposit of powder was established on the build plate ensuring that the two rails were free from powder before inerting the build chamber.

#### 4.3.6 Variables

##### 4.3.6.1 Phase 3a Variables (Single Bead Evaluation Against Energy Density)

Single beads were exposed using edges parameters to produce a single bead. Variables consisted of laser power and scan speed to achieve a range of energy densities in accordance with the energy density matrix in Table 16. Table 17 shows the Scan variables for the single bead experiment

**Table 17 Build Variables for Single Bead Experiment**

| Laser power (W) | Scan Speed (V) (mm/s) |     |     |     |     |     |     |     |      |      |
|-----------------|-----------------------|-----|-----|-----|-----|-----|-----|-----|------|------|
| 150             | 200                   | 222 | 250 | 286 | 333 | 400 | 500 | 667 | 1000 | 2000 |
| 250             | 200                   | 222 | 250 | 286 | 333 | 400 | 500 | 667 | 1000 | 2000 |
| 350             | 200                   | 222 | 250 | 286 | 333 | 400 | 500 | 667 | 1000 | 2000 |

##### 4.3.6.2 Phase 3a Attributes

For the software (EOSPrint 1.5) to produce single beads the following parameters were fixed for the build process (Table 18).

**Table 18 Build Attributes for Single Bead Experiment**

| Parameter Setting | Value                          |
|-------------------|--------------------------------|
| Hatch distance    | 0.24 mm                        |
| Stripe width      | 40 mm                          |
| Pre-Contours      | Off                            |
| Post-Contours     | Off                            |
| Rotation          | Off                            |
| X, Y              | X Only (Recoat along the bead) |
| Alternating       | Off                            |
| DMLS              | Off                            |
| Pre-Exposure      | Off                            |
| Up skin           | Off (Thickness = 0)            |
| Down skin         | Off (Thickness = 0)            |
| Beam expander     | Automatic                      |
| Platform heating  | 35°C                           |

## **4.4 Phase 2a: Development of Mechanical Alloying Process as a Homogenous Transportation Mechanism for MMC Feedstock.**

### **4.4.1 Overview of The Mechanical Alloying Experiment / Design**

Mechanical alloying (MA) was chosen to be explored as a method for combining reinforcement particles with matrix materials. This will allow the combined materials to be transported onto the build area for laser using the machine's recoater mechanism.

This section presents the research methodology to produce feedstock through the mechanical alloying method.

Due to the forces involved during the MA process, the challenge was to embed reinforcement material onto the surface of the matrix material without significant deformation and to retain flowability, but also to achieve homogeneity within the feedstock. The feedstock was therefore, periodically evaluated and benchmarked against existing Ti6Al4V powder analysis results with respect to size and morphology.

The aim was to determine the length of mixing time required to embed the reinforcement before altering the morphology of the matrix material. The following objectives were set.

- 1 Embed reinforcement material onto the surface of the matrix material.
- 2 Minimise increase in particle size.
- 3 Minimise change in particles morphology.
- 4 Homogeneously mix the reinforcement material throughout the feedstock.
- 5 Avoid contamination.

### **4.4.2 Mechanical Alloying Experimental Sample Size**

250 g of feedstock comprising of 7.0 g of SiC powder and 243.0 g of Ti6Al4V powder was added to 2500 g stainless steel balls (5 mm Ø) and mixed at 500 rev/min for up to 40 minutes in an argon atmosphere at a constant temperature of 20°C using the Zoz Symoloyer CM01 Mechanical Alloying Machine.

Samples were extracted at 5 min, 8 min, 16 min, 24 min, 32 min, and 40 min intervals for analysis for size and shape.

On completion of analysis the most appropriate milling time was used to produce a full batch of feedstock for Phase 3, In process parameter characterisation of MMC feedstock.

### **4.4.3 Restrictions and limitations**

Due to the available quantity of reinforcement material and the limited volume of material available per mill, it was only possible to take a small sample at each interval. Furthermore, this was kept to a minimum to avoid the risk of effecting the ball to powder ratio.

During processing, the Zoz Symoloyer CM01 monitored temperature but not oxygen levels, elimination of oxygen can only be achieved through the vacuum purge process and filling with an inert gas (argon), the purge process was repeated twice in this instance.

#### 4.4.4 Mechanical Alloying Equipment

The pre-process feedstock production equipment used is shown in Figure 30 and listed below:

- Symoloyer CM01 attrition mill
- Haake phoenix ii chiller
- Edwards vacuum pump
- Edwards vacuum meter
- Argon gas supply
- Maltoz computer software
- Sample containers
- Weighing scales
- Protective gloves

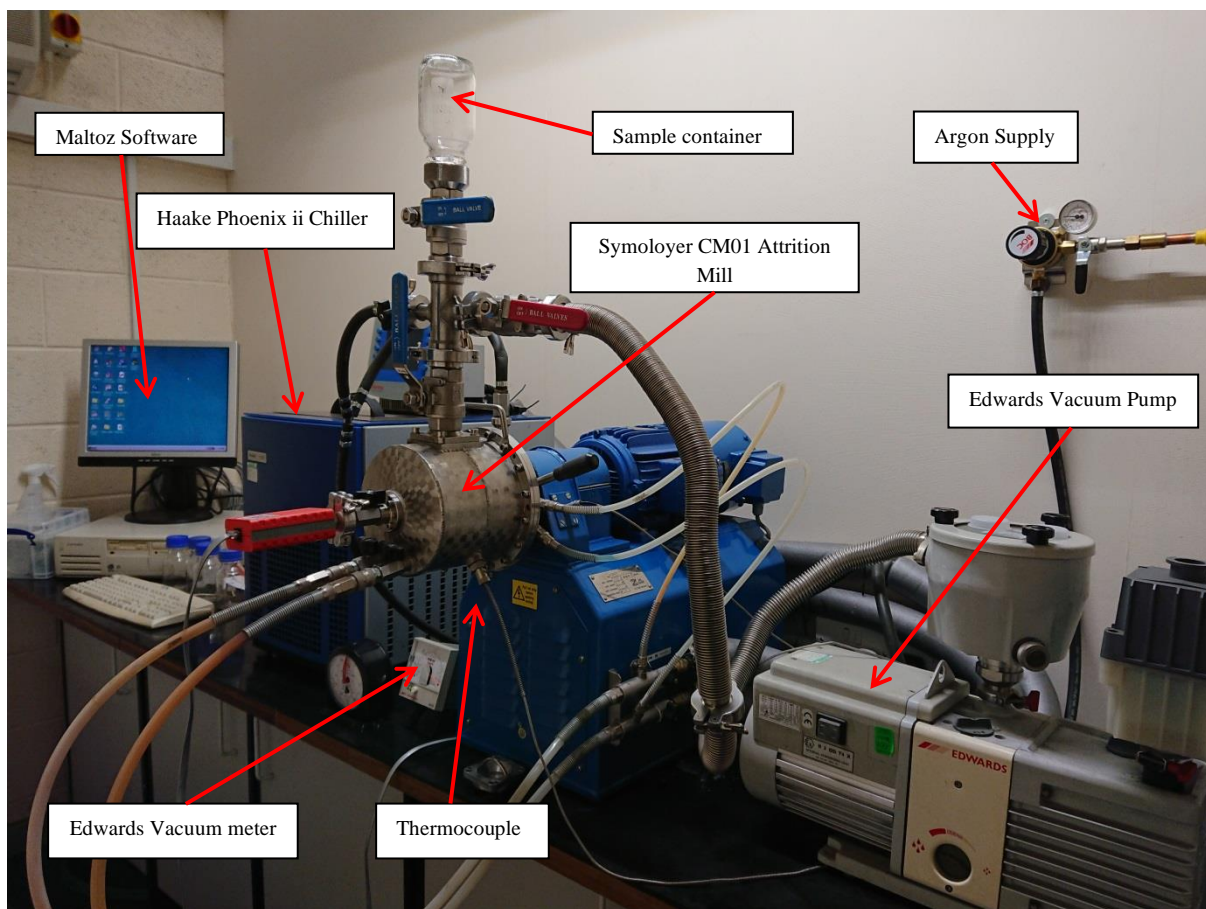
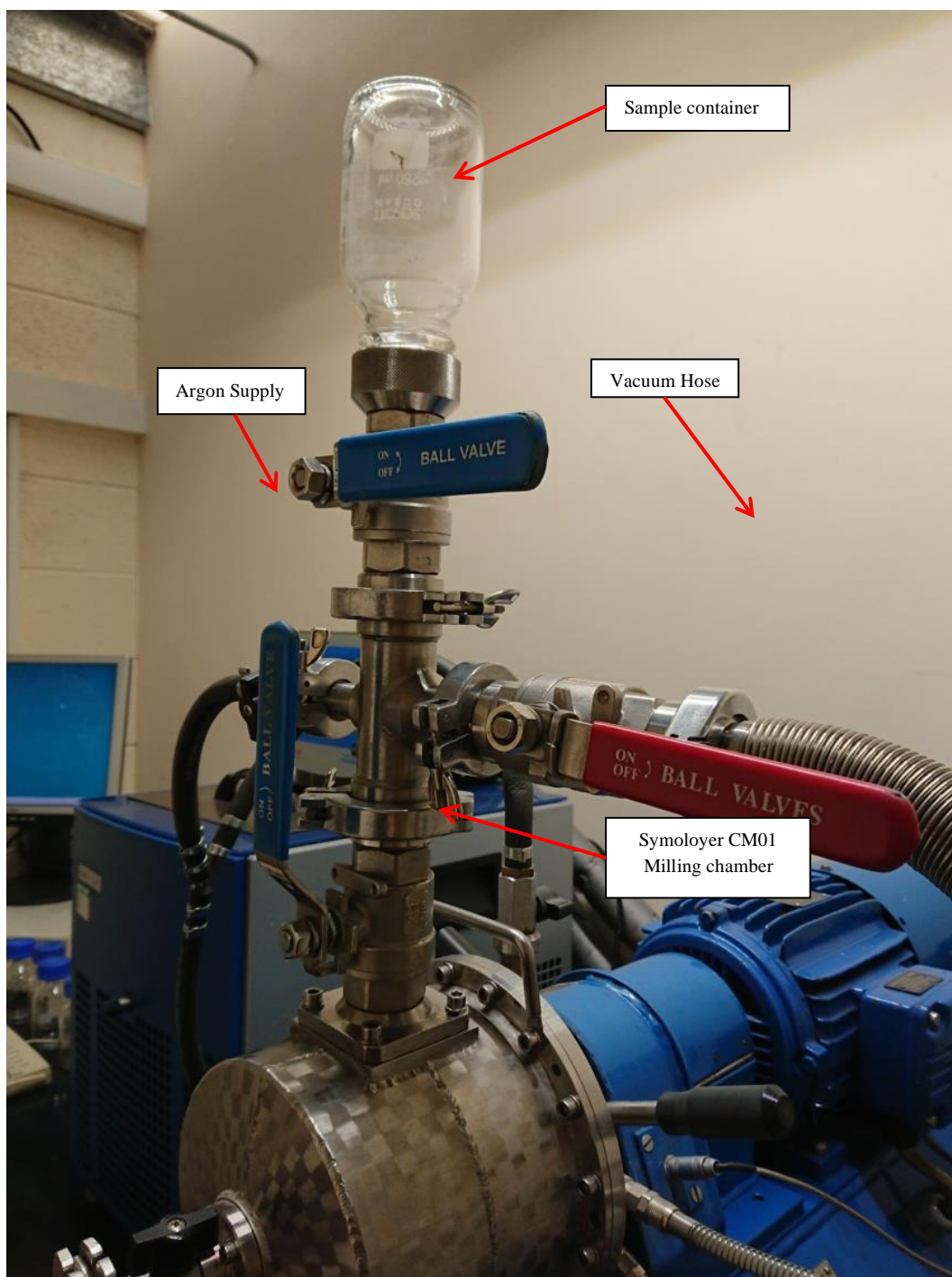


Figure 30 MA (Mechanical Alloying) Equipment

Figure 31 shows a more detailed view of the Symoloyer CM01. The milling chamber, detailed is locked into position (as shown) during milling and can be rotated through 180 degrees to enable samples to be taken at stages during the process.



**Figure 31** Symoloyer CM01 Detailed View

Control of temperature during the milling process was carried out by the Haake phoenix ii chiller unit (Figure 32) utilising the Simoloyer's double wall system to maintain the milling environment at 20°C





Figure 32 Haake Phoenix ii Chiller Unit

#### 4.4.5 Procedures

In accordance with the manufacturer's instructions, all the equipment was cleaned with isopropanol and checked for damage from previous use. The stainless-steel balls (2500 g) were cleaned and allowed to dry then placed into the milling chamber along with 250 g of feedstock comprising of 7.0 g of SiC and 243.0 g of Ti6Al4V powders.

The milling chamber was sealed and the sample container positioned vertically as shown in Figure 31, and the air was removed using the Edwards vacuum equipment, care was taken to use a low setting to avoid removing feedstock, air was removed until a vacuum reading of  $10^{-3}$  mbar was reached measured using the Edwards AGD Pirani gauge attached to the front of the milling chamber. The chamber was then filled with Argon gas at 1 bar (14.5 PSI) the rotor shaft was then rotated at 20 revs/min for 10 seconds using the Maltoz 3.2 software. The purge process was repeated once more.

Using the Maltoz 3.2 software the equipment was run at 500 rev/min for 5 min, 8 min, 16 min, 24 min, 32 min, and 40 min intervals where upon samples were taken for analysis of size and shape at each duration.

#### 4.4.6 Mechanical Alloying Variables for Surface Coverage by Reinforcement.

The use of MA for AM is concerned with forcing the smaller sized particles of reinforcement material (SiC) onto the surface of the larger and softer matrix material (Ti6Al4V). With this objective in mind it is only theoretically possible to embed a single covering of reinforcement particles onto the surface of the matrix material before the surface becomes fully saturated, any

remaining reinforcement material would therefore not become embedded but could remain present within the feedstock.

It was therefore the intention to accurately balance the volume ratio of reinforcement and matrix materials based on particle size, and to calculate an approximate value for the Maximum Volume of Reinforcement (MVR) at full saturation.

To calculate the Maximum Volume of Reinforcement (MVR), **Equation (6)** was developed. The calculation expresses the total achievable percentage of reinforcement material that can be embedded into the surface area of the matrix material and is based on the average particle sizes of the component materials.

$$MVR = \frac{\pi D_r D_m^2}{\pi D_r D_m^2 + D_m^3} 100 \quad \text{Equation (6)} \quad (\text{Lyall, I. 2018})$$

Where: **MVR** is the Maximum Volume of Reinforcement Material (%)

**D<sub>r</sub>** is the average particle size ( $X_{c \text{ min}}$ ) of the reinforcement material ( $\mu\text{m}$ )

**D<sub>m</sub>** is the average particle size ( $X_{c \text{ min}}$ ) of the matrix material ( $\mu\text{m}$ )

From measurements taken, the average particle size for the matrix material (Ti6Al4V) is approximately 37  $\mu\text{m}$ . This is atypical feedstock material currently used by the AM industry. The reinforcement material, however, can theoretically be any size. It is known from the work carried out by Tjong, Mai, (2008) and other researchers (Sivakumar, et al., 2016) that reducing the size of the reinforcement can significantly increase the strength of the composite. Tjong, and Mai, advocate the use of submicron reinforcement particulates and a reduced volume fraction of reinforcement. Much of the work within their 2008 paper used 10 vol.% reinforcement with positive results.

By using Equation (5) it is possible to determine the achievable volume of reinforcement based on average particle size.

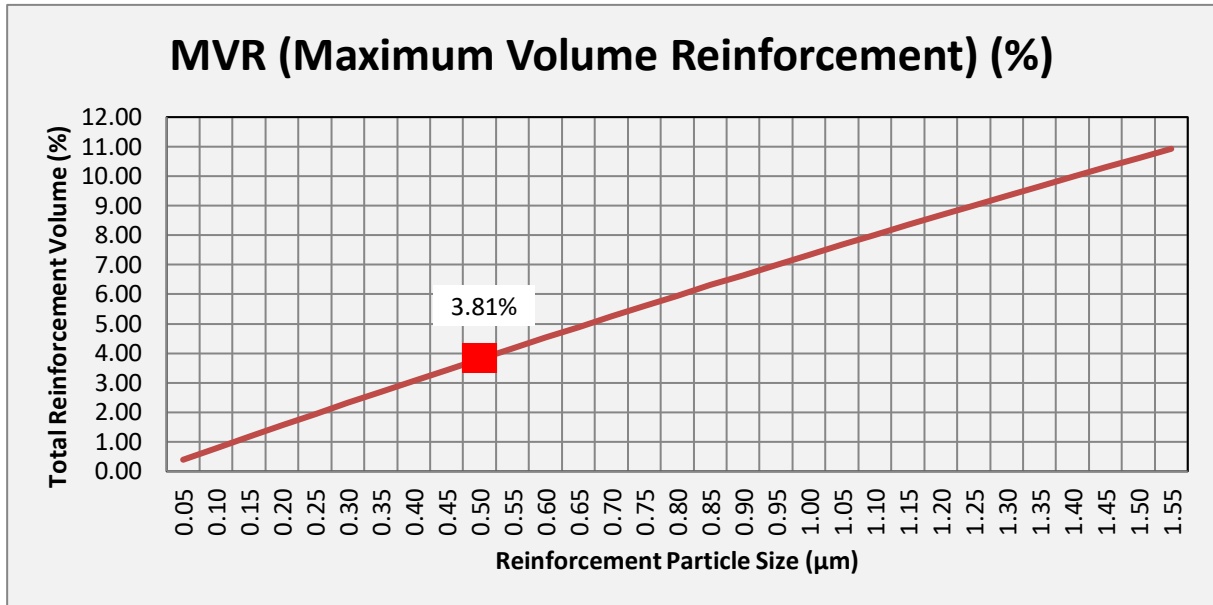


Figure 33 MVR (Maximum Volume Reinforcement) (%)

Figure 33 shows how the size of the reinforcement particles has an impact on the final volume of reinforcement within the MMC. With an average particle size for the matrix material ( $D_m$ ) of 39.7 µm and an average particle size for the reinforcement material ( $D_r$ ) of 0.50 µm it was calculated using Equation (6) that 3.81 vol.% of reinforcement within the MMC could be achieved. This would be in line with Tjong and Mai’s findings.

#### 4.4.6.1 Conversion from Volume Fraction to Weight Fraction of Reinforcement

Having calculated the volume fraction of reinforcement material ( $F$ ) it is necessary to convert this to weight (g) to accurately measure out the materials. Firstly, the total density of the matrix material is calculated using Equation (7). To accurately measure the reinforcement material (SiC) by weight it was necessary to convert the volume of reinforcement material to weight in grams using Equation (8).

$$P = F * Pr + (F - 1) * Pm \quad \text{Equation (7)} \quad (\text{Pilling, 2011})$$

Where: **P** is the density of the MMC (g/Cm<sup>3</sup>)

**F** is the Volume fraction of reinforcement material (%)

**Pr** is the density of the reinforcement material (g/Cm<sup>3</sup>)

**Pm** is the density of the matrix material (g/Cm<sup>3</sup>)

$$F_w = \frac{F * P_r}{F * P_r + (1 - F) * P_m} \quad \text{Equation (8)} \quad \text{(Pilling, 2011)}$$

Where:  $F_w$  is the volume fraction by weight of reinforcement material (%)

$F$  is the Volume fraction of reinforcement material (%)

$P_r$  is the density of the reinforcement material (g/Cm<sup>3</sup>)

$P_m$  is the density of the matrix material (g/Cm<sup>3</sup>)

Based on the maximum percentage of reinforcement (MVR) calculation, the calculation for quantities of component materials in relation to alloying balls can be seen in Figure 34.

|                                                                                 |         |                   |                |                                 |
|---------------------------------------------------------------------------------|---------|-------------------|----------------|---------------------------------|
| Percentage volume of matrix (Ti6Al4V)                                           | 96.19   | %                 | V <sub>m</sub> |                                 |
| Percentage volume of reinforcement (SiC)                                        | 3.81    | %                 | V <sub>r</sub> | F                               |
| Density of matrix material (Ti6Al4V)                                            | 4.42    | g/Cm <sup>3</sup> | P <sub>m</sub> |                                 |
| Density of reinforcement material (SiC)                                         | 3.21    | g/Cm <sup>3</sup> | P <sub>r</sub> |                                 |
| $P = F * P_r + (1-F) * P_m$                                                     |         |                   |                | Equation (7)                    |
| Calculated MMC Density                                                          | 4.34    | g/Cm <sup>3</sup> | P              |                                 |
| weight of balls                                                                 | 2500    | g                 |                |                                 |
| Weight of powder required for milling                                           | 250     | g                 |                | Balls to Powder Ratio = 10 to 1 |
| <b>Convert from volume fraction of Reinforcement to weight of reinforcement</b> |         |                   |                |                                 |
| $F_w = \frac{F * P_r}{F * P_r + (1 - F) * P_m}$                                 |         |                   |                | Equation (8)                    |
| Percentage reinforcement (wt.%)                                                 | 0.02796 |                   | 2.80           | %                               |
| Weight of reinforcement material                                                | 7.0     | g                 |                |                                 |
| Weight of matrix material                                                       | 243.0   | g                 |                |                                 |
| Total weight of powder for milling                                              | 250.0   | g                 |                |                                 |

Figure 34 Powder Mixing Calculations

## **4.5 Phase 2b: MMC Feedstock Analysis for Moisture, Size, Morphology and Rheology in Comparison to Baseline Assessment, Phase 1a.**

### **4.5.1 MMC Feedstock Analysis Overview of Experiment/Design**

Samples of mechanically alloyed feedstock were analysed to establish the adequacy of the MA method of feedstock production. Samples of the feedstock were taken at intervals of 5, 8, 16, 24, 32 and 40 minutes of alloying and analysed for size, size distribution and morphology using a Camsizer x2 (Retsch, 2017). The results were compared to those of Ti6Al4V established in phase 1a (section 4.2). based on the results an ideal set of mechanical alloying parameters was established and a batch of feedstock was produced.

### **4.5.2 Sample Size**

During the mechanical alloying process, samples of approximately 15 to 30 grams were removed from the process and using the Camsizer x2 (Retsch, 2017) particle size analyser. The process was then continued until 40 minutes had elapsed.

#### **4.5.1.2 MMC Feedstock Moisture and Rheological Analysis**

Following successful production of a batch of MMC feedstock, moisture and rheological analysis was carried out using apparent density and angle of repose. The results were compared to those of Ti6Al4V established in phase 1a (section 4.2).

## **4.6 Phase 3a: Assessment of MMC Single Beads Evaluated Against Energy Density in Comparison to Ti6Al4V Baseline.**

### **4.6.1 Overview of The Experiment/Design**

Following the experimental methodology used in phase 1b (section 4.3), the successfully alloyed MMC feedstock was processed using the EOS M290 machine and followed the same procedure as in section 4.3, using the scan parameters from Table 16 to ensure that the material was exposed to the known energy densities. The results were compared to the phase 1b results of Ti6Al4V.

Based on the findings a selection of single beads was chosen for phase 3b.

## **4.7 Phase 3b: Hatch Spacing Evaluation of Multiple Beads.**

### **4.7.1 Overview of The Experiment/Design**

Based on the results of phase 3a, a selection of successful parameters was chosen, the bead width was used to determine the most effective hatch spacing for phase 3b. A single layer of beads was produced within a 10 mm square with fixed scan direction, layer thickness and environmental conditions.

**Table 19 Hatch Spacing Calculation Form.**

| MMC Feedstock   |                |                                                 |                                     |                                    |                               |          |          |           |           |           |     |
|-----------------|----------------|-------------------------------------------------|-------------------------------------|------------------------------------|-------------------------------|----------|----------|-----------|-----------|-----------|-----|
| Laser Power (W) | Scan Speed (v) | Target Energy Density (Ed) (J/mm <sup>3</sup> ) | Bead height (h1) from phase 3a (μm) | Bead Width (w1) from phase 3a (mm) | Hatch Spacing (h) Calculation |          |          |           |           |           |     |
|                 |                |                                                 |                                     |                                    | 40% (w1)                      | 60% (w1) | 80% (w1) | 100% (w1) | 120% (w1) | 140% (w1) |     |
| 150             | 1000           | 50                                              | 51                                  | 0.099                              | 0.040                         | 0.059    | 0.079    | 0.099     | 0.119     | 0.139     | (h) |
|                 |                |                                                 |                                     |                                    |                               |          |          |           |           |           |     |
|                 |                |                                                 |                                     |                                    |                               |          |          |           |           |           |     |

Using Table 19, each successful set of parameters from phase 3a was built with the hatch spacing intervals ranging from 40% of the measured bead width ( $w_1$ ), up to 140% as shown in the example.

Beads on or close to the build platform are characteristically wider than those higher in the build due to differences between the volume of the build platform material and the part, surface finish of the build platform where a lower roughness promotes wetting and flowability, and initial temperature of the first few layers of build. It was therefore decided to begin with a hatch spacing 40% of the  $W_1$  measurement (Figure 8 Dimensioned cross sectioned 316L stainless steel single beads (Yadroitsev, et al., 2012) (Yadroitsev, et al., 2012), with the proceeding bead increasing in 20% increments up to 140% of the  $w_1$  measurement. A value of 100% giving a hatch spacing equal to that of the bead ( $w_1$ ).

#### 4.7.2 Phase 3b Variables

Multiple beads were exposed for a single layer using the two-rail method of build plate to establish a 45 μm to 50 μm layer thickness.

Variables consisted of laser power and scan speeds as calculated in Table 16, to achieve the same range of energy densities but to also evaluate the effect of hatch distance. It is at this point that the energy density equation used for calculations for single beads (Equation 5) can revert to the use of the hatch spacing term ( $h$ ) instead of spot size ( $s$ ) as in equation 1.

Based on the findings from phase 3a (single beads) only beads of a height less than 60 μm were taken forward to phase 3b, in order to maintain contact free recoating.

As an initial starting point, rather than selecting a fixed hatch distance a range of distances were used based on the measured bead widths from phase 3a as shown in Table 19.

#### 4.7.2 Phase 3b Attributes

For the software (EOSPrint 1.5) to produce multiple beads in the same direction, the following parameters were set for the build process (Table 20).

**Table 20 Build Attributes for Hatch Spacing Experiment**

| Parameter Setting | Value                          |
|-------------------|--------------------------------|
| Step over         | See Table 19                   |
| Stripe width      | 40 mm                          |
| Pre-Contours      | Off                            |
| Post-Contours     | Off                            |
| Rotation          | Off                            |
| X, Y              | X Only (Recoat along the bead) |
| Alternating       | Off                            |
| DMLS              | Off                            |
| Pre-Exposure      | Off                            |
| Up skin           | Off (Thickness = 0)            |
| Down skin         | Off (Thickness = 0)            |
| Beam expander     | Automatic                      |
| Platform heating  | 40°C                           |

## **4.8 Phase 3c: Multiple-Layer Evaluation of Density and Homogeneity of Reinforcement.**

### **4.8.1 Overview of the Experiment/Design**

Based on the results of phase 3b, successful hatch spacing's were processed to determine the effect of building multiple layers. Multiple layers were produced within a 10 mm by 10 mm cube with scan direction, layer thickness and rotation as for normal scan parameters used with Ti6Al4V on an EOS M290 machine. To alleviate the effect of the build platform, parts were built to a height of 4.0 mm before terminating the process. Parameters for contouring, UpSkin and DownSkin were not activated to ensure that the cubes produced would only contain beads scanned with the developed parameters, other features would be optimised through further research.

### **4.8.2 Phase 3c Variables**

Multiple layers were exposed using laser power, scan speed and hatch distances successful from phase 3b.

### **4.8.3 Phase 3c Attributes (Multiple Layer Evaluation of Density and Homogeneity of Reinforcement)**

For phase 3c the software (EOSPrint 1.5) was returned to standard parameters for exposing parts, the following parameters were set for the build process (Table 21) except for UpSkin and DownSkin that remained off, as in previous experiments. Laser power, scan speed and hatch spacing were those chosen from the results of phase 3b.

**Table 21 Build Attributes for Multiple Layer Experiment**

| Parameter Setting | Value                                           |
|-------------------|-------------------------------------------------|
| Step over         | See Table 17 (Successful results from phase 3b) |
| Stripe width      | 100 mm                                          |
| Pre-Contours      | Off                                             |
| Post-Contours     | Off                                             |
| Rotation          | On                                              |
| X, Y              | On                                              |
| Alternating       | On                                              |
| DMLS              | On                                              |
| Pre-Exposure      | On                                              |
| Up skin           | Off (Thickness = 0)                             |
| Down skin         | Off (Thickness = 0)                             |
| Beam expander     | Automatic                                       |
| Platform heating  | 35°C                                            |

#### **4.8.4 Phase 3c Statistical Treatment**

Due to the limitations on feedstock the builds were exposed once only however the analysis was conducted at multiple points to establish a statistical range where possible.

### **4.9 Phase 3d: Crystallographic and Chemical Analysis of MMC Material.**

#### **4.9.1 Overview of The Experiment / Design**

Cross sections of single bead samples produced from the MMC feedstock were chemically etched using Kroll's reagent (187), a 2:1 HF/Nitric acid mixture in an aqueous solution. The solution was prepared in order to make the microstructure more visible during optical microscopy.

Analysis of chemical composition was conducted using Energy Dispersive X-Ray Spectroscopy (EDS) for the detection of individual elements and X-Ray diffraction (XRD) for the detection of crystallography and chemical compounds.

#### **4.9.2 Phase 3d Variables**

##### **4.9.2.1 Chemical etching Variables**

Specimens were immersed for 15s and 20s then washing with distilled water for several minutes to ensure the removal of all chemicals. Ethanol was finally used to ensure specimens were clean and dry.



#### 4.9.2.2 X-Ray Spectroscopy (EDS) Variables

EDS was carried out using an Oxford instruments X-Max EDS system. Regions of interest were analysed using spot and area analysis, to obtain a fair result from various places across the samples. The EDS system was calibrated before use using cobalt (Figure 35).

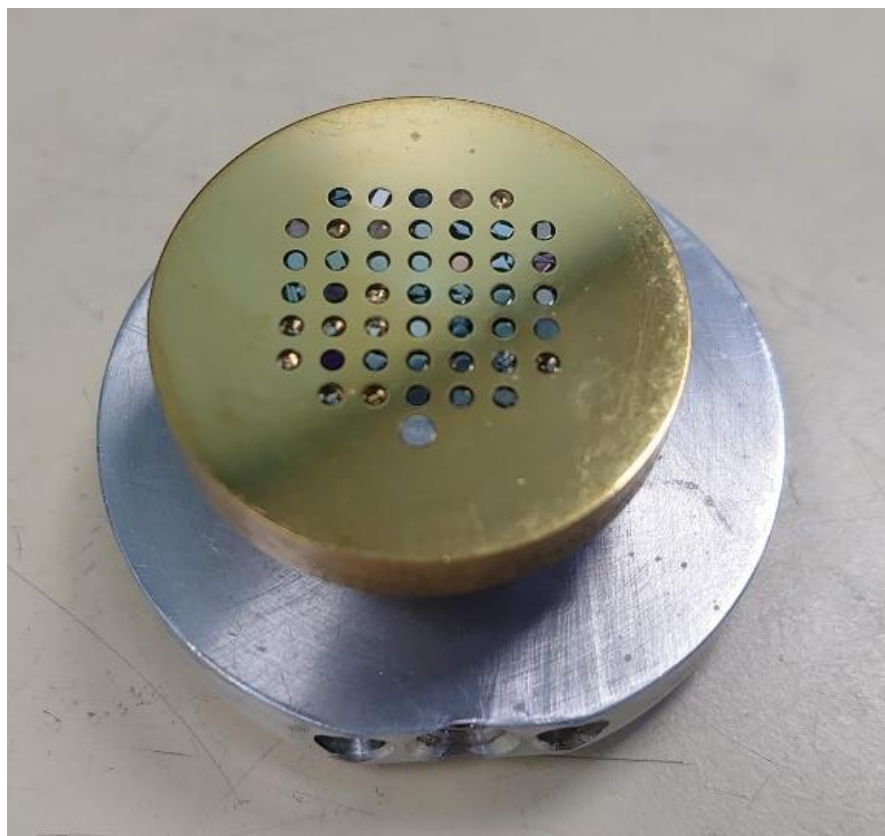


Figure 35 EDS Cobalt Calibration Sample

#### 4.9.2.3 X-Ray Diffraction (EDX) Variables

EDX was carried out using Panalytical Empyrean EDX apparatus (Figure 36), using the following variables:

- Anode material Copper,
- Step size 0.013 ( $^{\circ}$ 2Th.),
- Step time 8.670 (s)
- Generator settings 40 mA, 40 KV.

The sample was set to spin.



Figure 36 Panalytical Empyrean EDX apparatus

### 4.9.3 Phase 3d Attributes

#### 4.9.3.1 Chemical etching Attributes

For metallographic analysis Kroll's reagent was used, consisting of:

- 5 ml of  $\text{HNO}_3$
- 10 ml of HF (48% concentration)
- 85 ml  $\text{H}_2\text{O}$

# Chapter Five

## 5.0 Results and Discussion.

### 5.1 Introduction

Based on the structure of the research methodology (section 4.0), results and detailed analysis are presented and discussed within this section.

### 5.2 Phase 1a: Baseline Assessment of Raw Materials.

Within the research experimental results were compared to the standard characteristics of feedstock powders used within the industry. Analysis was conducted on the raw materials to establish a baseline for the following characteristics:

- Moisture content,
- Particle size and size distribution,
- Particle morphology,
- Rheological characteristics.

#### 5.2.1 Phase 1a Baseline Assessment of Moisture Content.

The moisture content of Ti6Al4V and SiC were measured using the loss of mass method (Cordova, Campos, Tinga, 2017). Three separate samples were analysed from different areas of the batch of material to establish an arithmetic mean. The results are shown in Table 22.

**Table 22** Moisture Content Results (Initial Analysis)

|                    | Moisture Content (%) |      |
|--------------------|----------------------|------|
|                    | Ti6Al4V              | SiC  |
| Test 1             | 0.59                 | 1.88 |
| Test 2             | 0.50                 | 1.55 |
| Test 3             | 0.67                 | 1.92 |
|                    |                      |      |
| Mean ( $\bar{x}$ ) | 0.59                 | 1.78 |

For Ti6Al4V the moisture levels were below the 1.0% maximum limit (section 4.2.4.1) and were therefore considered acceptable. For the samples of SiC, higher than expected levels of moisture were detected, this was most likely from either the storage or handling of the powder and it was suspected that this would be attributed to surface moisture as SiC does not readily react to moisture due to its chemical inertness. Due to the particulate's submicron size and therefore increased surface area, there becomes a higher probability of surface moisture being

introduced into the powder. The powder was spread on to a metal tray and heated in an oven at 150°C for twenty minutes then allowed to cool within the same environment. Once the powder was again at room temperature it was retested with the following results (Table 23).

**Table 23 Moisture Content Results After Moisture Removal Process**

|                    | Moisture Content (%)      |                             |
|--------------------|---------------------------|-----------------------------|
|                    | SiC<br>(initial analysis) | SiC<br>(secondary analysis) |
| Test 1             | 1.88                      | 0.79                        |
| Test 2             | 1.55                      | 0.97                        |
| Test 3             | 1.92                      | 1.13                        |
| Mean ( $\bar{x}$ ) | 1.78                      | 0.96                        |

It was evident from the results in Table 23 that the moisture could be driven off using a heating process but also that over a short space of time, the SiC powder would rapidly pick up moisture again. The duration of each moisture test was 20 minutes; therefore, the powder had been away from the oven for approximately 60 minutes and the moisture levels were returning to previous levels. It was concluded therefore that the SiC powder and subsequent alloyed feedstock should be stored in a dry environment at a temperature of around 80°C prior to use and furthermore, to eliminate the risk of moisture being introduced into the powder should be processed within 60 minutes.

### 5.2.2 Phase 1a Baseline Assessment of Rheological Characteristics.

Rheological analysis was conducted on the Ti6Al4V and SiC powders prior to MA to determine baseline values for apparent density and angle of repose. The results are shown in Table 24.

**Table 24 Rheological Characteristics for Ti6Al4V And Sic Powders Prior To MA**

| Rheological measurement        | Ti6Al4V                | SiC                    |
|--------------------------------|------------------------|------------------------|
| Material density               | 4.43 g/cm <sup>3</sup> | 3.21 g/cm <sup>3</sup> |
| Apparent density               | 2.24 g/cm <sup>3</sup> | 0.41 g/cm <sup>3</sup> |
| Percentage of physical density | 50.6%                  | 12.8%                  |
| Angle of repose                | 33°                    | 48°                    |

With regard to packing density, it could be seen that the apparent density of the Ti6Al4V powder was 50.6% in comparison to its material density, for the SiC powder this was 12.8% demonstrating a poor packing density in comparison to Ti6Al4V. Results for the angle of repose established a baseline for Ti6Al4V of 33 degrees, for SiC this increased to 48 degrees, this was expected due to the powders angularity and lack of roundness, hence the powders ability to lock together in formation rather than freely role. Due to the Ti6Al4V powder maintained a mean angle of 33 degrees, this was taken as the baseline value to benchmark against for the

mechanical alloying experiments in phase 2. In combination with the SiC powder, the angle of repose was expected to increase due to an expected increase in surface roughness.

### 5.2.3 Phase 1a Baseline Assessment of Particle Size, Size Distribution.

Using a Retsch Camsizer X2 particle size analyser a representative sample of Ti6Al4V and SiC powders were analysed to establish a baseline assessment with respect to the following characteristics:

$X_{c \min}$  Measures the shortest width ( $\mu\text{m}$ ) across a particles image and is taken as being representative of particle size and used as a direct correlation to sieving sizes.

$X_{\text{area}}$  Measures the width ( $\mu\text{m}$ ) of a circumferential boundary around a particle to include any irregularities such as satellites or agglomerations, for a round particle this would be equal to  $X_{c \min}$ .

b/l Measures the aspect ratio ( $\mathcal{R}$ ) between the shortest distance on the particle ( $X_{c \min}$ ) and the longest ( $X_{fe \max}$ ) and is a good indication of elongated particle.

#### 5.2.3.1 Ti6Al4V Particle Size and Size Distribution Baseline Assessment.

Table 25 shows results for  $X_{c \min}$  (particle size) frequency distribution curve for Ti6Al4V powder. The analysis showed a multi-modal size distribution from 0  $\mu\text{m}$  to 75  $\mu\text{m}$  with peaks at 3.5  $\mu\text{m}$ , 37  $\mu\text{m}$  and 44  $\mu\text{m}$ .

Table 25 Statistical Results for Ti6Al4V Particle Size and Distribution ( $X_{c \min}$ ) Baseline Results

| Statistical measurement | Baseline result ( $X_{c \min}$ ) |
|-------------------------|----------------------------------|
|                         |                                  |
| Q3 10%                  | 28.8 $\mu\text{m}$               |
| Q3 50%                  | 39.9 $\mu\text{m}$               |
| Q3 90%                  | 49.9 $\mu\text{m}$               |
| Mv3( $\bar{x}$ )        | 39.7 $\mu\text{m}$               |
| Mean b/l3               | 0.851                            |
| 1-Q3 (b/l = 0.850)      | 65%                              |

Table 25 shows the salient characteristics of the particle size analysis. It can be seen from the data that the predicted average particle size (Q3 50%) is 39.9  $\mu\text{m}$  and the mean particle size of the sample (Mv3( $\bar{x}$ )) is 39.7  $\mu\text{m}$ . the closeness of these two values, (within 0.2  $\mu\text{m}$ ), suggests a high degree of confidence in the results. The mean aspect ratio result (Mean b/l3) indicates that not all particles are spherical. Looking at the inverse statistical volume for the sample (1-Q3 (b/l = 0.850)) it can be seen that 65% of the sample would be classed as rounded, this was further evaluated using particle image analysis.

Further analysis was conducted with the same sample, evaluating the width ( $\mu\text{m}$ ) of the particles bounding circumference, ( $x_{\text{area}}$ ) (Figure 38). Where particles have a good aspect ratio fewer satellites and agglomerations are indicated and the statistical analysis would be comparable to the values for particle size  $X_{c \text{ min}}$ .

Analysis showed a multi-modal distribution with a range between 1  $\mu\text{m}$  to 85  $\mu\text{m}$  with peaks at 3.5  $\mu\text{m}$ , 37  $\mu\text{m}$  and 47  $\mu\text{m}$ .

**Table 26 Statistical Results for Ti6Al4V Particle Size and Distribution,  $X_{c \text{ min}}$  Versus  $X_{\text{area}}$  Baseline Results**

| Statistical measurement | Baseline result ( $X_{c \text{ min}}$ ) | Baseline result ( $x_{\text{area}}$ ) |
|-------------------------|-----------------------------------------|---------------------------------------|
| Q3 10%                  | 28.8 $\mu\text{m}$                      | 30.2 $\mu\text{m}$                    |
| Q3 50%                  | 39.9 $\mu\text{m}$                      | 43.1 $\mu\text{m}$                    |
| Q3 90%                  | 49.9 $\mu\text{m}$                      | 55.8 $\mu\text{m}$                    |
| Mv3( $\bar{x}$ )        | 39.7 $\mu\text{m}$                      | 42.7 $\mu\text{m}$                    |
| Mean b/l3               | 0.851                                   | 0.839                                 |
| 1-Q3 (b/l = 0.850)      | 65.0%                                   | 61.5%                                 |

Comparison of results from  $X_{c \text{ min}}$  and  $X_{\text{area}}$  suggests that the particles measured by area are marginally larger than those measured by size, (Table 26).  $X_{\text{area}}$  evaluates the distance across a circumferential boundary around the particles image, this boundary also includes aspects of the image that are not of the particle thus the value calculated is larger than  $X_{c \text{ min}}$ . Particles with more surface imperfections such as satellites and powder agglomerations exhibit a greater difference between the values of  $X_{c \text{ min}}$  and  $X_{\text{area}}$ . It is also possible for the cameras to capture images where two or more particles coexist, forming an elongated particle, these can be assessed using the image database.

Figure 39 and Figure 40 show volume-based distribution curves for Ti6Al4V baseline assessments. Volume based distribution makes it easier to compare results specific to gains or losses of a specific characteristic, in the case of  $X_{c \text{ min}}$ , the minimum distance across a particles image and for  $X_{\text{area}}$ , the area of a particle within a circumferential boundary.

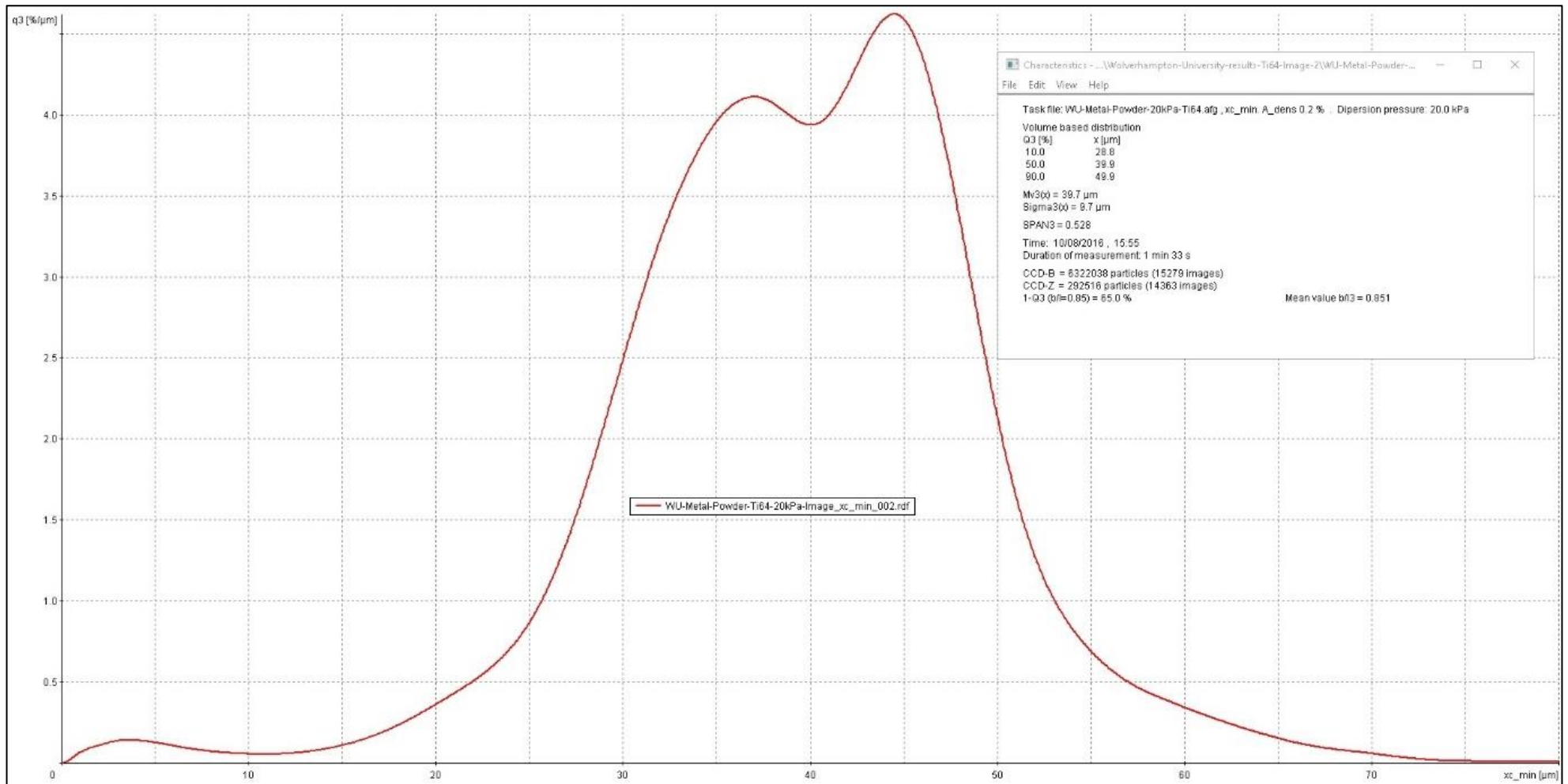


Figure 37 Ti6Al4V Size Distribution Baseline X<sub>c Min</sub>

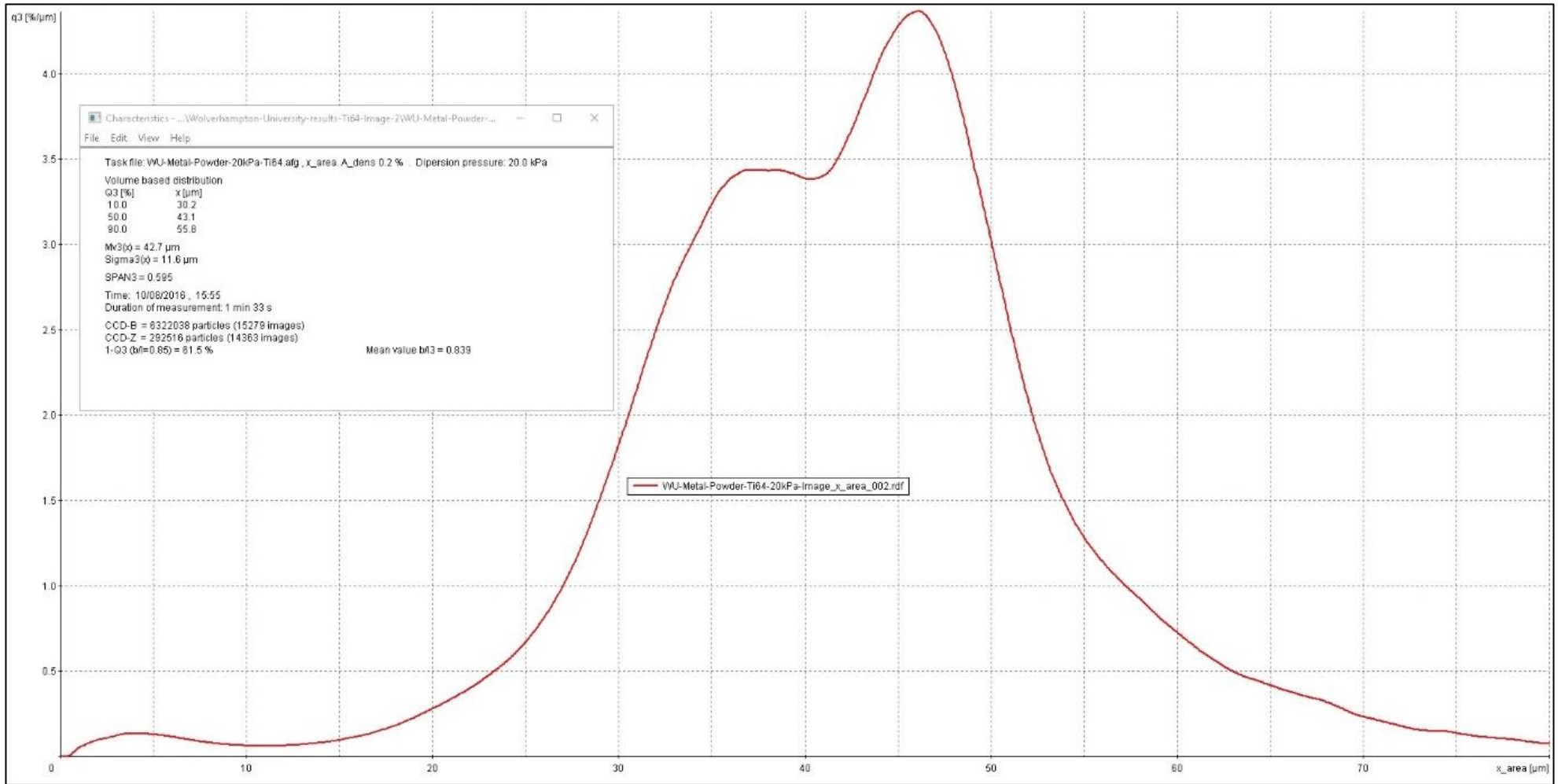


Figure 38 Ti6Al4V Size Distribution Baseline  $X_{area}$



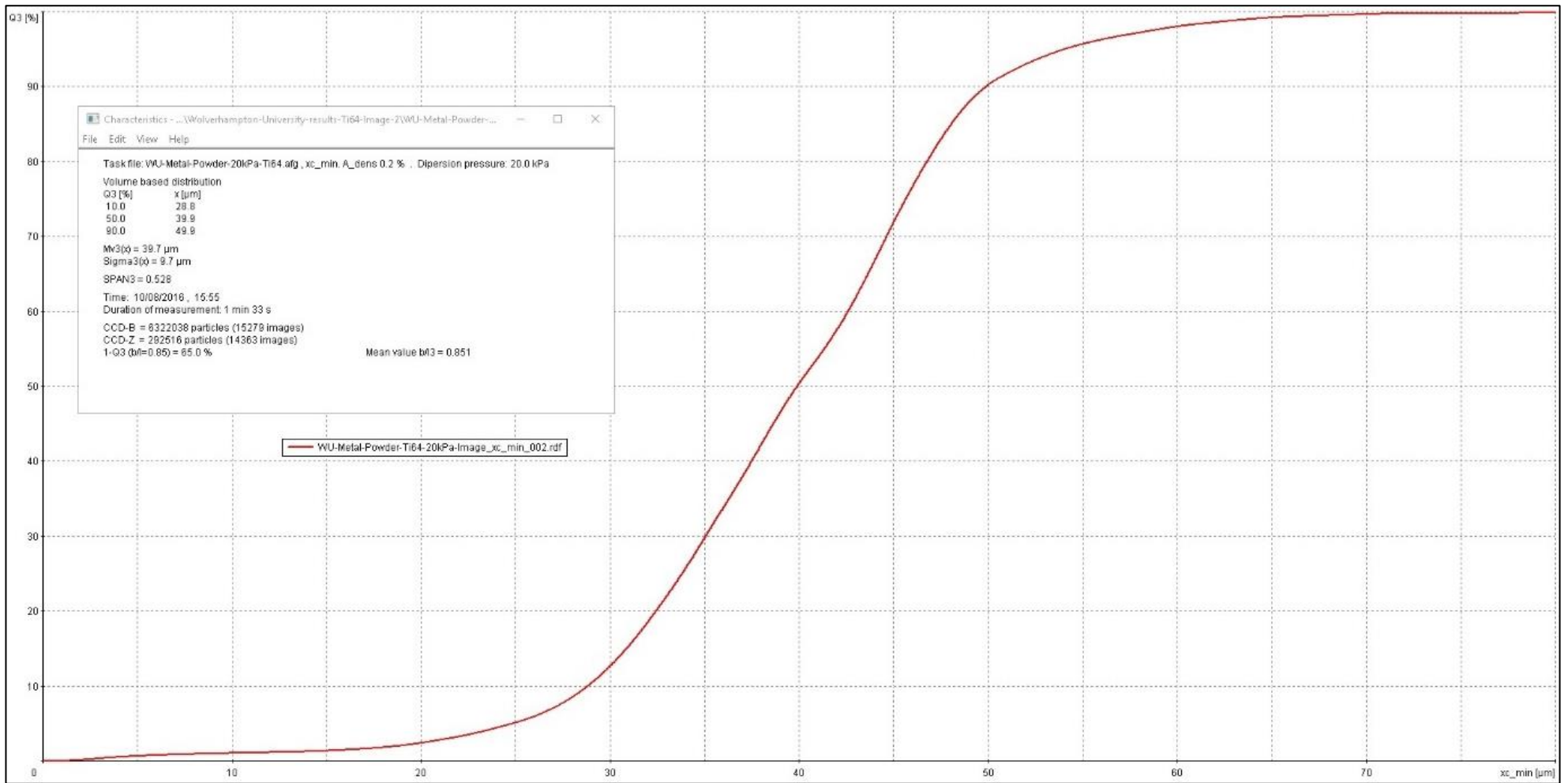


Figure 39 Volume Based Distribution Curve Results for Ti6Al4V Baseline X<sub>c</sub> Min

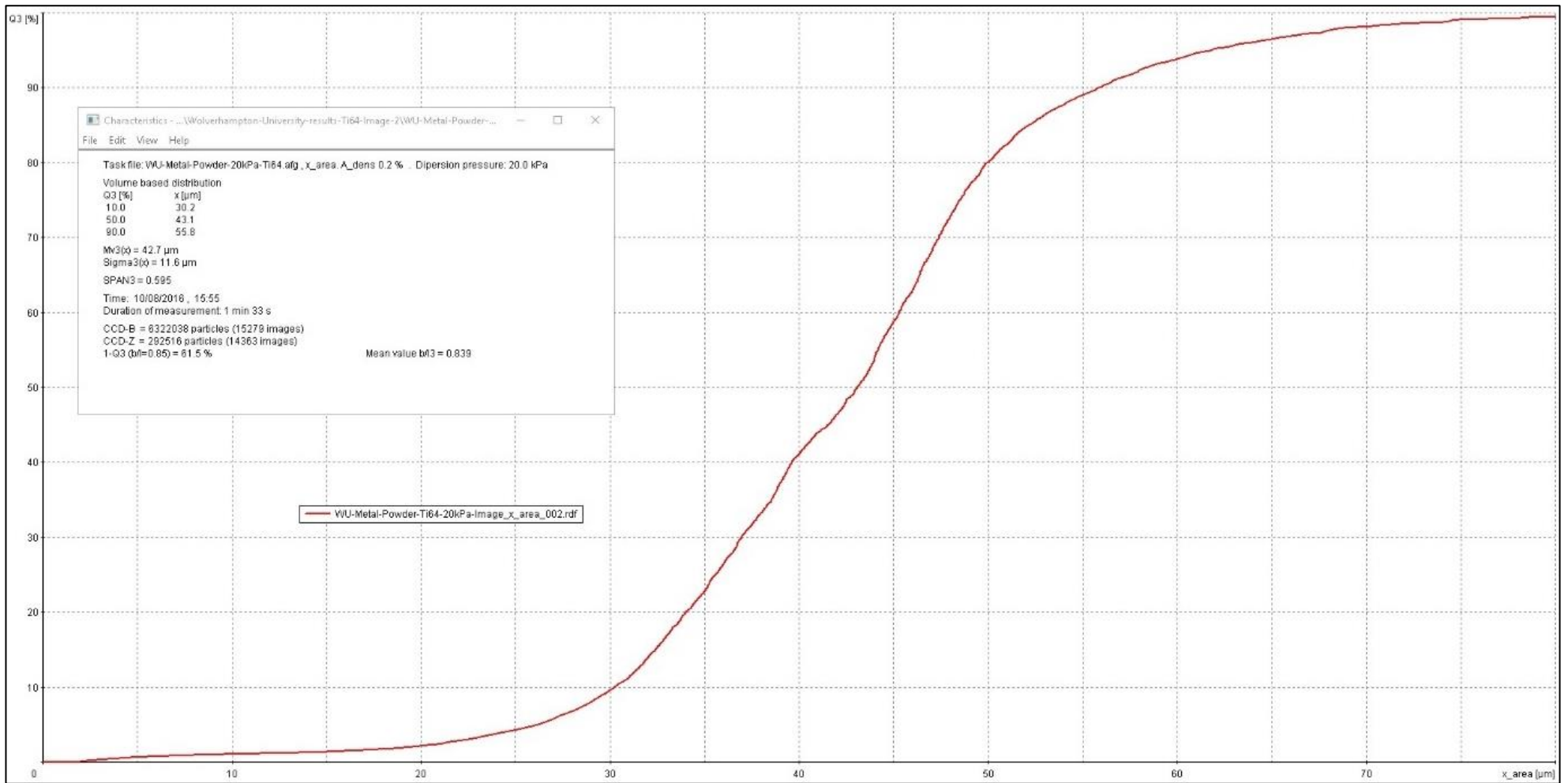


Figure 40 Volume Based Distribution Curve for Ti6Al4V Baseline X<sub>area</sub>

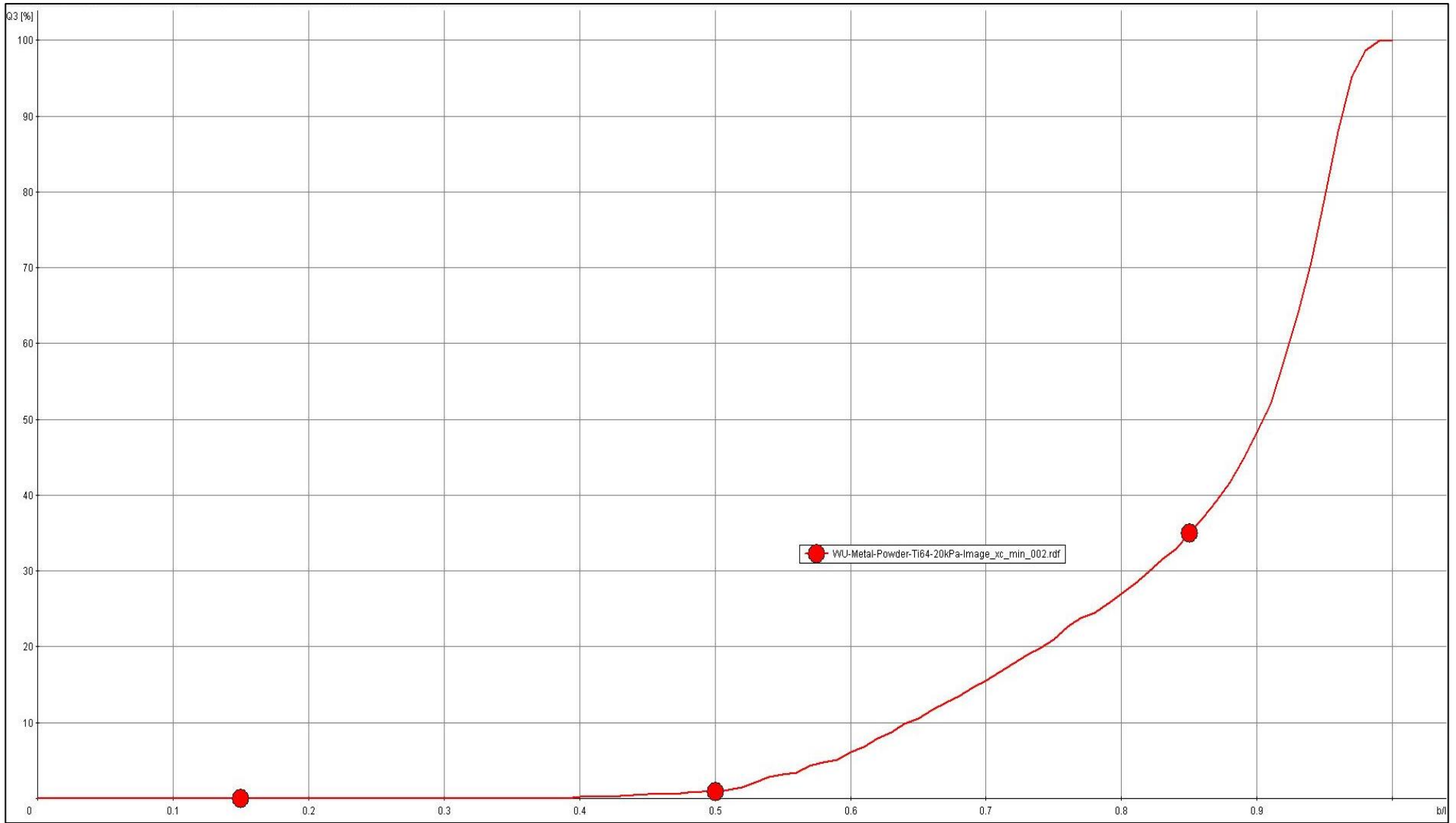


Figure 41 Volume Based Distribution Curve for Ti6Al4V Baseline b/I

### 5.2.3.2 SiC Particle Size and Size Distribution Baseline Assessment.

Figure 42 shows results for  $X_{c \text{ min}}$  (particle size) distribution curve for SiC powder.

**Table 27 Statistical Results for SiC Particle Size and Distribution ( $X_{c \text{ Min}}$ ) Baseline Results**

| Statistical measurement | Baseline result ( $X_{c \text{ min}}$ ) |
|-------------------------|-----------------------------------------|
|                         |                                         |
| Q3 10%                  | 7.6 $\mu\text{m}$                       |
| Q3 50%                  | 70.2 $\mu\text{m}$                      |
| Q3 90%                  | 49.9 $\mu\text{m}$                      |
| Mv3( $\bar{x}$ )        | 491.9 $\mu\text{m}$                     |
| Mean b/l3               | 0.762                                   |
| 1-Q3 (b/l = 0.850)      | 27%                                     |

Table 27 shows the salient characteristics of the particle size analysis. It can be seen from the data that the predicted average particle size (Q3 50%) is 70.2  $\mu\text{m}$  and the mean particle size of the sample (Mv3( $\bar{x}$ )) is 491.9  $\mu\text{m}$ . As these two values are at extremes, it suggests a low degree of confidence in the results. The mean aspect ratio (Mean b/l3) result indicates that very few particles are spherical. Looking at the inverse statistical volume for the sample (1-Q3 (b/l = 0.850)) it can be seen that 27% of the sample would be classed as rounded, this was further evaluated using the particle images.

Further analysis was conducted with the same sample, evaluating the width ( $\mu\text{m}$ ) of the particles bounding circumference, ( $X_{\text{area}}$ ). Where particles have a close aspect ratio indicating fewer satellites and agglomerations, the statistical analysis would be comparable to the values for particle size  $X_{c \text{ min}}$ .

Figure 43 shows results for  $X_{\text{area}}$  distribution curve for SiC powder.

**Table 28 Statistical Results for SiC Particle Size and Distribution,  $X_{c \text{ Min}}$  Versus  $X_{c \text{ Area}}$  Baseline Results.**

| Statistical measurement | Baseline result ( $X_{c \text{ min}}$ ) | Baseline result ( $X_{\text{area}}$ ) |
|-------------------------|-----------------------------------------|---------------------------------------|
|                         |                                         |                                       |
| Q3 10%                  | 7.6 $\mu\text{m}$                       | 8.4 $\mu\text{m}$                     |
| Q3 50%                  | 70.2 $\mu\text{m}$                      | 73.0 $\mu\text{m}$                    |
| Q3 90%                  | 49.9 $\mu\text{m}$                      | 559.7 $\mu\text{m}$                   |
| Mv3( $\bar{x}$ )        | 491.9 $\mu\text{m}$                     | 198.4 $\mu\text{m}$                   |
| Mean b/l3               | 0.762                                   | 0.753                                 |
| 1-Q3 (b/l = 0.850)      | 27%                                     | 25.1%                                 |

Comparison of results between  $X_{c \text{ min}}$  and  $X_{\text{area}}$  (Table 28) suggests that the particles measured by area are once again larger than those measured by size. It has been established from the

baseline assessment of the Ti6Al4V powder (4.2.5) that it is possible for the cameras to capture images where two or more particles coexist; this however would not cause such a large spread of results between the D10 and D90 values. It was also established that multiple particles within an image cap present as an elongated particle, once again this would not cause such a large spread of results. It was therefore, concluded that the values returned by the equipment did not relate to individual particles, but to agglomerations of the powder. Due to the large surface area and increased surface energy of the particles, the likelihood of agglomeration is significantly increased, the Camsizer X2's particle dispersion system is designed to aid separation of particles during analysis however it is evident that this was not possible for particles of this size.

The results were further confirmed using volume-based distribution Figure 44 and Figure 45.

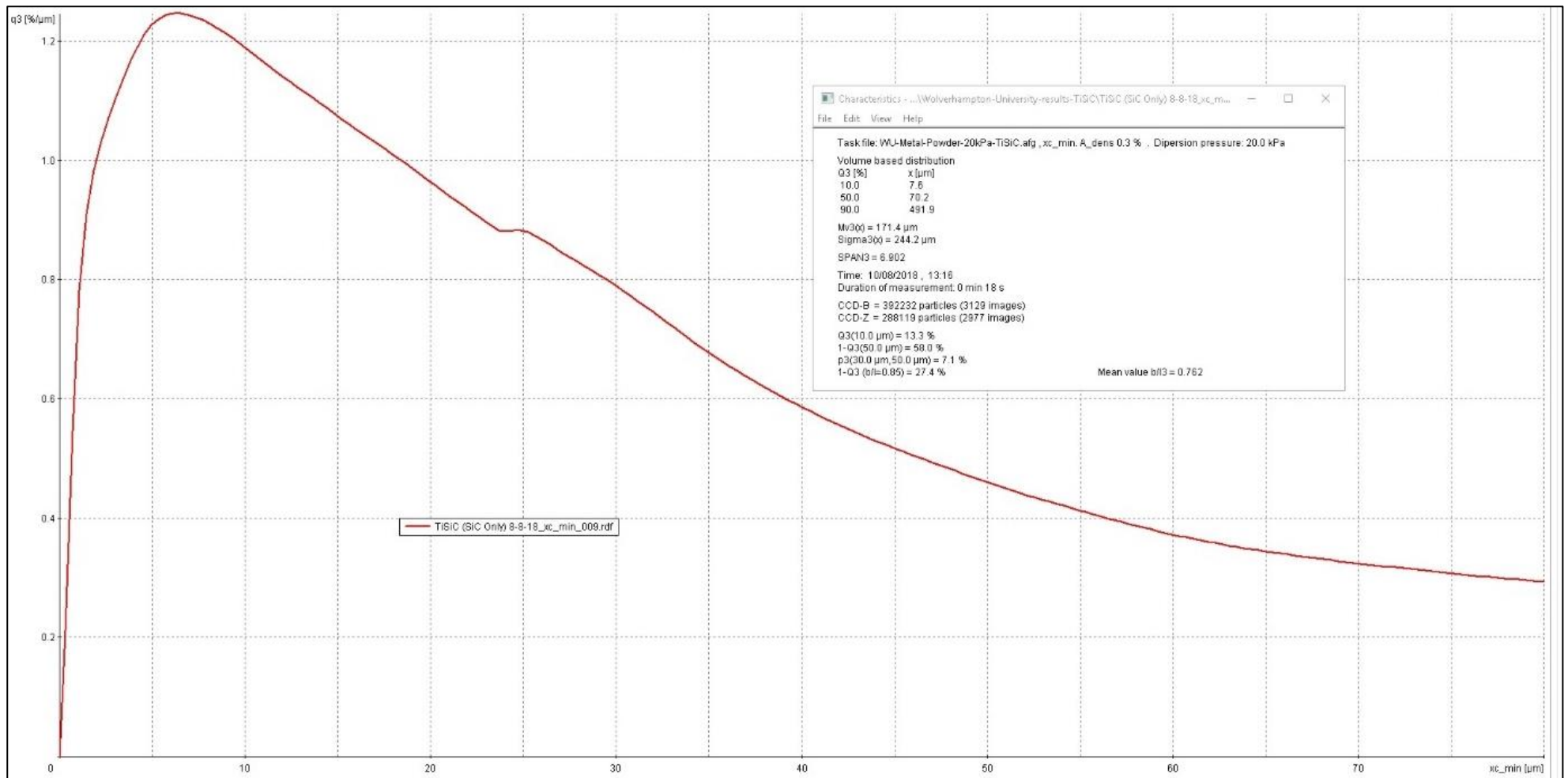


Figure 42 SiC Size Distribution baseline  $x_{c\text{min}}$

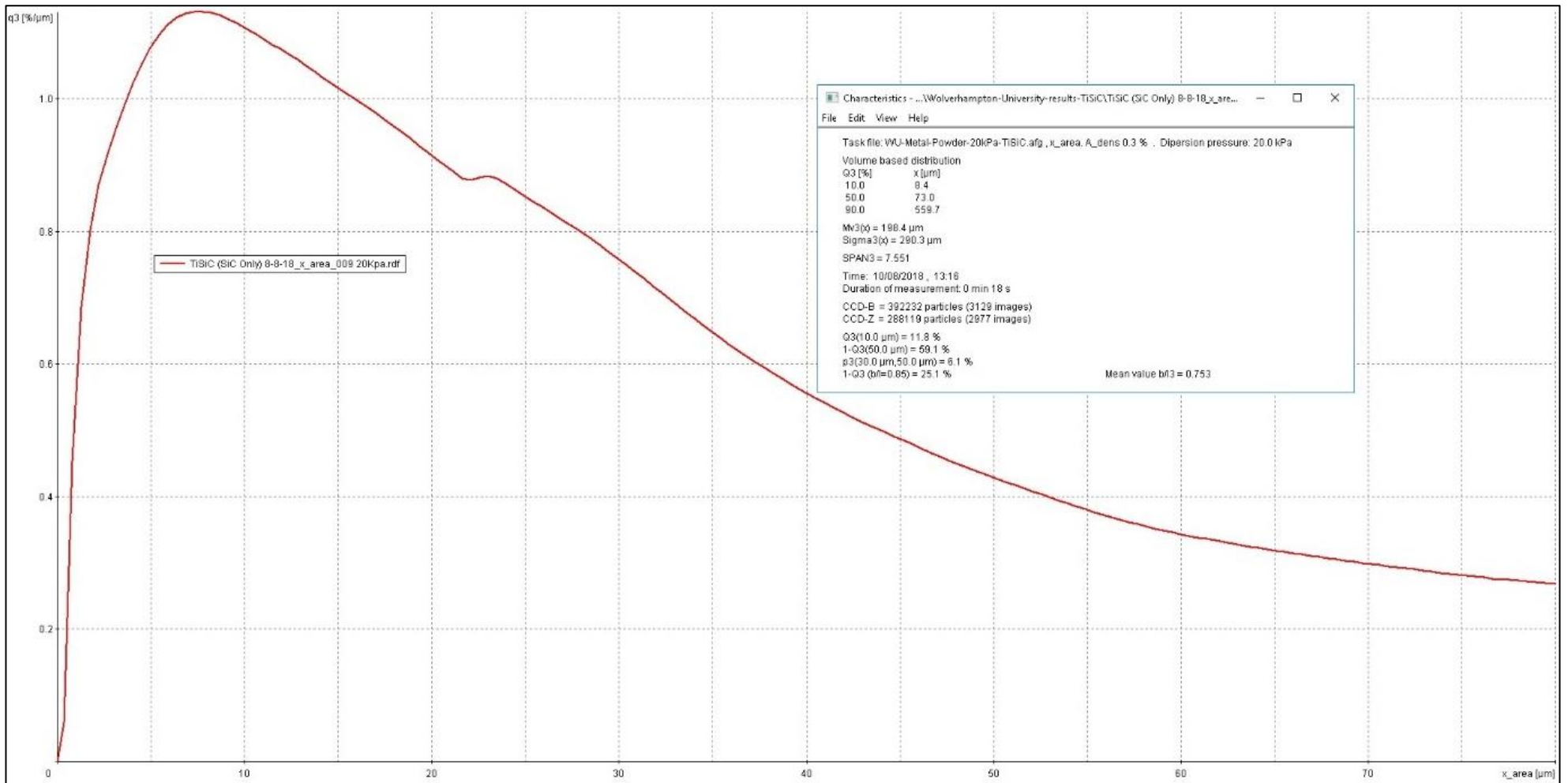


Figure 43 SiC Size Distribution Baseline Xarea

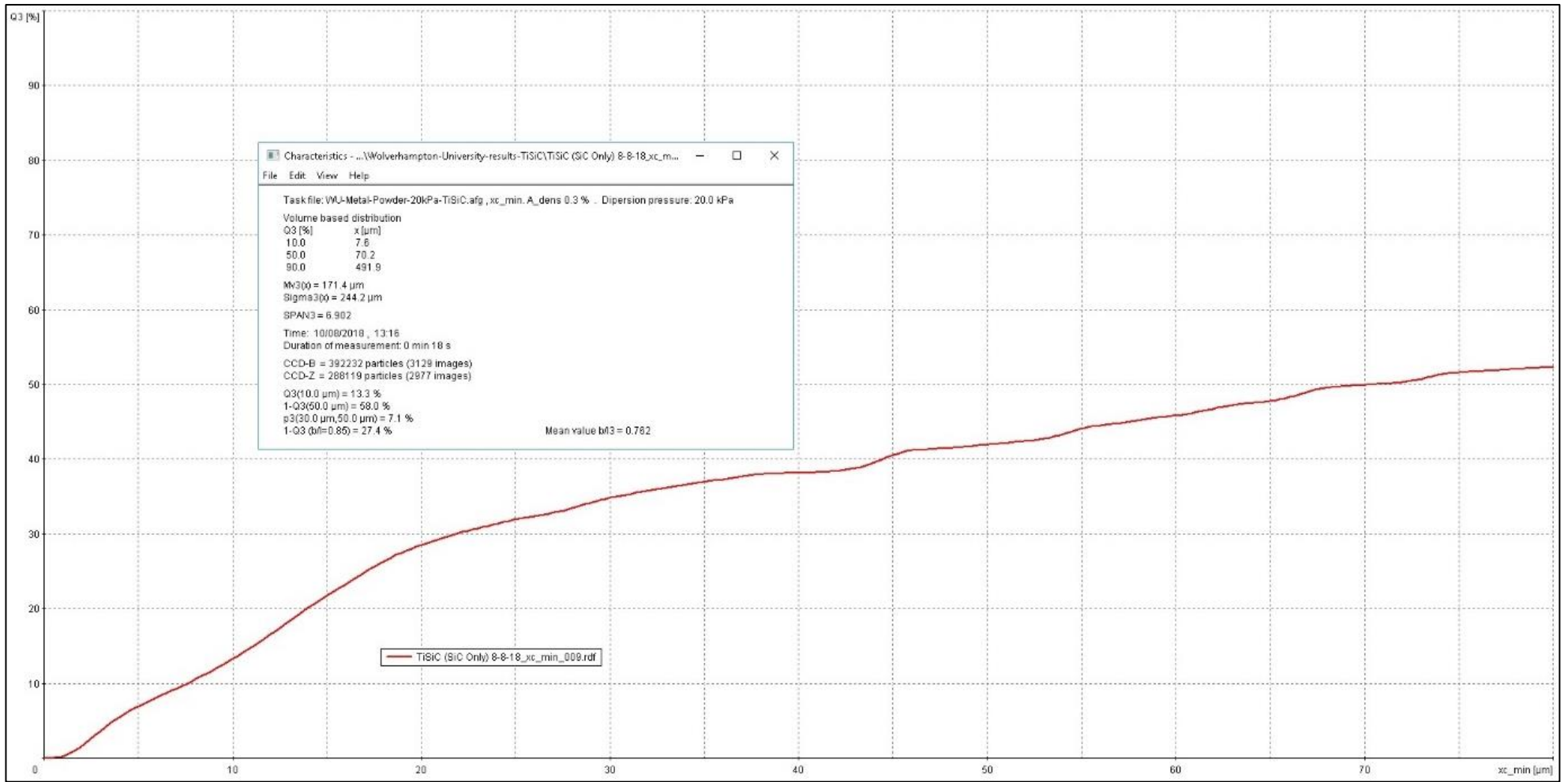


Figure 44 Volume Based Distribution Curve for SiC Baseline X<sub>c</sub> Min



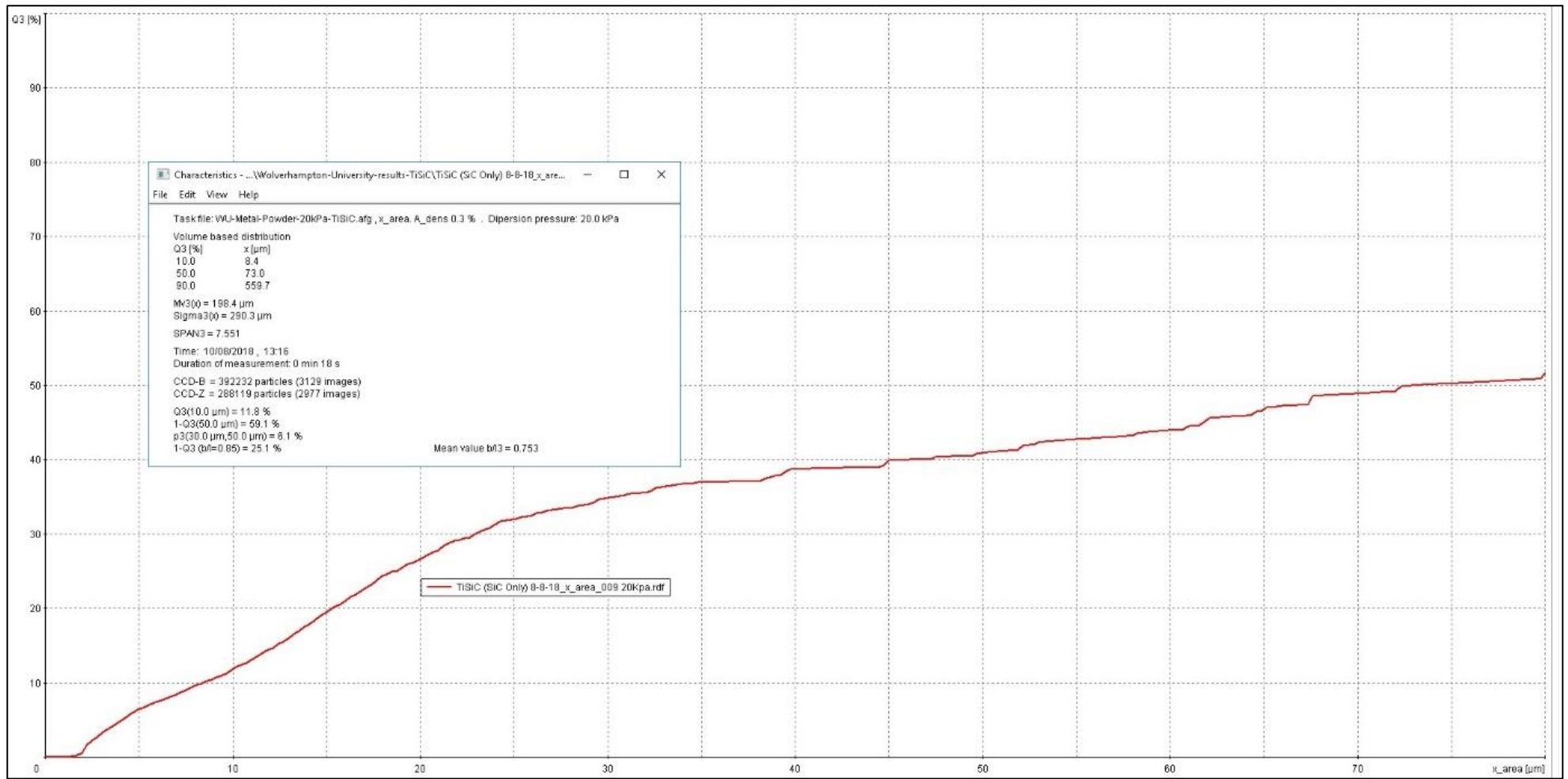


Figure 45 Volume Based Distribution Curve for SiC Baseline  $X_{area}$

## 5.2.4 Phase 1a Baseline Assessment of Ti6Al4V Particle Morphology.

Further analysis of the Ti6Al4V baseline assessment results using the Camsizer X2 was carried out using the image database. Using filters to locate specific criteria such as size and aspect ratio, it could be observed that the Camsizer software had difficulty recognising some particles.

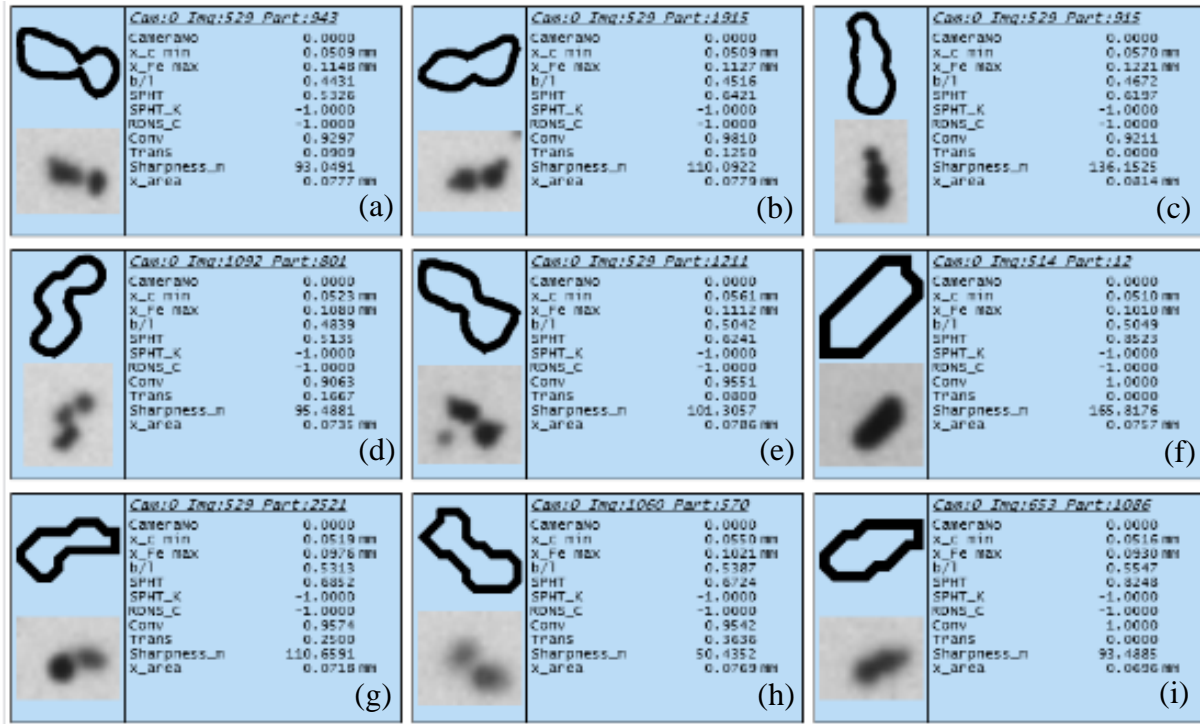


Figure 46 Retsch Camsizer X2 Database Images of Nonrounded Ti6Al4V Particles ( $B/L \leq 0.850$ )

Figure 46 shows a selection of images and software measurements using the Retsch Camsizer X2 database software. Elongated particles were isolated using the database filters,  $X_{c \min} \geq 0.010$  mm to filter out small fines and  $b/l \leq 0.850$   $\mathcal{R}$  to capture nonrounded particles. It was evident from the images that in some cases, the software failed to distinguish between individual particles in the images. In image (a) showed two disconnected particles, one that appeared to be rounded and one that was elongated. This was also the case with image (b), two particles appeared to be present in the image but were separated, both particles also appeared to have satellites. Image (c) presented what appeared to be three particles joined together, as the focus of the three particles appeared to be the same it was concluded that this was a complete particle. For image (d) it was concluded that this was three or more particles in the same image that were not joined. Images (e) presented similarities with (b) and whilst the camera image captured a third particle the software image has discounted this. Images (f) and (i) showed particles with clearly nonrounded forms whilst the camera image (g) showed two particles with varying focus of multiple particles, this indicated that the two particles were not in the same location in terms of distance from the cameras focal point. Image (h) two particles with poor focus, separated but possibly rounded. It was therefore deemed important to visually check the images to ensure the software had not falsely represented the particles data. Using the filters above, 285 out of 726 images were found that met the conditions, 39.3% nonrounded.

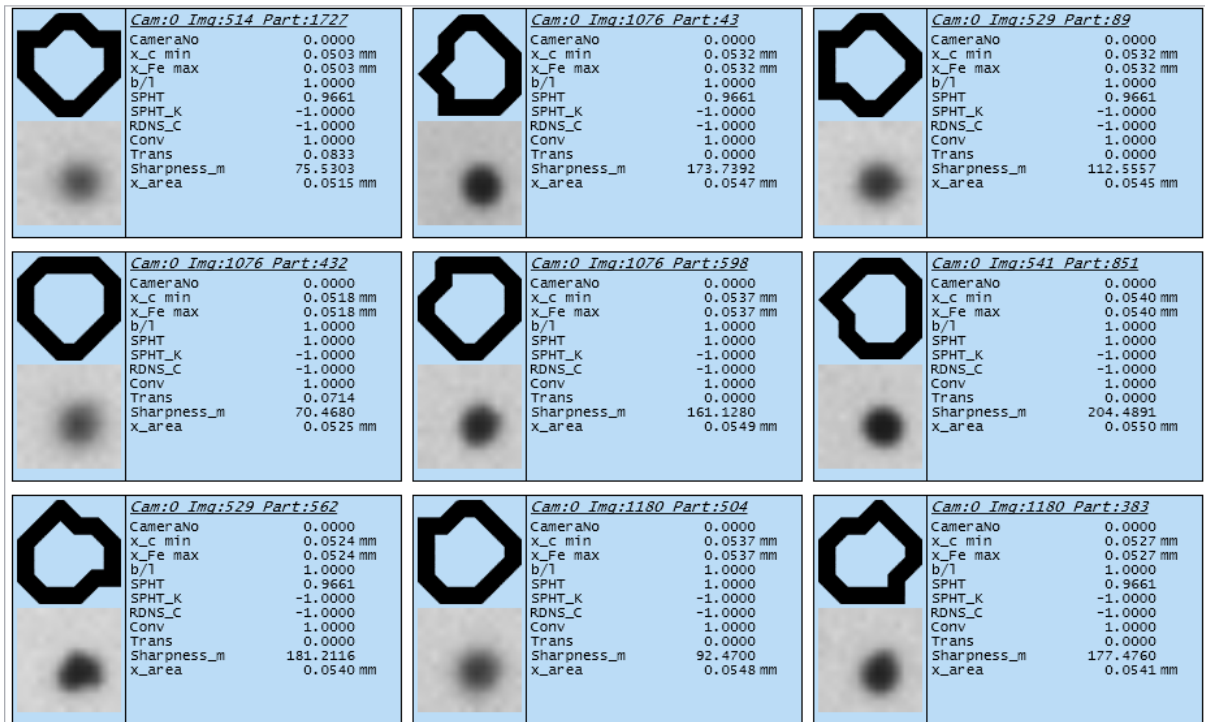
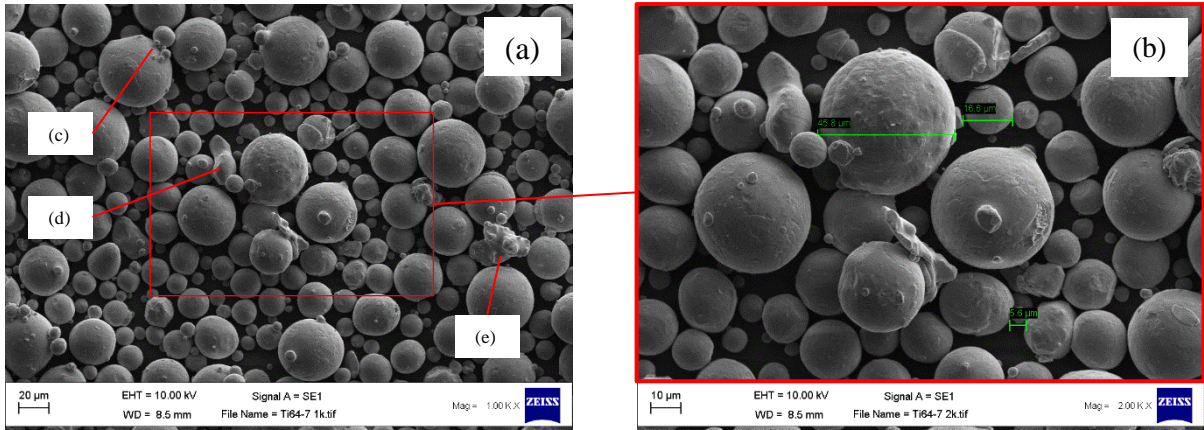


Figure 47 Retsch Camsizer X2 Database Images of Rounded Ti6Al4V Particles ( $B/L \geq 0.850$ )

Figure 47 shows a selection of images and software measurements showing nonrounded particles using the database filters,  $X_{c \min} \geq 0.010$  mm to filter out small fines and  $b/l \leq 0.850$   $\mathcal{R}$  to capture rounded particles. It was evident from the images that recognised rounded particles satisfactorily. Using the filters above, 424 out of 726 images were found that met the conditions, 58.4% rounded.

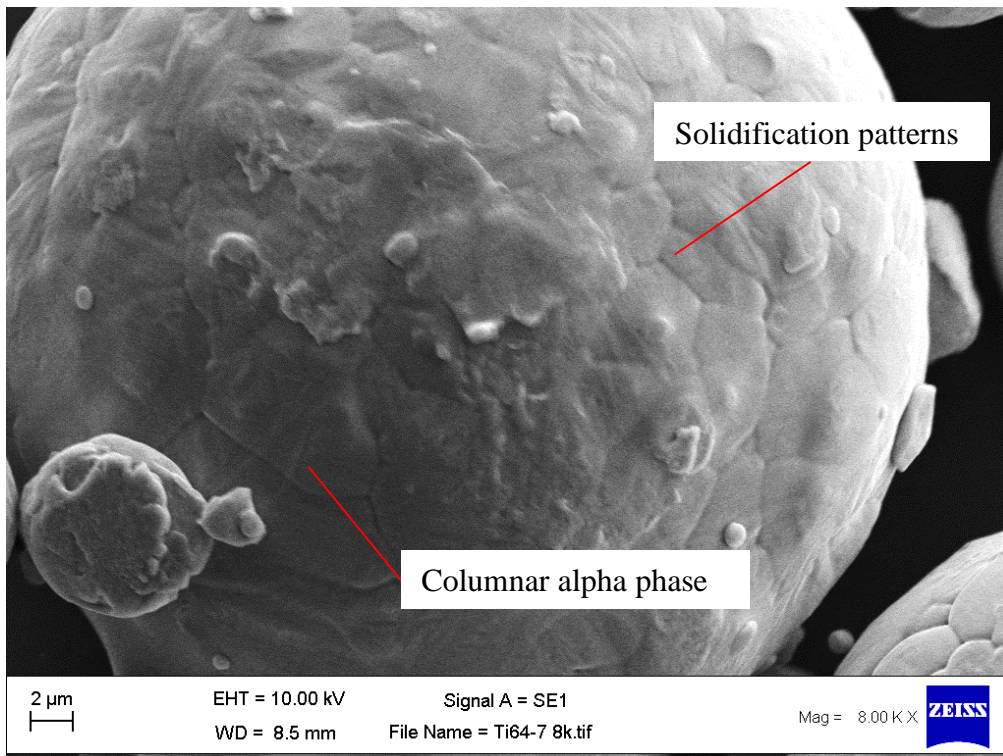
#### 5.2.4.1 Scanning Electron Microscopy of Ti6Al4V Powder.

Following on from analysis of the database images the powders were observed using Scanning electron microscopy (SEM). Figure 48 shows SEM images at (a) 1,000 x and (b) 2,000 x magnifications, it was clearly observed from the images that most of the particles were spherical with a range of sizes as shown. It was also observed that several particles were elongated (c), satellited (d) and possibly agglomerated (e).



**Figure 48 Scanning Electron Microscopy of Ti6Al4V Powder (A) 1000 X Magnification (B) 2000 X Magnification**

Figure 49 shows a Ti6Al4V powder particle at 8,000 x magnification measuring 45.8 µm. solidification patterns are visible on the surface along with columnar alpha phase.



**Figure 49 Scanning Electron Microscopy Of Ti6Al4V Powder 8,000 X Magnification.**

### 5.2.5 Phase 1a Baseline Assessment of SiC Particle Morphology.

Further analysis of the SiC baseline assessment results using the Camsizer X2 was carried out using the image database.

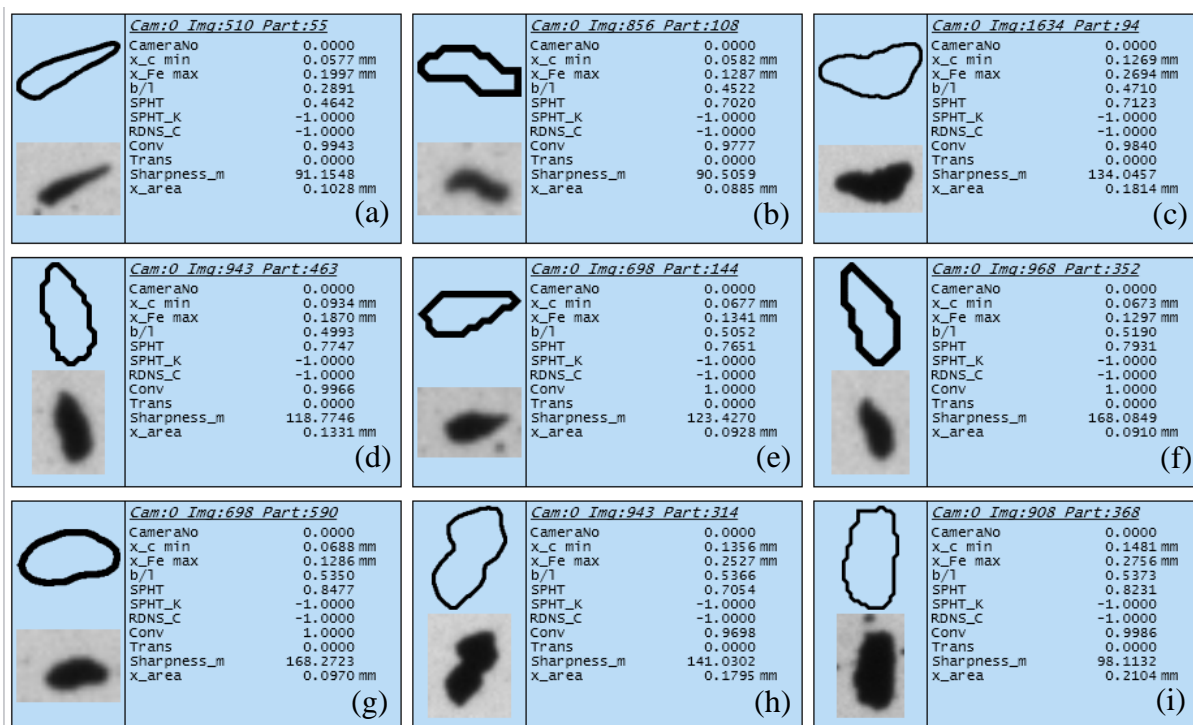


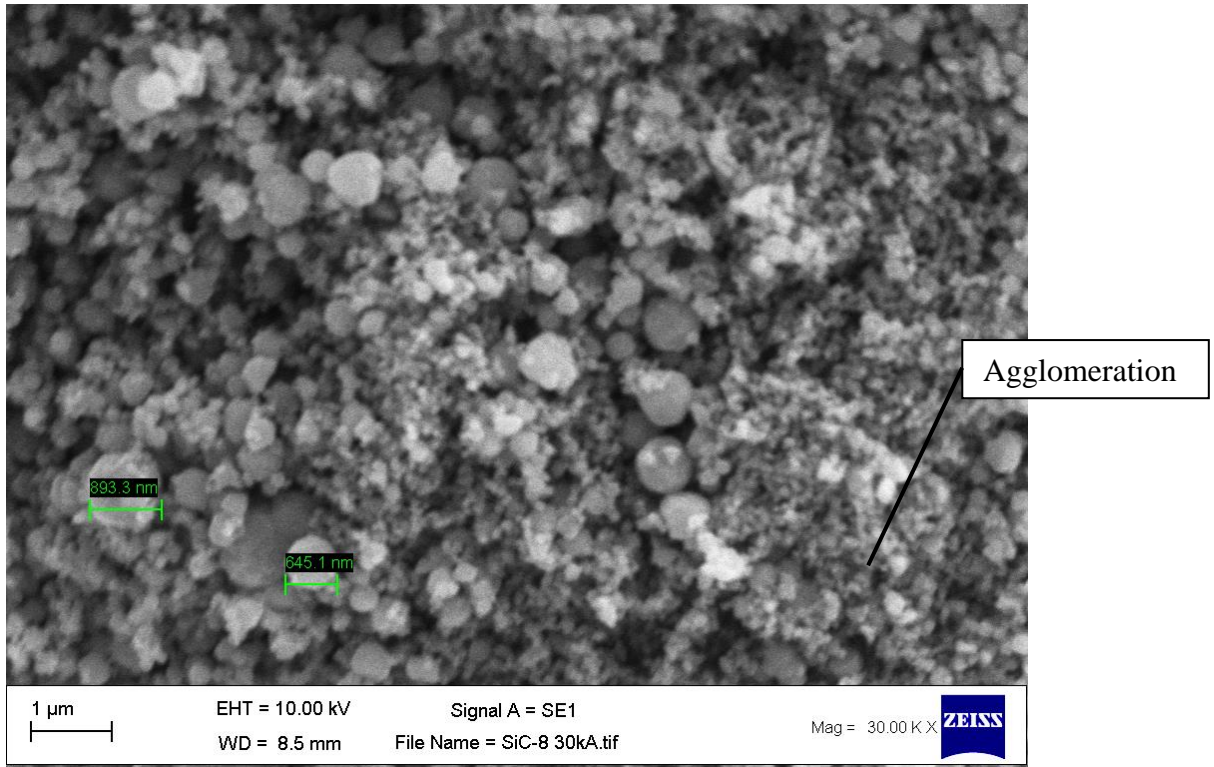
Figure 50 Retsch Camsizer X2 Database Images of Nonrounded SiC Particles ( $B/L \leq 0.600$ )

Figure 50 shows examples of the Retsch Camsizer X2 database images of nonrounded particles using database filters to isolate,  $X_{c \min} \geq 0.010$  mm and  $b/l \leq 0.850$   $\mathcal{R}$ . It was evident from the images that the software failed to distinguish between individual particles in the images. Using the filter  $X_{c \min} \geq 0.010$  mm to exclude particles smaller than 0.01 mm, should have selected no images as the largest particles are less than one micron. Images (a) to (i) exhibit minimum widths ( $X_{c \min}$ ) ranging from 0.057 mm to 0.148 mm.

Using the filters above, 852 out of 2631 images were found that met the conditions, this would suggest that 32.4% of the particles are statistically rounded however, based on SEM results there is enough evidence to show that these are agglomerations.

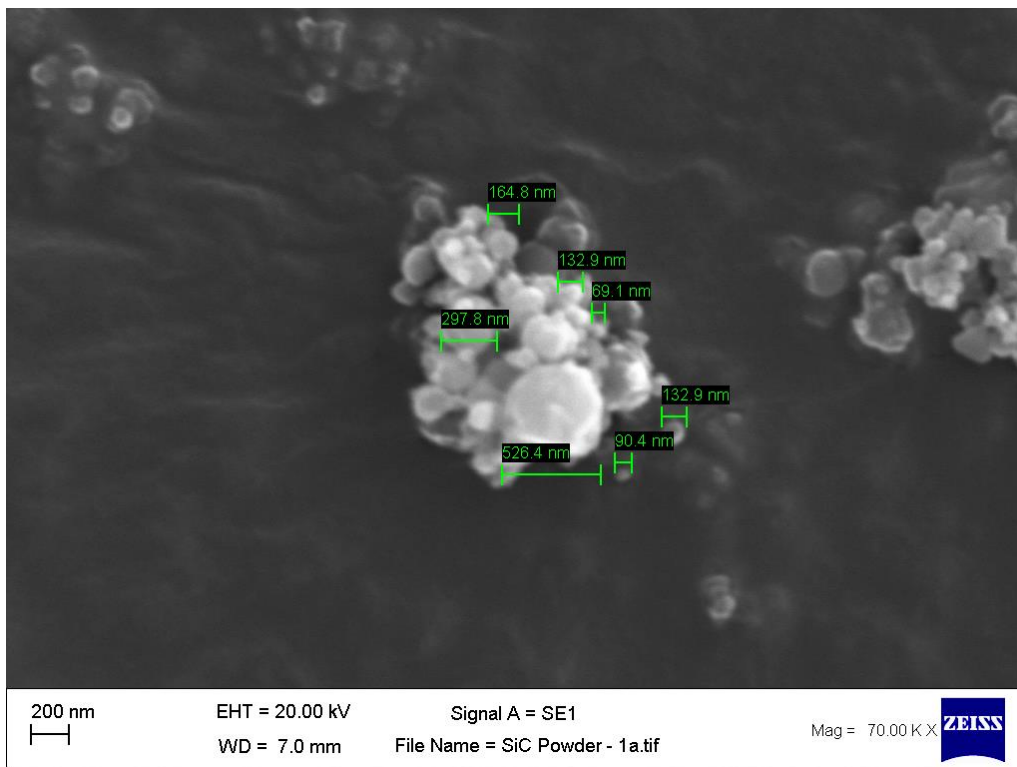
### 5.2.5.1 Scanning Electron Microscopy of SiC Powder.

Figure 51 shows an SEM image of SiC powder at 30,000 x magnification, it was observed from the image that the largest visible particles were approximately 0.89  $\mu\text{m}$  in width whilst most of the particles were substantially smaller.



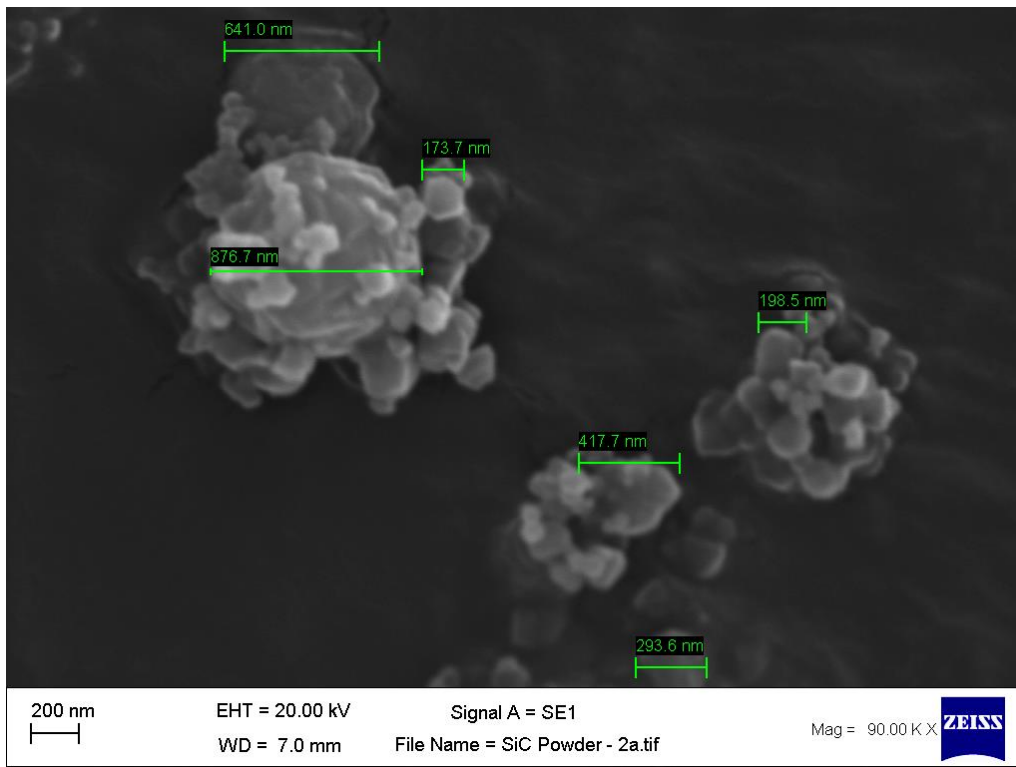
**Figure 51 Scanning Electron Microscopy of SiC Powder 30,000 X Magnification**

The image showed evidence of agglomerations within the sample, whilst this posed no issues for the MA process it did present a challenge in terms of accurate size analysis.



**Figure 52 Scanning Electron Microscopy of SiC Powder 70,000 X Magnification**

At 70,000 X magnification, individual particles were measured at between  $\sim 0.069 \mu\text{m}$  and  $\sim 0.526 \mu\text{m}$  wide Figure 52. However, it was not possible to evaluate the frequency distribution of all particle sizes within the range.



**Figure 53 Scanning Electron Microscopy of SiC Powder 90,000 X Magnification**

At 90,000 X magnification, Figure 53, evidence showed SiC particles in the range of  $\sim 0.173 \mu\text{m}$  to  $\sim 0.876 \mu\text{m}$ , It was therefore concluded that in this instance and with the data available the particle range should be taken to be from  $\sim 0.10 \mu\text{m}$  to  $\sim 0.90 \mu\text{m}$  with an average particle size of  $\sim 0.50 \mu\text{m}$  for use with Equation (6).

### **5.3 Phase 1b: Baseline Assessment of Ti6Al4V Single Beads Evaluated Against Energy Density.**

To provide a baseline by which the mechanically alloyed feedstock could be benchmarked against, Ti6Al4V powder was exposed to a range of varying laser powers and scan speeds as developed in Table 16. Using mini-platforms and the two-rail system, thirty tests were conducted. The samples were measured from above using a microscope to determine the mean bead width from five measurements, bead continuity, cracking and discoloration, then cross-sections of the beads were mounted using a CitoPress-5 (Struers 2018) and polished using a LaboForce-100 (Struers 2018) in accordance with the Struers Titanium Alloys (DiaPro, Application Note) (Appendix 2) to measure the following dimensions as per Figure 8.

- **(h1)** Bead height.
- **(h2)** Substrate penetration denoted by the depth of the dilution.

- (**w1**) Bead width and
- (**w2**) Width of the contact or dilution area.

(Yadroitsev et al., 2012)

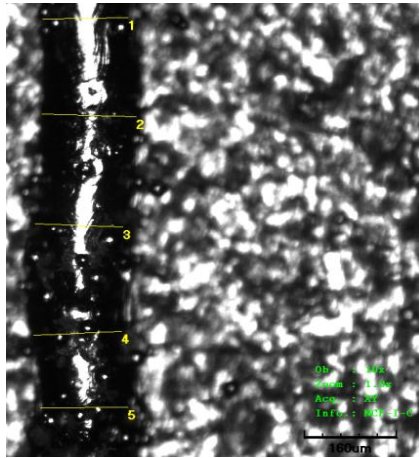
Results for Ti6Al4V powder exposed at 150 W are presented in Table 29.



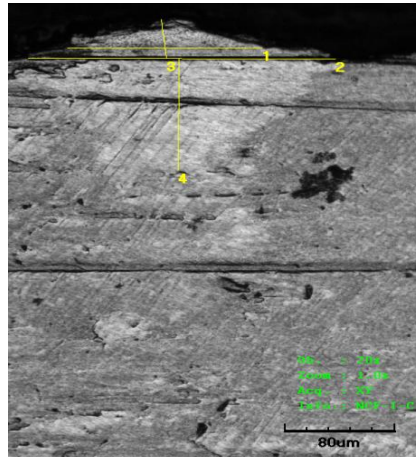
Table 29 Phase 1b, Baseline Assessment of Ti6Al4V Single Beads Evaluated Against Energy Density At 150 W

| View on Z axis at 10 x magnification | Cross sectional view at 20 x magnification | Observations and measurements.                                                                                                                                                                                                                                                                                                                                                                                                                               |
|--------------------------------------|--------------------------------------------|--------------------------------------------------------------------------------------------------------------------------------------------------------------------------------------------------------------------------------------------------------------------------------------------------------------------------------------------------------------------------------------------------------------------------------------------------------------|
|                                      |                                            | <p><b>Energy density</b><br/>250 J/mm<sup>3</sup><br/><b>Scan speed</b><br/>200 mm/s<br/><b>Mean bead width, vertical</b><br/>186.287 µm<br/><b>Bead continuity</b><br/>continuous<br/><b>Cracking and discoloration</b><br/>No cracking or discoloration<br/><b>h1 (Bead height)</b><br/>55.004 µm<br/><b>h2 (Substrate penetration)</b><br/>112.502 µm<br/><b>w1 (Bead width)</b><br/>273.128 µm<br/><b>w2 (width of dilution area)</b><br/>273.128 µm</p> |
|                                      |                                            | <p><b>Energy density</b><br/>225 J/mm<sup>3</sup><br/><b>Scan speed</b><br/>222 mm/s<br/><b>Mean bead width, vertical</b><br/>165.852 µm<br/><b>Bead continuity</b><br/>continuous<br/><b>Cracking and discoloration</b><br/>No cracking or discoloration<br/><b>h1 (Bead height)</b><br/>47.566 µm<br/><b>h2 (Substrate penetration)</b><br/>115.042 µm<br/><b>w1 (Bead width)</b><br/>168.144 µm<br/><b>w2 (width of dilution area)</b><br/>228.771 µm</p> |
|                                      |                                            | <p><b>Energy density</b><br/>200 J/mm<sup>3</sup><br/><b>Scan speed</b><br/>250 mm/s<br/><b>Mean bead width, vertical</b><br/>161.505 µm<br/><b>Bead continuity</b><br/>continuous<br/><b>Cracking and discoloration</b><br/>No cracking or discoloration<br/><b>h1 (Bead height)</b><br/>40.625 µm<br/><b>h2 (Substrate penetration)</b><br/>101.875 µm<br/><b>w1 (Bead width)</b><br/>196.884 µm<br/><b>w2 (width of dilution area)</b><br/>265.628 µm</p> |

**View on Z axis at 10 x magnification**

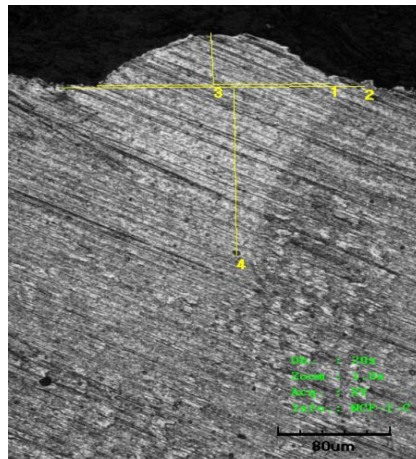
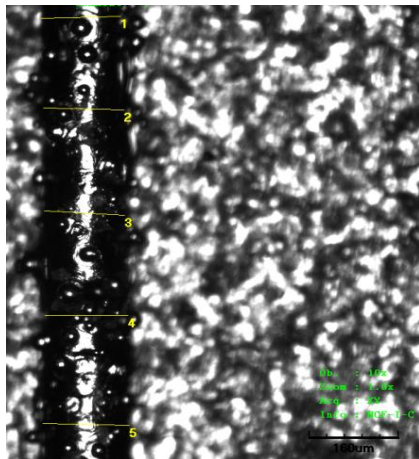


**Cross sectional view at 20 x magnification**

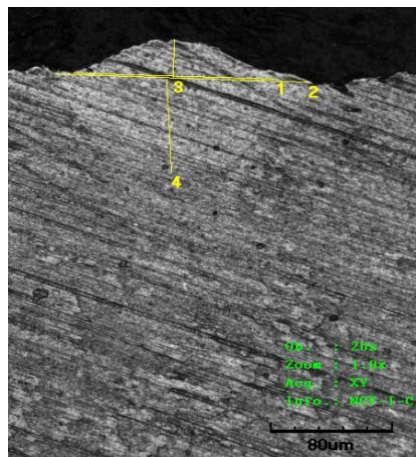
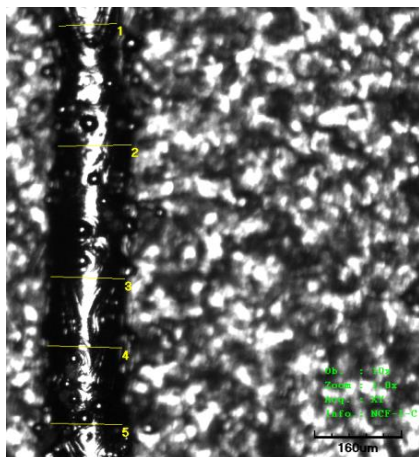


**Observations and measurements.**

**Energy density**  
 175 J/mm<sup>3</sup>  
**Scan speed**  
 286 mm/s  
**Mean bead width, vertical**  
 151.271 µm  
**Bead continuity**  
 continuous  
**Cracking and discoloration**  
 No cracking or discoloration  
**h1 (Bead height)**  
 35.200 µm  
**h2 (Substrate penetration)**  
 100.627 µm  
**w1 (Bead width)**  
 145.000 µm  
**w2 (width of dilution area)**  
 229.376 µm

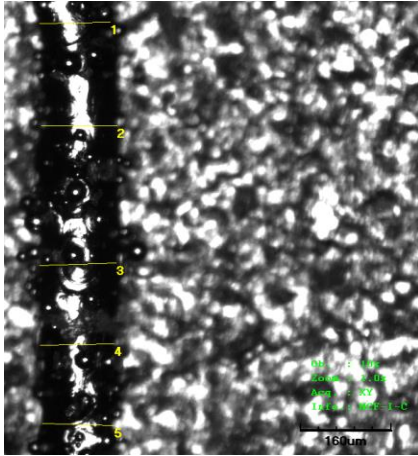


**Energy density**  
 150 J/mm<sup>3</sup>  
**Scan speed**  
 333 mm/s  
**Mean bead width, vertical**  
 150.580 µm  
**Bead continuity**  
 continuous  
**Cracking and discoloration**  
 No cracking or discoloration  
**h1 (Bead height)**  
 44.415 µm  
**h2 (Substrate penetration)**  
 145.012 µm  
**w1 (Bead width)**  
 170.010 µm  
**w2 (width of dilution area)**  
 221.879 µm

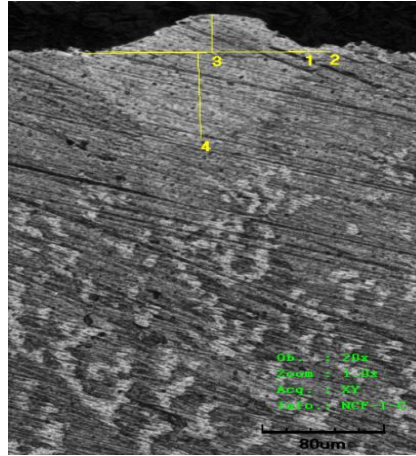


**Energy density**  
 125 J/mm<sup>3</sup>  
**Scan speed**  
 400 mm/s  
**Mean bead width, vertical**  
 131.802 µm  
**Bead continuity**  
 continuous  
**Cracking and discoloration**  
 No cracking or discoloration  
**h1 (Bead height)**  
 28.757 µm  
**h2 (Substrate penetration)**  
 70.694 µm  
**w1 (Bead width)**  
 136.945 µm  
**w2 (width of dilution area)**  
 171.364 µm

**View on Z axis at 10 x magnification**

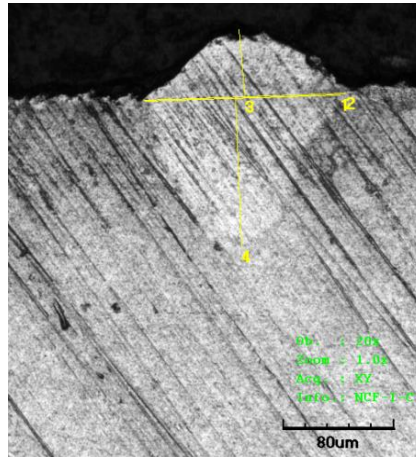
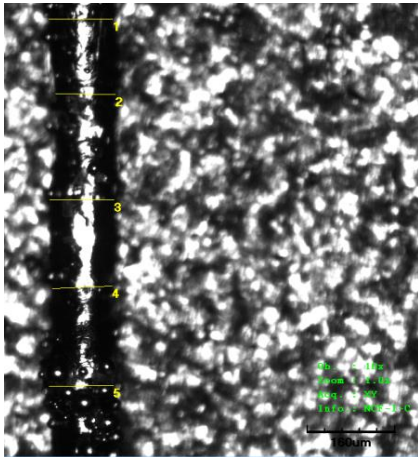


**Cross sectional view at 20 x magnification**

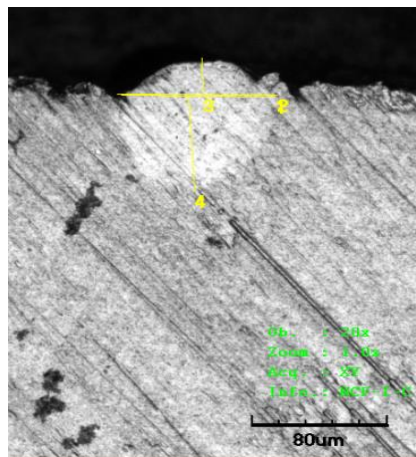
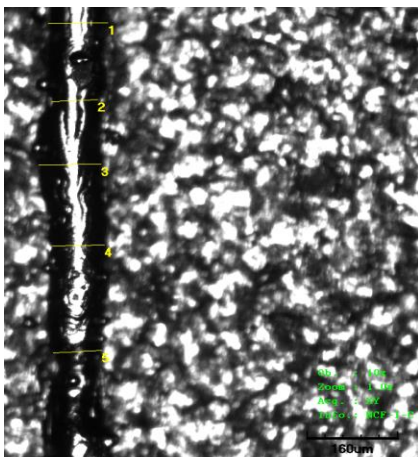


**Observations and measurements.**

**Energy density**  
100 J/mm<sup>3</sup>  
**Scan speed**  
500 mm/s  
**Mean bead width, vertical**  
133.288 µm  
**Bead continuity**  
continuous  
**Cracking and discoloration**  
No cracking or discoloration  
**h1 (Bead height)**  
32.500 µm  
**h2 (Substrate penetration)**  
71.899 µm  
**w1 (Bead width)**  
133.750 µm  
**w2 (width of dilution area)**  
166.261 µm

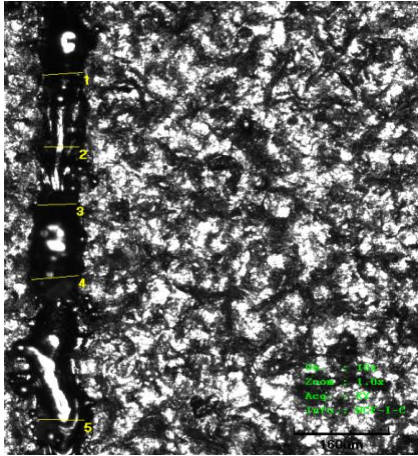


**Energy density**  
75 J/mm<sup>3</sup>  
**Scan speed**  
667 mm/s  
**Mean bead width, vertical**  
116.275 µm  
**Bead continuity**  
continuous  
**Cracking and discoloration**  
No cracking or discoloration  
**h1 (Bead height)**  
49.568 µm  
**h2 (Substrate penetration)**  
108.838 µm  
**w1 (Bead width)**  
145.066 µm  
**w2 (width of dilution area)**  
150.085 µm

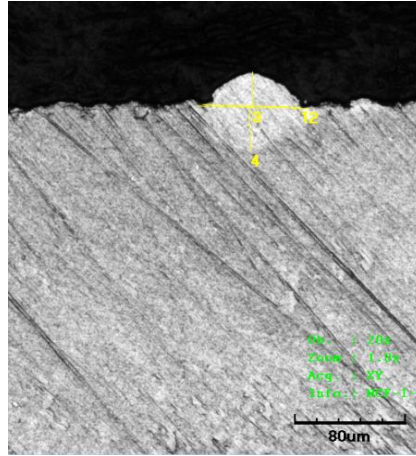


**Energy density**  
50 J/mm<sup>3</sup>  
**Scan speed**  
1000 mm/s  
**Mean bead width, vertical**  
96.805 µm  
**Bead continuity**  
continuous  
**Cracking and discoloration**  
No cracking or discoloration  
**h1 (Bead height)**  
25.633 µm  
**h2 (Substrate penetration)**  
65.108 µm  
**w1 (Bead width)**  
93.133 µm  
**w2 (width of dilution area)**  
96.877 µm

**View on Z axis at 10 x magnification**



**Cross sectional view at 20 x magnification**



**Observations and measurements.**

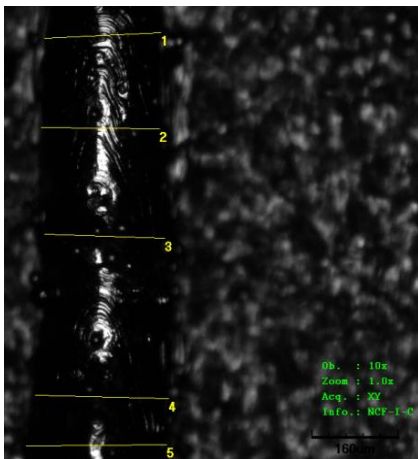
**Energy density**  
25 J/mm<sup>3</sup>  
**Scan speed**  
2000 mm/s  
**Mean bead width, vertical**  
70.618 µm  
**Bead continuity**  
Not continuous  
**Cracking and discoloration**  
No cracking or discoloration  
**h1 (Bead height)**  
27.500 µm  
**h2 (Substrate penetration)**  
33.756 µm  
**w1 (Bead width)**  
72.543 µm  
**w2 (width of dilution area)**  
82.521 µm

All single beads using Ti6Al4V powder exposed at 150 W showed evidence of miscibility with the substrate and an ability to form a continuous bead whilst maintaining a uniform width and height. The exception to this being the bead exposed at 2000 mm/s, whilst there was substrate penetration and evidence of bead formation, it was clear that the progression of the laser exposed powder sporadically, it is also possible that the speed of the laser’s movement could cause powder to be forced away from the meltpool producing the observed discontinuous bead.

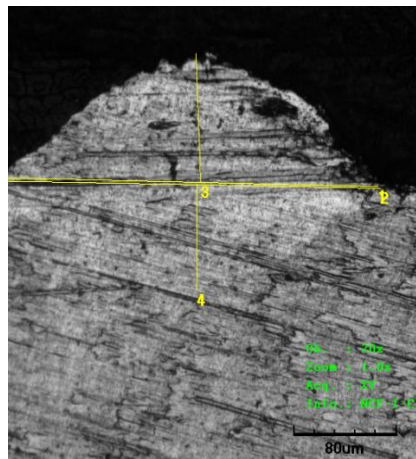
Results for Ti6Al4V powder exposed at 250 W are presented in Table 30.

**Table 30 Phase 1b, Baseline Assessment of Ti6Al4V Single Beads Evaluated Against Energy Density at 250 W**

**View on Z axis at 10 x magnification**



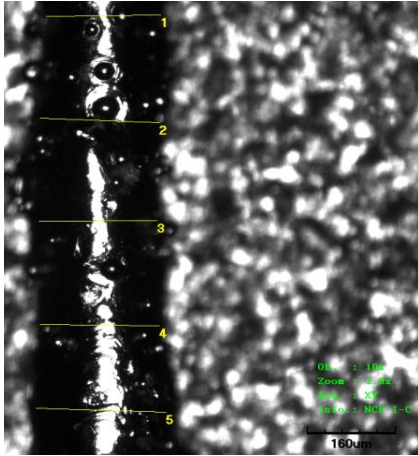
**Cross sectional view at 20 x magnification**



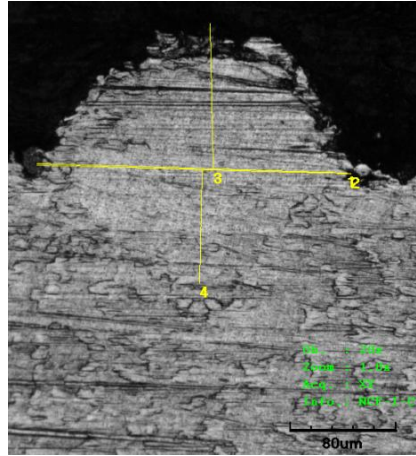
**Observations and measurements.**

**Energy density**  
417 J/mm<sup>3</sup>  
**Scan speed**  
200 mm/s  
**Mean bead width, vertical**  
239.340 µm  
**Bead continuity**  
continuous  
**Cracking and discoloration**  
No cracking or discoloration  
**h1 (Bead height)**  
96.323 µm  
**h2 (Substrate penetration)**  
79.375 µm  
**w1 (Bead width)**  
312.576 µm  
**w2 (width of dilution area)**  
315.675 µm

**View on Z axis at 10 x magnification**

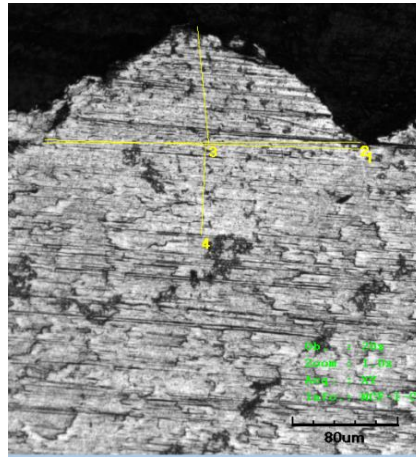
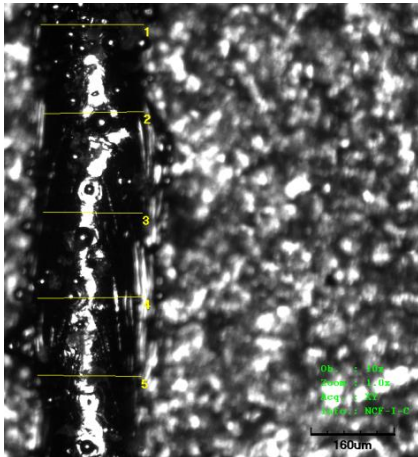


**Cross sectional view at 20 x magnification**

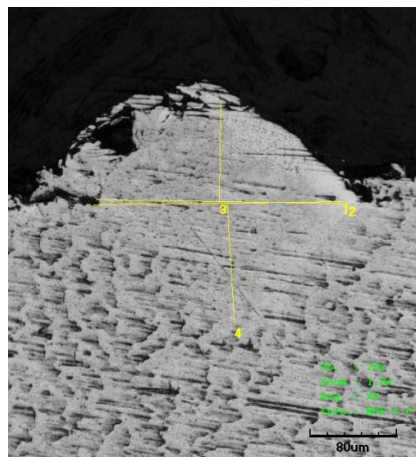
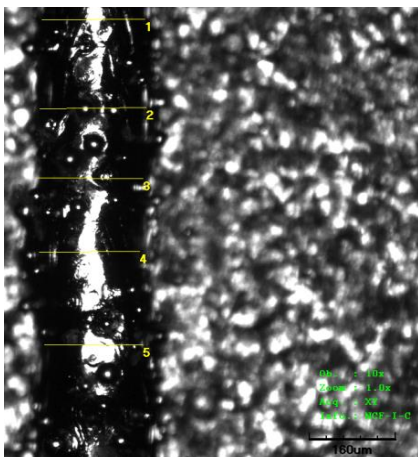


**Observations and measurements.**

**Energy density**  
375 J/mm<sup>3</sup>  
**Scan speed**  
222 mm/s  
**Mean bead width, vertical**  
223.314 µm  
**Bead continuity**  
continuous  
**Cracking and discoloration**  
No cracking or discoloration  
**h1 (Bead height)**  
115.652 µm  
**h2 (Substrate penetration)**  
90.020 µm  
**w1 (Bead width)**  
240.742 µm  
**w2 (width of dilution area)**  
243.847 µm

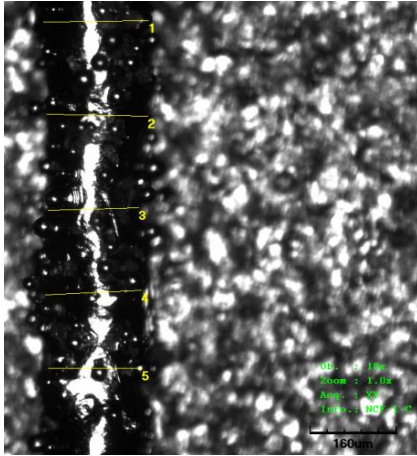


**Energy density**  
333 J/mm<sup>3</sup>  
**Scan speed**  
250 mm/s  
**Mean bead width, vertical**  
201.514 µm  
**Bead continuity**  
continuous  
**Cracking and discoloration**  
No cracking or discoloration  
**h1 (Bead height)**  
95.402 µm  
**h2 (Substrate penetration)**  
74.441 µm  
**w1 (Bead width)**  
249.488 µm  
**w2 (width of dilution area)**  
246.251 µm

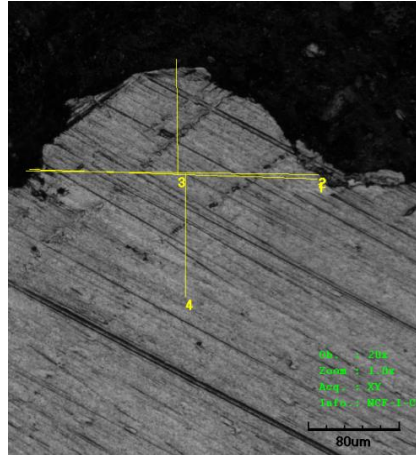


**Energy density**  
291 J/mm<sup>3</sup>  
**Scan speed**  
286 mm/s  
**Mean bead width, vertical**  
195.505 µm  
**Bead continuity**  
continuous  
**Cracking and discoloration**  
No cracking or discoloration  
**h1 (Bead height)**  
90.634 µm  
**h2 (Substrate penetration)**  
113.334 µm  
**w1 (Bead width)**  
235.646 µm  
**w2 (width of dilution area)**  
238.779 µm

**View on Z axis at 10 x magnification**

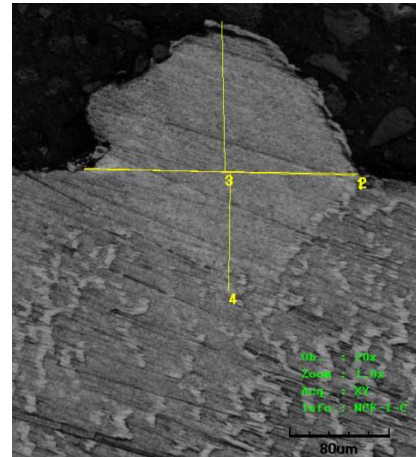
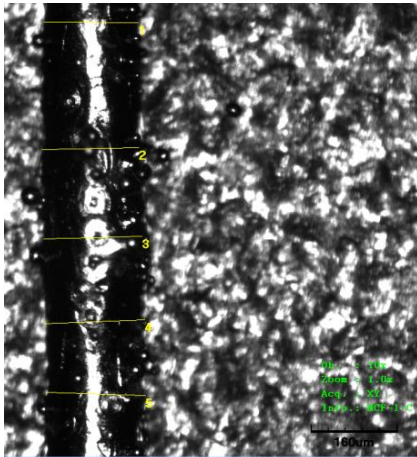


**Cross sectional view at 20 x magnification**

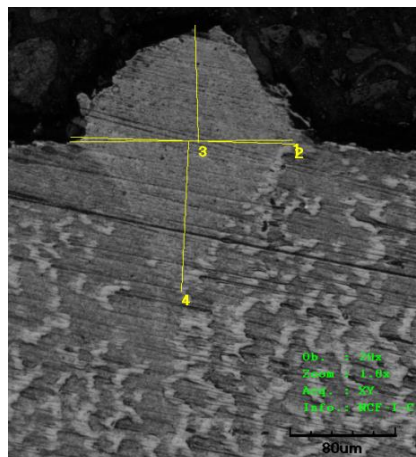
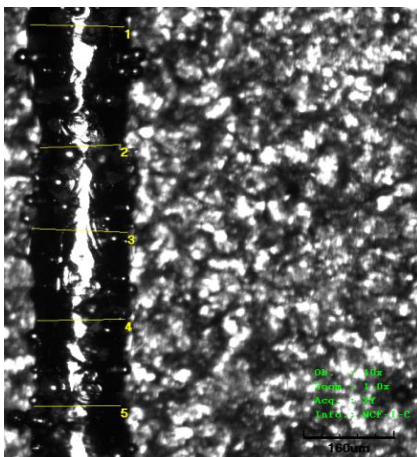


**Observations and measurements.**

**Energy density**  
250 J/mm<sup>3</sup>  
**Scan speed**  
333 mm/s  
**Mean bead width, vertical**  
185.067 µm  
**Bead continuity**  
continuous  
**Cracking and discoloration**  
No cracking or discoloration  
**h1 (Bead height)**  
98.133 µm  
**h2 (Substrate penetration)**  
105.000 µm  
**w1 (Bead width)**  
259.502 µm  
**w2 (width of dilution area)**  
263.769 µm

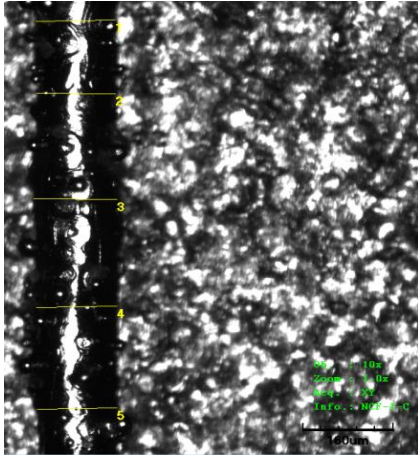


**Energy density**  
208 J/mm<sup>3</sup>  
**Scan speed**  
400 mm/s  
**Mean bead width, vertical**  
186.822 µm  
**Bead continuity**  
continuous  
**Cracking and discoloration**  
No cracking or discoloration  
**h1 (Bead height)**  
121.901 µm  
**h2 (Substrate penetration)**  
95.633 µm  
**w1 (Bead width)**  
223.821 µm  
**w2 (width of dilution area)**  
226.281 µm

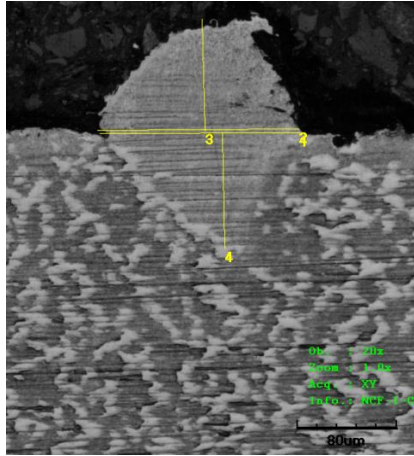


**Energy density**  
167 J/mm<sup>3</sup>  
**Scan speed**  
500 mm/s  
**Mean bead width, vertical**  
161.322 µm  
**Bead continuity**  
continuous  
**Cracking and discoloration**  
No cracking or discoloration  
**h1 (Bead height)**  
95.658 µm  
**h2 (Substrate penetration)**  
122.005 µm  
**w1 (Bead width)**  
173.130 µm  
**w2 (width of dilution area)**  
174.466 µm

**View on Z axis at 10 x magnification**

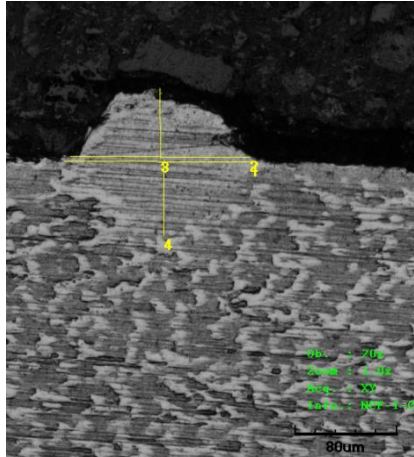
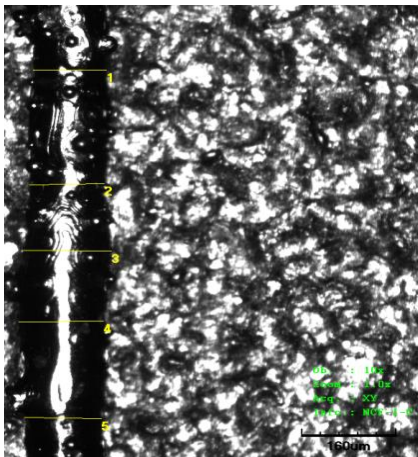


**Cross sectional view at 20 x magnification**

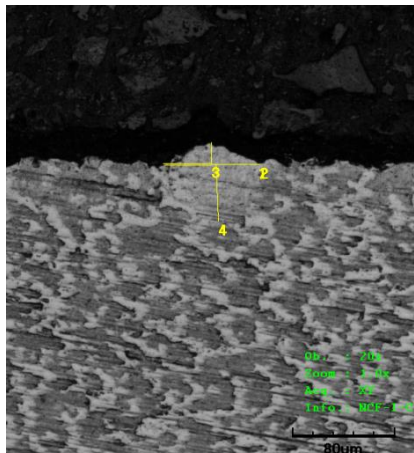
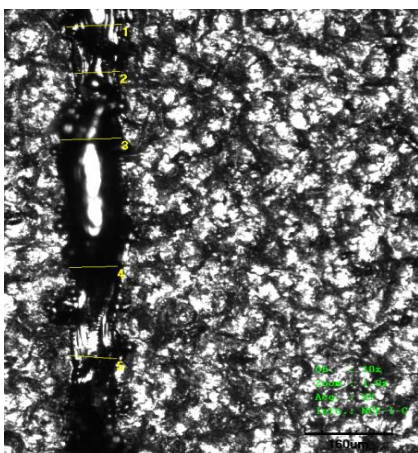


**Observations and measurements.**

**Energy density**  
125 J/mm<sup>3</sup>  
**Scan speed**  
667 mm/s  
**Mean bead width, vertical**  
145.765 µm  
**Bead continuity**  
continuous  
**Cracking and discoloration**  
No cracking or discoloration  
**h1 (Bead height)**  
92.534 µm  
**h2 (Substrate penetration)**  
95.643 µm  
**w1 (Bead width)**  
165.001 µm  
**w2 (width of dilution area)**  
166.255 µm



**Energy density**  
83 J/mm<sup>3</sup>  
**Scan speed**  
1000 mm/s  
**Mean bead width, vertical**  
138.262 µm  
**Bead continuity**  
continuous  
**Cracking and discoloration**  
No cracking or discoloration  
**h1 (Bead height)**  
55.629 µm  
**h2 (Substrate penetration)**  
60.625 µm  
**w1 (Bead width)**  
150.001 µm  
**w2 (width of dilution area)**  
145.001 µm



**Energy density**  
42 J/mm<sup>3</sup>  
**Scan speed**  
2000 mm/s  
**Mean bead width, vertical**  
95.605 µm  
**Bead continuity**  
Not continuous  
**Cracking and discoloration**  
No cracking or discoloration  
**h1 (Bead height)**  
16.875 µm  
**h2 (Substrate penetration)**  
45.039 µm  
**w1 (Bead width)**  
75.003 µm  
**w2 (width of dilution area)**  
77.503 µm

All single beads using Ti6Al4V powder exposed at 250 W showed evidence of miscibility with the substrate and ability to form a continuous bead maintaining a uniform width and height. The only exception to this being the bead exposed at 2000 mm/s, whilst there was substrate

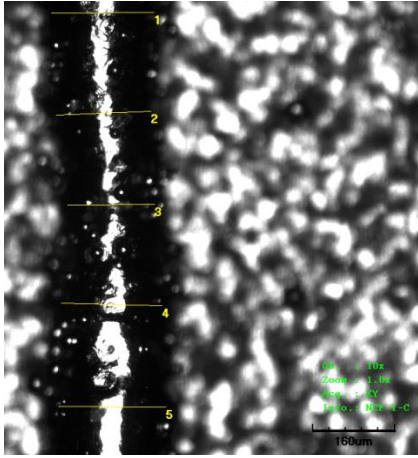
penetration and evidence of bead formation, it was clear that the progression of the laser only exposed powder sporadically, as with those exposed at 150 W Table 29.

**Table 31 Phase 1b, Baseline Assessment of Ti6Al4V Single Beads Evaluated Against Energy Density at 350 W**

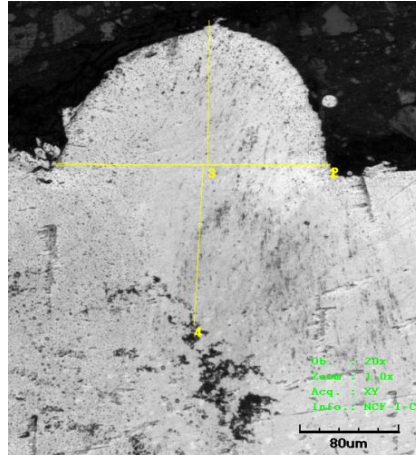
| View on Z axis at 10 x magnification | Cross sectional view at 20 x magnification | Observations and measurements.                                                                                                                                                                                                                                                                                                                                                                                                                                |
|--------------------------------------|--------------------------------------------|---------------------------------------------------------------------------------------------------------------------------------------------------------------------------------------------------------------------------------------------------------------------------------------------------------------------------------------------------------------------------------------------------------------------------------------------------------------|
|                                      |                                            | <p><b>Energy density</b><br/>583 J/mm<sup>3</sup><br/><b>Scan speed</b><br/>200 mm/s<br/><b>Mean bead width, vertical</b><br/>240.017 μm<br/><b>Bead continuity</b><br/>continuous<br/><b>Cracking and discoloration</b><br/>No cracking or discoloration<br/><b>h1 (Bead height)</b><br/>125.631 μm<br/><b>h2 (Substrate penetration)</b><br/>133.126 μm<br/><b>w1 (Bead width)</b><br/>296.886 μm<br/><b>w2 (width of dilution area)</b><br/>293.756 μm</p> |
|                                      |                                            | <p><b>Energy density</b><br/>526 J/mm<sup>3</sup><br/><b>Scan speed</b><br/>222 mm/s<br/><b>Mean bead width, vertical</b><br/>238.778 μm<br/><b>Bead continuity</b><br/>continuous<br/><b>Cracking and discoloration</b><br/>No cracking or discoloration<br/><b>h1 (Bead height)</b><br/>126.950 μm<br/><b>h2 (Substrate penetration)</b><br/>122.005 μm<br/><b>w1 (Bead width)</b><br/>281.919 μm<br/><b>w2 (width of dilution area)</b><br/>282.544 μm</p> |
|                                      |                                            | <p><b>Energy density</b><br/>467 J/mm<sup>3</sup><br/><b>Scan speed</b><br/>250 mm/s<br/><b>Mean bead width, vertical</b><br/>220.097 μm<br/><b>Bead continuity</b><br/>continuous<br/><b>Cracking and discoloration</b><br/>No cracking or discoloration<br/><b>h1 (Bead height)</b><br/>148.972 μm<br/><b>h2 (Substrate penetration)</b><br/>171.893 μm<br/><b>w1 (Bead width)</b><br/>283.761 μm<br/><b>w2 (width of dilution area)</b><br/>290.003 μm</p> |



**View on Z axis at 10 x magnification**

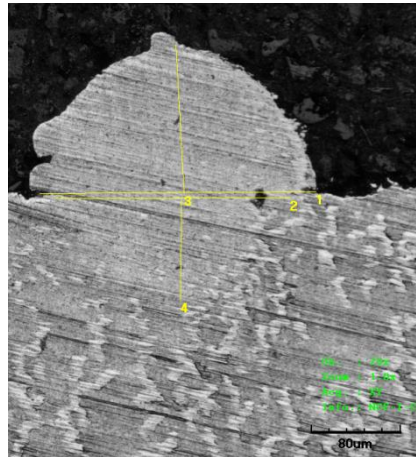
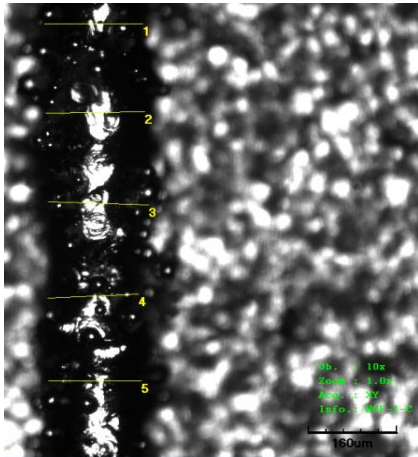


**Cross sectional view at 20 x magnification**

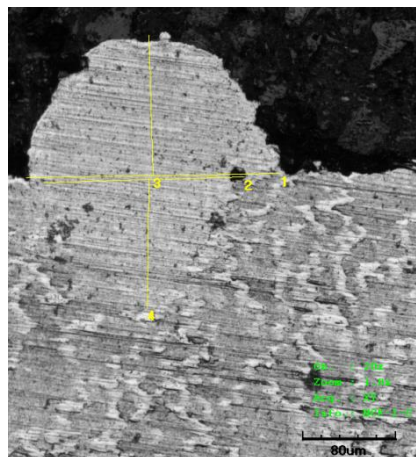
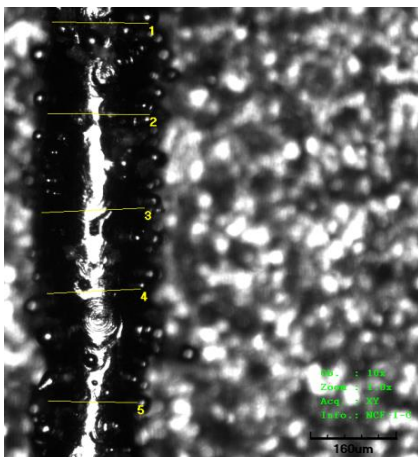


**Observations and measurements.**

**Energy density**  
408 J/mm<sup>3</sup>  
**Scan speed**  
286 mm/s  
**Mean bead width, vertical**  
196.545 µm  
**Bead continuity**  
continuous  
**Cracking and discoloration**  
No cracking or discoloration  
**h1 (Bead height)**  
131.256 µm  
**h2 (Substrate penetration)**  
142.697 µm  
**w1 (Bead width)**  
228.758 µm  
**w2 (width of dilution area)**  
228.126 µm

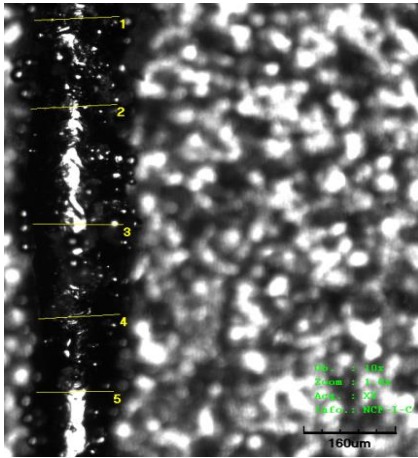


**Energy density**  
350 J/mm<sup>3</sup>  
**Scan speed**  
333 mm/s  
**Mean bead width, vertical**  
178.808 µm  
**Bead continuity**  
continuous  
**Cracking and discoloration**  
No cracking or discoloration  
**h1 (Bead height)**  
134.584 µm  
**h2 (Substrate penetration)**  
91.252 µm  
**w1 (Bead width)**  
253.757 µm  
**w2 (width of dilution area)**  
215.626 µm

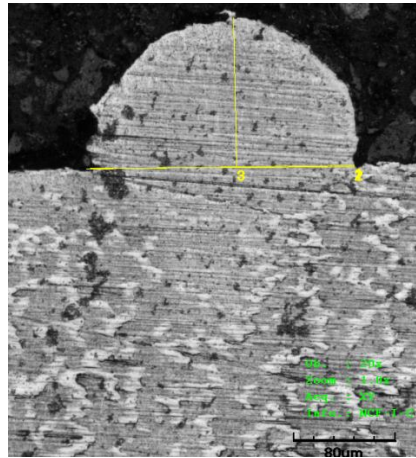


**Energy density**  
292 J/mm<sup>3</sup>  
**Scan speed**  
400 mm/s  
**Mean bead width, vertical**  
184.840 µm  
**Bead continuity**  
continuous  
**Cracking and discoloration**  
No cracking or discoloration  
**h1 (Bead height)**  
123.807 µm  
**h2 (Substrate penetration)**  
113.757 µm  
**w1 (Bead width)**  
177.570 µm  
**w2 (width of dilution area)**  
224.406 µm

**View on Z axis at 10 x magnification**

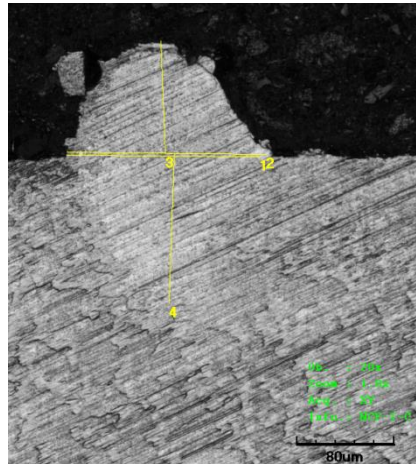
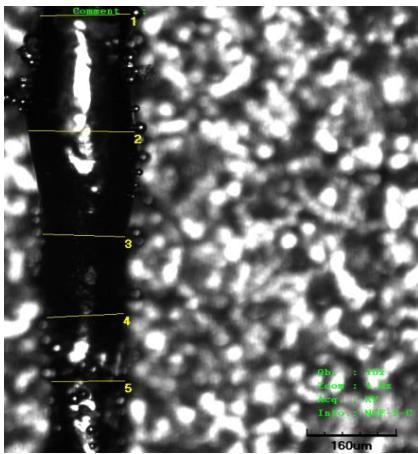


**Cross sectional view at 20 x magnification**

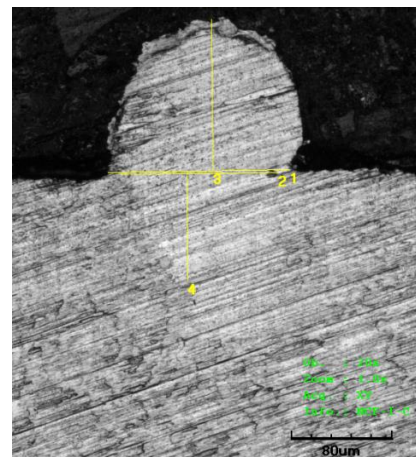
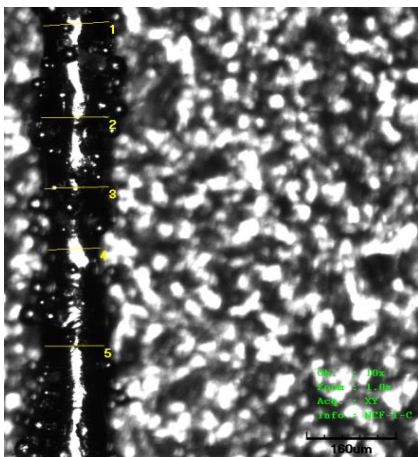


**Observations and measurements.**

**Energy density**  
233 J/mm<sup>3</sup>  
**Scan speed**  
500 mm/s  
**Mean bead width, vertical**  
149.892 µm  
**Bead continuity**  
continuous  
**Cracking and discoloration**  
No cracking or discoloration  
**h1 (Bead height)**  
124.400 µm  
**h2 (Substrate penetration)**  
- µm  
**w1 (Bead width)**  
216.273 µm  
**w2 (width of dilution area)**  
213.129 µm

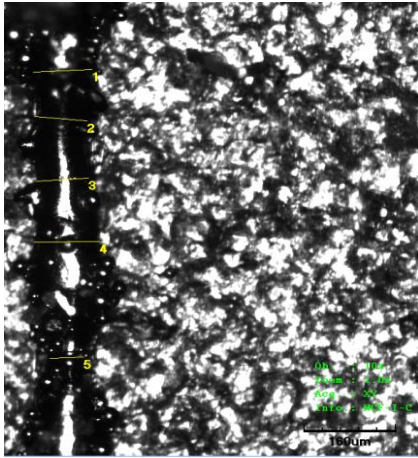


**Energy density**  
175 J/mm<sup>3</sup>  
**Scan speed**  
667 mm/s  
**Mean bead width, vertical**  
156.570 µm  
**Bead continuity**  
continuous  
**Cracking and discoloration**  
No cracking or discoloration  
**h1 (Bead height)**  
93.825 µm  
**h2 (Substrate penetration)**  
123.827 µm  
**w1 (Bead width)**  
162.505 µm  
**w2 (width of dilution area)**  
168.135 µm

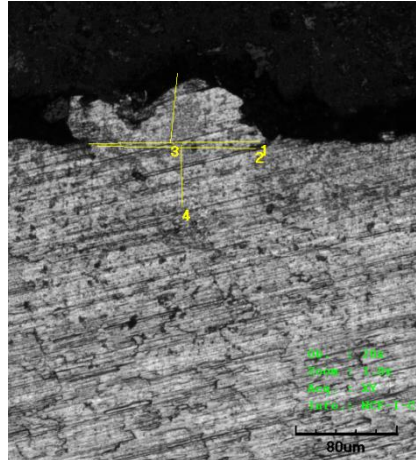


**Energy density**  
117 J/mm<sup>3</sup>  
**Scan speed**  
1000 mm/s  
**Mean bead width, vertical**  
113.076 µm  
**Bead continuity**  
continuous  
**Cracking and discoloration**  
No cracking or discoloration  
**h1 (Bead height)**  
127.506 µm  
**h2 (Substrate penetration)**  
90.627 µm  
**w1 (Bead width)**  
148.146 µm  
**w2 (width of dilution area)**  
128.756 µm

**View on Z axis at 10 x magnification**



**Cross sectional view at 20 x magnification**



**Observations and measurements.**

**Energy density**  
 58 J/mm<sup>3</sup>  
**Scan speed**  
 2000 mm/s  
**Mean bead width, vertical**  
 93.909 μm  
**Bead continuity**  
 Not continuous  
**Cracking and discoloration**  
 No cracking or discoloration  
**h1 (Bead height)**  
 55.287 μm  
**h2 (Substrate penetration)**  
 48.754 μm  
**w1 (Bead width)**  
 138.763 μm  
**w2 (width of dilution area)**  
 128.139 μm

All single beads using Ti6Al4V powder exposed at 350 W showed evidence of miscibility with the substrate and ability to form a continuous bead maintaining a uniform width and height. The only exception to this being the bead exposed at 2000 mm/s, whilst there was substrate penetration and evidence of bead formation, it was clear that the progression of the laser only exposed powder sporadically, as with those exposed at 150 W and 250 W.

Across all three laser energy ranges there was evidence of spatter adhered to the surface of the beads, indicating a degree of volatility within the meltpools of subsequent beads, this however, was not excessive and therefore could be considered acceptable for this material. There was no evidence of balling around the bead, demonstrating thermal synergy between the feedstock, meltpool and substrate.

Regarding cracking, there was no evidence to show that cracks had propagated longitudinally or laterally on the beads surface. This was a clear indication that the material within the bead was sufficiently ductile to withstand the forces involved in solidification.

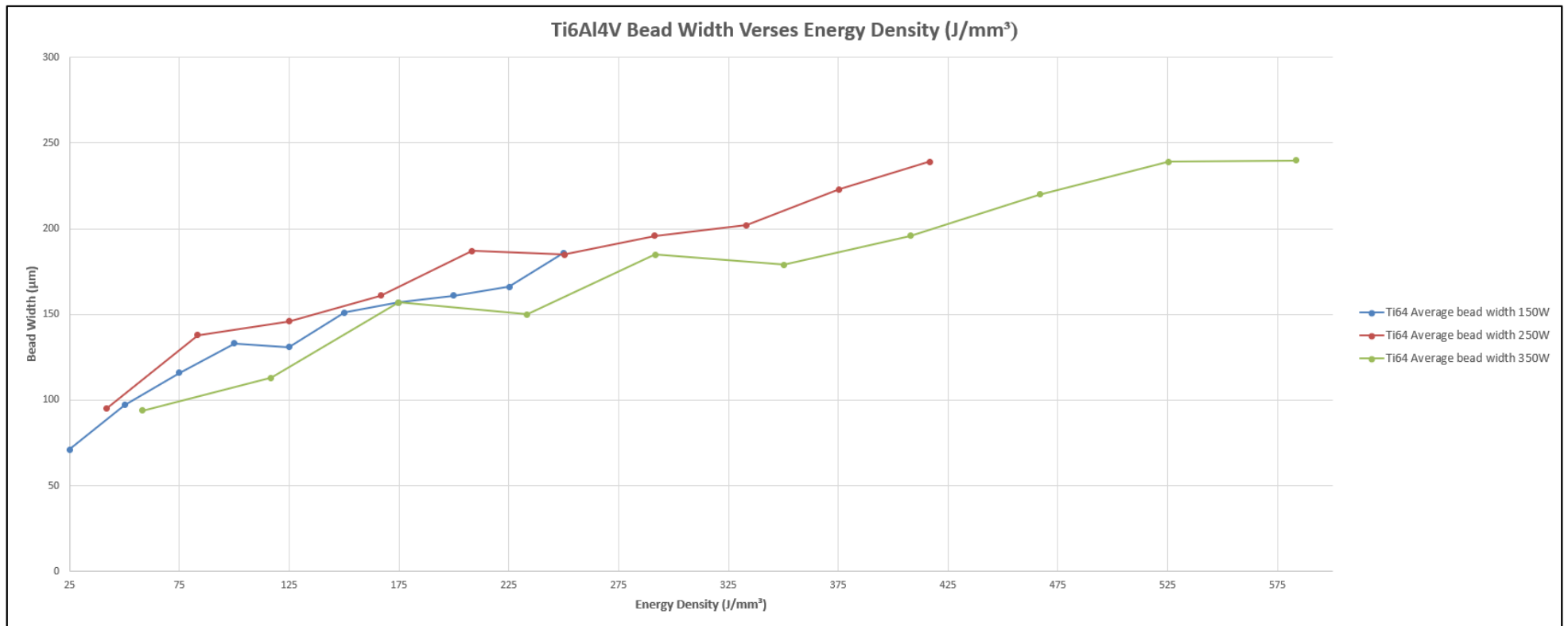


Figure 54 Comparison Between Ti6Al4V Bead Widths ( $w_1$ ) at 150 W, 250 W and 350 W Versus Energy Density

Figure 54 shows the Comparison between Ti6Al4V Bead widths at 150 W, 250 W and 350 W versus energy density, calculated as the mean value from measurements taken from five places along the bead, viewed in the vertical axis. With respect to bead width, as the energy density is increased so does the width of the bead. As the range of scan speeds were identical as with layer thickness it is evident that the increase in laser power is influential in the increased consumption of feedstock thus producing a wider bead. The width of bead is unrestricted regarding how wide it can be, only influencing hatch distance, which should be calculated with bead width in mind, in order to produce the best parts (Yadroitsev, et al., 2013).

Whilst the width of bead is significant regarding its influence over hatch distance and therefore must be measured and taken into consideration when experimenting with multiple beads and multiple layers, bead height is far more crucial to processability. Due to the nature of feedstock delivery, contact free recoating is essential. Contact with the laser melted surface results in ridges in the recoat surface from the recoat arm which become worse after each recoat leading ultimately to part failure.

Figure 55 shows comparison between Ti6Al4V bead heights ( $h_1$ ) at 150 W, 250 W and 350 W versus energy density. It can be seen from the results that as with bead width, the bead height increases in size as a function of energy density. It was observed that for beads exposed at 150 W, the bead height remained below 60  $\mu\text{m}$ . The value of 60  $\mu\text{m}$  was chosen as a maximum cut-off value for bead height given the processes requirement for contact free recoating. Given that the two-rail system was employed to produce beads with a layer thickness of  $\sim 45 \mu\text{m}$  to  $\sim 50 \mu\text{m}$  it would be conceivable that a bead height of  $\sim 75 \mu\text{m}$  to  $\sim 80 \mu\text{m}$  would contact the recoater blade given that the build plate would be lowered by 30  $\mu\text{m}$  before recoating. A maximum bead height of 60  $\mu\text{m}$  would therefore not contact the recoater blade and allow for  $\sim 20 \mu\text{m}$  variation.

Beads produced with 150 W laser power resulted in bead heights within the maximum height and could be taken forward for experimentation into hatch spacing (Phase 3c) and multiple layer evaluation (Phase 3d). as laser power is increased to 250 W and 350 W, most beads fail to remain within the 60  $\mu\text{m}$  maximum due to the increased consumption of feedstock. Two values with a laser power of 250 W remained below 60  $\mu\text{m}$ , having scan speeds of 2000 mm/s and 1000 mm/s. whilst the bead produced at 1000 mm/s was of an acceptable quality the bead produced at 2000 mm/s was found to have discontinuity and would therefore, not be of suitable quality (Table 30). This was also found to be the case for beads exposed with a laser power of 350 W. One bead was found to have a height of less than 60  $\mu\text{m}$ , with a scan speed of 2000 mm/s. this bead however, also exhibited evidence of discontinuity along the length of the bead (Table 31).

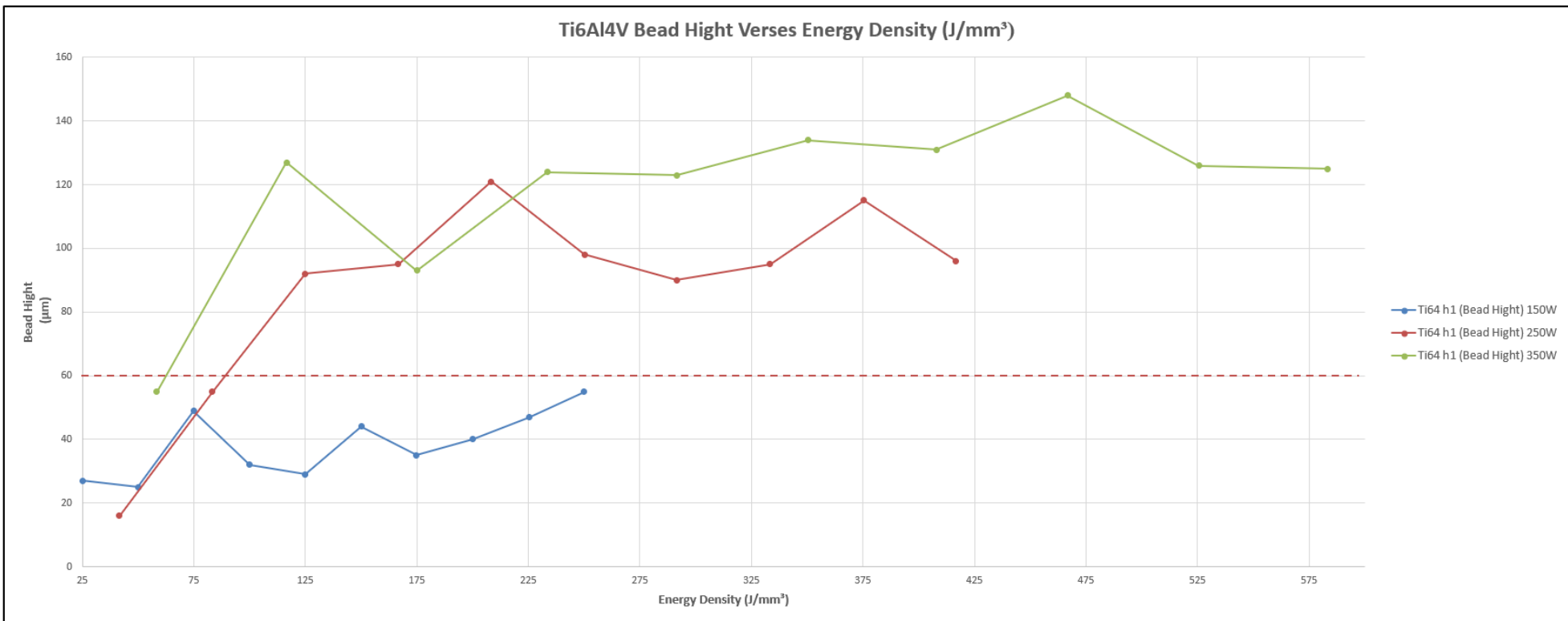


Figure 55 Comparison Between Ti6Al4V Bead Heights ( $h_1$ ) at 150 W, 250 W and 350 W Versus Energy Density

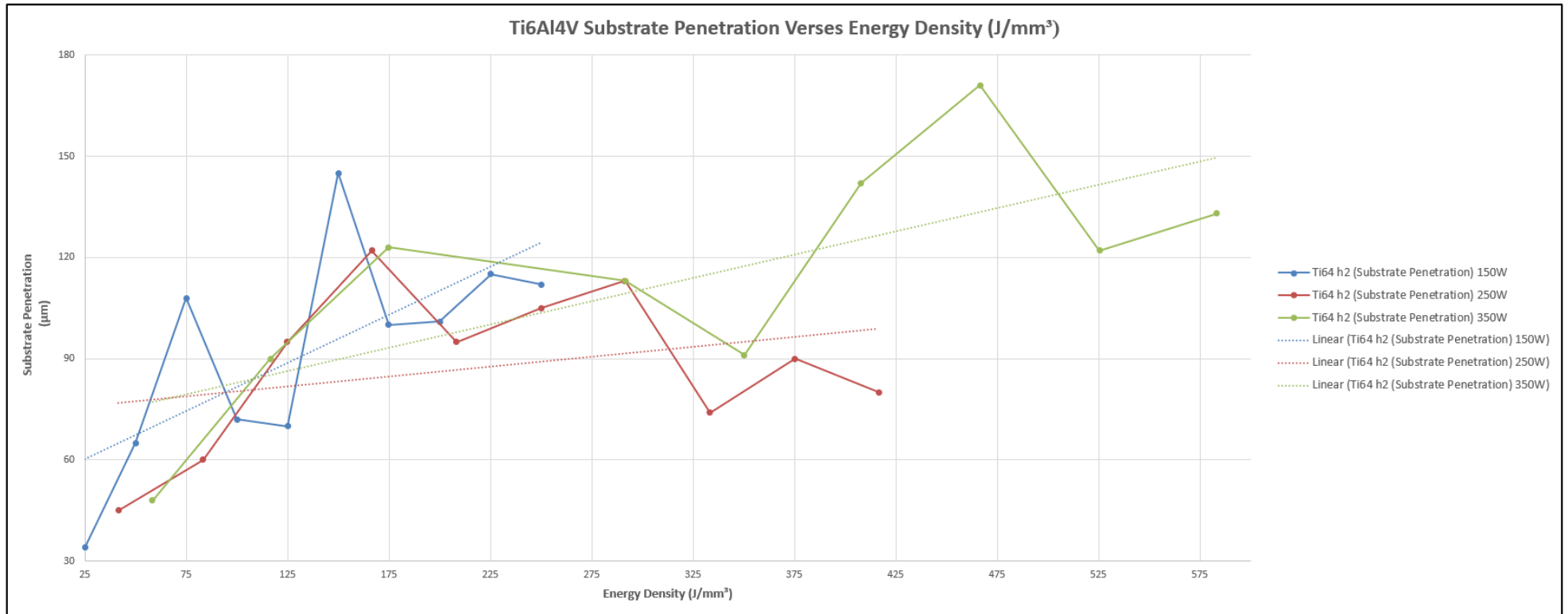


Figure 56 Comparison Between Ti6Al4V Substrate Penetration (*h*<sub>2</sub>) at 150 W, 250 W and 350 W Versus Energy Density

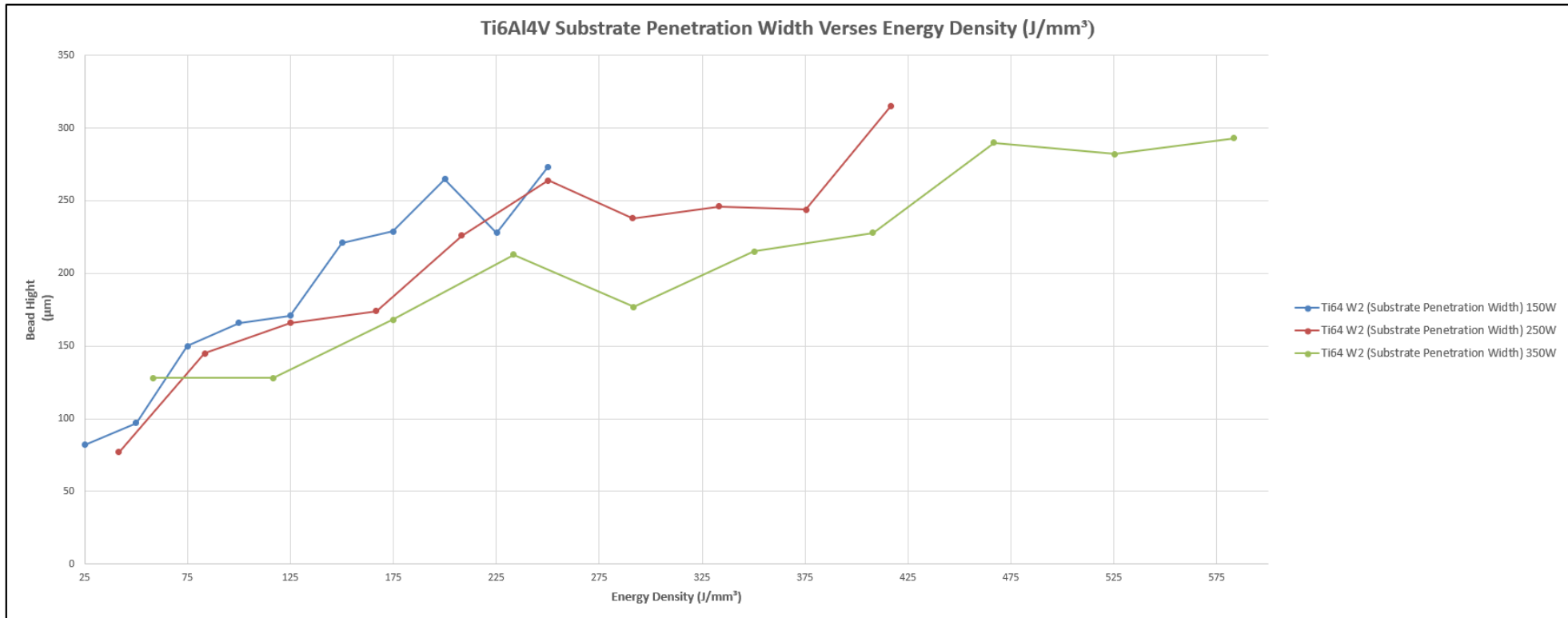


Figure 57 Comparison Between Ti6Al4V Substrate Penetration Width (W2) at 150 W, 250 W and 350 W Versus Energy Density



The values for substrate penetration ( $h_2$ ) shown in Figure 56, were circa 90  $\mu\text{m}$  suggesting that with a laser power of 150 W the energy penetrates the substrate adequately, for a layer thickness of 30  $\mu\text{m}$  this would equate to penetrating approximately three previous layers.

Increasing the laser power to 250 W had no additional effect on substrate penetration with a maximum depth of 122  $\mu\text{m}$  at an energy density of 167  $\text{J}/\text{mm}^3$ . As energy density increased from around 175  $\text{J}/\text{mm}^3$  to 325  $\text{J}/\text{mm}^3$ , the depth of penetration remained between 65  $\mu\text{m}$  and 100  $\mu\text{m}$  deep. This suggested that the increase in energy density was having a greater effect on the surrounding feedstock and not the substrate. This is further supported by a steady increase in bead width ( $w_1$ , Figure 54) and a marginal increase in bead height ( $h_1$ , Figure 55). Similarly, an increase in laser power to 350 W showed a depth of penetration of 122  $\mu\text{m}$  at an energy density of 176  $\text{J}/\text{mm}^3$  with subsequent measurements following the same trend as with a laser power of 250 W up to an energy density of 350  $\text{J}/\text{mm}^3$  where penetration increases to 171.893  $\mu\text{m}$ . Bead height ( $h_1$ ) at these elevated energy densities remain constant, somewhat levelling off whilst bead width ( $w_1$ ) maintained the same upward trend. It is therefore evident that the additional levels of energy do little to consume additional feedstock from the surrounding area, and therefore serve only to further penetrate the substrate.

Regarding the substrate penetration width ( $w_2$ ) (Figure 57) and the width of the bead ( $w_1$ , Figure 54), it was observed that these measurements remained like each other in terms of width but also regarding trend. This suggested that by increasing laser power and therefore energy density, powder consumption around the meltpool and the width of dilution area increased simultaneously suggesting the two were interdependent. With little or no migration of the bead width beyond the dilution area it is evident that the flow of the melt pool is dependent on the molten substrate and is not free to flow across the substrate.

## 5.4 Phase 2a: Mechanically Alloyed MMC Feedstock.

MMC feedstock was mechanically alloyed in accordance with the criteria specified in section 4.4, with the aim to determine the length of mixing time required to embed the reinforcement before altering the morphology of the matrix material. The objectives were:

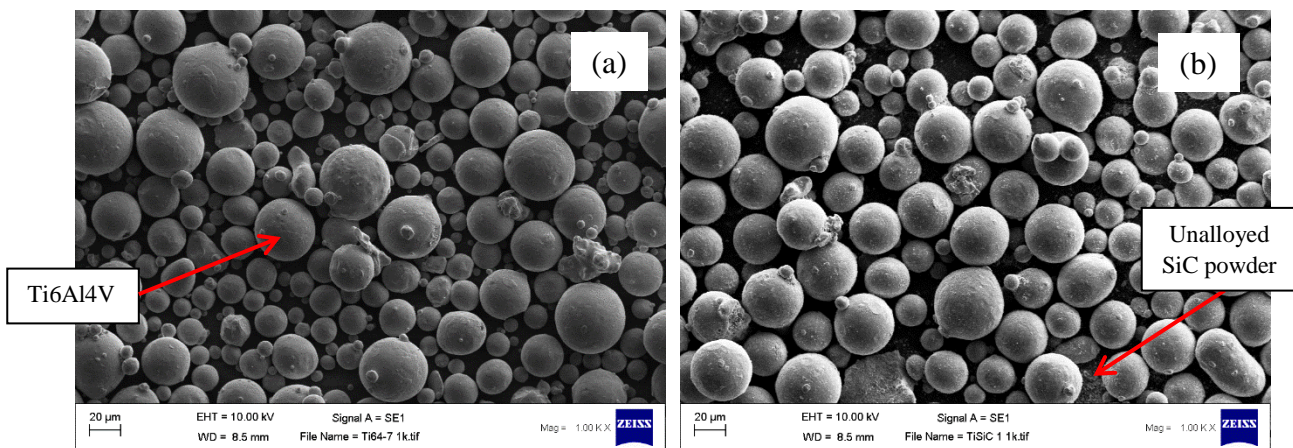
- 1 Reinforcement material embed onto the surface of the matrix material.
- 2 Minimise increase in particle size.
- 3 Minimise change in particle morphology.
- 4 Homogeneously mix the reinforcement material throughout the feedstock.
- 5 Avoid contamination.

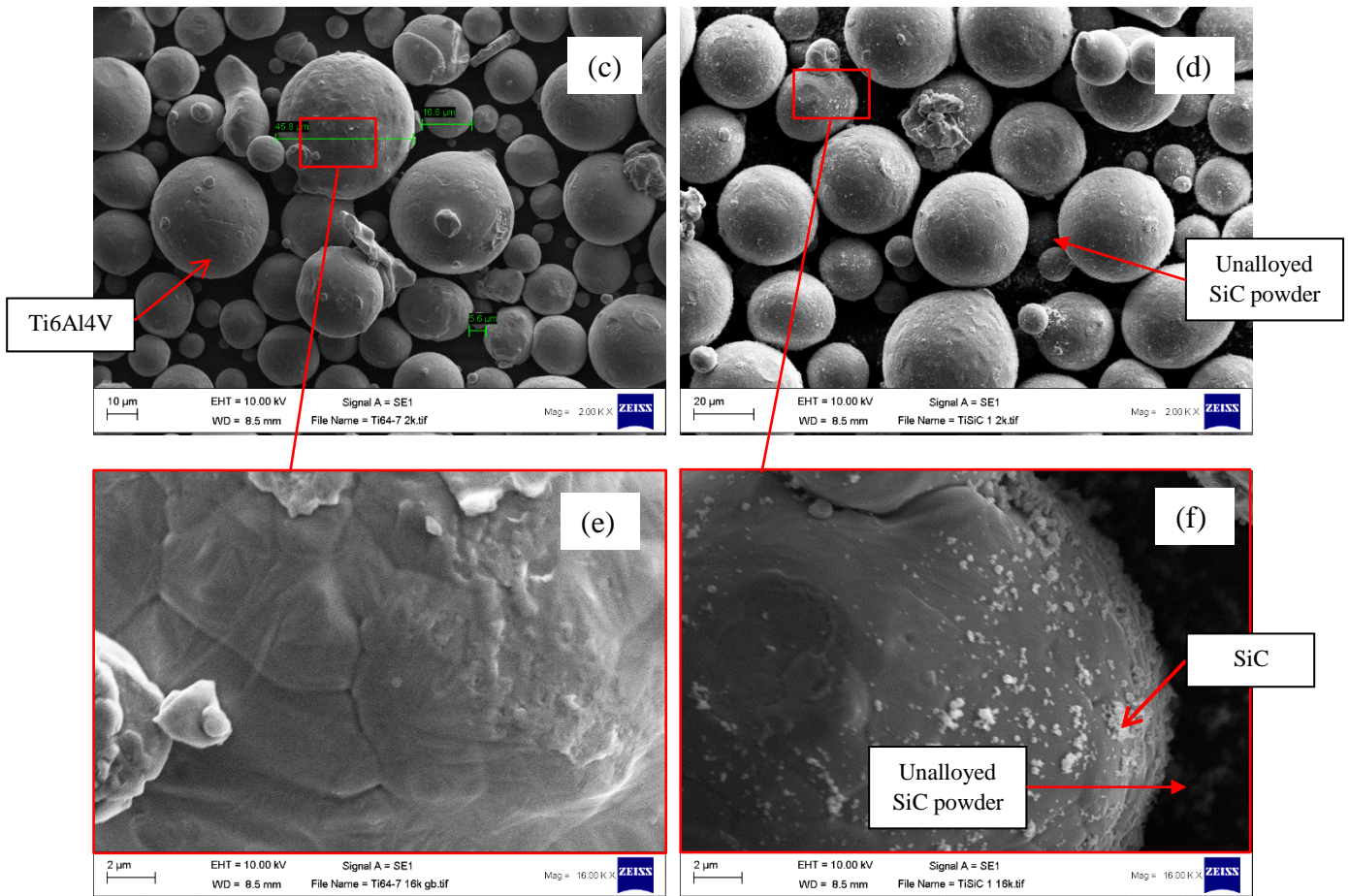
Samples were extracted at 5 min, 8 min, 16 min, 24 min, 32 min, and 40 min intervals for analysis.

### 5.4.1 Reinforcement Material Embed onto the Surface of the Matrix Material.

Using scanning electron microscopy (SEM), images were analysed to determine the extent of surface coverage by the reinforcement and the degree of embedment into the surface of the matrix material in comparison to the non-mechanically alloyed Ti6Al4V material.

Using SEM images of the Ti6Al4V virgin powder for reference, (Figure 58a, c, e), images of the MA powders were compared. At 1,000 x magnification it was observed that a light coating of SiC had been deposited on to the surface of the Ti6Al4V powder particles (Figure 58b). the coverage appeared to be even across all Ti6Al4V particles within the image. However, evidence of unalloyed SiC powder was also visible.





**Figure 58 Comparison between Ti6Al4V Powder (a, c, e) and MA Feedstock (b, d, f) After 5 Minutes at 1,000 X (a, b), 2,000 X (c, d) and 16,000 X Magnification (e, f).**

At 2,000 x magnification (Figure 58d), it was clearer that only partial coverage of the Ti6Al4V powder particles had been achieved. This was further confirmed at 16,000 X magnification (Figure 58f). There was no evidence of changes to the morphology of the matrix particles. There was scope for further processing to increase embedded percentage.

The feedstock was mechanically alloyed for a total of eight minutes and analysed using the SEM. At 2,000 x magnification it was observed that more SiC had coated the surface of the Ti6Al4V powder particles (Figure 59a). It was further observed that the coverage of SiC was not even across all Ti6Al4V particles but appeared to be thicker on some as shown in Figure 59b. However, there was less evidence of unalloyed SiC powder, this indicated that at eight minutes of alloying the there was still a lack of homogeneity within the feedstock.

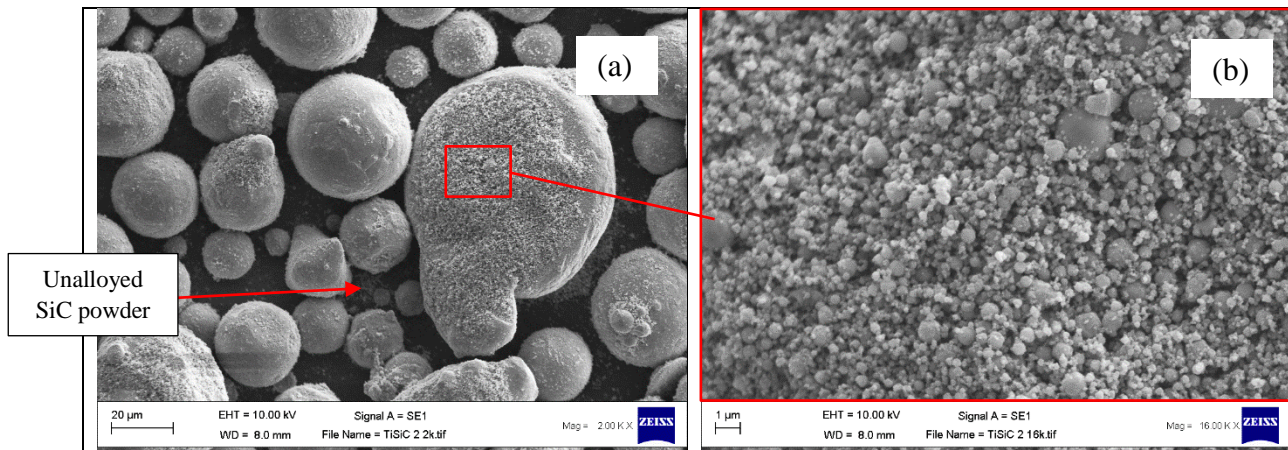


Figure 59 MA Feedstock After 8 Minutes at 2,000 X Magnification (a) and at 16,000 X Magnification (b).

After sixteen minutes of alloying a sample was taken and analysed using SEM. At 2,000 x magnification it was observed that the coating of SiC had become more consistent and uniform on the surface of the Ti6Al4V powder particles (Figure 60a). there appeared to be a moderately high number of rounded particles remaining however, the number of agglomerated particles was now increasing and leading to flattened or flake like particles that could hinder the SLM process.

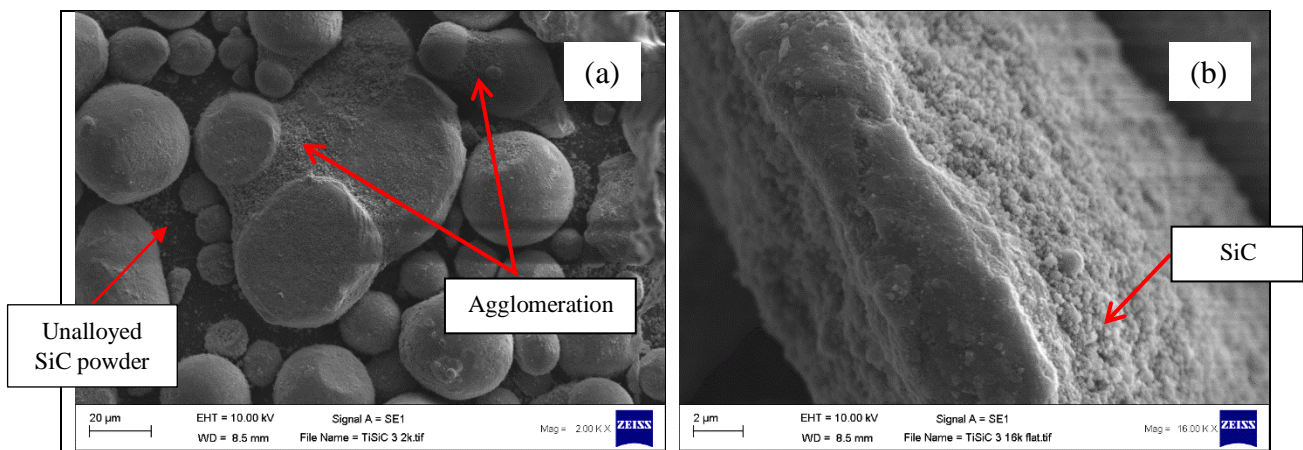


Figure 60 MA Feedstock After 16 Minutes Compared at 2,000 X Magnification (a) and 16,000 X Magnification (b).

At 16,000 x magnification it was observed that the SiC particulates adhered to agglomerated particles around the areas where the two particles had joined. It is thought that the SiC is adhering to coarser surfaces. It was also commonly observed across such areas that the SiC particles are shielded from other larger particles, suggesting that whilst the SiC is coating the Ti6Al4V, it is subsequently being removed by impacts as particles rub together.

Figure 61a and b show the feedstock after twenty-four minutes. At 1,000 x magnification the image shows an even coating of SiC on to the surface of the Ti6Al4V powder particles. Flat or flake like deformed particles were observed along with other irregular shaped particles.

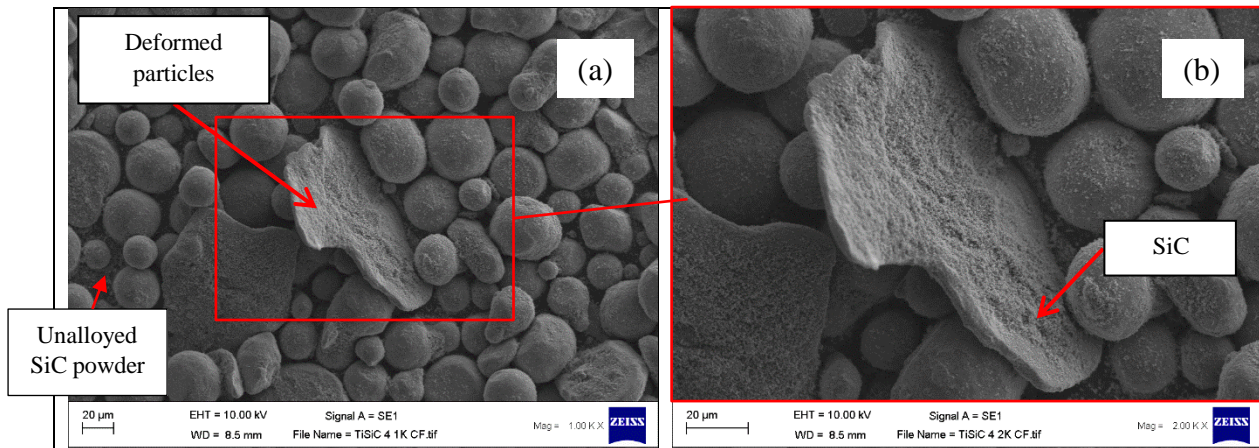


Figure 61 MA Feedstock After 24 Minutes at 1,000 X Magnification (a) and at 2,000 X Magnification (b).

At a magnification of 2,000 x (Figure 61b), it was clearer that a better coverage of the Ti6Al4V powder particles had been achieved. There was no evidence of the SiC preferentially adhering to selective regions of agglomerates, this would indicate that the SiC had better fixation to the Ti6Al4V powder surface. This would provide a higher level of confidence that the SiC would be transported successfully within the SLM process to achieve a homogeneous distribution. At twenty-four minutes of processing, there was good evidence of successful coverage and a lack of excessive deformation.

The process was continued until thirty-two minutes to determine the effects of prolonged alloying. At 1,000 x magnification (Figure 62a), it was observed that the coating of SiC was no better than at twenty-four minutes, there was however, an increase in deformed particles in the form of cylindrical particles, flat discs and flakes.

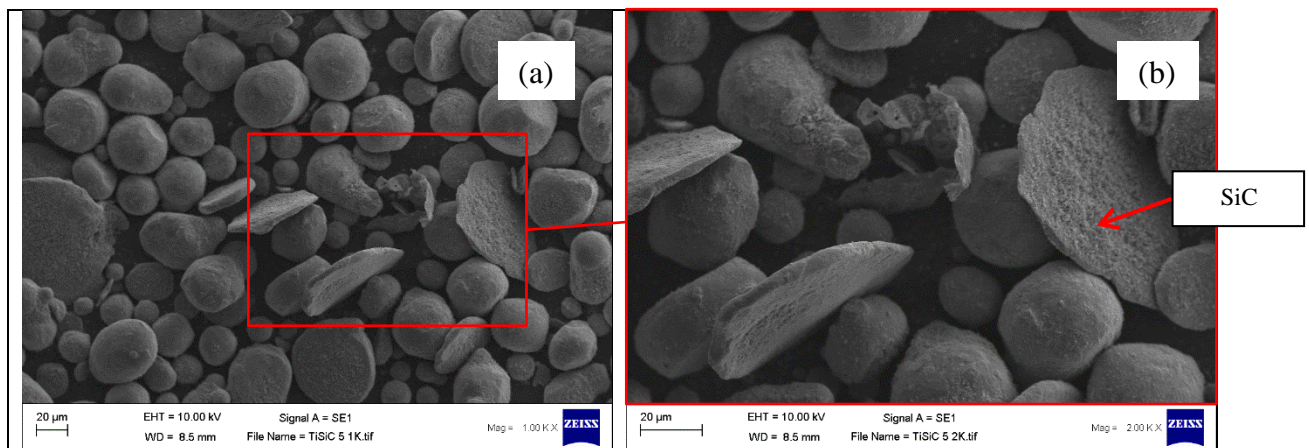
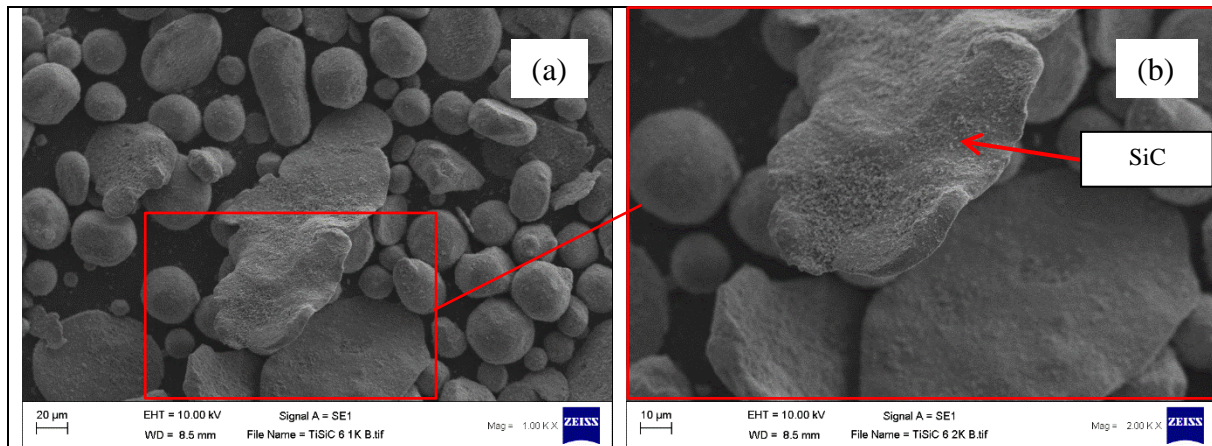


Figure 62 MA Feedstock After 32 Minutes at 1,000 X Magnification (a) and at 2,000 X Magnification (b).

At 2,000 x magnification (Figure 62b), it was clearer that prolonged processing lead to more deformed particles whilst achieving no additional coverage of SiC.

At forty minutes of processing, visual evidence by SEM showed no increase in surface coverage of SiC and continued deformation of particles. At 1,000 x magnification (Figure 63a) it can be observed that the coating of SiC had not changed significantly since the observations taken after twenty-four minutes. The coverage of SiC and the deformed particles can be clearly seen. At 2,000 x magnification (Figure 63b), there is good evidence that there is nothing to be gained by proceeding with further alloying.



**Figure 63** MA Feedstock After 40 Minutes at 1,000 X Magnification (a) and at 2,000 X Magnification (b).

Characterisation of these particles found seven distinct shape characteristics:

1. Rounded,
2. Non-rounded,
3. Cylindrical,
4. Flattened,
5. Agglomerated,
6. Cleaved agglomerated,
7. Flattened agglomerated.

From the optical results, evidence showed that as the mechanical alloying process progressed the morphology of the powder changed. Beginning with simple rounded particles, single impacts produced a non-rounded particle leading to flattened particles. Cylindrical particles were produced where particles were forced to roll in a single direction around the processing chamber, applied forces leading to cylindrical forms being produced.

#### **5.4.1.1 Rounded Particles**

All samples exhibited rounded particles (Figure 64), the degree of roundness across the sample reduced as the powder was processed for longer periods of time.

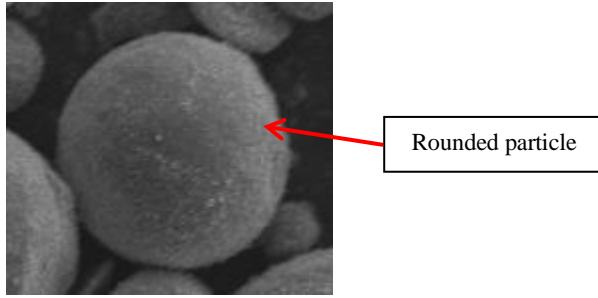


Figure 64 Rounded Powder Particle (SEM 1,000 X Magnification, Thirty-Two Minutes Processing)

#### 5.4.1.2 Non-rounded particles

It was evident that as the processing continues the powder particles are deformed in stages. A single impact produces a small flat area on the particle (Figure 65).

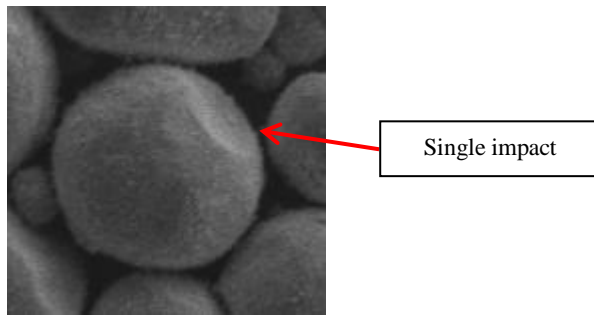


Figure 65 Single Impact on Powder Particle (SEM 1,000 X Magnification, Thirty-Two Minutes Processing)

As these impacts multiply, particles become less rounded or non-rounded leading to become disks or flake-like in appearance.

#### 5.4.1.3 Cylindrical Particles.

Cylindrical particles were characterised as being formed by particles that are forced to travel around the processing chamber walls.

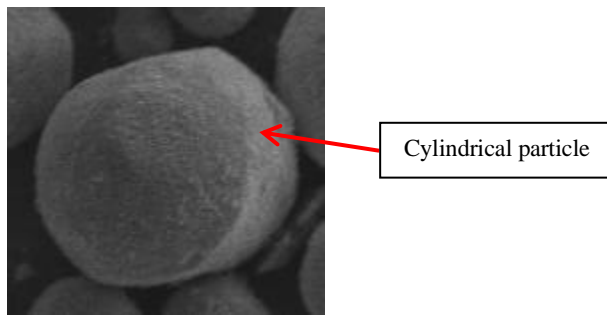


Figure 66 Cylindrical Ti6Al4V Powder Particle (SEM 1,000 X Magnification, Thirty-Two Minutes Processing)

To maintain roundness, particles must adopt a random path with applied force to all areas of the particles surface, however, due to the configuration of the Zoz Simoloyer CM01, this is not possible for short processing times. Within the grinding chamber, the rotor shaft does not reach to the inside surface of the chamber, therefore a proportion of the powder batch can form a

moving layer around the chamber wall held in place by the bulk of the powder being processed and the processing balls. This unidirectional path can produce cylindrically shaped particles (Figure 67). Prolonged processing would make this phenomenon worse. It is suggested that a short five second pauses in the process may help to randomise the chamber contents and reduce the number of cylindrical particles, this could also be achieved by changing the direction.

It is also important to note that a relatively low rotor shaft speed of 500 rev/min was selected in order to minimise centrifugal forces and reduce the likelihood of producing cylindrical particles. This is in line with previous research (Olowofela, et al., 2013 and Lyall, et al., 2015) which concluded that 500 rev/min was the maximum rotor shaft speed capable of maintaining spheroids.

#### 5.4.1.4 Flattened Particles.

The production of flatten particles marked a significant point in the mechanical alloying process. At this point, particles had been produced that would not flow within the SLM process and furthermore would not pack optimally on the powder bed. The flattened particles are produced as a result of high levels of impacts from the milling balls and a direct result of prolonged processing times.

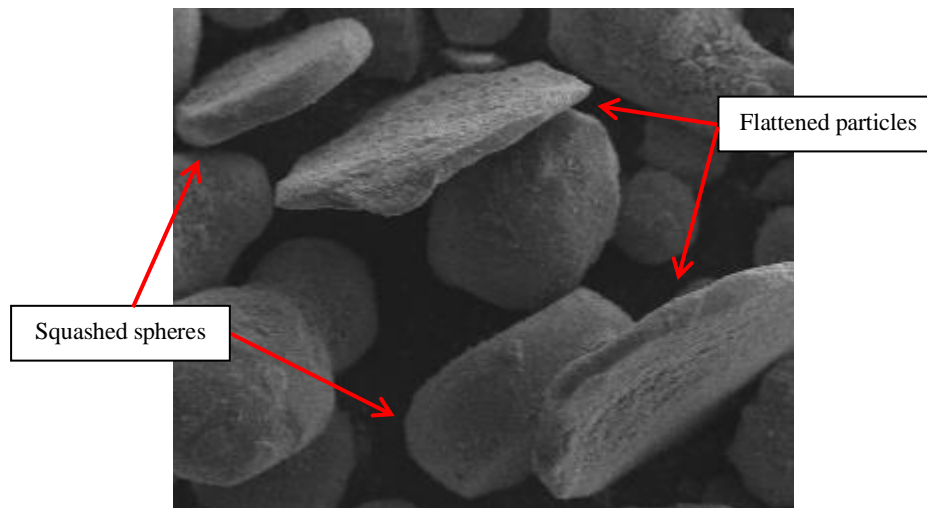


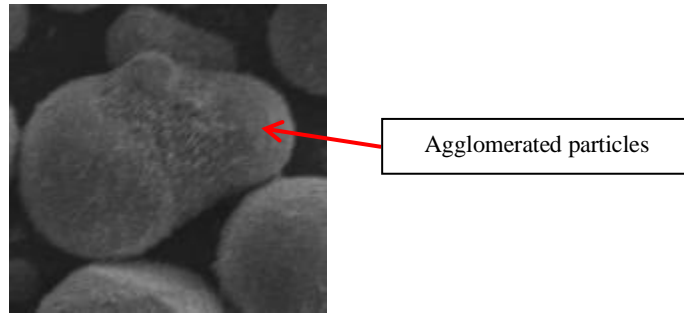
Figure 67 Flattened Powder Particle (SEM 1,000 X Magnification, Thirty-Two Minutes Processing)

Figure 67 shows flattened particles after thirty-two minutes of processing. The particles inability to rotate within the chamber in combination with multiple impacts, firstly produced a squashed sphere, leading to flattened particles.

#### 5.4.1.5 Agglomerated Particles.

There was a lower than expected level of agglomerated particles. It is thought that as the Ti6Al4V particles become coated with SiC and two particles are forced together, the SiC coating prevents them from adhering to each other and a flat surface is produced on the particles instead, evident in Figure 65.



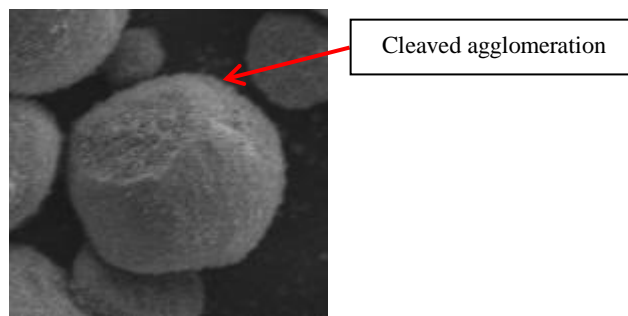


**Figure 68 Agglomerated Powder Particles (SEM 1,000 X Magnification, Thirty-Two Minutes Processing)**

Figure 68 shows agglomerated particles joined prior to being coated with SiC, it is evident for samples taken at sixteen minutes processing time, that the thinner necked region of the agglomeration protected the SiC reinforcement material from being subsequently wiped from the surface by other particles.

#### **5.4.1.6 Cleaved Agglomerated Particles.**

Possible fracture surfaces were also observed (Figure 69) on some particles indicating areas where particles had been cleaved apart

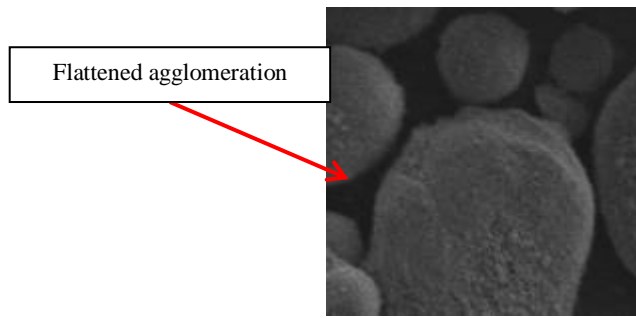


**Figure 69 Cleaved Agglomerated Powder Particle (SEM 1,000 X Magnification, Thirty-Two Minutes Processing)**

This indicated that particles that had become united earlier in the processing time had become detached as a result of prolonged processing.

#### **5.4.1.7 Flattened Agglomerated Particles.**

Evidence was also shown of agglomerated particles that had subsequently become flattened due to the prolonged processing time. In Figure 70 it can be seen where two additional particles of Ti6Al4V have combined to an existing particle and have subsequently become flattened over prolonged processing time.



**Figure 70** Flattened Agglomerated Ti6Al4V Powder Particle (SEM 1,000 X Magnification, Thirty-Two Minutes Processing)

In conclusion, from a microscopic investigational point of view, this evidence reinforces the decision that a processing time of twenty-four minutes was adequate to embed the reinforcement material into the surface of the matrix material without excessive damage to the morphology of the matrix material. Sieving was considered as a possible solution to the removal of large particles from the feedstock however, evidence showed that these became prevalent only after twenty-four minutes of processing and should the process be halted at this time, the risk of large particles would be minimised.

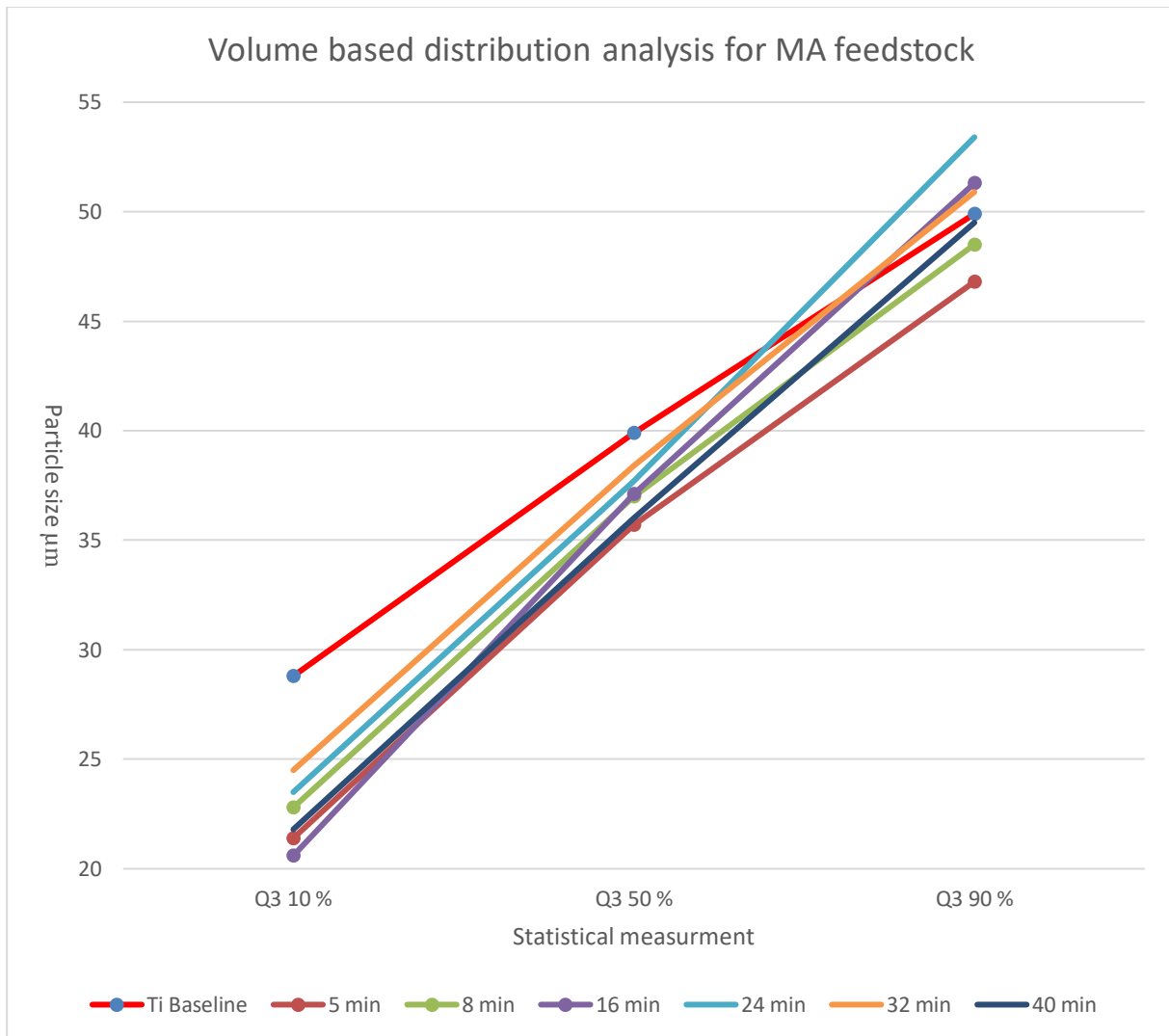
#### 5.4.2 Minimise Increase in Particle Size.

To determine the effect of time on particle size from the mechanical alloying process, samples taken at regular intervals were analysed using a Retsch Camsizer X2. Table 32 shows results for  $X_c$  min measurements calculated for Q3 10%, Q3 50% and Q3 90% with the sample mean represented by  $Mv3(\bar{x})$ . samples were also analysed for aspect ratio (Mean b/l3) to determine whether this increased over time, indicating a loss of roundness.

**Table 32** Volume Based Distribution Analysis Comparison for MA Feedstock

| Statistical measurement | Baseline result<br>( $X_c$ min) | MA feedstock<br>5 min<br>( $X_c$ min) | MA feedstock<br>8 min<br>( $X_c$ min) | MA feedstock<br>16 min<br>( $X_c$ min) | MA feedstock<br>24 min<br>( $X_c$ min) | MA feedstock<br>32 min<br>( $X_c$ min) | MA feedstock<br>40 min<br>( $X_c$ min) |
|-------------------------|---------------------------------|---------------------------------------|---------------------------------------|----------------------------------------|----------------------------------------|----------------------------------------|----------------------------------------|
| Q3 10%                  | 28.8 $\mu\text{m}$              | 21.4 $\mu\text{m}$                    | 22.8 $\mu\text{m}$                    | 20.6 $\mu\text{m}$                     | 23.5 $\mu\text{m}$                     | 24.5 $\mu\text{m}$                     | 21.8 $\mu\text{m}$                     |
| Q3 50%                  | 39.9 $\mu\text{m}$              | 35.7 $\mu\text{m}$                    | 37.0 $\mu\text{m}$                    | 37.1 $\mu\text{m}$                     | 37.7 $\mu\text{m}$                     | 38.4 $\mu\text{m}$                     | 36.0 $\mu\text{m}$                     |
| Q3 90%                  | 49.9 $\mu\text{m}$              | 46.8 $\mu\text{m}$                    | 48.5 $\mu\text{m}$                    | 51.3 $\mu\text{m}$                     | 53.4 $\mu\text{m}$                     | 50.9 $\mu\text{m}$                     | 49.5 $\mu\text{m}$                     |
| $Mv3(\bar{x})$          | 39.7 $\mu\text{m}$              | 35.0 $\mu\text{m}$                    | 36.6 $\mu\text{m}$                    | 38.2 $\mu\text{m}$                     | 39.7 $\mu\text{m}$                     | 39.1 $\mu\text{m}$                     | 38.5 $\mu\text{m}$                     |
| Mean b/l3               | 0.851 $\mathcal{R}$             | 0.870 $\mathcal{R}$                   | 0.859 $\mathcal{R}$                   | 0.838 $\mathcal{R}$                    | 0.819 $\mathcal{R}$                    | 0.807 $\mathcal{R}$                    | 0.825 $\mathcal{R}$                    |

The results from Table 32 were collated as a graph shown in Figure 71.



**Figure 71 Volume Based Distribution Analysis for  $X_c$  Min, MA Feedstock**

It was observed from Figure 71 that the MA samples all demonstrated similar values for Q3 10%, all being less than the Ti6Al4V baseline sample, showing average particle sizes between 21.4 µm and 24.5 µm as opposed to 28.8 µm for the Ti6Al4V baseline sample. This would indicate a smaller particle size overall, indicative of non-alloyed SiC powder present within the experiment.

Whilst this is also true of the results for 16 minutes, the Q3 90% value is increasing above that of the Ti6Al4V baseline result, indicating an increased volume of larger particles. This would, therefore, indicate that whilst there appears to be no loss of small fines, the larger fines are increasing in size due to being coated with SiC. It has been established that the Retsch Camsizer X2 has difficulty measuring submicron particles and therefore, even though the volume percentage of small particles remains unchanged the Ti6Al4V is being coated. At 24 minutes the results indicate that the maximum amount of coating has been reached, further experimentation for 32 minutes and 40 minutes showed a decrease in the values for Q3 90% indicating that no further coating is being applied.

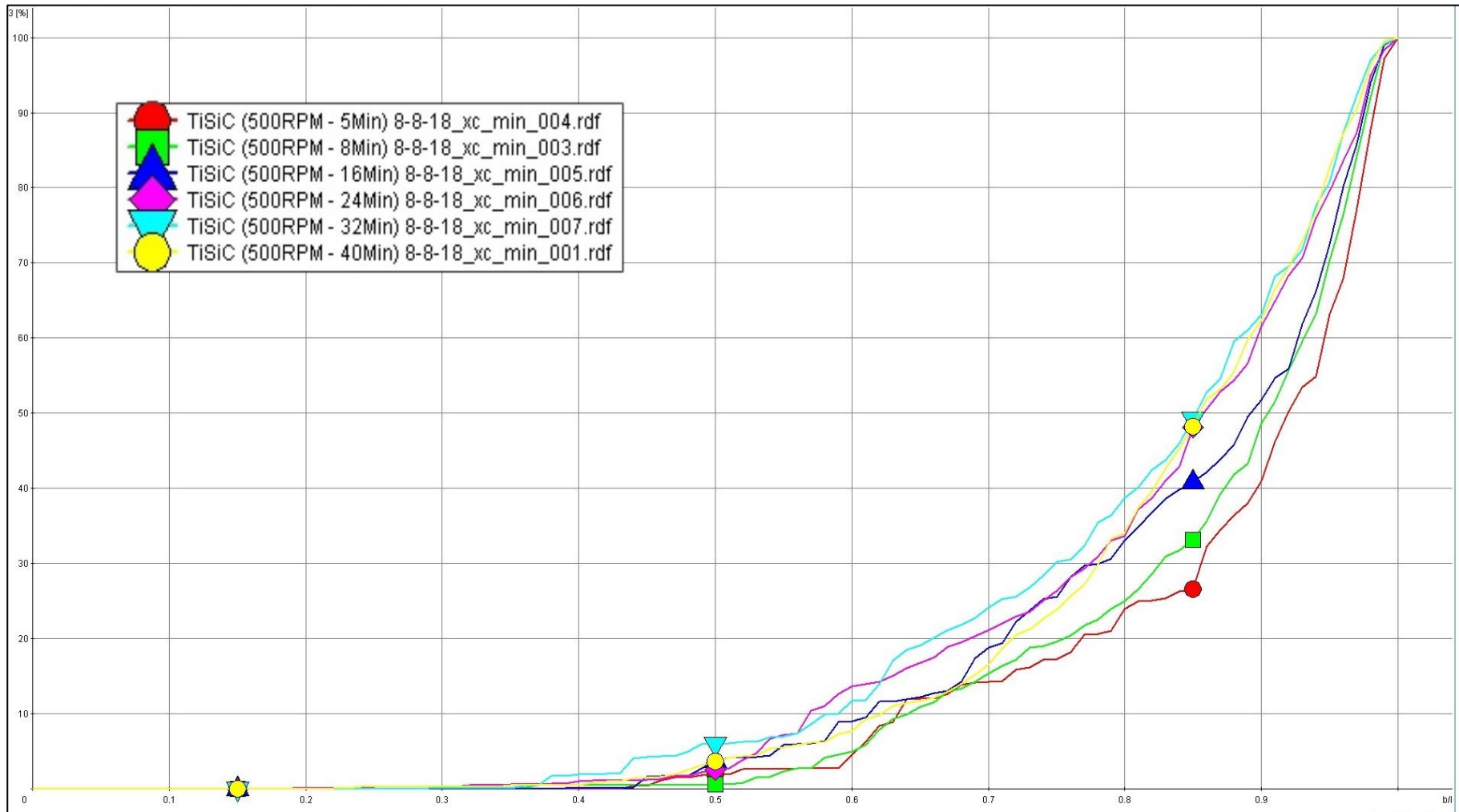


Figure 72 Volume Based Comparison of Aspect Ratio (b/l) For Mechanically Alloyed Feedstock

Figure 72 further reinforces this by demonstrating a steady decrease in the percentage of particles exhibiting an aspect ratio better than 0.850  $\mathcal{R}$ . After the first five minutes of alloying 73.341% of the sample was better than 0.850  $\mathcal{R}$ , after eight minutes this reduced to 66.871%, after sixteen minutes it reduced to 59.083% and at twenty-four minutes only 50.816% of the sample has an aspect ratio better than 0.850  $\mathcal{R}$ . Further MA for thirty-two (50.816%) and forty minutes (51.894%) had no further effect. Based on this evidence, an alloying duration of 24 minutes was chosen to be an optimal duration for alloying.

### 5.4.3 Minimise Change in Particles Morphology.

It has been established that by using the Retch Camsizer X2 and by analysing changes in morphology as a function of aspect ratio, morphological changes increased over the time of the experiment. As the Camsizer X2 uses photogrammetry to determine morphological characteristics within the sample it can be open to inaccuracies due to the interpretation of the captured image. Using the Retch image analysis software, it was possible, using the database search tools, to filter out anomalous readings for manual inspection. Using the criteria:  $X_{C \text{ Min}} \geq 0.010$  mm to remove images of particles smaller than ten microns,  $b/l \leq 0.600$  to display images with an aspect ratio that would be far removed from the roundness acceptance limit of 0.850  $\mathcal{R}$  in order to select particles with the worst aspect ratio and a Trans value of  $\geq 0.100$  to eliminate blurred or out of focus images. All samples were evaluated with these criteria individually and a selection of the results for each are presented.

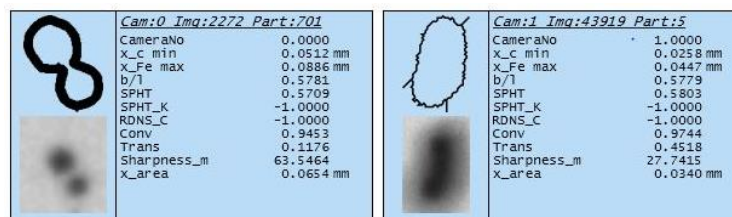


Figure 73 Mechanical Alloying Ti6Al4V - SiC (5 Min)

Figure 73 shows image database results for powder alloyed for five minutes. The image on the left shows a particle with a size of 0.0512 mm whilst the particle to the right is half the size at 0.0258 mm, both would be acceptable. Regarding aspect ratio, both values are comparable at 0.5781  $\mathcal{R}$  and 0.5779  $\mathcal{R}$  respectively, there is a clear difference when viewing the images. To the right the image is elongated and could well be a single particle or small agglomeration, the image to the left, however, shows two particles that on close inspection demonstrate individual roundedness. By using the aspect ratio term within the search criteria, it was possible to gather such images for closer inspection and whilst this data cannot be removed from the sample set and therefore remains part of the results, it assists in better understanding the images used and gain confidence in the results presented. At five minutes of alloying the search showed very few anomalous images, as was expected.

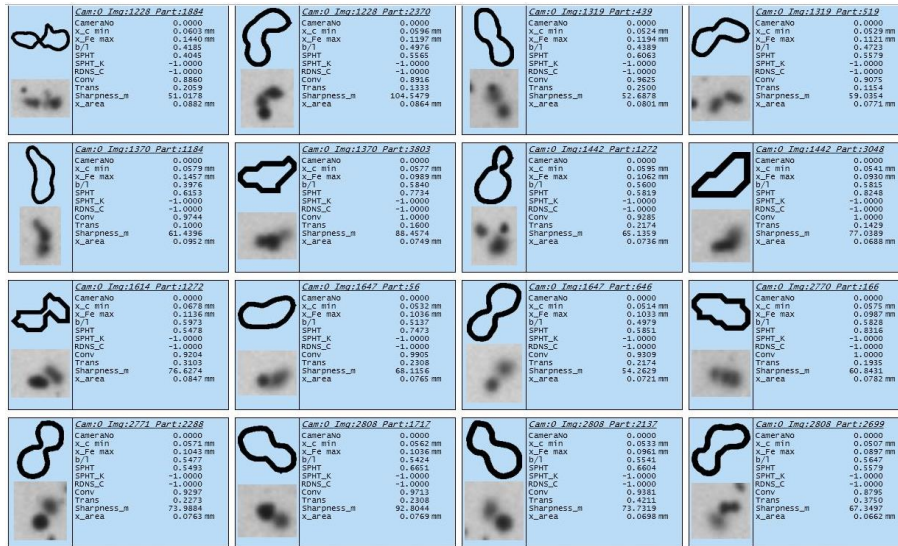


Figure 74 Mechanical Alloying Ti6Al4V - SiC (8 Min)

After eight minutes, the search found a larger number of images fitting the criteria, Figure 74. On closer inspection of the images, again, most images are comprised of individual particle that have been captured on the same image giving rise to the result that this is an image of a large misshapen particle. Where images show multiple particles with varying sharpness to the outer edges, this would clearly indicate that the sharper particle is closer to the focal point than the other and therefore not connected. Of the sixteen images shown, all can be described as multiple particles sharing the same image. This would indicate that there is a high level of confidence in the particles still being rounded after eight minutes.

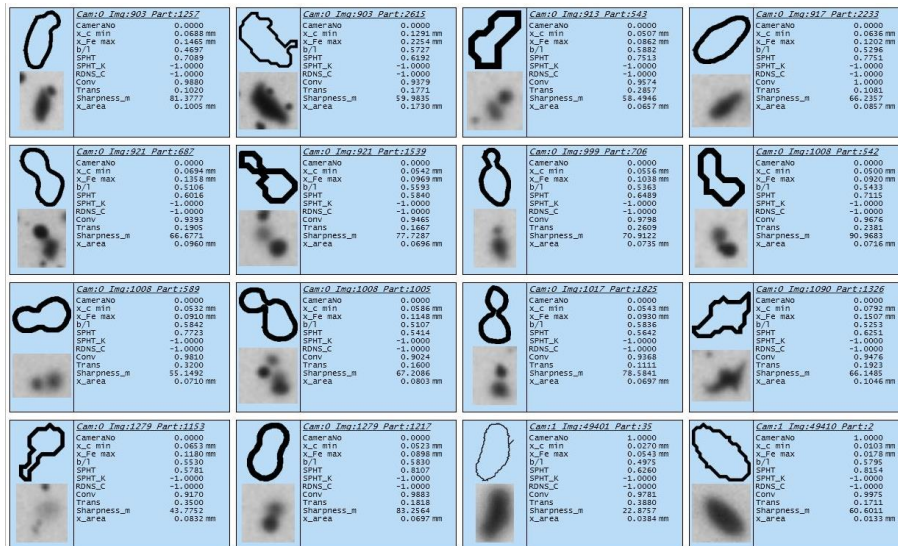


Figure 75 Mechanical Alloying Ti6Al4V - SiC (16 Min)

At sixteen minutes (Figure 75), this characteristic continued with most images found, displaying multiple particles that had been interpreted as a single particle. However, out of the sixteen images above, six images showed particle that are either not round or agglomerations. Part 1257 shows a particle with an Xc min value of 0.0688 mm, as this constitutes a particle

larger than the parent materials, this would be considered an agglomeration. This could also be the case for part 2233. Parts 2, and 35 are smaller particles that appear to be individual but nonrounded.

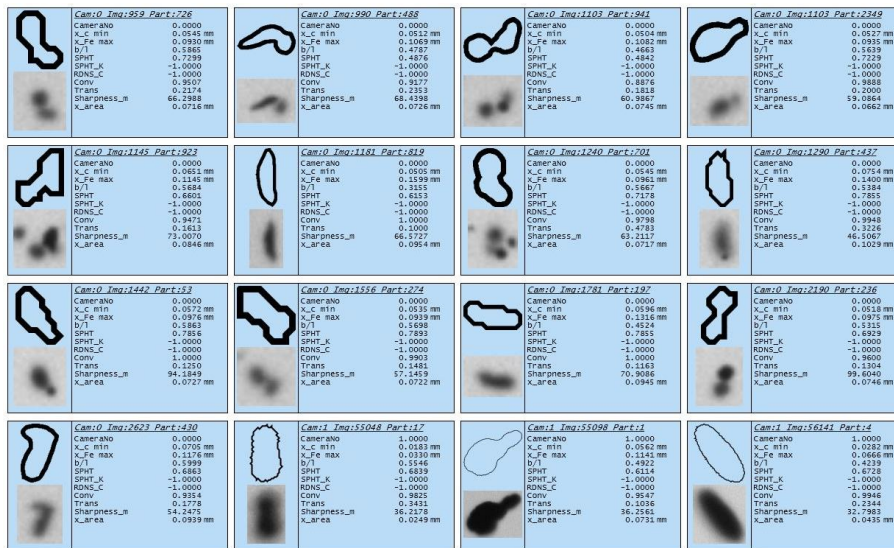


Figure 76 Mechanical Alloying Ti6Al4V - SiC (24 Min)

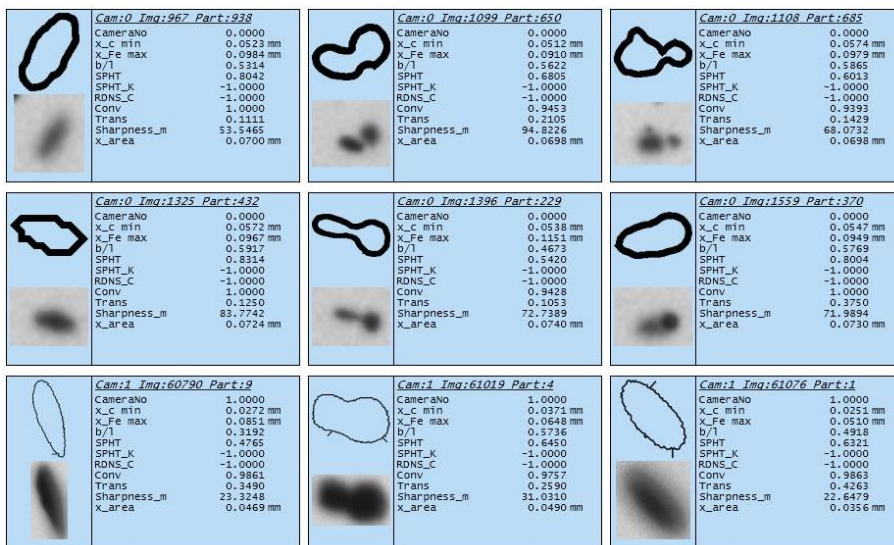


Figure 77 Mechanical Alloying Ti6Al4V - SiC (32 Min)

At twenty-four minutes (Figure 76) and at thirty-two minutes (Figure 77), the images demonstrate similar characteristics with a mixture of coexistent particles within images, agglomerations and genuine nonrounded particles. Based on the minimal return in search results, there was no evidence to give uncertainty in the graphical results. This was also true for samples taken after forty minutes of alloying (Figure 78).

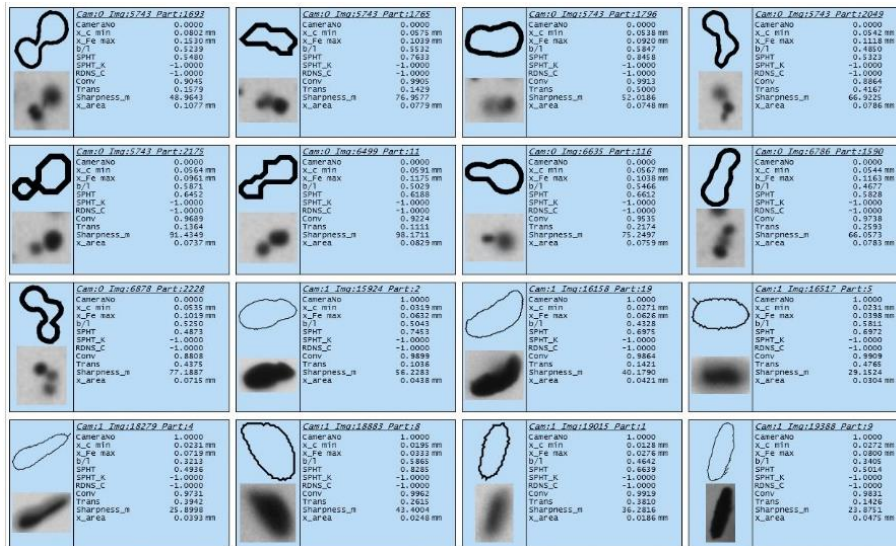


Figure 78 Mechanical Alloying Ti6Al4V - SiC (40 Min)

In applying these search criteria across all samples, very few anomalous results were returned, demonstrating that the data presented in graphical form is reliable and that changes in particle morphology were successfully kept to a minimum.

#### 5.4.4 Homogeneously Mix the Reinforcement Material Throughout the Feedstock.

Not only was it important to achieve homogeneity of the SiC throughout the MA feedstock but also to determine whether the SiC had adhered to the surface of the Ti6Al4V powder. Where SiC had not adhered to the Ti6Al4V powder this would be evidenced by a higher concentration of small fines when graphically representing size distribution. As the smaller particles become combined with the larger Ti6Al4V particles the curve was expected to shift to the right due to an increase in size. This effect was also evident in Table 32 and Figure 71 where the slope of the plots changed due to processing time, showing that as the smaller particles are combining with the larger, values for D10 reduce and values for D90 increase for samples taken at sixteen minutes and after. Images of the alloyed feedstock (Section 5.3.1), also add supporting evidence in the form of unalloyed SiC powder visible in images taken after five minutes (Figure 58b) eight minutes (Figure 59a), sixteen minutes (Figure 60a) and twenty-four minutes (Figure 61a). Unalloyed SiC is not visible however, within SEM images taken after thirty-two minutes (Figure 62) and forty minutes (Figure 63). It was therefore concluded that at twenty-four minutes of MA, the SiC particles had homogeneously combined with the Ti6Al4V particles.

#### 5.4.5 Avoid Contamination.

A major consideration throughout the MA processing was the risk of contamination from materials liberated from the processing apparatus and oxygen from processing atmosphere.

Regarding the liberation of materials from the chamber walls, alloying balls and rotor shaft, the rotor shaft was inspected for loose fragments of metal liable to fragment during processing and was cleaned thoroughly as were the chamber and alloying balls.



Furthermore, to ensure that the atmosphere was free from oxygen whilst processing, the parent materials were stored in a non-humid atmosphere at room temperature. Prior to processing the chamber was purged of Air under vacuum and the atmosphere was replaced with Argon gas and the contents of the chamber was rotated at 100 rev/min to agitate and remove trapped Air. The atmosphere was again removed under vacuum and replaced with Argon before starting the process (see appendix 1).

Analysis for contamination was carried out on specimens manufactured from the successfully MA feedstock and standard Ti6Al4V for comparison. Samples were removed from the build platform using wire EDM, mounted in Struers ConduFast conductive acrylic resin and polished in accordance with Struers titanium alloys DiaPro application notes (Appendix 2). EDS (Energy Dispersive X-Ray Spectroscopy), was conducted using a voltage range of 0 KeV to 10 KeV. Regions of interest (ROI) were analysed using both area and spot analysis. The optimisation element used for calibration was Cobalt (Co).

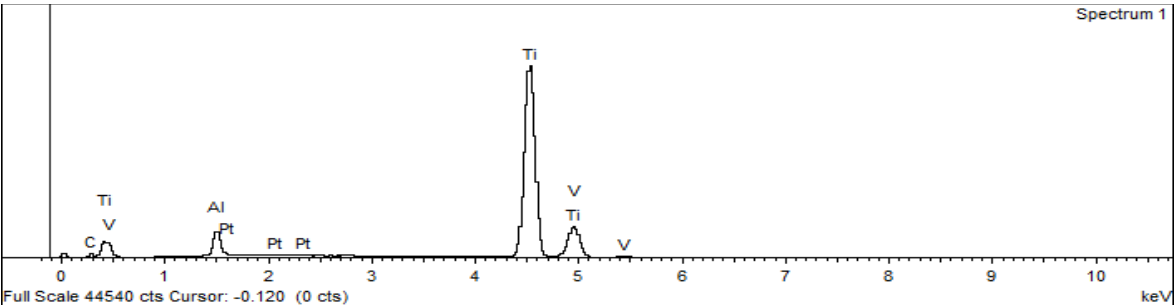
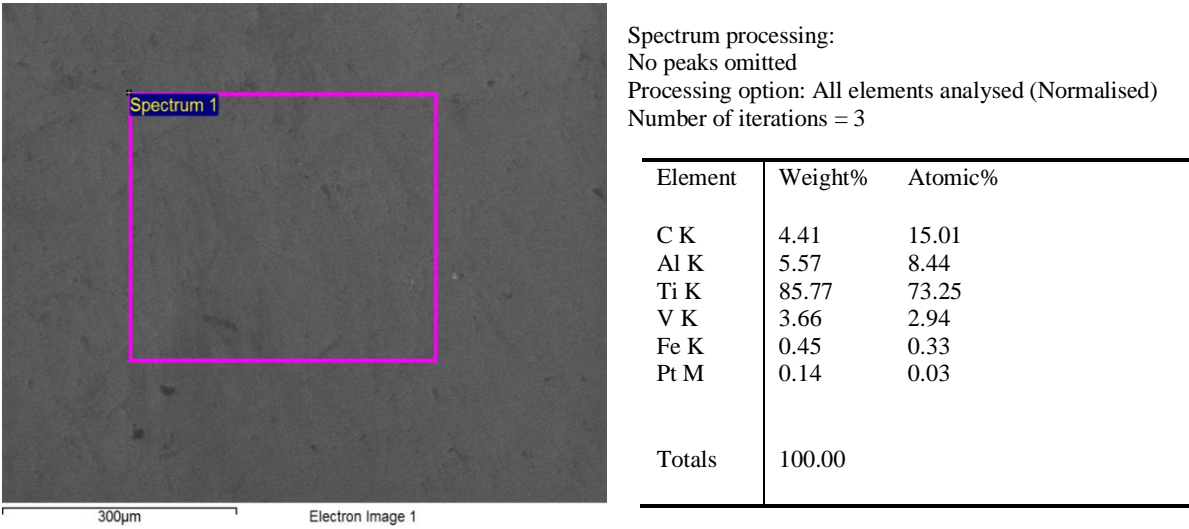


Figure 79 EDS Area Analysis of Ti6Al4V Sample1, Sectioned Horizontally

Figure 79 shows an area analysis carried out on Ti6Al4V produced using standard parameters on an EOS M290 machine. The sample was produced using standard material and has not been MA, and therefore should not show evidence of contamination. The surface being analysed was in the horizontal orientation. Values for aluminium (Al) and vanadium (V) were typically around that expected with Al being 5.57 Wt.% (6.0) and V being 3.66 Wt.% (4.0) fractionally above the minimum value of 3.50 Wt.%. The bulk of the remaining elements being titanium

(Ti) at 85.77 Wt.%. Carbon (C) was also found to be present at 4.41 Wt.% along with traces of Iron (Fe), 0.45 Wt.% and Platinum (Pt), 0.14 Wt.%.

Elements of concern include C, Fe and Pt. The technical data sheet provided by EOS GmbH (Table 2) quantifies C to be a maximum of 0.080 Wt.% therefore a value of 4.41 Wt.% is unusual and would require further investigation to eliminate the source. At this stage it was classed as contamination. Quantities of Fe at 0.45 Wt.% were approximately twice that described in the technical data sheet (max 0.250 Wt.%) and Pt was an unexpected element and therefore classed as contamination.

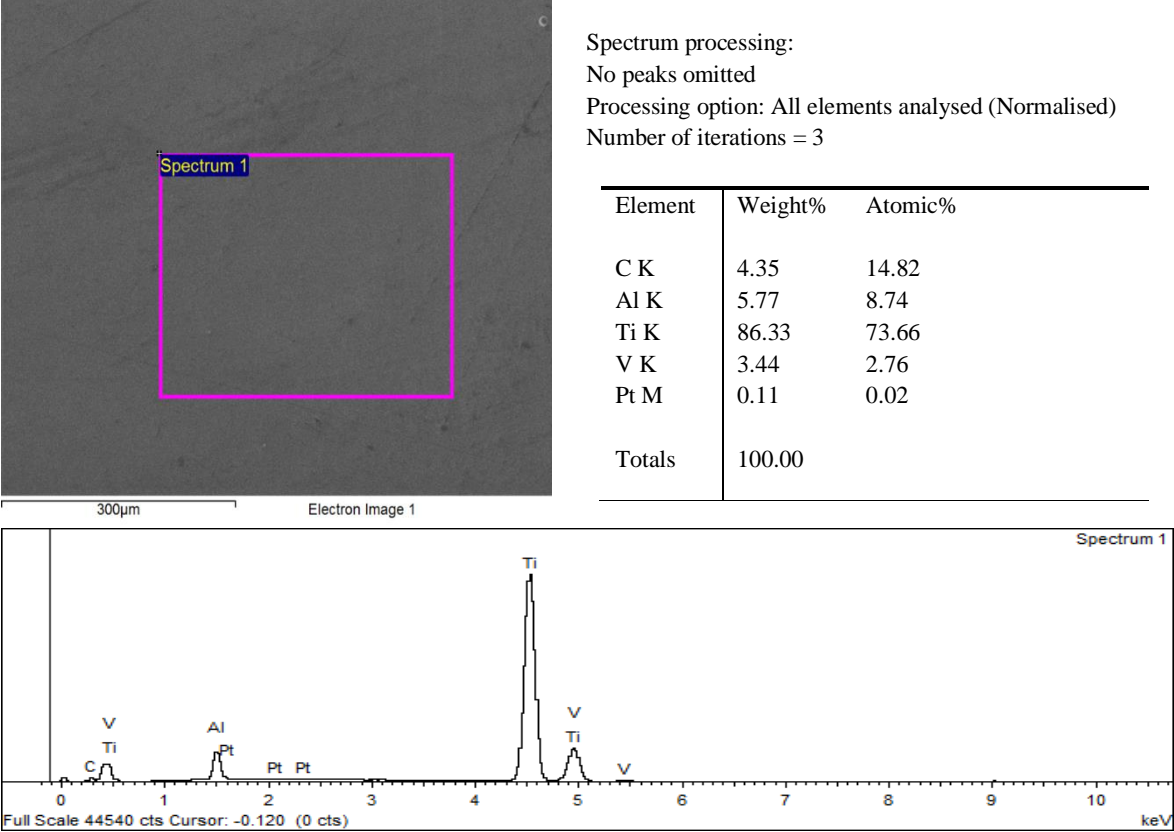
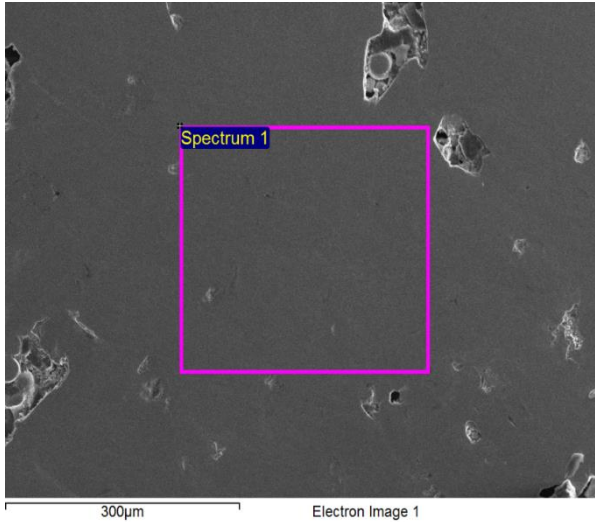


Figure 80 EDS Area Analysis of Ti6Al4V Sample 2, Sectioned Vertically

In Figure 80 a sample of Ti6Al4V produced using standard parameters on an EOS M290 machine was sectioned in the vertical plane, mounted and polished. Results compared favourably with Figure 79 with the omission of Fe.



Spectrum processing:  
Peak possibly omitted: 6.411 keV

Processing option: All elements analysed (Normalised)  
Number of iterations = 3

| Element | Weight% | Atomic% |
|---------|---------|---------|
| C K     | 5.63    | 18.28   |
| Al K    | 5.55    | 8.01    |
| Si K    | 2.80    | 3.88    |
| Ti K    | 82.83   | 67.41   |
| V K     | 3.16    | 2.42    |
| Pt M    | 0.04    | 0.01    |
| Totals  | 100.00  |         |

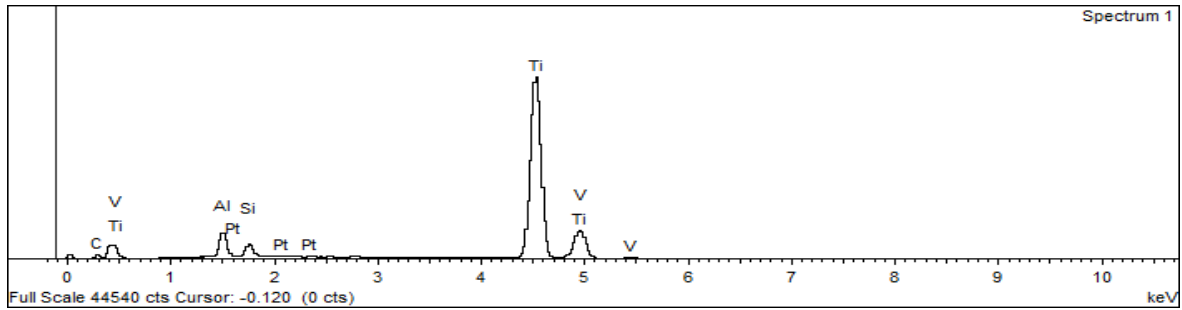
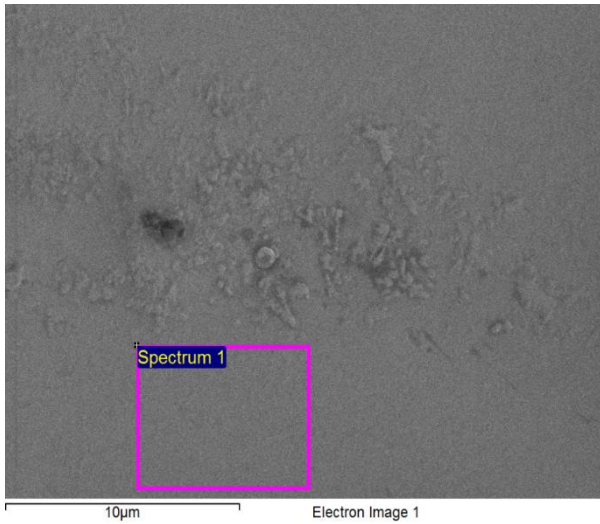


Figure 81 EDS Area 1 Analysis of MMC Sample 3, Sectioned Horizontally

Figure 81 shows an area analysis carried out on MA MMC sample produced on an EOS M290 machine. The surface being analysed was sectioned horizontally. The ROI selected was such that it showed little evidence of SiC present and bore much resemblance to that of Ti6Al4V. Values were comparable with Figure 79 and Figure 80 with the addition of Silicone (Si), 2.80 Wt.%. There was an increase also in C, 5.63 Wt.% and a decrease in Pt, 0.04 Wt.%. The detection of Si and C indicating the presence of SiC

At higher magnification, Figure 82 shows a ROI near SiC deposits. Results are again comparable to Figure 81.



Spectrum processing:  
No peaks omitted

Processing option: All elements analysed (Normalised)  
Number of iterations = 3

| Element | Weight% | Atomic% |
|---------|---------|---------|
| C K     | 4.81    | 15.93   |
| Al K    | 6.08    | 8.95    |
| Si K    | 2.40    | 3.40    |
| Ti K    | 83.06   | 68.91   |
| V K     | 3.33    | 2.60    |
| Fe K    | 0.29    | 0.21    |
| Pt M    | 0.02    | 0.00    |
| Totals  | 100.00  |         |

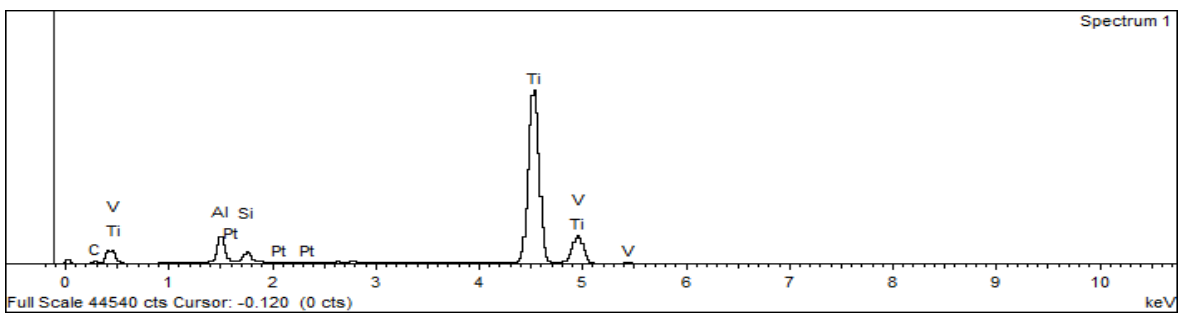


Figure 82 EDS Area 2 Analysis of MMC Sample 3, Sectioned Horizontally



Spectrum processing:  
Peaks possibly omitted: 2.780, 6.432, 9.026 keV

Processing option: All elements analysed (Normalised)  
Number of iterations = 3

| Element | Weight% | Atomic% |
|---------|---------|---------|
| C K     | 8.97    | 26.59   |
| Al K    | 4.38    | 5.78    |
| Si K    | 6.34    | 8.04    |
| Ti K    | 77.19   | 57.41   |
| V K     | 3.12    | 2.18    |
| Totals  | 100.00  |         |

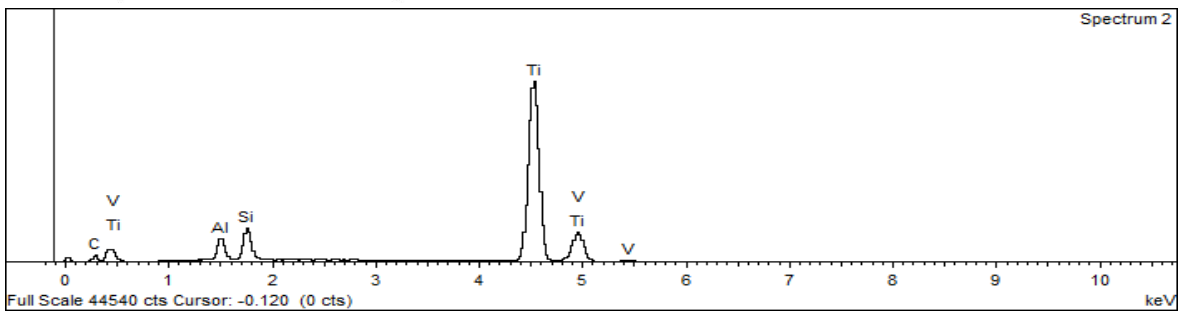


Figure 83 EDS Area 3 Analysis of MMC Sample 3, Sectioned Horizontally

Closer analysis of the region of SiC deposits was carried out using an area ROI (Figure 83). Results showed levels of Al, 4.38 Wt.% and V 3.12 Wt.% to be typical with V below the minimum expected value as was the case throughout. Increased levels of C 8.97 Wt.% and Si 6.34 Wt.% proved the existence of SiC within the ROI.

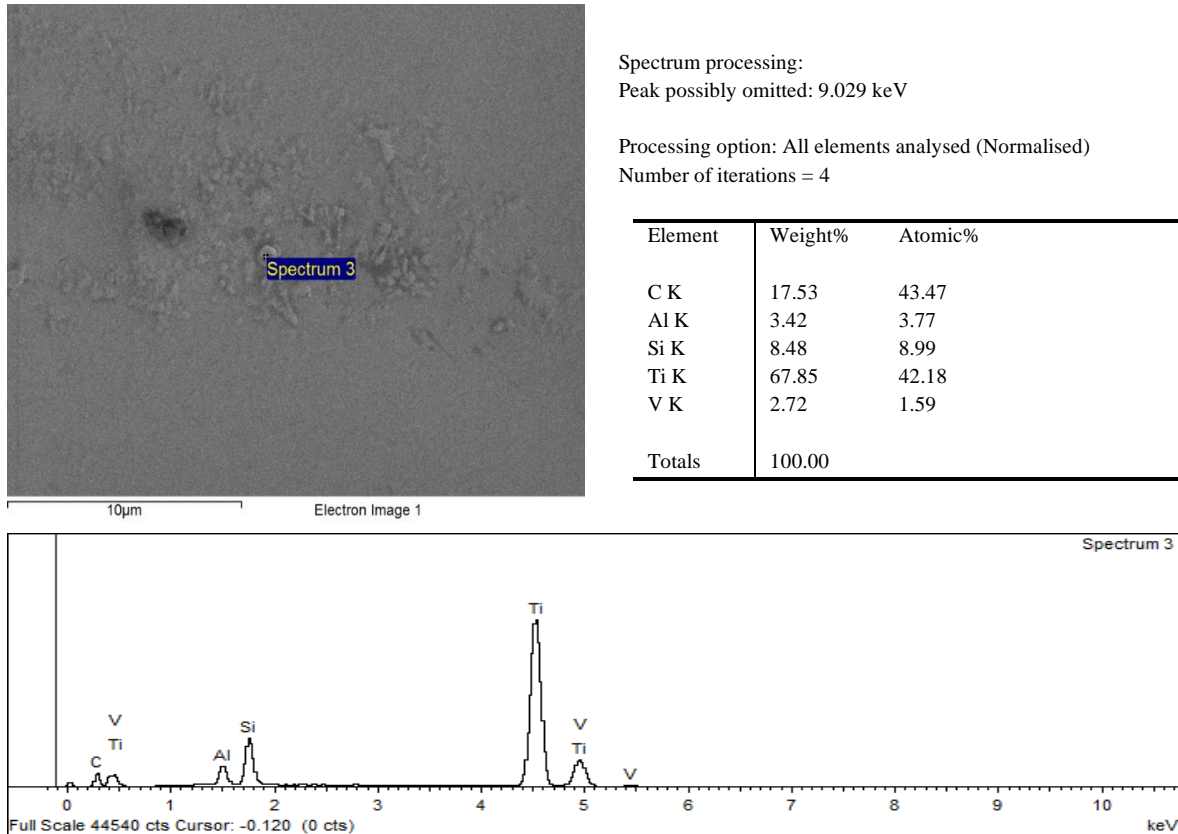
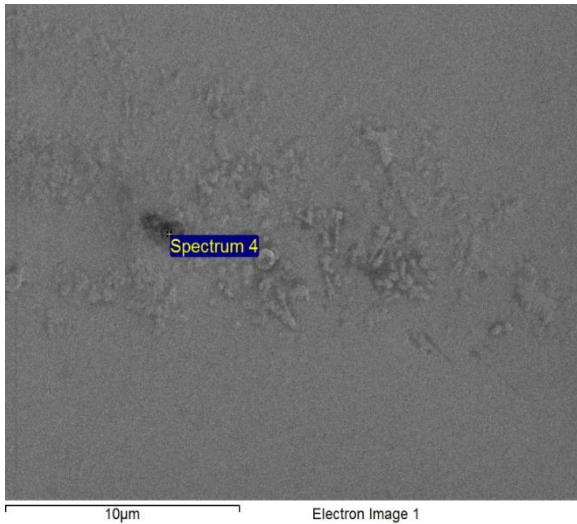


Figure 84 EDS Spot 1 Analysis of MMC Sample 3, Sectioned Horizontally

Further spot analyses were conducted on individual ROI suspected of being particles of SiC. Results confirmed high levels of C 17.53 Wt.% and Si 8.48 Wt.% (Figure 84), with T, Al and V remaining like previous measurements. Analysis of spot 2, (Figure 85), a darker region to the left of the image returned values of C 25.55 Wt.% and Si 24.64 Wt.%. due to the increase in both C and Si it was concluded that the ROI was a SiC particle. In comparison to Figure 86, the particle demonstrated characteristics of SiC with elevated readings of C 10.90 Wt.% and Si 6.18 Wt.% however not to the levels of spot 2. It is believed that the particles of SiC observed in the SEM images have a coating of TiC, the interfacial material between the Ti6Al4V and the SiC. As this material is exceptionally wear resistant it was able to withstand the polishing stages of the sample preparation. The darker area to the left is possibly the site of a removed particle of SiC. The higher levels of C and Si detected in spot 2 confirm this hypothesis.

Unexpected levels of Fe, Pt and C were present in samples one and two for Ti6Al4V, which failed to increase as a result of MA, concluding that there was no contamination from the process.



Spectrum processing:  
Peaks possibly omitted: 6.260, 9.020 keV

Processing option: All elements analysed (Normalised)  
Number of iterations = 4

| Element | Weight% | Atomic% |
|---------|---------|---------|
| C K     | 25.55   | 51.79   |
| O K     | 1.10    | 1.67    |
| Al K    | 1.20    | 1.08    |
| Si K    | 24.64   | 21.36   |
| Ti K    | 45.87   | 23.31   |
| V K     | 1.64    | 0.78    |
| Totals  | 100.00  |         |

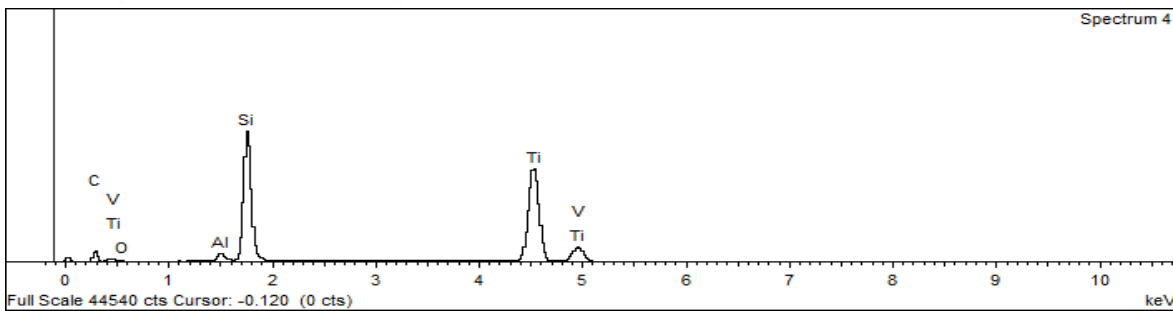
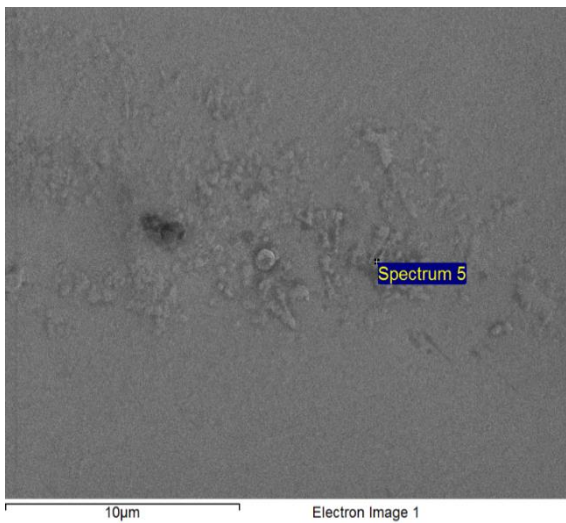


Figure 85 EDS Spot 2 Analysis of MMC Sample 3, Sectioned Horizontally



Spectrum processing:  
Peaks possibly omitted: 2.761, 9.030, 9.437 keV

Processing option: All elements analysed (Normalised)  
Number of iterations = 3

| Element | Weight% | Atomic% |
|---------|---------|---------|
| C K     | 10.90   | 31.10   |
| Al K    | 3.90    | 4.95    |
| Si K    | 6.18    | 7.55    |
| Ti K    | 75.87   | 54.30   |
| V K     | 2.82    | 1.90    |
| Fe K    | 0.33    | 0.20    |
| Totals  | 100.00  |         |

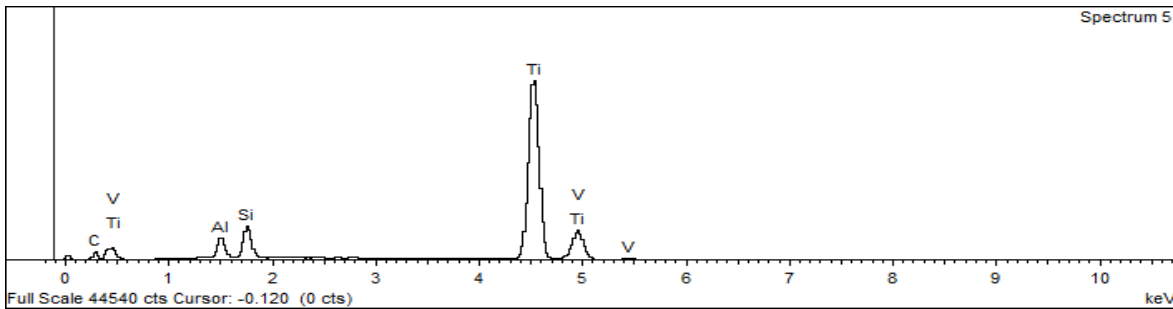


Figure 86 EDS Spot 3 Analysis of MMC Sample 3, Sectioned Horizontally

## 5.5 Phase 2b: MMC Feedstock Analysis for Moisture, Size, Morphology and Rheology in Comparison to Baseline Assessment.

MMC feedstock processed by mechanical alloying for a total of twenty-four minutes was chosen as optimal (section 5.3), a usable quantity of feedstock was produced using the selected parameters and the resultant batch was compared against the baseline data generated earlier (section 5.1).

### 5.5.1 Assessment of MMC Feedstock Moisture Content.

The moisture content of MMC feedstock was measured using the loss of mass method. Three separate samples were analysed from different areas of the batch to establish an arithmetic mean and compared to the baseline results previously obtained (Section 5.1.1). The results are shown in Table 33.

Table 33 Moisture Content Results for MA Feedstock in Comparison to baseline Assessments.

|                    | Moisture Content (%) |      |      |
|--------------------|----------------------|------|------|
|                    | Ti6Al4V              | SiC  | MMC  |
| Test 1             | 0.59                 | 0.79 | 0.61 |
| Test 2             | 0.50                 | 0.97 | 1.20 |
| Test 3             | 0.67                 | 1.13 | 0.79 |
| Mean ( $\bar{x}$ ) | 0.59                 | 0.96 | 0.86 |

For the MMC feedstock the moisture levels were below the 1.0% maximum limit (section 4.2.4.1) and were therefore considered acceptable. It was noted that the mean values for the MMC feedstock fell between the lower value for the Ti6Al4V powder (0.59%) and the higher value for SiC (0.96%). This was due to the percentage ratio of Ti6Al4V to SiC. It was evident from the baseline assessments that the SiC powder absorbed moisture more than the Ti6Al4V powder due to the high surface area and therefore increased surface energy. The presence of SiC within the MMC feedstock is therefore evident by the increased percentage of moisture however, this not of the magnitude previously exhibited and remains within acceptable limits.

### 5.5.2 Assessment of MMC Feedstock Size and Morphology.

Using a Retsch Camsizer X2 particle size analyser a representative sample of MMC feedstock powder was analysed in comparison to baseline assessments acquired in section 5.2.3, with respect to the characteristics:  $X_{c\ min}$ ,  $X_{area}$  and b/l. the results were compared to the baseline data obtained for Ti6Al4V as these results best represented standard feedstock and constitute the bulk of the MMC.

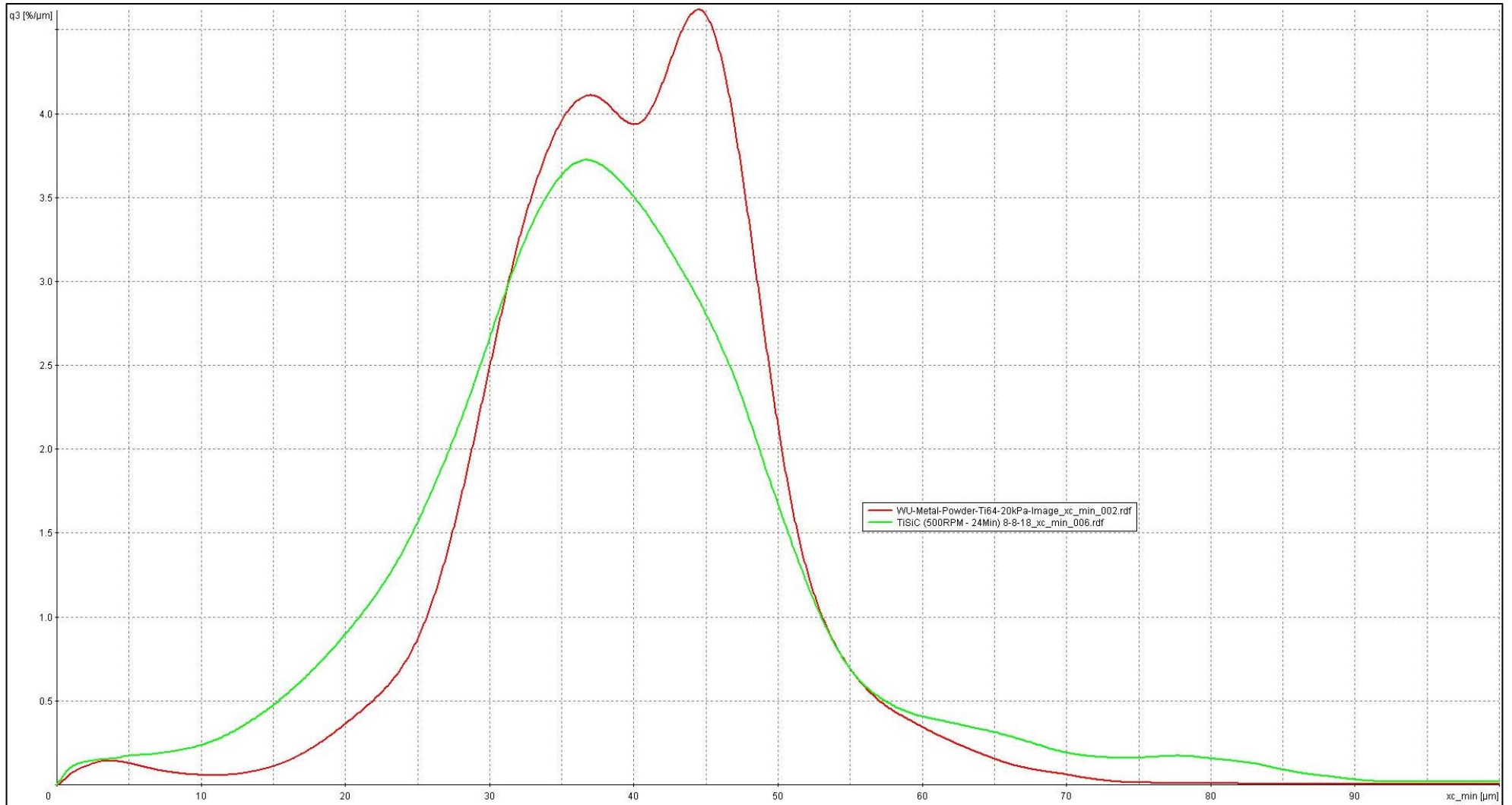


Figure 87  $X_{c\ Min}$  Comparison Between Ti6Al4V Baseline and MMC Feedstock Alloyed for 24 Minutes



### 5.5.2.1 MMC feedstock Particle Size and Size Distribution Comparison.

Figure 87 shows graphical results for  $X_{c \min}$  frequency distribution curve for MMC feedstock powder in comparison to Ti6Al4V powder. The analysis showed a multi-modal size distribution between  $\sim 0 \mu\text{m}$  to  $\sim 75 \mu\text{m}$  for the Ti6Al4V powder (Red line), with peaks at  $3.5 \mu\text{m}$ ,  $37 \mu\text{m}$  and  $44 \mu\text{m}$ . in comparison, the MMC material shown here in green, has a single peak size distribution, having arrange from  $\sim 0 \mu\text{m}$  to  $\sim 100 \mu\text{m}$  with a peak at  $37 \mu\text{m}$ . The distribution curve for the MMC material exhibited higher quantities of particles within the range of  $0 \mu\text{m}$  to  $30 \mu\text{m}$  indicating a higher quantity of small fines. Within the range of  $55 \mu\text{m}$  to  $90 \mu\text{m}$  this can also be seen to a lesser degree, indicating that particles within this range are larger, this was predicted as a result of the smaller SiC particles fixing to the surface of the Ti6Al4V and increasing the size.

**Table 34 Statistical Results for Ti6Al4V Particle Size and Distribution ( $X_{c \min}$ ) Baseline Results**

| Statistical measurement | Baseline result ( $X_{c \min}$ ) | MMC feedstock results ( $X_{c \min}$ ) |
|-------------------------|----------------------------------|----------------------------------------|
| Q3 10%                  | 28.8 $\mu\text{m}$               | 23.5 $\mu\text{m}$                     |
| Q3 50%                  | 39.9 $\mu\text{m}$               | 37.7 $\mu\text{m}$                     |
| Q3 90%                  | 49.9 $\mu\text{m}$               | 53.4 $\mu\text{m}$                     |
| Mv3( $\bar{x}$ )        | 39.7 $\mu\text{m}$               | 39.7 $\mu\text{m}$                     |
| Mean b/l3               | 0.851                            | 0.819                                  |
| 1-Q3 (b/l = 0.850)      | 65%                              | 51.9%                                  |

Table 34 shows the salient characteristics of the particle size analysis. It was evident For Ti6Al4V, that the volume based statistical average particle size (Q3 50%) was  $39.9 \mu\text{m}$  with a mean particle size (Mv3( $\bar{x}$ )) of  $39.7 \mu\text{m}$ . the closeness of these two values, (within  $0.2 \mu\text{m}$ ), showed a high degree of confidence in the results.

In comparison, values for the MMC feedstock showed a smaller Q3 50% size of  $37.7 \mu\text{m}$  however, the mean particle size (Mv3( $\bar{x}$ )) was  $39.7 \mu\text{m}$ , identical to that of the Ti6Al4V. Although the statistical mean for the sample was identical, it can be observed that the value for Q3 10% was lower and the value for Q3 90% was higher, indicating that at the lower percentile, smaller particles were detected, most likely to be SiC and that at the higher percentile larger particles were detected, likely to be Ti6Al4V coated with SiC. This data confirms the results analysed in Figure 87.

The mean aspect ratio (Mean b/l3) for Ti6Al4V was 0.851, indicating that the sample was classified as rounded. Results for Mean b/l3 for the MMC feedstock however, showed a value of 0.819. this sample would not be classified as rounded in this instance. Further comparison of the mean aspect ratio results indicated that the inverse statistical volume (1-Q3 (b/l = 0.850)) for the Ti6Al4V sample was 65%. In comparison, the MMC feedstock result was 51.9%, indicating that fewer particles were rounded. This was as a result of the mechanical alloying process.

Further comparisons were made between the baseline assessments and the MMC feedstock, evaluating  $X_{area}$  (Figure 88). In much the same way as results for  $X_{c\ min}$ , the distribution curve for  $X_{area}$  showed increases in particles sized at the lower and higher ends of the distribution with a lower count of particles within the mid-range. A more detailed analysis of this comparison was required.

Table 35 details Statistical Results for Ti6Al4V Particle Size and Distribution,  $X_{c\ Min}$  and  $X_{area}$  Baseline Results Versus MMC material results.

**Table 35 Statistical Results for Ti6Al4V Particle Size and Distribution,  $X_{c\ Min}$  Versus  $X_{area}$  Baseline Results**

| Statistical measurement | Baseline result ( $X_{c\ min}$ ) | Baseline result ( $X_{area}$ ) | Percentage increase $\emptyset$ | MMC result ( $X_{c\ min}$ ) | MMC result ( $X_{area}$ ) | Percentage increase $\emptyset$ |
|-------------------------|----------------------------------|--------------------------------|---------------------------------|-----------------------------|---------------------------|---------------------------------|
| Q3 10%                  | 28.8 $\mu\text{m}$               | 30.2 $\mu\text{m}$             | 4.6%                            | 23.5 $\mu\text{m}$          | 26.0 $\mu\text{m}$        | 9.6%                            |
| Q3 50%                  | 39.9 $\mu\text{m}$               | 43.1 $\mu\text{m}$             | 7.4%                            | 37.7 $\mu\text{m}$          | 41.4 $\mu\text{m}$        | 8.9%                            |
| Q3 90%                  | 49.9 $\mu\text{m}$               | 55.8 $\mu\text{m}$             | 10.6%                           | 53.4 $\mu\text{m}$          | 60.3 $\mu\text{m}$        | 11.4%                           |
| Mv3( $\bar{x}$ )        | 39.7 $\mu\text{m}$               | 42.7 $\mu\text{m}$             | 7.0%                            | 39.7 $\mu\text{m}$          | 44.4 $\mu\text{m}$        | 10.6%                           |
| Mean b/13               | 0.851                            | 0.839                          |                                 | 0.819                       | 0.795                     |                                 |
| 1-Q3 (b/1 = 0.850)      | 65.0%                            | 61.5%                          |                                 | 51.9%                       | 46.3%                     |                                 |

By comparing  $X_{area}$  to  $X_{c\ min}$  it is possible to better understand surface irregularities such as satellites. The closer values are between min and  $X_{area}$ , the fewer surface irregularities there are. Therefore, using the Ti6Al4V baseline data as a reference, it was observed that the percentage increase in diameter ranged from 4.6% to 10.6% with an increase of 7.0% for mean b/13. It has been established that the baseline material performs satisfactorily within the process and therefore these values can be considered typical. In comparison, results for the MMC material showed percentage increases from  $X_{c\ min}$  to  $X_{area}$  of between 8.9% to 11.4% with an increase of 10.6% for mean b/13. This being a result of the MA processing would indicate that an increase in surface roughness and of satellites was evident. Based on the severity of difference from  $X_{c\ min}$  to  $X_{area}$  for the Ti6Al4V material, the material MA for twenty-four minutes shows similar results.

Further Comparison Between Ti6Al4V Baseline and MMC Feedstock Alloyed for 24 Minutes is given in Figure 88 for  $X_{area}$ . The frequency of both smaller (less than 30  $\mu\text{m}$ ) and larger particles (more than 54  $\mu\text{m}$ ) has increased whilst particles within the range of 30  $\mu\text{m}$  to 54  $\mu\text{m}$  has decreased.

Figure 89 compares  $X_{c\ min}$  volume-based distribution for Ti6Al4V baseline assessment with MMC feedstock MA for twenty-four minutes, it can be seen that there is a shift to the left for the green line (MMC material) in comparison to the red (Ti6Al4V), indicating that the powder is finer however the reduction in the slope angle indicates a wider spread of values. This is clarified by the results for  $X_{area}$  Figure 90.

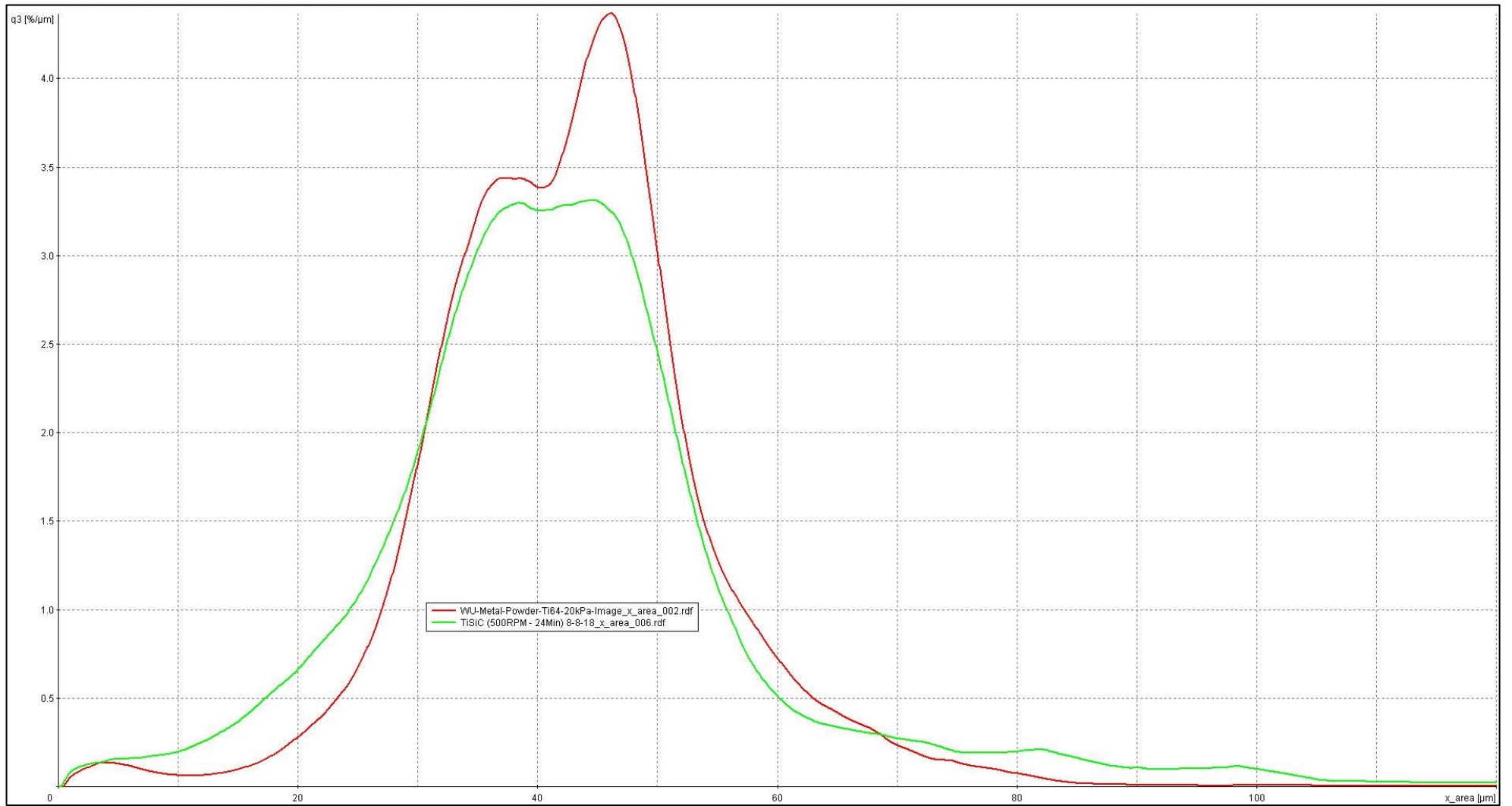


Figure 88 X<sub>area</sub> Comparison Between Ti6Al4V Baseline and MMC Feedstock Alloyed for 24 Minutes

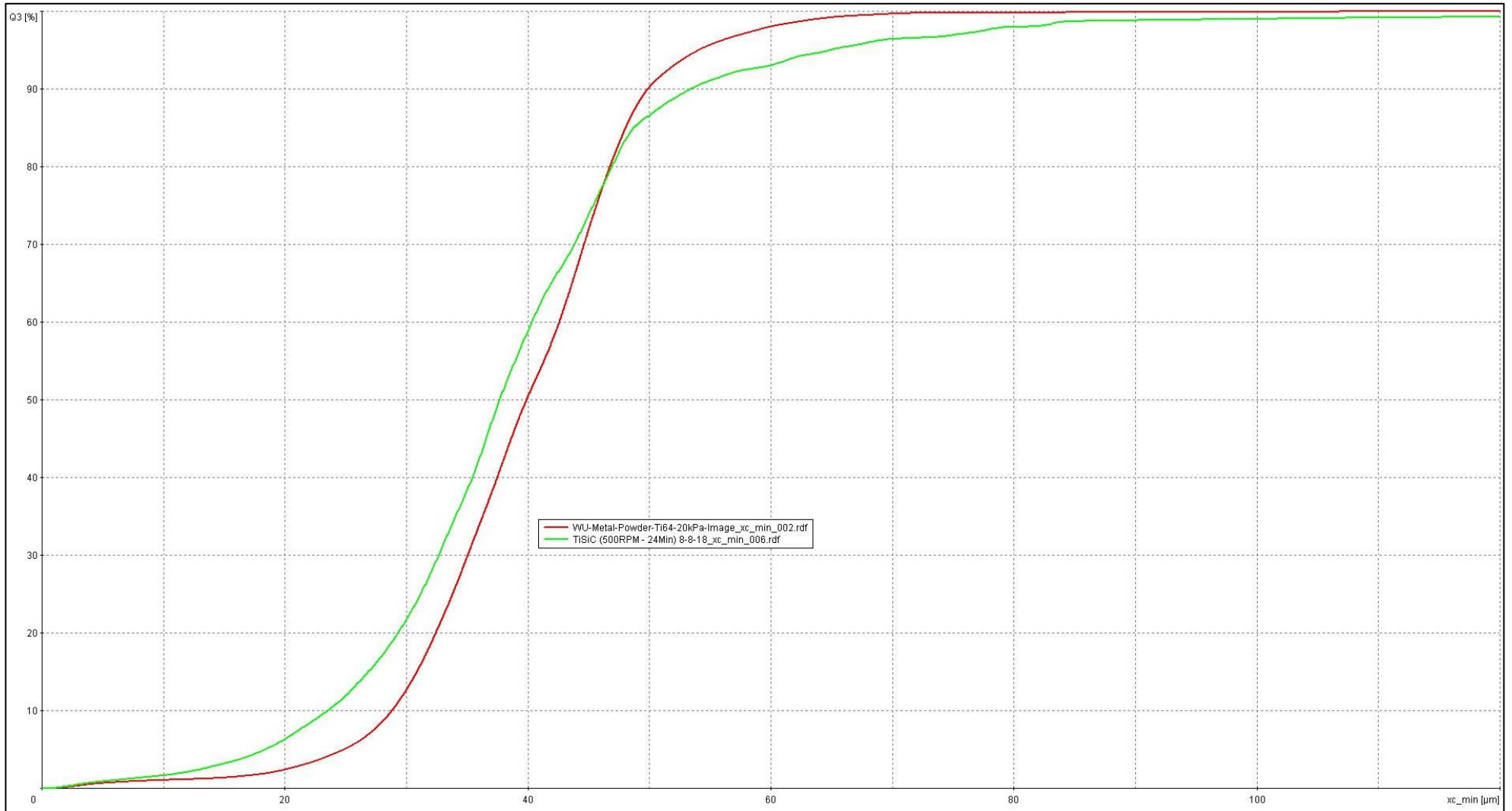


Figure 89  $X_{c\_min}$  Volume Based Distribution Curve Comparison Between Ti6Al4V Baseline and MMC Feedstock Alloyed for 24 Minutes.

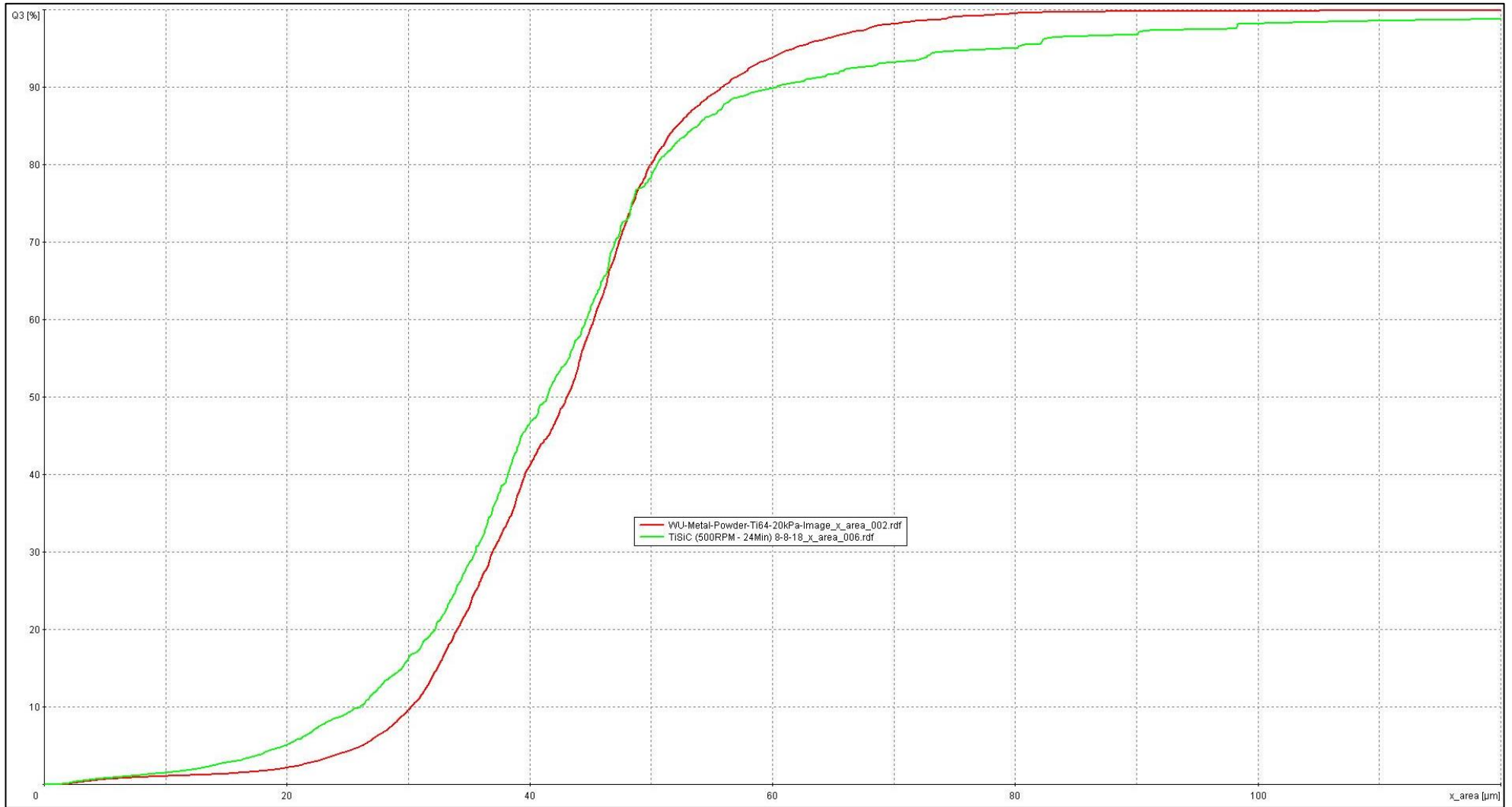


Figure 90 X<sub>area</sub> Volume Based Distribution Curve Comparison Between Ti6Al4V Baseline and MMC Feedstock Alloyed for 24 Minutes.

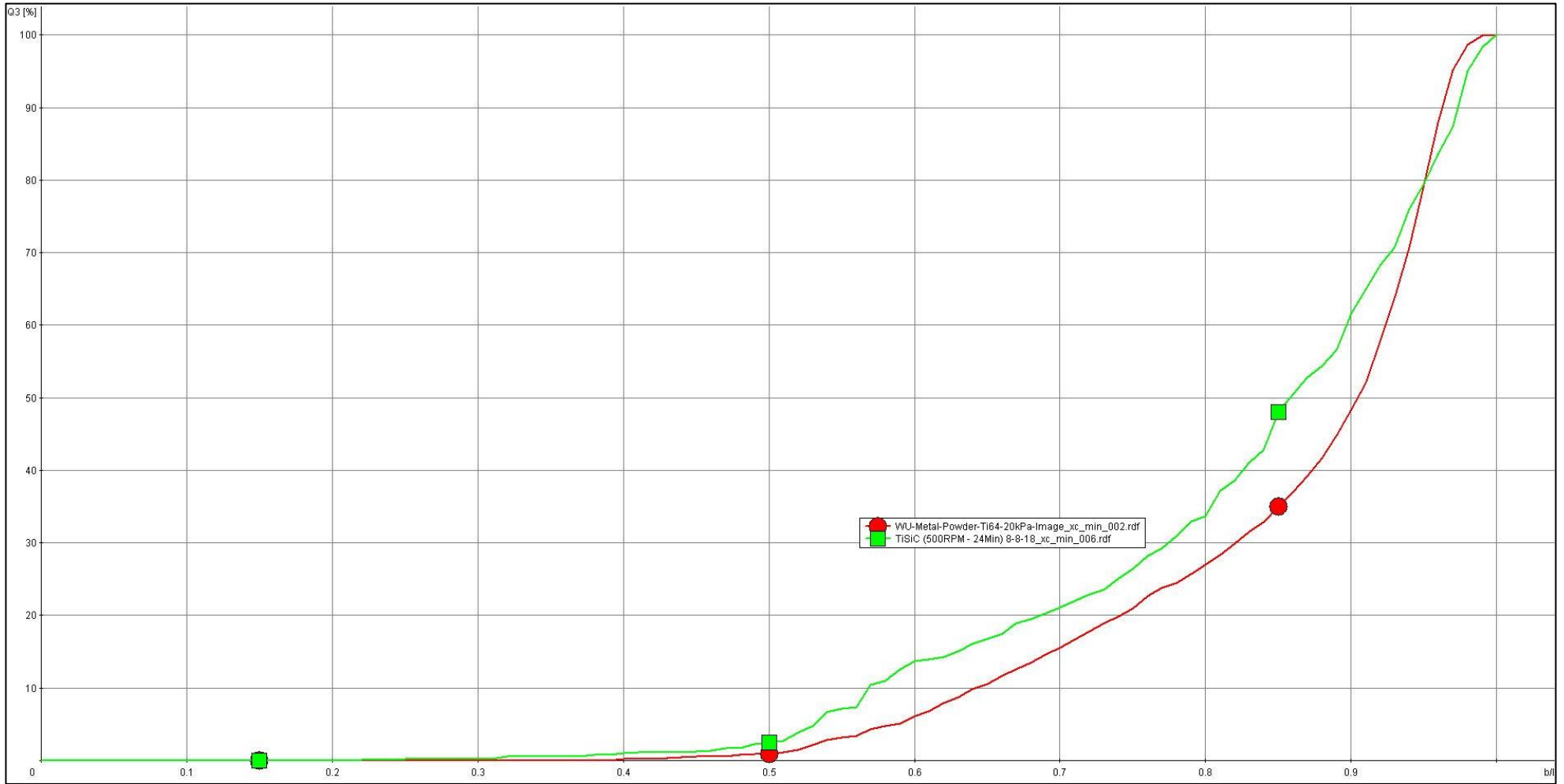


Figure 91 b/l Volume Based Distribution Curve Comparison Between Ti6Al4V Baseline and MMC Feedstock Alloyed for 24 Minutes

Figure 91 shows b/l Volume Based Distribution Curve Comparison Between Ti6Al4V Baseline and MMC Feedstock Alloyed for 24 Minutes, again it can be seen that the results for the MMC material (green) has shifted to the left of the Ti6Al4V material (red), indicating that fewer particles are classed as rounded (~52%).

### 5.5.3 MMC Feedstock Rheology comparison against Ti6Al4V.

Comparison of rheological characteristics were conducted between the MMC feedstock milled for twenty-four minutes and both the Ti6Al4V and SiC baseline results to determine the effect of the MA process. Tests included, apparent density, tap density and the angle of repose. The results are shown in Table 36.

**Table 36 Comparison of Rheological Characteristics for Ti6Al4V And MMC Feedstock.**

| Rheological measurement        | Ti6Al4V                | SiC                    | MMC feedstock          |
|--------------------------------|------------------------|------------------------|------------------------|
| Material density               | 4.43 g/cm <sup>3</sup> | 3.21 g/cm <sup>3</sup> | 4.34 g/cm <sup>3</sup> |
| Apparent density               | 2.24 g/cm <sup>3</sup> | 0.41 g/cm <sup>3</sup> | 1.99 g/cm <sup>3</sup> |
| Percentage of physical density | 50.6%                  | 12.8%                  | 45.8%                  |
| Tap density                    | 2.63 g/cm <sup>3</sup> | 0.57 g/cm <sup>3</sup> | 2.43 g/cm <sup>3</sup> |
| Percentage of physical density | 59.5%                  | 17.8%                  | 56.1%                  |
| Angle of repose                | 33°                    | 48°                    | 38°                    |

The analysis confirmed that post MA the powder exhibited a reduction in packing and tap densities. As it is always the aim to maintain the highest apparent density, this reduction was concerning as this could lead to porosity in the parts. As tap density relates primarily to the packing density in the powder dispenser, this was not considered a problem. These reductions in packing densities indicated a loss of rounded particles and further reinforces the earlier powder morphology results.

Results for the angle of repose showed an increased angle for the MMC feedstock of 38 degrees in comparison to Ti6Al4V, 33 degrees. This was due to the MMC powder's increased surface roughness and reduced roundness, hence the steeper angle. The implications of the increased angle of repose would be that the powder may resist spreading by the recoater arm between layers. This would need to be investigated.

### 5.6 Phase 3a: MMC Single Bead Evaluation Against Energy Density Compared to Baseline Results.

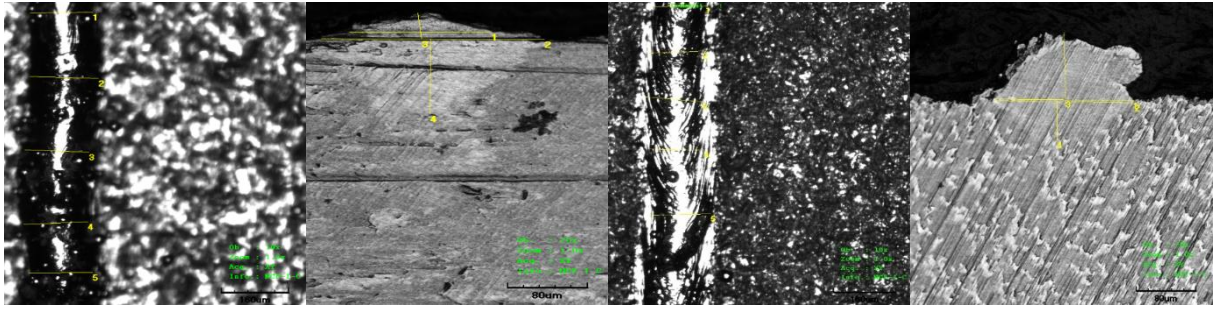
Using the MMC feedstock MA for twenty-four minutes, single beads were exposed for one layer only. The two rail system was used to ensure a reliable layer thickness and beads were exposed using the same variable (Table 17) and attributes (Table 18), as were used for the baseline evaluation of Ti6Al4V.

As with the baseline assessments of Ti6Al4V, measurements were taken of the mean bead width in a vertical direction along with the width of the bead ( $w_1$ ), the width of the substrate penetration ( $w_2$ ), the height of the bead ( $h_1$ ) and the depth of the substrate penetration ( $h_2$ ), for comparison.

**Table 37 Phase 3a; MMC Single Bead Evaluation Against Energy Density Compared to Baseline Results At 150 W**

| Ti6Al4V View on Z axis<br>(10 x magnification)                                                                                                  | Ti6Al4V Cross section<br>(20 x magnification) | MMC View on Z axis<br>(10 x magnification)                                                                                                      | MMC Cross section<br>(20 x magnification) |
|-------------------------------------------------------------------------------------------------------------------------------------------------|-----------------------------------------------|-------------------------------------------------------------------------------------------------------------------------------------------------|-------------------------------------------|
|                                                                                                                                                 |                                               |                                                                                                                                                 |                                           |
| E = 250 J/mm <sup>3</sup> V = 200 mm/s Mean bead width, vertical = 186.287 μm<br>h1 = 55.004 μm h2 = 112.502 μm w1 = 273.128 μm w2 = 273.128 μm |                                               | E = 250 J/mm <sup>3</sup> V = 200 mm/s Mean bead width, vertical = 199.316 μm<br>h1 = 85.021 μm h2 = 117.581 μm w1 = 232.568 μm w2 = 251.288 μm |                                           |
|                                                                                                                                                 |                                               |                                                                                                                                                 |                                           |
| E = 225 J/mm <sup>3</sup> V = 222 mm/s Mean bead width, vertical = 165.852 μm<br>h1 = 47.566 μm h2 = 115.042 μm w1 = 168.144 μm w2 = 228.771 μm |                                               | E = 225 J/mm <sup>3</sup> V = 222 mm/s Mean bead width, vertical = 192.458 μm<br>h1 = 68.197 μm h2 = 78.187 μm w1 = 221.875 μm w2 = 222.514 μm  |                                           |
|                                                                                                                                                 |                                               |                                                                                                                                                 |                                           |
| E = 200 J/mm <sup>3</sup> V = 250 mm/s Mean bead width, vertical = 161.505 μm<br>h1 = 40.625 μm h2 = 101.875 μm w1 = 196.884 μm w2 = 265.628 μm |                                               | E = 200 J/mm <sup>3</sup> V = 250 mm/s Mean bead width, vertical = 172.530 μm<br>h1 = 86.985 μm h2 = 91.259 μm w1 = 198.759 μm w2 = 200.004 μm  |                                           |





E = 175 J/mm<sup>3</sup> V = 286 mm/s Mean bead width, vertical = 151.271  $\mu$ m  
 h1 = 35.200  $\mu$ m h2 = 100.627  $\mu$ m w1 = 145.000  $\mu$ m w2 = 229.376  $\mu$ m

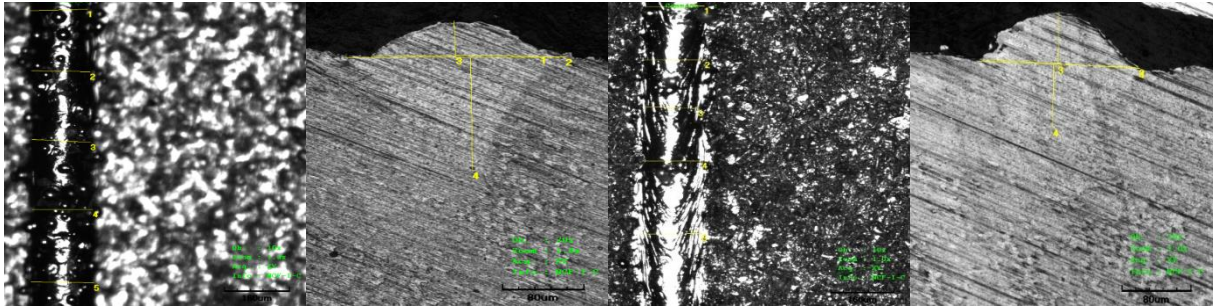
E = 175 J/mm<sup>3</sup> V = 286 mm/s Mean bead width, vertical = 147.963  $\mu$ m  
 h1 = 91.909  $\mu$ m h2 = 53.125  $\mu$ m w1 = 191.259  $\mu$ m w2 = 193.775  $\mu$ m

**Ti6Al4V View on Z axis  
 (10 x magnification)**

**Ti6Al4V Cross section  
 (20 x magnification)**

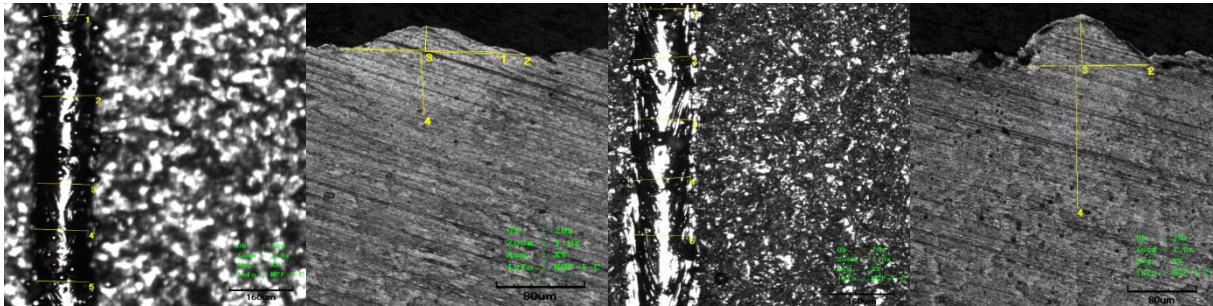
**MMC View on Z axis  
 (10 x magnification)**

**MMC Cross section  
 (20 x magnification)**



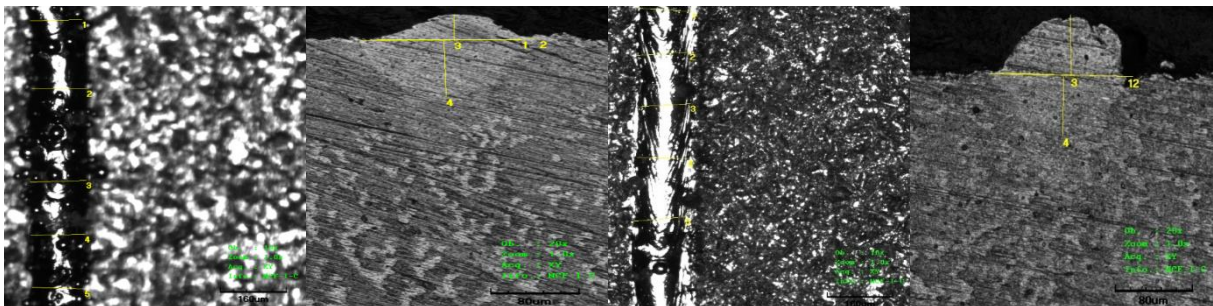
E = 150 J/mm<sup>3</sup> V = 333 mm/s Mean bead width, vertical = 150.580  $\mu$ m  
 h1 = 44.415  $\mu$ m h2 = 145.012  $\mu$ m w1 = 170.010  $\mu$ m w2 = 221.879  $\mu$ m

E = 150 J/mm<sup>3</sup> V = 333 mm/s Mean bead width, vertical = 152.777  $\mu$ m  
 h1 = 62.512  $\mu$ m h2 = 74.378  $\mu$ m w1 = 186.553  $\mu$ m w2 = 190.772  $\mu$ m



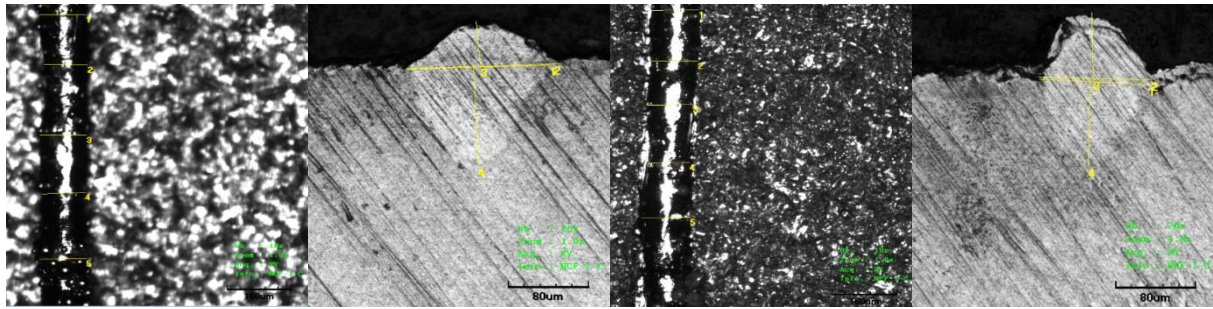
E = 125 J/mm<sup>3</sup> V = 400 mm/s Mean bead width, vertical = 131.802  $\mu$ m  
 h1 = 28.757  $\mu$ m h2 = 70.694  $\mu$ m w1 = 136.945  $\mu$ m w2 = 171.364  $\mu$ m

E = 125 J/mm<sup>3</sup> V = 400 mm/s Mean bead width, vertical = 149.158  $\mu$ m  
 h1 = 60.654  $\mu$ m h2 = 169.380  $\mu$ m w1 = 150.005  $\mu$ m w2 = 155.011  $\mu$ m



E = 100 J/mm<sup>3</sup> V = 500 mm/s Mean bead width, vertical = 133.288  $\mu$ m  
 h1 = 32.500  $\mu$ m h2 = 71.899  $\mu$ m w1 = 133.750  $\mu$ m w2 = 166.261  $\mu$ m

E = 100 J/mm<sup>3</sup> V = 500 mm/s Mean bead width, vertical = 132.086  $\mu$ m  
 h1 = 65.003  $\mu$ m h2 = 63.128  $\mu$ m w1 = 133.803  $\mu$ m w2 = 152.532  $\mu$ m



$E = 75 \text{ J/mm}^3$   $V = 667 \text{ mm/s}$  Mean bead width, vertical = 116.275  $\mu\text{m}$   
 $h1 = 49.568 \mu\text{m}$   $h2 = 108.838 \mu\text{m}$   $w1 = 145.066 \mu\text{m}$   $w2 = 150.085 \mu\text{m}$

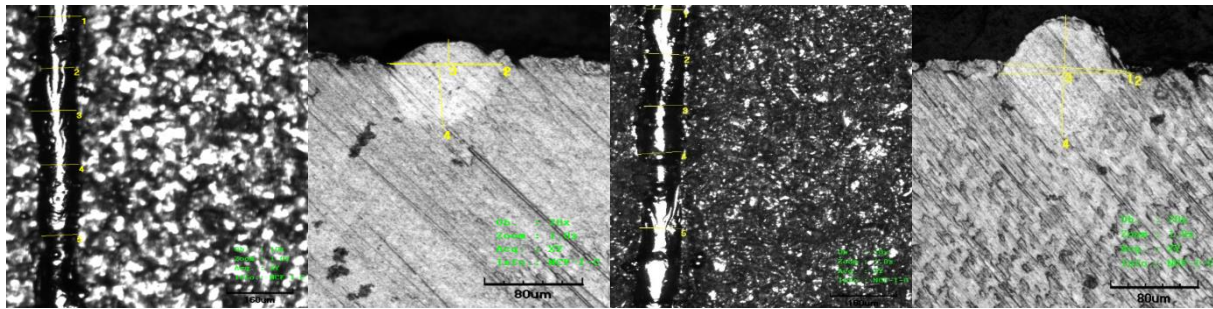
$E = 75 \text{ J/mm}^3$   $V = 667 \text{ mm/s}$  Mean bead width, vertical = 120.770  $\mu\text{m}$   
 $h1 = 69.386 \mu\text{m}$   $h2 = 89.395 \mu\text{m}$   $w1 = 112.016 \mu\text{m}$   $w2 = 115.652 \mu\text{m}$

**Ti6Al4V View on Z axis  
(10 x magnification)**

**Ti6Al4V Cross section  
(20 x magnification)**

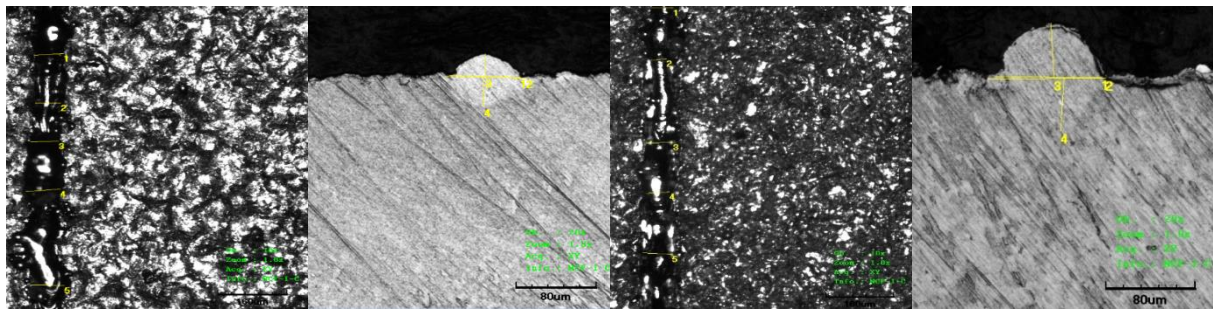
**MMC View on Z axis  
(10 x magnification)**

**MMC Cross section  
(20 x magnification)**



$E = 50 \text{ J/mm}^3$   $V = 1000 \text{ mm/s}$  Mean bead width, vertical = 96.805  $\mu\text{m}$   
 $h1 = 25.633 \mu\text{m}$   $h2 = 65.108 \mu\text{m}$   $w1 = 93.133 \mu\text{m}$   $w2 = 96.877 \mu\text{m}$

$E = 50 \text{ J/mm}^3$   $V = 1000 \text{ mm/s}$  Mean bead width, vertical = 98.851  $\mu\text{m}$   
 $h1 = 51.879 \mu\text{m}$   $h2 = 61.878 \mu\text{m}$   $w1 = 115.170 \mu\text{m}$   $w2 = 126.877 \mu\text{m}$



$E = 25 \text{ J/mm}^3$   $V = 2000 \text{ mm/s}$  Mean bead width, vertical = 70.618  $\mu\text{m}$   
 $h1 = 27.500 \mu\text{m}$   $h2 = 33.756 \mu\text{m}$   $w1 = 72.543 \mu\text{m}$   $w2 = 82.521 \mu\text{m}$

$E = 25 \text{ J/mm}^3$   $V = 2000 \text{ mm/s}$  Mean bead width, vertical = 57.883  $\mu\text{m}$   
 $h1 = 50.687 \mu\text{m}$   $h2 = 48.226 \mu\text{m}$   $w1 = 96.877 \mu\text{m}$   $w2 = 108.127 \mu\text{m}$

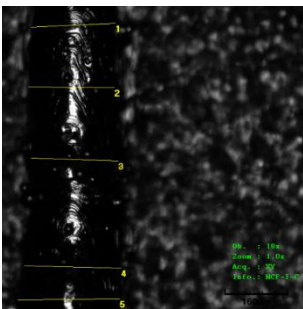
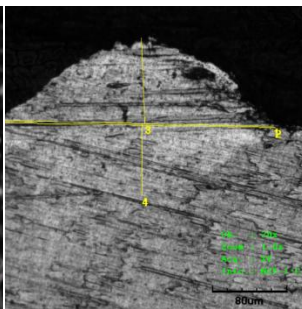
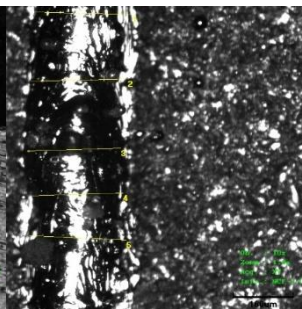
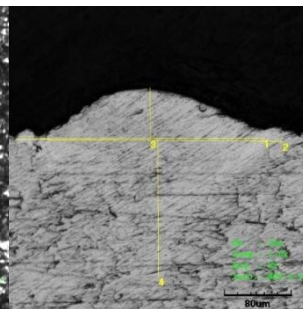
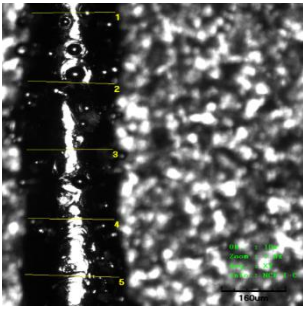
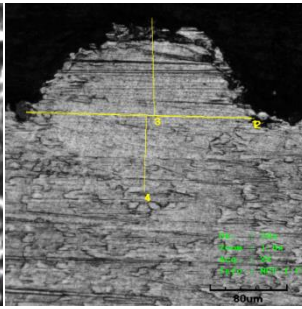
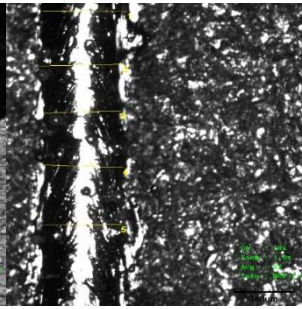
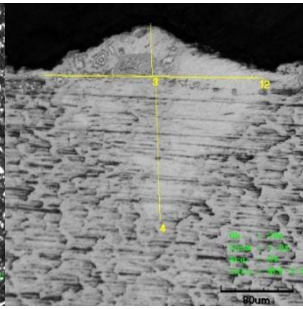
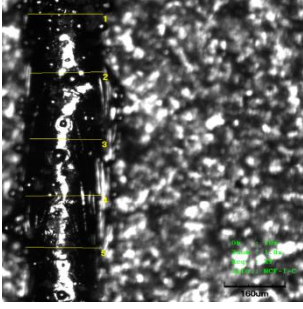
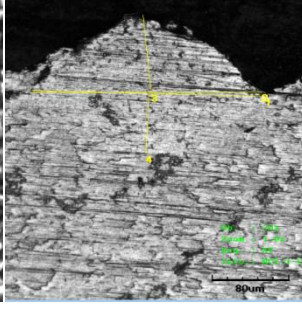
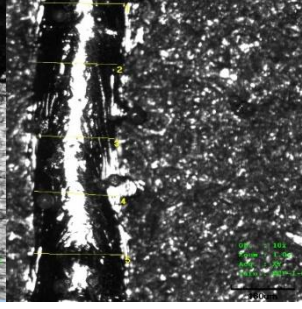
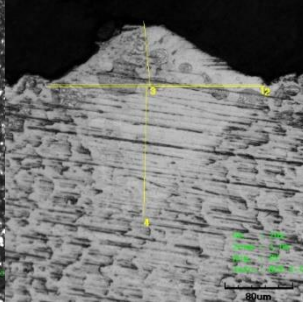
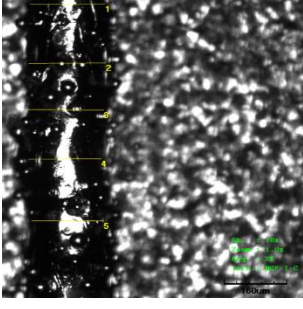
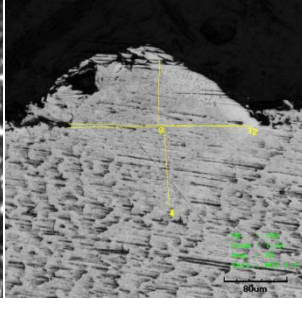
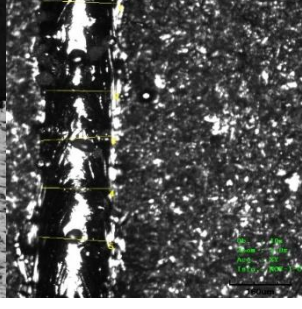
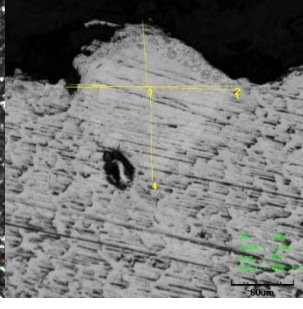
Table 37 shows MMC single bead evaluation results compared to initial baseline results in terms of energy density using a laser power of 150 W. In Initial observations the MMC powder exposed at 150 W showed evidence of miscibility with the substrate and an ability to form a continuous bead whilst maintaining a uniform width and height. In comparison to Ti6Al4V, the bead formations appear to be similar, with the MMC beads having improved flow across the substrate, demonstrated as regions either side of the bead. This is thought to be a result of lower surface tension and therefore increased fluidity of the melt pool. At lower energy density range of 25 J/mm<sup>3</sup> to 75 J/mm<sup>3</sup> this phenomenon is less evident. This phenomenon is also only visible within a vertical perspective, unmeasurable in the cross-sectional views meaning that this could merely be a wetting effect and not contributing to the physical bead. It is however intriguing as

to why this only occurs with higher energy densities, it could also be plausible that these areas are the result of the material expanding during its liquidus stage before contracting to form the solid bead, leaving evidence behind. This would require further investigation, but if so, could demonstrate that the MMC material forms better at lower energy densities.

Beads exposed at 2000 mm/s, displayed discontinuity within the bead due to the high velocity of the laser. All beads showed good penetration of the substrate. There was no evidence of balling and spatter appeared to be less prominent with the MMC material than with Ti6Al4V. bead size also appeared to be larger for the MMC material in comparison to Ti6Al4V, this will be discussed further within this section.

Table 38 shows MMC single bead evaluation results compared to initial baseline results in terms of energy density using a laser power of 250 W.

**Table 38 Phase 3a; MMC Single Bead Evaluation Against Energy Density Compared to Baseline Results At 250 W**

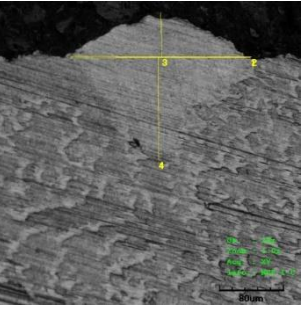
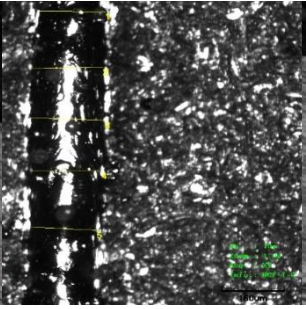
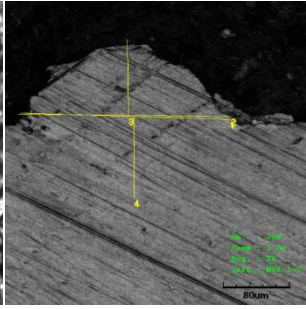
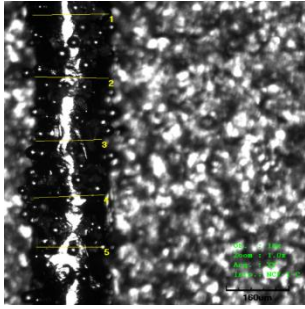
| Ti6Al4V View on Z axis<br>(10 x magnification)                                                                                                                        | Ti6Al4V Cross section<br>(20 x magnification)                                       | MMC View on Z axis<br>(10 x magnification)                                                                                                                            | MMC Cross section<br>(20 x magnification)                                             |
|-----------------------------------------------------------------------------------------------------------------------------------------------------------------------|-------------------------------------------------------------------------------------|-----------------------------------------------------------------------------------------------------------------------------------------------------------------------|---------------------------------------------------------------------------------------|
|                                                                                      |    |                                                                                     |    |
| <p><b>E = 417 J/mm<sup>3</sup> V = 200 mm/s Mean bead width, vertical = 239.340 μm</b><br/> <b>h1 = 96.323 μm h2 = 79.375 μm w1 = 312.576 μm w2 = 315.675 μm</b></p>  |                                                                                     | <p><b>E = 417 J/mm<sup>3</sup> V = 200 mm/s Mean bead width, vertical = 260.883 μm</b><br/> <b>h1 = 62.503 μm h2 = 168.126 μm w1 = 273.751 μm w2 = 326.885 μm</b></p> |                                                                                       |
|                                                                                     |   |                                                                                    |   |
| <p><b>E = 375 J/mm<sup>3</sup> V = 222 mm/s Mean bead width, vertical = 223.314 μm</b><br/> <b>h1 = 115.652 μm h2 = 90.020 μm w1 = 240.742 μm w2 = 243.847 μm</b></p> |                                                                                     | <p><b>E = 375 J/mm<sup>3</sup> V = 222 mm/s Mean bead width, vertical = 217.052 μm</b><br/> <b>h1 = 60.029 μm h2 = 166.325 μm w1 = 243.779 μm w2 = 255.019 μm</b></p> |                                                                                       |
|                                                                                    |  |                                                                                   |  |
| <p><b>E = 333 J/mm<sup>3</sup> V = 250 mm/s Mean bead width, vertical = 201.514 μm</b><br/> <b>h1 = 95.402 μm h2 = 74.441 μm w1 = 249.488 μm w2 = 246.251 μm</b></p>  |                                                                                     | <p><b>E = 333 J/mm<sup>3</sup> V = 250 mm/s Mean bead width, vertical = 217.671 μm</b><br/> <b>h1 = 78.484 μm h2 = 158.156 μm w1 = 253.125 μm w2 = 264.376 μm</b></p> |                                                                                       |
|                                                                                    |  |                                                                                   |  |
| <p><b>E = 291 J/mm<sup>3</sup> V = 286 mm/s Mean bead width, vertical = 195.505 μm</b><br/> <b>h1 = 90.634 μm h2 = 113.334 μm w1 = 235.646 μm w2 = 238.779 μm</b></p> |                                                                                     | <p><b>E = 291 J/mm<sup>3</sup> V = 286 mm/s Mean bead width, vertical = 187.973 μm</b><br/> <b>h1 = 87.723 μm h2 = 123.764 μm w1 = 219.483 μm w2 = 223.753 μm</b></p> |                                                                                       |

**Ti6Al4V View on Z axis  
(10 x magnification)**

**Ti6Al4V Cross section  
(20 x magnification)**

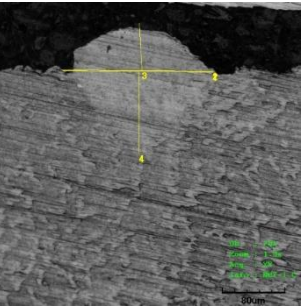
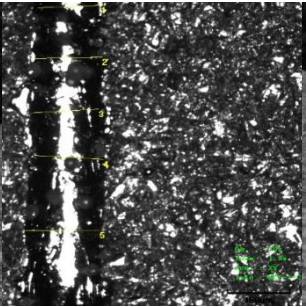
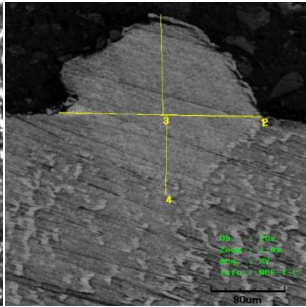
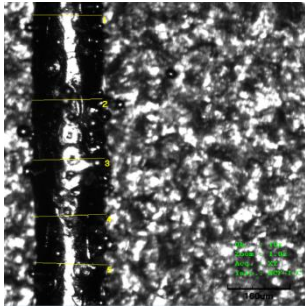
**MMC View on Z axis  
(10 x magnification)**

**MMC Cross section  
(20 x magnification)**



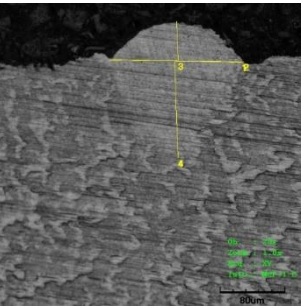
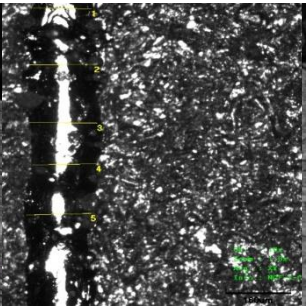
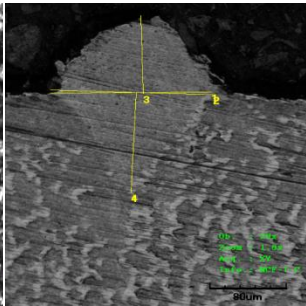
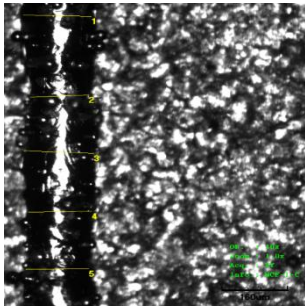
**E = 250 J/mm<sup>3</sup> V = 333 mm/s Mean bead width, vertical = 185.067 µm  
h1 = 98.133 µm h2 = 105.000 µm w1 = 259.502 µm w2 = 263.769 µm**

**E = 250 J/mm<sup>3</sup> V = 333 mm/s Mean bead width, vertical = 182.331 µm  
h1 = 56.606 µm h2 = 131.251 µm w1 = 231.253 µm w2 = 232.503 µm**



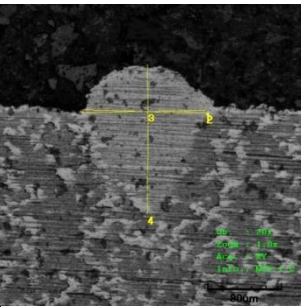
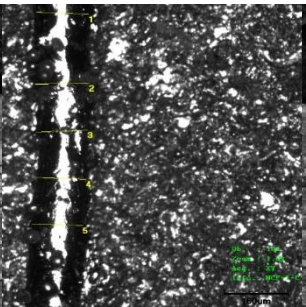
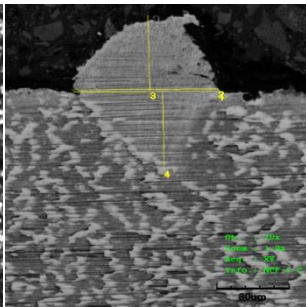
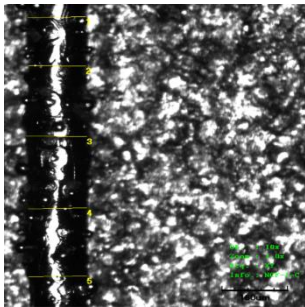
**E = 208 J/mm<sup>3</sup> V = 400 mm/s Mean bead width, vertical = 186.822 µm  
h1 = 121.901 µm h2 = 95.633 µm w1 = 223.821 µm w2 = 226.281 µm**

**E = 208 J/mm<sup>3</sup> V = 400 mm/s Mean bead width, vertical = 179.433 µm  
h1 = 61.330 µm h2 = 106.875 µm w1 = 196.259 µm w2 = 198.129 µm**



**E = 167 J/mm<sup>3</sup> V = 500 mm/s Mean bead width, vertical = 161.322 µm  
h1 = 95.658 µm h2 = 122.005 µm w1 = 173.130 µm w2 = 174.466 µm**

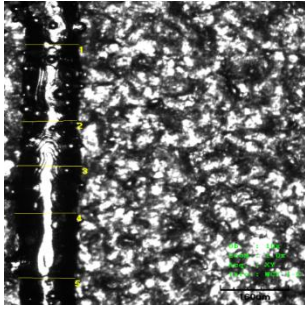
**E = 167 J/mm<sup>3</sup> V = 500 mm/s Mean bead width, vertical = 161.322 µm  
h1 = 50.035 µm h2 = 122.578 µm w1 = 168.779 µm w2 = 169.385 µm**



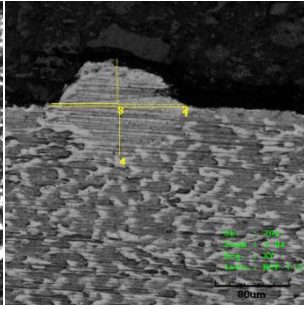
**E = 125 J/mm<sup>3</sup> V = 667 mm/s Mean bead width, vertical = 145.765 µm  
h1 = 92.534 µm h2 = 95.643 µm w1 = 165.001 µm w2 = 166.255 µm**

**E = 125 J/mm<sup>3</sup> V = 667 mm/s Mean bead width, vertical = 131.603 µm  
h1 = 52.504 µm h2 = 115.002 µm w1 = 137.523 µm w2 = 137.551 µm**

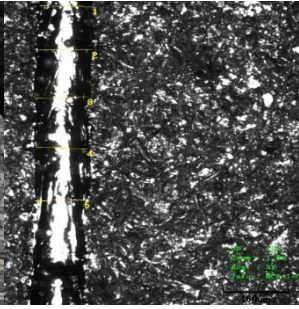
**Ti6Al4V View on Z axis  
(10 x magnification)**



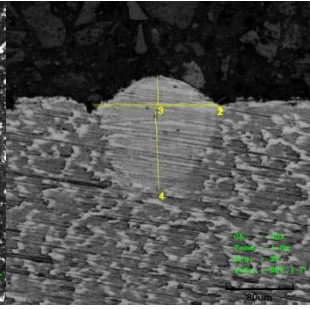
**Ti6Al4V Cross section  
(20 x magnification)**



**MMC View on Z axis  
(10 x magnification)**

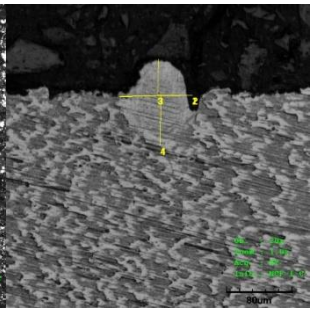
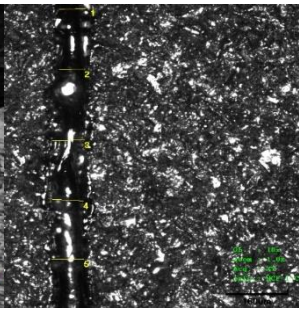
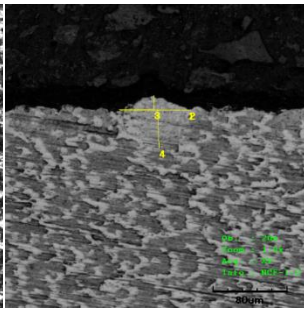
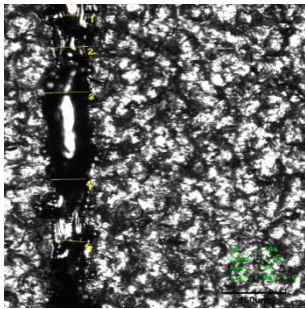


**MMC Cross section  
(20 x magnification)**



**E = 83 J/mm<sup>3</sup> V = 1000 mm/s Mean bead width, vertical = 138.262 µm  
h1 = 55.629 µm h2 = 60.625 µm w1 = 150.001 µm w2 = 145.001 µm**

**E = 83 J/mm<sup>3</sup> V = 1000 mm/s Mean bead width, vertical = 129.547 µm  
h1 = 35.630 µm h2 = 102.593 µm w1 = 151.251 µm w2 = 151.251 µm**



**E = 42 J/mm<sup>3</sup> V = 2000 mm/s Mean bead width, vertical = 95.605 µm  
h1 = 16.875 µm h2 = 45.039 µm w1 = 75.003 µm w2 = 77.503 µm**

**E = 42 J/mm<sup>3</sup> V = 2000 mm/s Mean bead width, vertical = 82.548 µm  
h1 = 45.017 µm h2 = 62.503 µm w1 = 87.502 µm w2 = 90.644 µm**

Observations the MMC powder exposed at 250 W once again showed good evidence of miscibility with the substrate with continuous beads for scan speeds up to 1000 mm/s. beads for both the MMC material and Ti5Al4V materials showed discontinuity. Comparison between Ti6Al4V and MMC beads showed similarities in the form of the bead without significant undercutting. There was no evidence of balling and a reduction in spatter shown with the MMC material in comparison to Ti6Al4V.

The improved wettability phenomenon was once again observed with the MMC beads having improved flow across the substrate for energy density levels from 250 J/mm<sup>3</sup> to 417 J/mm<sup>3</sup> demonstrated as regions either side of the bead.

Table 39 shows MMC single bead evaluation results compared to initial baseline results in terms of energy density using a laser power of 350 W.

**Table 39 Phase 3a; MMC Single Bead Evaluation Against Energy Density Compared to Baseline Results At 350 W**

| <b>Ti6Al4V View on Z axis<br/>(10 x magnification)</b>                                                                                                                 | <b>Ti6Al4V Cross section<br/>(20 x magnification)</b> | <b>MMC View on Z axis<br/>(10 x magnification)</b>                                                                                                                    | <b>MMC Cross section<br/>(20 x magnification)</b> |
|------------------------------------------------------------------------------------------------------------------------------------------------------------------------|-------------------------------------------------------|-----------------------------------------------------------------------------------------------------------------------------------------------------------------------|---------------------------------------------------|
|                                                                                                                                                                        |                                                       |                                                                                                                                                                       |                                                   |
| <p><b>E = 583 J/mm<sup>3</sup> V = 200 mm/s Mean bead width, vertical = 240.017 μm</b><br/> <b>h1 = 125.631 μm h2 = 133.126 μm w1 = 296.886 μm w2 = 293.756 μm</b></p> |                                                       | <p><b>E = 583 J/mm<sup>3</sup> V = 200 mm/s Mean bead width, vertical = 265.808 μm</b><br/> <b>h1 = 96.925 μm h2 = 175.005 μm w1 = 310.807 μm w2 = 309.466 μm</b></p> |                                                   |
|                                                                                                                                                                        |                                                       |                                                                                                                                                                       |                                                   |
| <p><b>E = 526 J/mm<sup>3</sup> V = 222 mm/s Mean bead width, vertical = 238.778 μm</b><br/> <b>h1 = 126.950 μm h2 = 122.005 μm w1 = 281.919 μm w2 = 282.544 μm</b></p> |                                                       | <p><b>E = 526 J/mm<sup>3</sup> V = 222 mm/s Mean bead width, vertical = 244.538 μm</b><br/> <b>h1 = 84.375 μm h2 = 176.069 μm w1 = 290.649 μm w2 = 286.267 μm</b></p> |                                                   |
|                                                                                                                                                                        |                                                       |                                                                                                                                                                       |                                                   |
| <p><b>E = 467 J/mm<sup>3</sup> V = 250 mm/s Mean bead width, vertical = 220.097 μm</b><br/> <b>h1 = 148.972 μm h2 = 171.893 μm w1 = 283.761 μm w2 = 290.003 μm</b></p> |                                                       | <p><b>E = 467 J/mm<sup>3</sup> V = 250 mm/s Mean bead width, vertical = 246.832 μm</b><br/> <b>h1 = 82.509 μm h2 = 126.877 μm w1 = 241.257 μm w2 = 242.513 μm</b></p> |                                                   |
|                                                                                                                                                                        |                                                       |                                                                                                                                                                       |                                                   |
| <p><b>E = 408 J/mm<sup>3</sup> V = 286 mm/s Mean bead width, vertical = 196.545 μm</b><br/> <b>h1 = 131.256 μm h2 = 142.697 μm w1 = 228.758 μm w2 = 228.126 μm</b></p> |                                                       | <p><b>E = 408 J/mm<sup>3</sup> V = 286 mm/s Mean bead width, vertical = 206.038 μm</b><br/> <b>h1 = 85.147 μm h2 = 191.480 μm w1 = 240.000 μm w2 = 240.001 μm</b></p> |                                                   |

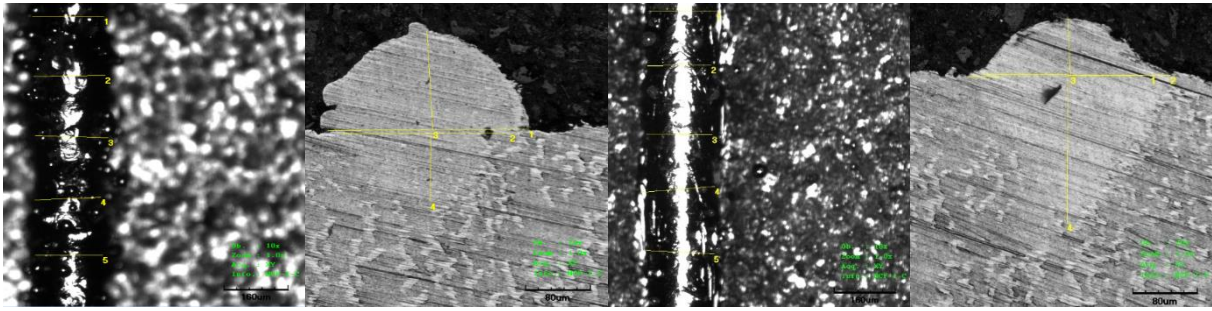


**Ti6Al4V View on Z axis  
(10 x magnification)**

**Ti6Al4V Cross section  
(20 x magnification)**

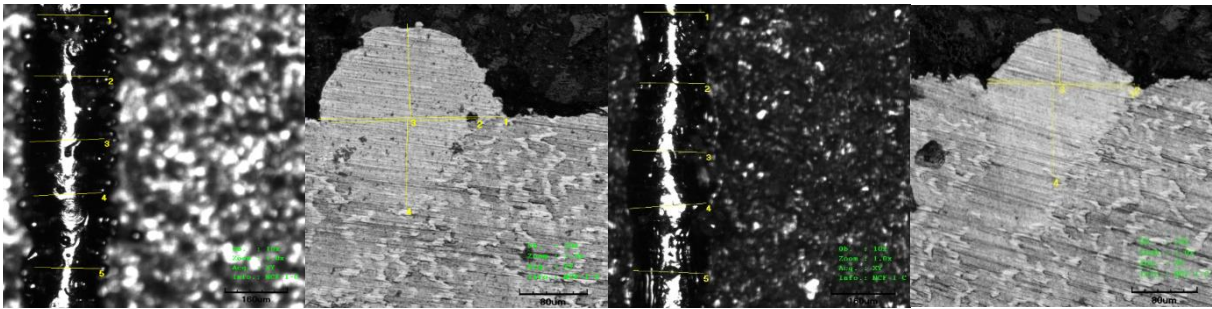
**MMC View on Z axis  
(10 x magnification)**

**MMC Cross section  
(20 x magnification)**



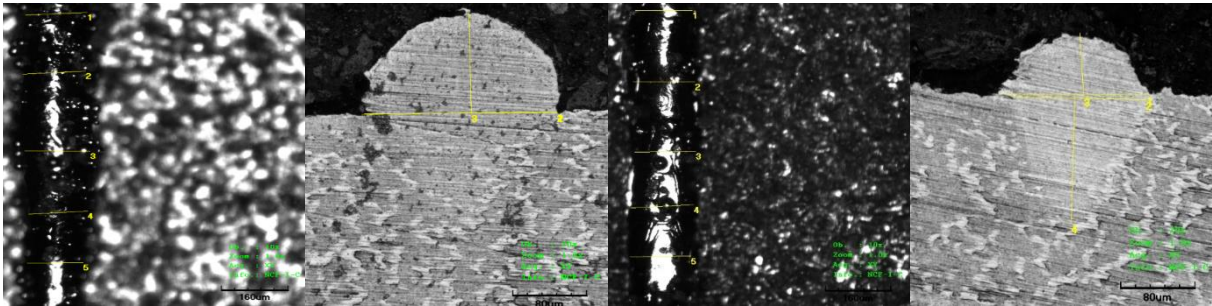
**E = 350 J/mm<sup>3</sup> V = 333 mm/s Mean bead width, vertical = 178.808 μm  
h1 = 134.584 μm h2 = 91.252 μm w1 = 253.757 μm w2 = 215.626 μm**

**E = 350 J/mm<sup>3</sup> V = 333 mm/s Mean bead width, vertical = 181.692 μm  
h1 = 74.469 μm h2 = 183.751 μm w1 = 213.126 μm w2 = 256.257 μm**



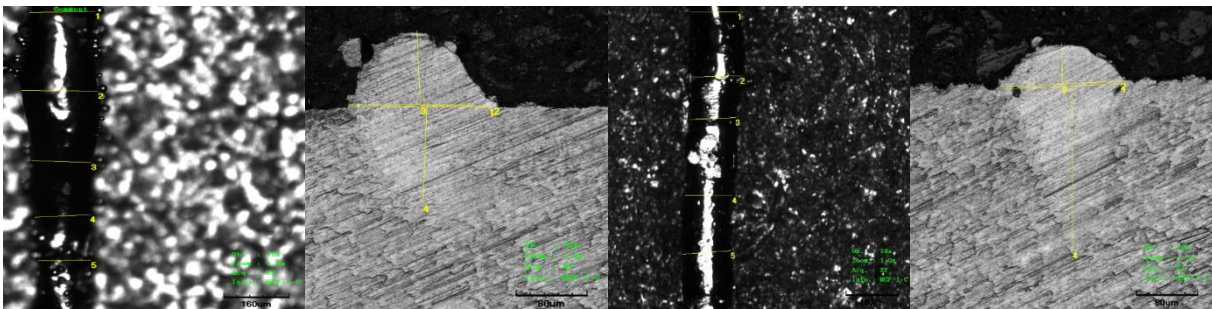
**E = 292 J/mm<sup>3</sup> V = 400 mm/s Mean bead width, vertical = 184.840 μm  
h1 = 123.807 μm h2 = 113.757 μm w1 = 177.570 μm w2 = 224.406 μm**

**E = 292 J/mm<sup>3</sup> V = 400 mm/s Mean bead width, vertical = 177.424 μm  
h1 = 70.636 μm h2 = 116.875 μm w1 = 179.768 μm w2 = 185.010 μm**



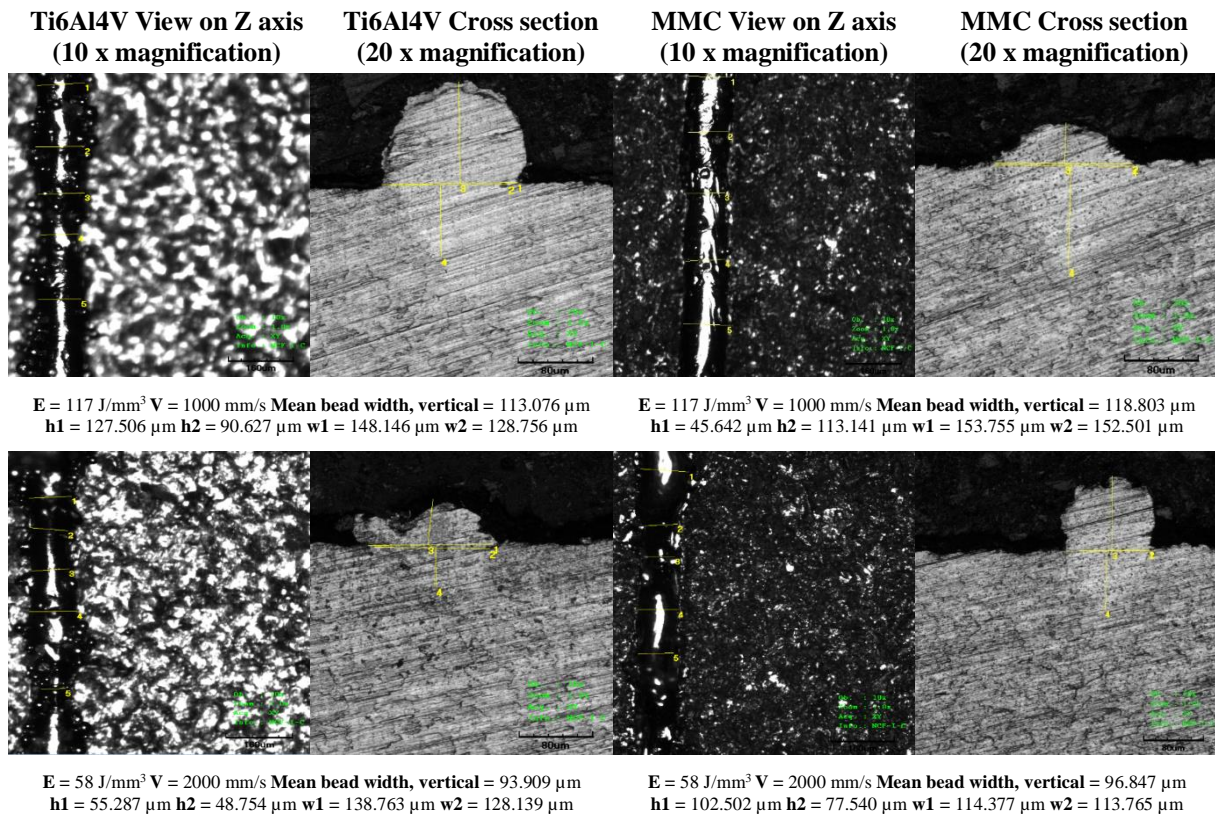
**E = 233 J/mm<sup>3</sup> V = 500 mm/s Mean bead width, vertical = 149.892 μm  
h1 = 124.400 μm h2 = - μm w1 = 216.273 μm w2 = 213.129 μm**

**E = 233 J/mm<sup>3</sup> V = 500 mm/s Mean bead width, vertical = 152.307 μm  
h1 = 70.137 μm h2 = 138.801 μm w1 = 161.876 μm w2 = 146.271 μm**



**E = 175 J/mm<sup>3</sup> V = 667 mm/s Mean bead width, vertical = 156.570 μm  
h1 = 93.825 μm h2 = 123.827 μm w1 = 162.505 μm w2 = 168.135 μm**

**E = 175 J/mm<sup>3</sup> V = 667 mm/s Mean bead width, vertical = 148.590 μm  
h1 = 56.253 μm h2 = 221.876 μm w1 = 159.523 μm w2 = 159.551 μm**



At 350 W the visual evidence presented a similar picture to the images for 150 W and 250 W with good bead continuity, reduced spatter with the MMC material and no evidence of balling. At all scan speeds the quality of bead was acceptable except for beads produced at 2000 mm/s. The improved wettability phenomenon was once again observed with the MMC beads having improved flow across the substrate for an energy density range from 408 J/mm<sup>3</sup> to 583 J/mm<sup>3</sup>.

There was no evidence to show that cracks had propagated longitudinally or laterally on the beads surface. This were clear indications that the material within both the Ti6Al4V beads and the MMC beads were ductile.

Figure 92 shows the Comparison between MMC and Ti6Al4V Bead widths represented as the mean value from measurements taken from five places along the bead, viewed in the vertical axis.

Comparison between the two feedstocks showed no significant variation. However, by representing the results in the form of linear trends (Figure 93), it was possible to see that as the energy density increased, the beads produced from the MMC feedstock became wider. This indicated that the meltpool remained at a high temperature for a longer period, such that it could consume additional powder particles producing a wider bead.

This would indicate that the MMC material requires less energy density.

This phenomenon, however, only appears at specific energy densities for each laser power, below which the bead widths for the MMC feedstock are narrower than Ti6Al4V. For a laser

power of 150 W this point was at  $\sim 112 \text{ J/mm}^3$ , for 250 W the point was at  $\sim 260 \text{ J/mm}^3$ , and for 350 W it was at  $\sim 150 \text{ J/mm}^3$ .

For this phenomenon to be significant there would also need to be a similar trend evident with the height of beads.

Figure 94 shows comparison between MMC and Ti6Al4V bead height ( $h_1$ ) at 150 W, 250 W and 350 W versus energy density. It can be seen from the results that the bead height increases in size as a function of energy density.

In comparison between feedstock materials, for Ti6Al4V beads exposed at 150 W, the bead height remained below  $60 \mu\text{m}$ , however, the bead height for the MMC material is above, only two values remained below, these being at the lower range of energy densities.

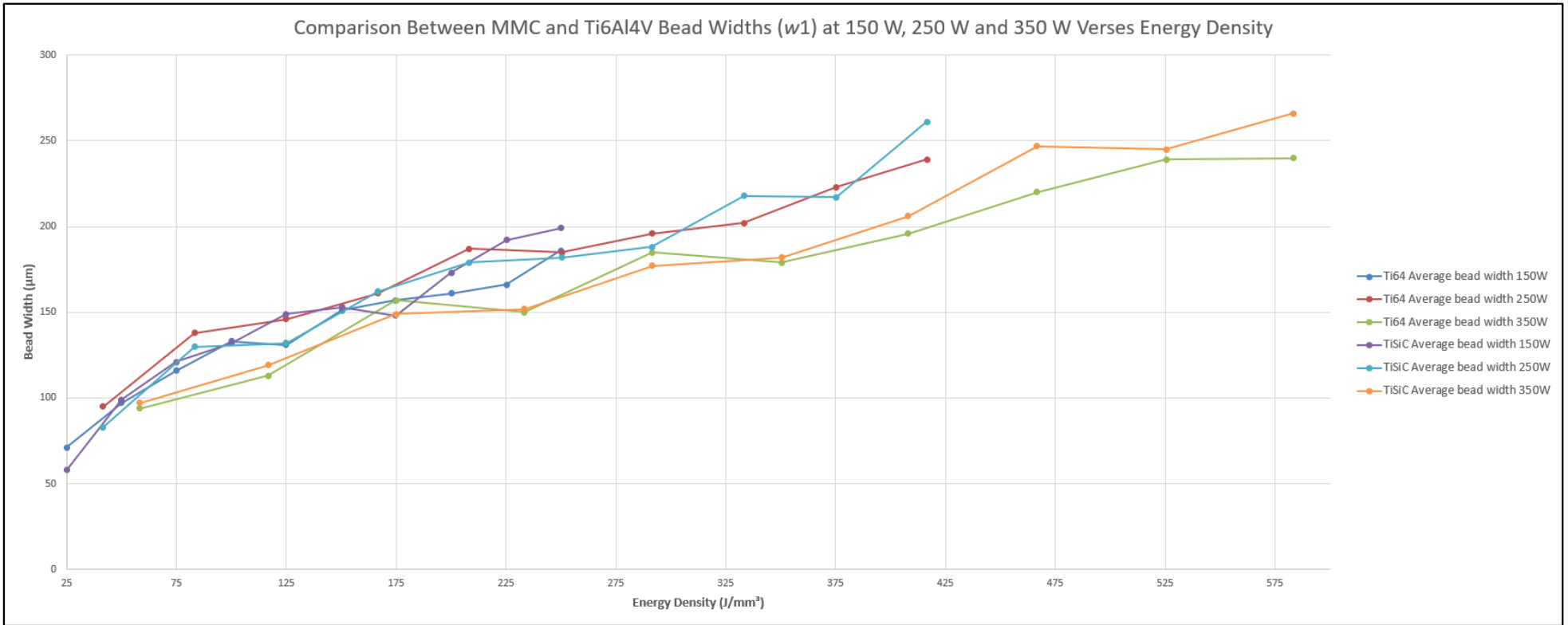
This evidence would also confirm the hypothesis that the MMC material requires less energy.

This however was not the case for MMC beads produced with a laser power of 250W, a large proportion of the beads were lower in height than the equivalent Ti6Al4V beads. This was also the case for MMC beads produced with a 350 W laser power.

Analysis of substrate penetration (Figure 95) showed that for a laser power of 150 W, penetration remained below  $90 \mu\text{m}$ , and was less than that of the Ti6Al4V material. For laser powers of 250 W and 350 W, substrate penetration exceeded that of Ti6Al4V indicating that the additional laser power, whilst demonstrating reductions in bead height, also increased the depth of substrate penetration with no benefit to the process.

Figure 96 shows comparison between MMC and Ti6Al4V substrate penetration width ( $w_2$ ) at 150 W, 250 W and 350 W versus energy density. As with initial observations of the baseline material, the width of substrate penetration increased as a function of energy density. Comparison between materials showed no significant change in width per energy density.

Combined analysis of all four bead characteristics showed that the beads formed using the MMC feedstock were predominately larger than those from Ti6Al4V, indicating that similar sized beads could be produced with lower energy densities. Increases in energy density, whilst still producing satisfactory bead formations, failed to improve on those produced at the lower range, beads appeared wider, flatter and substrate penetration increased excessively.



**Figure 92** Comparison Between MMC and Ti6Al4V Bead Widths ( $w_1$ ) at 150 W, 250 W and 350 W Versus Energy Density.

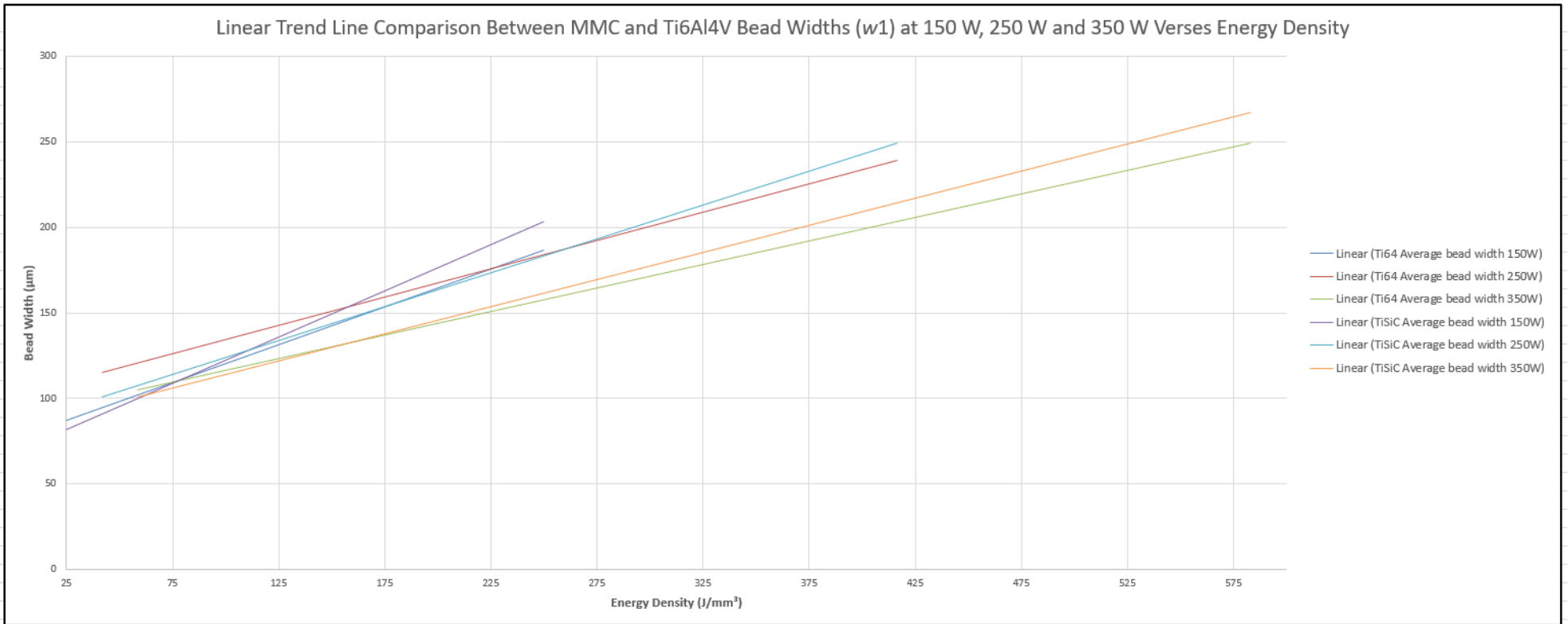


Figure 93 Linear Trend Line Comparison Between MMC and Ti6Al4V Bead Widths ( $w_1$ ) at 150 W, 250 W and 350 W Versus Energy Density.

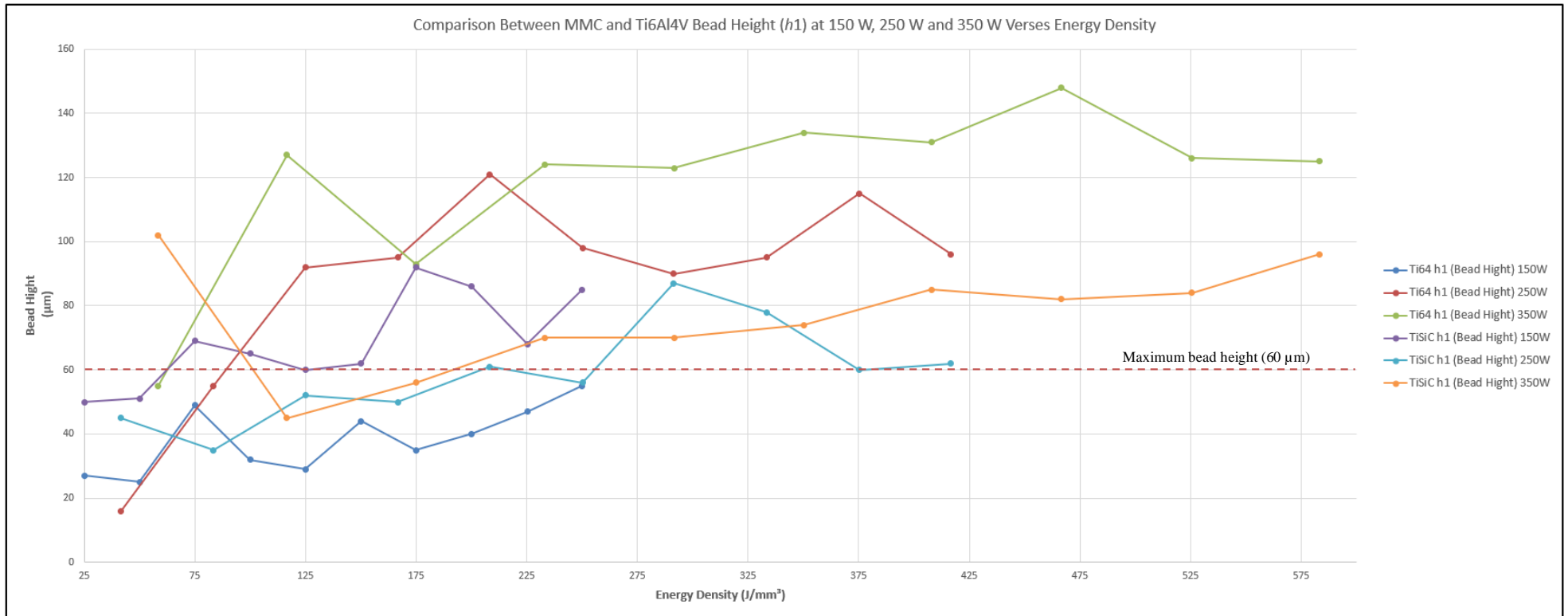
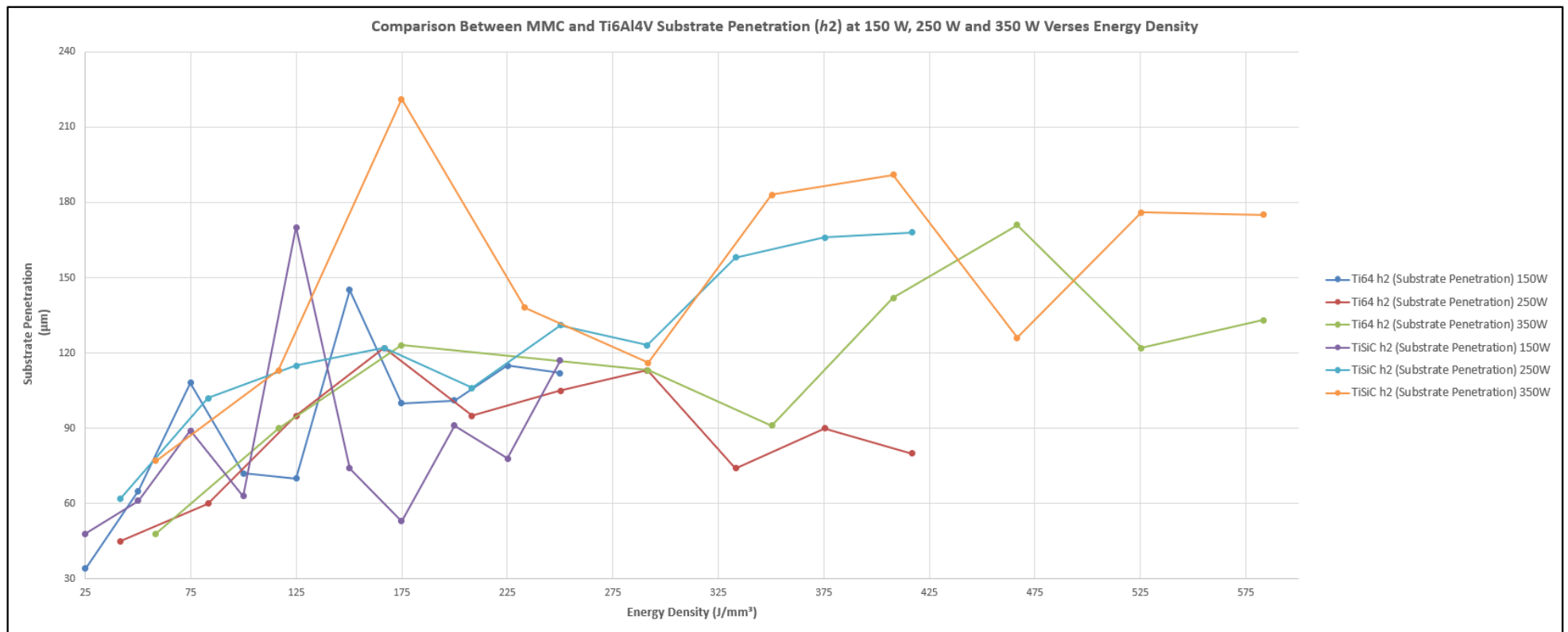


Figure 94 Comparison Between MMC and Ti6Al4V Bead Height ( $h_1$ ) at 150 W, 250 W and 350 W Verses Energy Density



**Figure 95 Comparison Between MMC and Ti6Al4V Substrate Penetration (h2) at 150 W, 250 W and 350 W Versus Energy Density.**

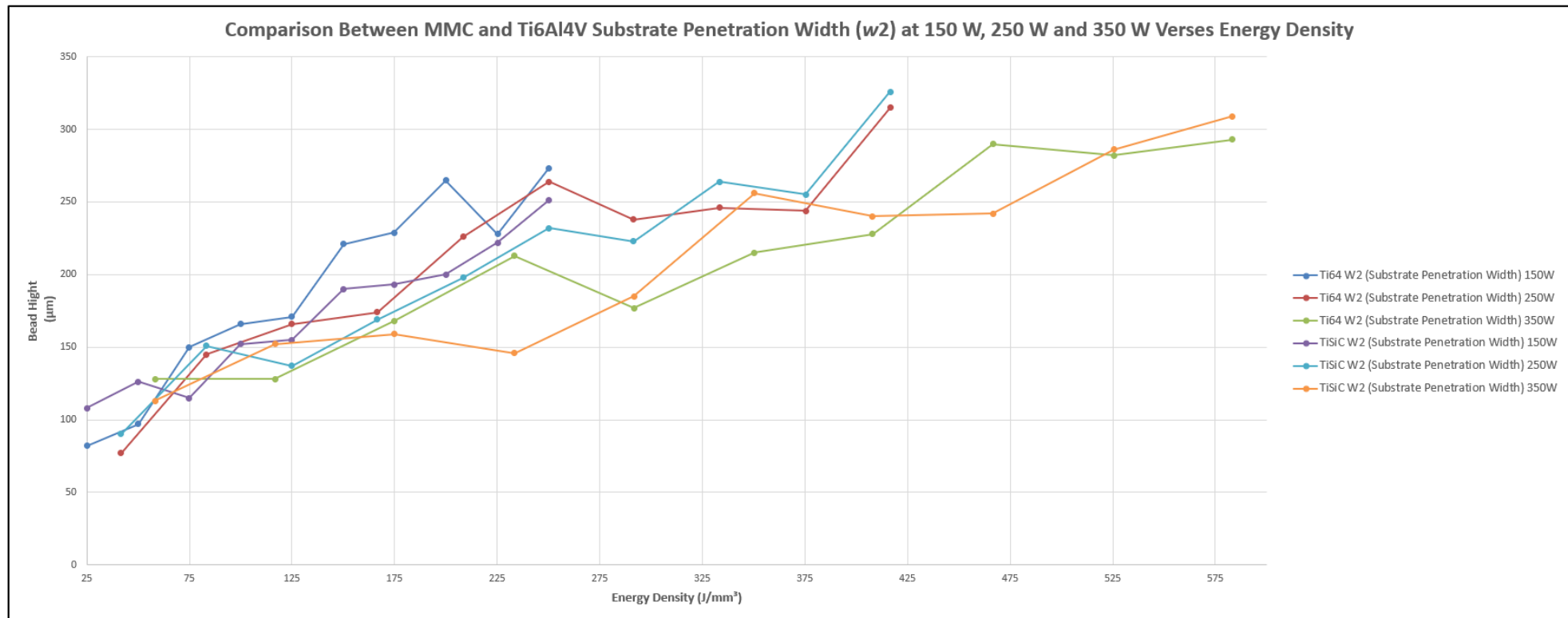


Figure 96 Comparison Between MMC and Ti6Al4V Substrate Penetration Width ( $w_2$ ) at 150 W, 250 W and 350 W Verses Energy Density.



## 5.7 Phase 3b: Hatch Spacing Evaluation of Multiple Beads.

In order to evaluate the effect of producing samples from bulk material, selected MMC feedstock beads were produced with a range of hatch distances with a view to better select a hatch spacing parameter suitable for multiple layer production. This would also assist in better understanding the data acquired during the single bead evaluations. Beads were selected from phase 3a based on bead height giving eleven suitable beads in total. At this stage it is unclear whether these parameters will produce fully dense parts, it is however known that the single beads produced, achieved satisfactory shape, substrate penetration and were lower than 60  $\mu\text{m}$  in height. Based on the width of the bead, the hatch spacing was calculated in accordance with Table 19 (section 4.7). to further filter selected beads, those scanned at 2000 mm/s were discounted on the basis that such beads were discontinuous. The remaining hatch spacing calculations are found in Table 40.

Table 40 Hatch Spacing Calculation.

| MMC Feedstock   |                |                                          |                                                  |                                    |                               |          |          |           |           |           |     |
|-----------------|----------------|------------------------------------------|--------------------------------------------------|------------------------------------|-------------------------------|----------|----------|-----------|-----------|-----------|-----|
| Laser Power (W) | Scan Speed (v) | Energy Density (Ed) (J/mm <sup>3</sup> ) | Bead height (h1) from phase 3a ( $\mu\text{m}$ ) | Bead Width (w1) from phase 3a (mm) | Hatch Spacing (h) Calculation |          |          |           |           |           | (h) |
|                 |                |                                          |                                                  |                                    | 40% (w1)                      | 60% (w1) | 80% (w1) | 100% (w1) | 120% (w1) | 140% (w1) |     |
| 150             | 1000           | 50                                       | 51                                               | 0.099                              | 0.040                         | 0.059    | 0.079    | 0.099     | 0.119     | 0.139     | (h) |
| 250             | 1000           | 83                                       | 35                                               | 0.130                              | 0.052                         | 0.078    | 0.104    | 0.130     | 0.156     | 0.182     | (h) |
|                 | 667            | 125                                      | 52                                               | 0.132                              | 0.053                         | 0.079    | 0.106    | 0.132     | 0.158     | 0.185     | (h) |
|                 | 500            | 167                                      | 50                                               | 0.162                              | 0.065                         | 0.097    | 0.130    | 0.162     | 0.194     | 0.227     | (h) |
|                 | 333            | 250                                      | 56                                               | 0.182                              | 0.073                         | 0.109    | 0.146    | 0.182     | 0.218     | 0.255     | (h) |
|                 | 1000           | 117                                      | 45                                               | 0.119                              | 0.048                         | 0.071    | 0.095    | 0.119     | 0.143     | 0.167     | (h) |
| 350             | 667            | 175                                      | 56                                               | 0.149                              | 0.060                         | 0.089    | 0.119    | 0.149     | 0.179     | 0.209     | (h) |

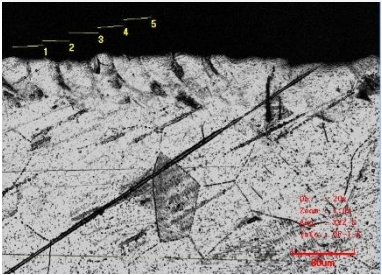
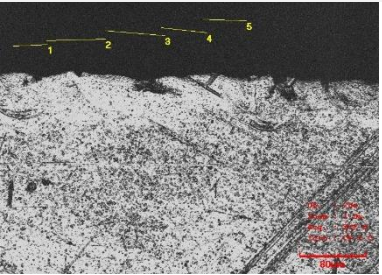
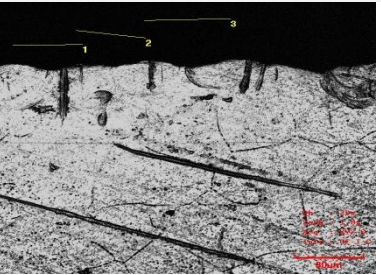
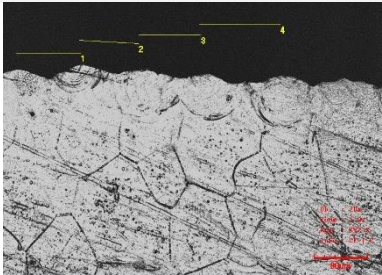
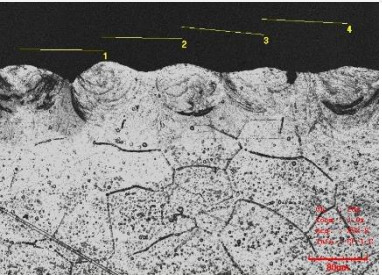
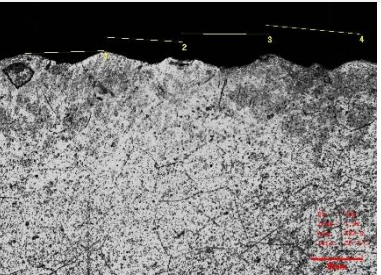
Tests were conducted in accordance with the methodology in section 4.7, cross-sectional samples were obtained using wire electro discharge machining (WEDM), polished using Struers polishing equipment and following the Struers polishing application notes appendix 2. Samples were observed using an Olympus confocal microscope and where possible, measurements were taken between beads. Results are shown below.

Where possible, measurements were taken between peaks and compared with the calculated hatch spacings shown in Table 40.

Table 41 shows Cross-sectional Views of Hatch Spacings ranging from 40% of the bead's original width ( $w_1$ ), up to 140%. Laser power was 150 (W), scan speed was 1000 mm/s ( $v$ ) and the layer thickness remained at 0.030 mm ( $t$ ). the two-rail system was used to ensure an accurate layer of feedstock.

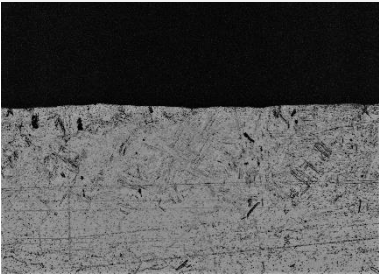
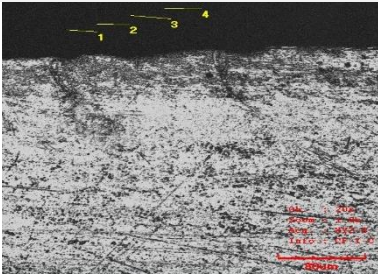
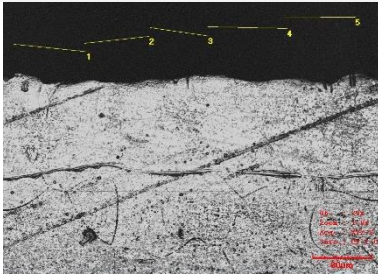
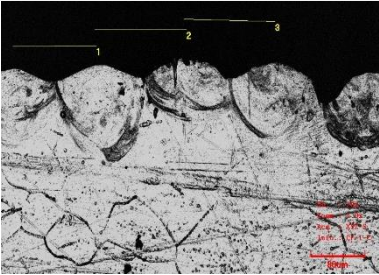
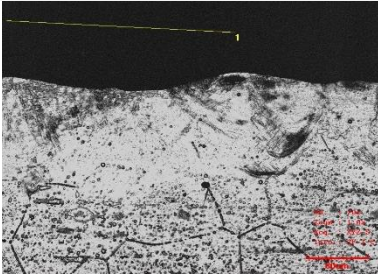
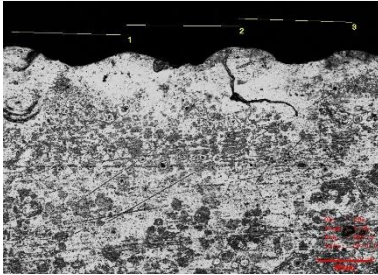
At 150 W, beads can be clearly seen, and the measurements taken are comparable with those calculated. All spacings appear to be equal with a consistently level progression is seen, demonstrating uniform use of feedstock. Preferred hatch spacings from these tests would be those at 100% and 120% of  $w_1$ , based on the beads being neither too close nor too far apart, therefore a hatch spacing of between 0.099 mm to 0.119 mm.

**Table 41 Cross-sectional Views of Hatch Spacing, 150 (W), 1000 mm/s (v) 0.030 mm (t).**


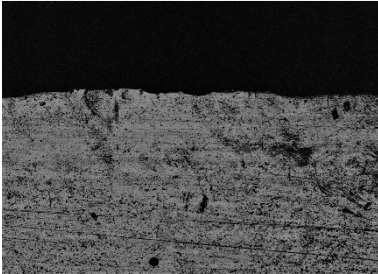
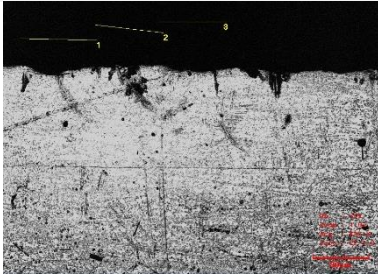
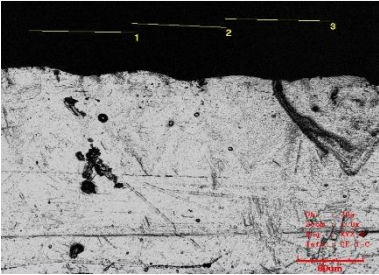
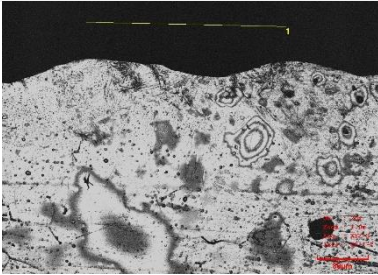
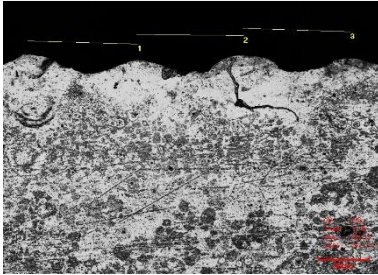
| 40% ( $w_1$ )                                                                     | 60% ( $w_1$ )                                                                     | 80% ( $w_1$ )                                                                       |
|-----------------------------------------------------------------------------------|-----------------------------------------------------------------------------------|-------------------------------------------------------------------------------------|
|  |  |  |
| Calculated $h = 0.040$ mm, Measured $h = 0.037$ mm                                | Calculated $h = 0.059$ mm, Measured $h = 0.060$ mm                                | Calculated $h = 0.079$ mm, Measured $h = 0.088$ mm                                  |
| 100% ( $w_1$ )                                                                    | 120% ( $w_1$ )                                                                    | 140% ( $w_1$ )                                                                      |
|  |  |  |
| Calculated $h = 0.099$ mm, Measured $h = 0.101$ mm                                | Calculated $h = 0.119$ mm, Measured $h = 0.116$ mm                                | Calculated $h = 0.139$ mm, Measured $h = 0.137$ mm                                  |

In Table 42 laser power was 250 (W), scan speed was 1000 mm/s (v) and the layer thickness remained at 0.030 mm (t). Beads are more challenging to distinguish and measure, at 40% of  $w_1$ , there appears to be a flat surface, substrate penetration can be seen. At 60%  $w_1$ , the shape of individual beads can be seen, however, these do not correlate with the calculated hatch spacing and therefore would not be accurate in this case. This would indicate that beads created with a hatch spacing of 40% or 60% merely re-melts the existing structure. Measurements taken for hatch spacings of 80%  $w_1$  and 100%  $w_1$ , compared accurately with calculated values, as did the hatch spacing at 140%. At 120%  $w_1$ , difficulties in determining points to measure resulted in inaccurate measurements. This is unfortunate as this may prove to be a good spacing. At 100%  $w_1$ , the beads overlap resulting in a minor gap between the fourth and fifth peaks. This is due to insufficient feedstock. Similarly, it could be argued that the hatch spacing for 140%  $w_1$ , is too far apart, all beads are similar in shape indicating that they received equal quantities of feedstock, however, this spacing could result in porosity within parts produced. This said, the preferred hatch spacings from these tests would be those at 100%, 120% and 140% of  $w_1$ , based on the beads being neither too close nor too far apart, therefore a hatch spacing of between 0.130 mm to 0.182 mm, would be chosen.

**Table 42 Cross-sectional Views of Hatch Spacing, 250 (W), 1000 mm/s (v) 0.030 mm (t).**

| 40% (w1)                                                                          | 60% (w1)                                                                          | 80% (w1)                                                                            |
|-----------------------------------------------------------------------------------|-----------------------------------------------------------------------------------|-------------------------------------------------------------------------------------|
|  |  |  |
| Calculated $h = 0.052$ mm, Measured $h = -$                                       | Calculated $h = 0.078$ mm, Measured $h = 0.033$ mm                                | Calculated $h = 0.104$ mm, Measured $h = 0.096$ mm                                  |
| 100% (w1)                                                                         | 120% (w1)                                                                         | 140% (w1)                                                                           |
|  |  |  |
| Calculated $h = 0.130$ mm, Measured $h = 0.134$ mm                                | Calculated $h = 0.156$ mm, Measured $h = 0.303$ mm                                | Calculated $h = 0.182$ mm, Measured $h = 0.174$ mm                                  |

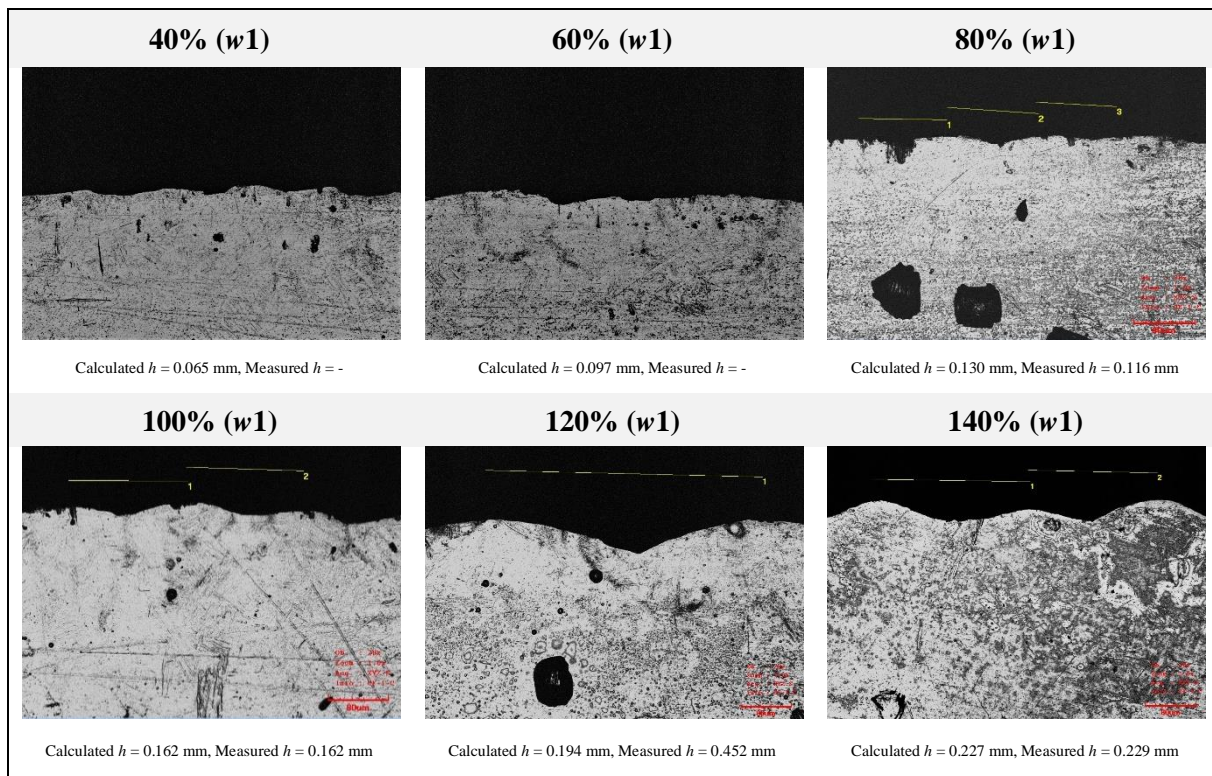
**Table 43 Cross-sectional Views of Hatch Spacing, 250 (W), 667 mm/s (v) 0.030 mm (t).**

| 40% (w1)                                                                            | 60% (w1)                                                                            | 80% (w1)                                                                              |
|-------------------------------------------------------------------------------------|-------------------------------------------------------------------------------------|---------------------------------------------------------------------------------------|
|  |  |  |
| Calculated $h = 0.053$ mm, Measured $h = -$                                         | Calculated $h = 0.079$ mm, Measured $h = -$                                         | Calculated $h = 0.106$ mm, Measured $h = 0.102$ mm                                    |
| 100% (w1)                                                                           | 120% (w1)                                                                           | 140% (w1)                                                                             |
|  |  |  |
| Calculated $h = 0.132$ mm, Measured $h = 0.128$ mm                                  | Calculated $h = 0.158$ mm, Measured $h = 0.319$ mm                                  | Calculated $h = 0.185$ mm, Measured $h = 0.174$ mm                                    |

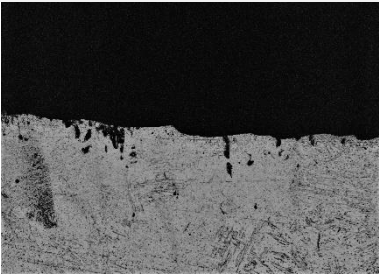

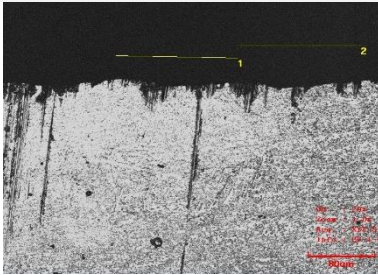
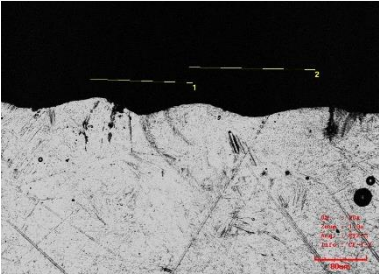
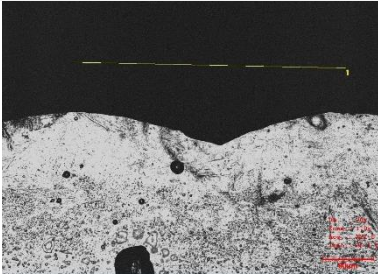
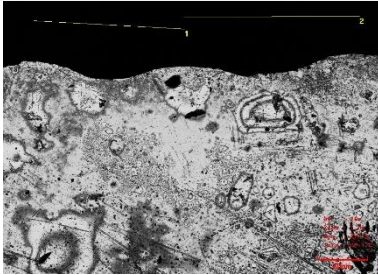
In Table 43 laser power was 250 (W), scan speed was 667 mm/s (v) and the layer thickness remained at 0.030 mm (t). Beads are again more challenging to distinguish and measure, at 40% and 60% of  $w_1$ , where the surface appears flat. At 80%  $w_1$ , the shape of individual beads can be seen, and the measured values correlate with the calculated values, as do those at 100% and 140% of  $w_1$ . Beads measured at 120%  $w_1$  were incorrect owing to the indistinguishability of the peaks. This again is due to the manner in which the feedstock is consumed, due to the energy density levels, the single bead consumes excessive amounts of feedstock from the surrounding area, the subsequent hatch spacing is therefore too small to encounter sufficient feedstock and is therefore smaller than required, the next bead is then produced in an area of sufficient feedstock and the bead is once again the correct size. It can also be seen that at 100%  $w_1$ , the profile is relatively flat, however, the substrate penetration is large ( $\sim 80 \mu\text{m}$ ), this would indicate that rather than producing a satisfactory bead, the process is removing feedstock from the area and the energy is going into the substrate. Therefore, based on the evidence, the best hatch spacing would be around 0.185 mm (140%  $w_1$ ).

This phenomenon is similar in Table 44 with hatch spacings at 40% and 60% of  $w_1$  producing near flat surfaces, hatch spacings of 80%, 100% and 140% of  $w_1$  producing measurements comparable with those calculated and a hatch spacing of 120%  $w_1$  demonstrating evidence of feedstock deficiencies. The hatch spacing of 100% of  $w_1$  can be seen to overlap marginally, this would prove inefficient during production and could lead to higher residual stress levels. Therefore, for a laser power of 250 W and a scan speed of 500 mm/s, the chosen hatch spacing should be approximately 0.227 mm (140%  $w_1$ ).

**Table 44** Cross-sectional Views of Hatch Spacing, 250 (W), 500 mm/s (v) 0.030 mm (t).



**Table 45 Cross-sectional Views of Hatch Spacing, 250 (W), 333 mm/s (v) 0.030 mm (t).**

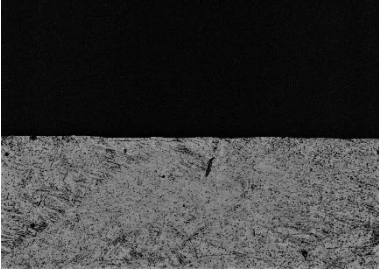
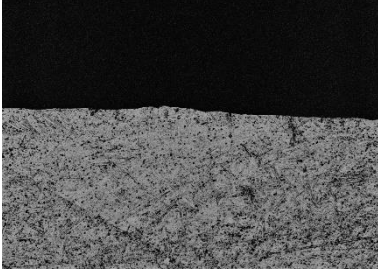
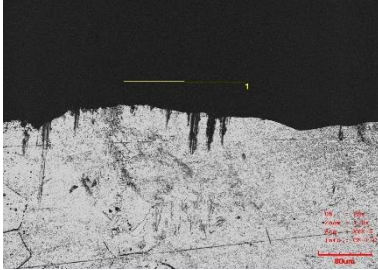
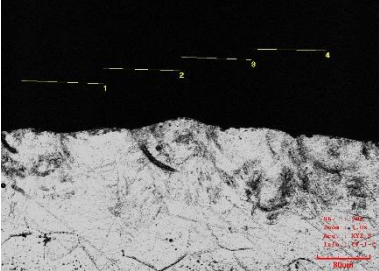
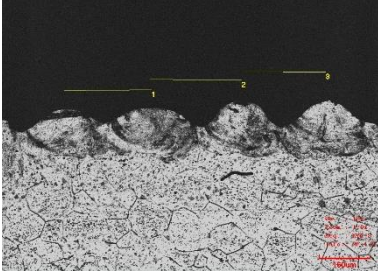
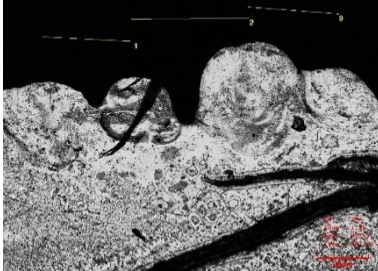
|                                                                                   |                                                                                   |                                                                                     |
|-----------------------------------------------------------------------------------|-----------------------------------------------------------------------------------|-------------------------------------------------------------------------------------|
| <b>40% (w1)</b>                                                                   | <b>60% (w1)</b>                                                                   | <b>80% (w1)</b>                                                                     |
|  |  |  |
| Calculated $h = 0.073$ mm, Measured $h = -$                                       | Calculated $h = 0.109$ mm, Measured $h = -$                                       | Calculated $h = 0.146$ mm, Measured $h = 0.150$ mm                                  |
| <b>100% (w1)</b>                                                                  | <b>120% (w1)</b>                                                                  | <b>140% (w1)</b>                                                                    |
|  |  |  |
| Calculated $h = 0.182$ mm, Measured $h = 0.180$ mm                                | Calculated $h = 0.218$ mm, Measured $h = 0.141$ mm                                | Calculated $h = 0.255$ mm, Measured $h = 0.270$ mm                                  |

From Table 45 with a laser power of 250 W and a scan speed of 333 mm/s, similar observations can be made to Table 44. A hatch spacing of 0.255 mm would be chosen based on the evidence (140% w1).

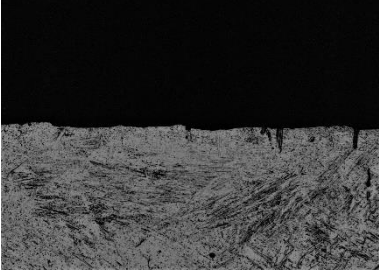
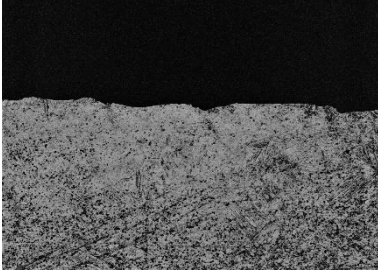
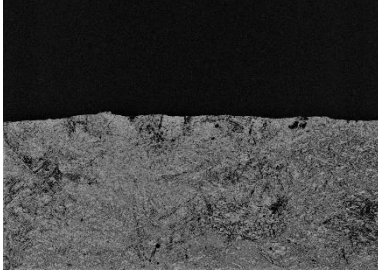
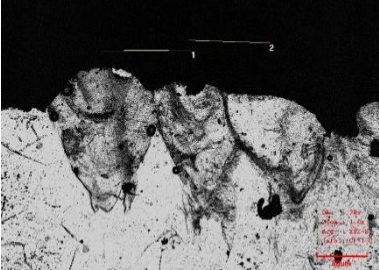
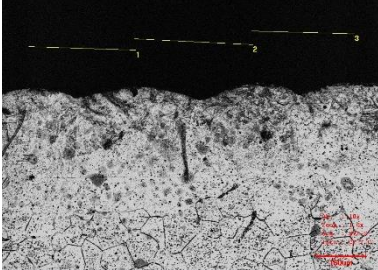
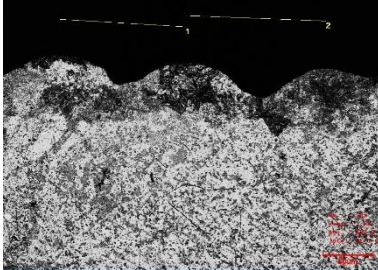
Samples analysed from Cross-sectional views of hatch spacings produced at 350 W, with a scan speed of 1000 mm/s are presented in Table 46. Hatch spacings from 40% to 100% of w1 are largely characterised as flat, whilst it appeared possible to obtain measurements at 80% w1, this was not comparable with the calculated value. Similarly, measurements taken at 100% w1 were accurate but showed excessive overlapping of the beads. At 120% w1, individual beads can be seen however, these are twice that of the calculated hatch spacing, indicating that feedstock is being consumed preferentially, leaving gaps in the hatch spacing sequence. At 140% w1, the measured hatch spacing correlates with that calculated, however, the surface is excessively rough and would be problematic during production. Therefore, there would be no hatch spacing selected from Table 46.

This would also be the case for hatch spacings produced at 350 W and a scan speed of 667 mm/s (Table 47). Due to the excessive energy density levels, surfaces produced are either devoid of feedstock, predominately substrate penetration or excessively rough. This would not be conducive with acceptable part production.

**Table 46** Cross-sectional Views of Hatch Spacing, 350 (W), 1000 mm/s (v) 0.030 mm (t).

| 40% (w1)                                                                          | 60% (w1)                                                                          | 80% (w1)                                                                            |
|-----------------------------------------------------------------------------------|-----------------------------------------------------------------------------------|-------------------------------------------------------------------------------------|
|  |  |  |
| Calculated $h = 0.048$ mm, Measured $h = -$                                       | Calculated $h = 0.071$ mm, Measured $h = -$                                       | Calculated $h = 0.095$ mm, Measured $h = 0.188$ mm                                  |
| 100% (w1)                                                                         | 120% (w1)                                                                         | 140% (w1)                                                                           |
|  |  |  |
| Calculated $h = 0.119$ mm, Measured $h = 0.118$ mm                                | Calculated $h = 0.143$ mm, Measured $h = 0.285$ mm                                | Calculated $h = 0.167$ mm, Measured $h = 0.163$ mm                                  |

**Table 47** Cross-sectional Views of Hatch Spacing, 350 (W), 667 mm/s (v) 0.030 mm (t).

| 40% (w1)                                                                            | 60% (w1)                                                                            | 80% (w1)                                                                              |
|-------------------------------------------------------------------------------------|-------------------------------------------------------------------------------------|---------------------------------------------------------------------------------------|
|  |  |  |
| Calculated $h = 0.060$ mm, Measured $h = -$                                         | Calculated $h = 0.089$ mm, Measured $h = -$                                         | Calculated $h = 0.119$ mm, Measured $h = -$                                           |
| 100% (w1)                                                                           | 120% (w1)                                                                           | 140% (w1)                                                                             |
|  |  |  |
| Calculated $h = 0.149$ mm, Measured $h = 0.138$ mm                                  | Calculated $h = 0.179$ mm, Measured $h = 0.359$ mm                                  | Calculated $h = 0.209$ mm, Measured $h = 0.219$ mm                                    |

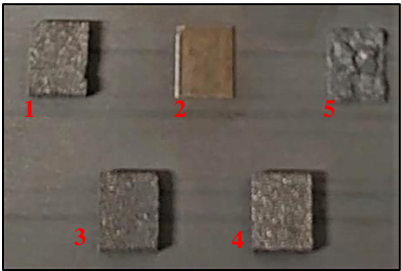
In summary, based on the evidence presented in Table 41 to Table 47, the following build parameters were chosen as acceptable for multiple layers experimentation (Table 48).

**Table 48 Phase 3c Build Parameters**

| <b>Phase 3c Build Parameters</b> |             |            |               |                 |
|----------------------------------|-------------|------------|---------------|-----------------|
|                                  | laser power | Scan speed | Hatch spacing | layer thickness |
| Table 41                         | 150         | 1000       | 0.109         | 0.03            |
| Table 42                         | 250         | 1000       | 0.156         | 0.03            |
| Table 43                         | 250         | 667        | 0.185         | 0.03            |
| Table 44                         | 250         | 500        | 0.227         | 0.03            |
| Table 45                         | 250         | 333        | 0.255         | 0.03            |
| Table 46                         | 350         | 1000       | -             | 0.03            |
| Table 47                         | 350         | 667        | -             | 0.03            |

**5.8 Phase 3c: Multiple Layer Evaluation of Density and Homogeneity of Reinforcement.**

Whilst multi-layer structures were produced as part of the research, it was clear that this was an area that would require further investigation in order to optimise the parameters developed throughout this research.



**Figure 97 Multiple Layer Evaluation of Density and Homogeneity of Reinforcement.**

It was evident from the cubes produced that there was still research to be done in terms of parameter optimisation. Cracks were found in all parts with increasing severity from sample one to sample five, this was due to increases in internal stress caused by the thermal gradient on solidification resulting in cracking and the catastrophic failure of sample five. Sample two has been removed for Crystallographic and chemical analysis. The density of the samples was not evaluated as it was visually evident that there was still work to be done to improve the density of the samples, therefore, measurements would provide little meaning.



## 5.9 Phase 3d: Crystallographic and chemical analysis of MMC Material.

Much of the Crystallographic and chemical analysis has been discussed in section 5.4.5, areas of high concentration of SiC were analysed and the results confirmed the presence of SiC in the approximate quantities predicted. Characteristically, concentrations of the SiC reinforcement material typically inhabited regions along the grain boundaries as seen in Figure 98.

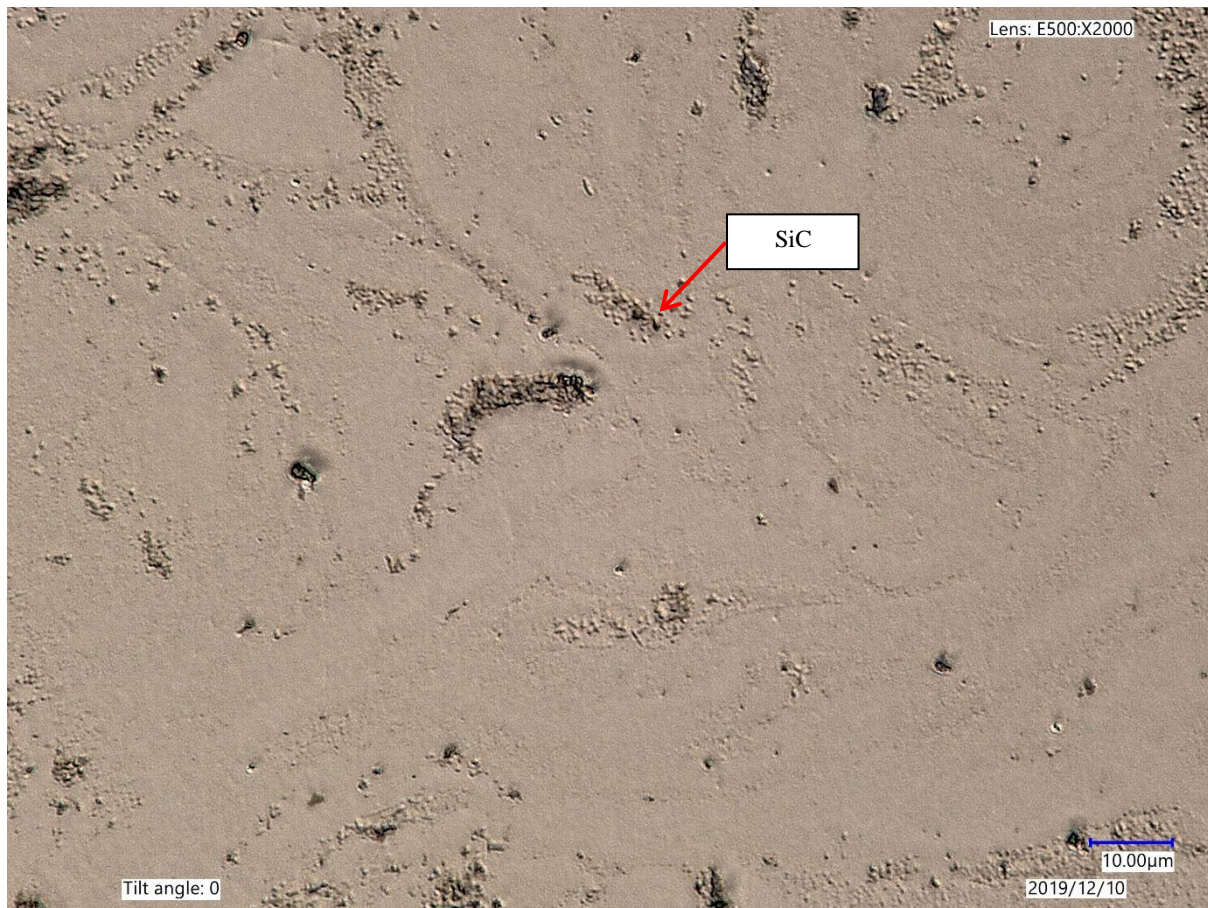


Figure 98 Optical microscopic view of MMC material (2K x magnification)

EDX analysis detected three primary compounds:

- Silicon Carbide  $C_1Si_1$  Hexagonal
- Titanium Silicide  $Ti_5Si_4$  Orthorhombic
- Silicon Oxide  $O_2Si_1$  Anorthic

The detection of SiC was due to the remaining presence of the reinforcement material, unaffected by the process. The analysis reported a high level of confidence in this result with a score of 45. Silicon oxide had a score of 37, with titanium silicide scoring 32. Whilst evidence of titanium silicide is encouraging, it does further explain issues of cracking within the structures. Titanium silicide is known to be brittle with poor fracture toughness, cracks are often

found because of the different coefficients of thermal expansion of  $Ti_5Si_4$  in different crystal directions, Therefore, tensile stresses and crack initiation occur.

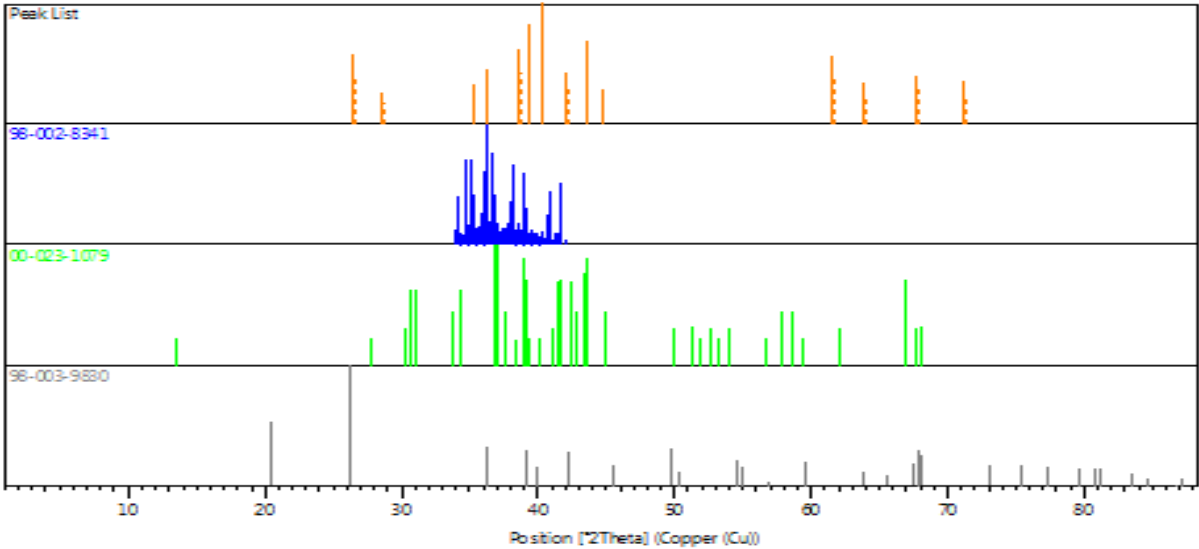


Figure 99 XRD Stick Pattern (98-002-8341  $C_1Si_1$ , 00-023-1079  $Ti_5Si_4$ , 98-003-9830  $O_2Si_1$ )

Figure 99 shows the XRD stick patterns in isolation showing the three primary compounds. Figure 100 shows the original diffractogram.

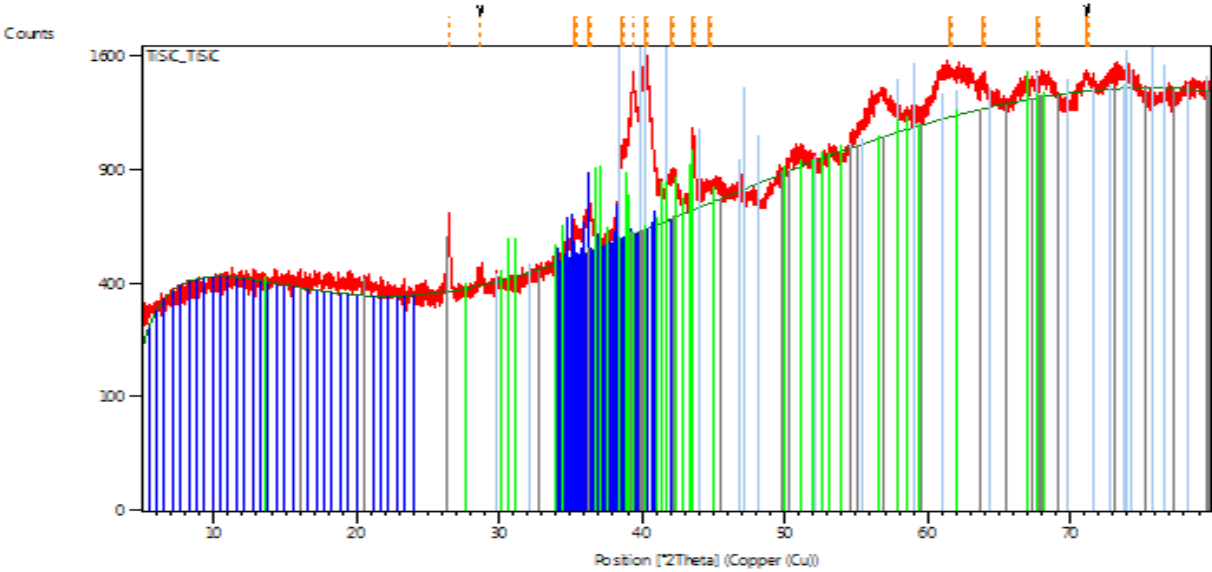


Figure 100 XRD Diffractogram ( $C_1Si_1$  green,  $Ti_5Si_4$  Blue,  $O_2Si_1$  Grey)

Full results can be found in appendix 3.

# Chapter Six

## 6.0 Conclusions

The aim of this research was to characterise MMC feedstock production through a mechanical alloying route and evaluate the materials characteristics regarding the SLM processing route. A comprehensive multistage mechanical alloying methodology was presented along with in-depth characterisation of in-process parameters and their effects on MMC material where contributions have been made to knowledge. This feedstock route cannot be tailored for all MMC formulations and guidelines are presented.

### 6.1 Baseline assessment of raw materials (Ti6Al4V).

- 1 The moisture content of Ti6Al4V was significantly low (0.59%), apparent density was 50.6% that of the density of Ti6Al4V with a measured angle of repose of 33°. It was concluded that these values were typical for Ti6Al4V.
- 2 Size and size distribution were carried out using Retsch Camsizer X2, results showed statistically calculated results as Q3 10% 28.8  $\mu\text{m}$ , Q3 50% 39.9  $\mu\text{m}$ , Q3 90% 49.9  $\mu\text{m}$ ,  $Mv3(\bar{x})$  39.7  $\mu\text{m}$ , Mean b/13 0.851 with 65% of the sample rounded (1-Q3 (b/1 = 0.850)). It was concluded that these values were also typical for Ti6Al4V.
- 3 Morphologically, the Ti6Al4V feedstock was analysed and an image database was obtained during the measurement of size. This was used to further understand the size and size distribution results by providing additional confirmation. In conclusion, the image database was able to successfully identify images of significance although these were low, therefore providing a high level of confidence in the results.
- 4 The Ti6Al4V powder was found to be of good roundness with a distribution range between 3  $\mu\text{m}$  to 75  $\mu\text{m}$ . agglomerations were few as were satellites.

### 6.2 Baseline assessment of raw materials (SiC).

- 5 The moisture content of SiC was low (1.78%), however, this was thought unacceptable within this research. After processing to remove moisture it was accepted at 0.96%. apparent density was 12.8% that of the density of SiC with a measured angle of repose of 48°. It was concluded that these values were typical for SiC.
- 6 The SiC powder was found to be angular in shape with a distribution range between ~0.10  $\mu\text{m}$  to ~0.90  $\mu\text{m}$ . The material agglomerated excessively making measurement challenging.

### **6.3 Baseline assessment of Ti6Al4V Single beads.**

- 7 A new approach for the evaluation and comparison of single beads was presented. Based across three laser power ranges (150 W, 250 W and 350 W) to evaluate a linear progression in energy density. The innovative approach enabled results to be better presented in comparison to the increased energy. In conclusion this method worked accurately and would provide a useful tool in the characterisation of new materials.
- 7.1 It was also concluded that this approach would work successfully on all metal platforms manufactured.
- 8 Mini platforms were developed and successfully utilised throughout this research, facilitating the economical use of smaller batch quantities of feedstock.
- 9 The two-rail system was developed to ensure that while conducting single layer characterisation, an accurate, reliable and repeatable deposit of feedstock can be achieved, whilst this was developed for a square platform system with the recoater-arm type mechanism, the principle can be developed for all systems.
- 10 Results for Ti6Al4V single beads showed that as energy densities increased, so did the volume of the bead, that said however, it became evident that increased laser power contributed to a flatter bead and increased substrate penetration. Reduced scan speed contributed to a larger volume of bead with increased bead height.
- 10.1 It was concluded that the development of the methodology based on energy density was effective in characterising a range of energy densities that typified the feedstock investigated. Once established, the methodology was also able to successfully show the effect the main parameters had on the bead's formation for further development.

### **6.4 Mechanical alloying (MA) of metal matrix composite (MMC) materials.**

- 11 Mechanical alloying (MA) was chosen as a system for combining dissimilar materials for transportation into the SLM system to overcome the effect that transportation and the powder delivery mechanism has on manually mixed powders. A new and novel equation was presented that calculated the resultant volume percentages of both matrix and reinforcement materials based on particle size. By using this equation it was shown that whilst the MA for AM methodology was successfully able to deliver accurate quantities of reinforcement material homogeneously throughout the matrix.
- 12 MA results showed that at low rotational speeds (500 rev/min), and an alloying time of twenty-four minutes was optimal to produce MMC feedstock exhibiting:
- Reinforcement material embed onto the surface of the matrix material.
  - Minimal increase in particle size.

- Minimal change in particles morphology.
- Reinforcement material homogeneously mixed throughout the feedstock.
- Avoided contamination.

## **6.5 MMC feedstock analysis for moisture, size, morphology and rheology in comparison to baseline assessment.**

- 13 In comparison to Ti6Al4V, the moisture content of the MMC feedstock increased due to the incorporation of the SiC reinforcement, however, this was less than the upper limit established within the research and lower than SiC alone, there was no need to further process the feedstock.
- 14 Particle size and size distribution for the MMC material alloyed for twenty-four minutes exhibited changes in the size distribution curve with increases in small and large fines. It was concluded that an increased quantity of small fines was attributed to un-alloyed SiC and the increase in large fines was due to the SiC coating the surface of the Ti6Al4V particles. These results varied between alloying times and was optimal at twenty-four minutes.
- 15 Rheologically, the results for the MMC feedstock sat between those of Ti6Al4V and SiC. In comparison to Ti6Al4V, apparent density decreased from 50.6% to 45.8%, an indication that 4.8% less material would be available per recoated layer. Angle of repose increased from 33° to 38° indicating that the surface of the particles was rougher and less likely to flow during recoat.

## **6.6 Assessment of MMC Single beads evaluated against energy density in comparison to Ti6Al4V baseline.**

- 16 Comparison between the MMC feedstock and the baseline assessments showed close similarities from increased energy densities.
- 17 The MMC feedstock required less energy to form beads of equivalent volume due to reduced reflectivity and retention of thermal energy. This was in contradiction to initial theories that increased energy was required for synthesis.

## **6.7 Hatch spacing evaluation of MMC material, multiple beads.**

- 18 Single beads with appropriate characteristics (bead height and substrate penetration) were selected and the characteristics of multiple beads was evaluated. Cross-sections of the beads were analysed to determine efficient use of feedstock in the formation of beads. It was concluded that at higher laser powers (250 W and 350 W), beads became flat and substrate penetration increased. Five sets of build parameters were selected:

Table 49 Selected Build Parameters from Phase 3b.

| Phase 3c Build Parameters |             |            |               |                 |
|---------------------------|-------------|------------|---------------|-----------------|
|                           | laser power | Scan speed | Hatch spacing | layer thickness |
| Table 41                  | 150         | 1000       | 0.109         | 0.03            |
| Table 42                  | 250         | 1000       | 0.156         | 0.03            |
| Table 43                  | 250         | 667        | 0.185         | 0.03            |
| Table 44                  | 250         | 500        | 0.227         | 0.03            |
| Table 45                  | 250         | 333        | 0.255         | 0.03            |

## 6.8 Multi-layer evaluation of density and homogeneity of reinforcement.

19 Five test samples were produced with the selected build parameters (Table 49), evidence showed that internal stresses were significantly high leading to catastrophic failure in sample five owing to a laser power of 250 W and a scan speed of 333 mm/s. the most successful sample was processed at 250 W with a scan speed of 1000 mm/s and a hatch spacing of 0.156 mm. this produced a sample with no visible cracking. It was concluded that a scan speed circa 1000 mm/s was acceptable but a lower laser power, circa 50 W may produce better parts.

## 6.9 Crystallographic and chemical analysis of MMC material.

20 Cryptographically, samples analysed exhibited excellent homogeneity of reinforcement indicating the robustness of the methodology. SiC was found along grain boundaries which would indicate improvements in fracture toughness may be possible.

21 Chemical analysis found SiC, SiO<sub>2</sub> and Ti<sub>5</sub>Si<sub>4</sub>. Silicon oxide was an unexpected chemical composition as there had as yet been no evidence of oxygen present within the system, Silicon carbide was expected, not only due to the addition as a reinforcement, but also as this was not expected to chemical dissolve into the system but remain as precipitates to improve wear resistance. Titanium silicide, whist predicted could be synthesised, was unexpected at large quantities, this will have implications for the printing of semiconductors.

22 It was concluded that the evidence of cracking within the samples was primarily due to incompatibilities in linear expansion coefficients between the matrix and reinforcement and temperature gradients during the build process.

# Chapter Seven

## 7.0 Recommendations for future work.

Within the research a complete and comprehensive methodology has been developed and presented for the mechanical alloying of small batch feedstock for experimentation and material development specifically within the SLM industry. Rigorous analytical methods have also been presented and demonstrated to yield reliable and confident results. There are, however, many areas that warrant further investigation and research to further the scientific understand.

- 1 Develop the energy density-based methodology to include 50 w laser powers.
- 2 Development of the multiple bead experiment to better understand the correlation between the single and multiple beads.
- 3 Analysis of mechanical properties (tensile strength, fracture toughness, hardness) of the MMC material.
- 4 Synthesise materials with similar linear expansion coefficients such as titanium boride and titanium carbide.
- 5 further research would benefit from the investigation of temperature gradients during the build process and the effect on the samples by monitoring the meltpool.

# Chapter Eight

## 8.0 Contribution to knowledge

- 1 A new approach for the evaluation and comparison of single beads was presented to evaluate linear progression in energy density. This enabled results for cross sections of single beads to be better presented in comparison to the increased energy and could be used successfully on all metal platforms manufactured.
- 2 Mini platforms were developed and successfully utilised throughout this research, facilitating the economical use of smaller batch quantities of feedstock. Heated mini platforms were also developed in the belief that increased heat would be required for synthesis, however, these were not required.
- 3 The two-rail system was developed for single layer characterisation to guarantee an accurate, reliable and repeatable deposit of feedstock.
- 4 Equation 5 was presented as an alternative to the energy density equation, substituting the laser spot size for hatch distance, when conducting single bead experiments.
- 5 Equation 6 was presented to calculate the maximum volume of reinforcement material achievable from particle size data.



# Chapter Nine

## 9.0 References

3T RPD. AM Reduces production steps, lead time and cost. Case studies.

A basic guide to particle characterisation. Malvern instruments worldwide. [WWW.malvern.com/contact](http://WWW.malvern.com/contact) 2012.

Agius, D. Kourousis, K.I. and Wallbrink, C. (2017) A Review of the As-Built SLM Ti-6Al-4V Mechanical Properties towards Achieving Fatigue Resistant Designs, *Metals* **8**, 75.

Algarth, J. et al., (2017) State of the art for additive manufacturing of metals. RAMP-UP; Roadmap for research and innovation to industrialize additive manufacturing of metals in Sweden (2016-03898).

Ahsana, M. N. Pinkertona, A. J. Richard Moatb, J. Shackletonb, J. (2011) A comparative study of laser direct metal deposition characteristics using gas and plasma-atomized Ti-6Al-4V powders, *Materials Science and Engineering A* (528), pp.7648-7657.

Asgari, H. Baxter, C. Hosseinkhani, K. Mohammadi, M. (2017) On microstructure and mechanical properties of additively manufactured AlSi10Mg 200C using recycled powder, *Materials Science & Engineering A* (707), pp.148-158.

Attar, H. Prashanth, K. G. Zhang, L. C. Calin, M. Okulov, I. V. Scudino, S. Yang, S. Eckert, J. (2015) Effect of Powder Particle Shape on the Properties of In Situ Ti-TiB Composite Materials Produced by Selective Laser Melting, *Journal of Materials Science & Technology* 31, pp.1001-1005.

Alman, D.E. and Hawk, J.A. (1999) The abrasive wear of sintered titanium-ceramic particle reinforced composites, *Wear*, 225-229, pp.629-639.

Al-Shemmeri, T.T. (2010) Engineering thermodynamics. Ventus publishing Aps.

Al-Shemmeri, T.T. (2012) Engineering thermodynamics solutions manual. Bookboon.com: Ventus publishing Aps.

Anish, R. Robert Singh and Sivapragash, M (2012) Techniques for processing metal matrix composite; A survey, *Procedia engineering* 38, pp.3846-3854.

Andrade, A. Morcelli, A. Lobo, R. (2010) Deformation and fracture of alpha-beta titanium alloy, *Revista Matéria*. **15**(2), pp. 364-370.

Atazadeh, N. Heydari, M.S. Baharvandi, H.R. and Ehsani, N. (2016) Reviewing the effects of different additives on the synthesis of the Si<sub>3</sub>SiC<sub>2</sub> MAX phase by mechanical alloying technique. *Int. Journal of refractory metals and hard materials*, 61, pp.67-78.

- Attar, H. Calin, M. Zhang, L.C. Scudino, S. and Eckert, J. (2014) Manufacture by selective laser melting and mechanical behaviour of commercially pure titanium. *Journal of materials science and engineering A* (593), pp.170-177.
- Axelsson, S. (2012) Surface characterization of titanium powders with x-ray photoelectron spectroscopy, Masters Diploma, ChSLMers University of Technology.
- Azeem, M.A. and Dye, D. (2014) In situ evaluation of the transformation behaviour of NiTi-based high temperature shape memory alloys. *Intermetallics*, 46, pp.222-230.
- Azom. (2004) Titanium Silicocarbide (Ti<sub>3</sub>SiC<sub>2</sub>) Titanium Silicon Carbide – Properties and Applications, <https://www.azom.com/article.aspx?ArticleID=2363>
- Bao, Y. Newkirk, J. Ruan, J. Sparks, T.E. and Liou, F. (2008) Effect of mechanical surface treatments on Ti-6Al-4V direct metal deposition parts, *Journal of manufacturing processes*, 10, pp.56-60.
- Banerjee, S. (2008) Simple derivation of Young, Wenzel and Cassie-Baxter equations, and its interpretations, Surface Physics Division, Saha Institute of Nuclear Physics, 1/AF Bidhannagar, Kolkata 700 064, India.
- Bandyopadhyay, D. (2004) The Ti-Si-C System (Titanium-Silicon-Carbon). *Journal of Phase Equilibria and Diffusion*, **25**(5).
- Barsoum, M.W. (2000) The Mn<sub>1</sub>AX<sub>n</sub> phase: a new class of solids; Thermodynamically stable nanolaminates, *Prog Solid St Chem*, **28**, pp.201-281.
- Baitimerov, R. Lykov, P. Zherebtsov, D. Radionova, L. Shultc, A and Gokuldoss Prashanth, K. (2018) Influence of Powder Characteristics on Processability of AlSi12 Alloy Fabricated by Selective Laser Melting. *Materials* **11**, (742).
- Baufeld, B. Van der biest, O. and Gault, R. (2010) Additive manufacturing of Ti-6Al-4V components by shaped metal deposition: microstructure and mechanical properties. *Materials and Design* **31**, pp.s106-s111.
- Baufeld, B. Brandl, E and Van der biest, O. (2011) Wire based additive layer manufacturing: Comparison of microstructure and mechanical properties of Ti-6Al-4V components fabricated by laser-beam deposition and shaped metal deposition. *Journal of materials processing technology* **211**, pp.1146-1158.
- Benson, J.M. and Snyders, E. (2015) The need for powder characterisation in the additive manufacturing industry and the establishment of a national facility. *South African Journal of Industrial Engineering*, **26**(2), pp.104-114.
- Bergstrom, D. Powell, J. Kaplan, A. F. H. (2007) The absorptance of steel to Nd:YLF and Nd:YAG laser light at room temperature. *Applied surface science* 253(11), pp.5017-2028.
- Berretta, S. Ghita, O. Evans, K.E. Anderson, and Newman, C. (2013) Size, Shape and flow of powders for use in selective laser sintering (SLS)
- Beuth, J. (2017) Additive manufacturing challenges for the gas turbine industry. Next Manufacturing centre, Carnegie Mellon University,

- Biffi, C.A. Figini, A. Tuissi, A. (2014) Influence of compositional ratio on microstructure and martensitic transformation of CuZr shape memory Alloys, *Intermetallics* **46**, pp.4-11.
- Brandl, E. Greitemeier, D. (2012) Microstructure of additive layer manufactured Ti-6Al-4V after exceptional post heat treatments. *Materials Letters* **81**, pp.84-87.
- Buvashekar, G. Shanmugam, S.N. Sankaranarayanan, K. and Sabarickan, R. (2009) A study of laser welding modes with varying beam energy levels, Proceedings of the Institution of mechanical engineers, part C: *journal of mechanical engineering science* **223**, pp.1141-1156.
- CAM2 Centre for additive manufacturing – metal, ChSLMers University of Technology, SE-412 96 Gothenburg, Sweden. +46 (0)31-772 10 00 [www.chSLMers.se](http://www.chSLMers.se)
- Cao, X. Jahazi, M. Immarigeon, J.P. and Wallace, W. (2006) A review of laser welding techniques for magnesium alloys, *Journal of materials processing technology* **171**, pp.188-207.
- Chalabyan, Avetik. Jansch, Elena. Niemann, Tom. Otto, Tobias. Zeumer, Benedikt. Zhuravleva, Ksenia. How 3-D printing will transform the metals industry. McKinsey and Company. 2017.
- Chang, F. Gu, D. Dai, D. Yuan, P. (2015), Selective laser melting of in-situ Al<sub>4</sub>SiC<sub>4</sub> + SiC hybrid reinforced Al matrix composites: Influence of starting SiC particle size, *Surface & Coatings Technology* **272**, pp.15-24.
- Chen, B. Shi, T.L. Li, M. Yang, F. Yan F. and Liao, G.L. (2014) Laser welding of annealed Zr<sub>55</sub>Cu<sub>30</sub>Ni<sub>5</sub>Al<sub>10</sub> bulk metallic glass, *Intermetallics* **46**, pp.111-117.
- Chen, X. and Bei, G. (2017) Toughening mechanisms on nanolayered MAX phase ceramics – A review, *Materials* **10**, 366. [www.mdpi.com/journal/materials](http://www.mdpi.com/journal/materials)
- Chun, S. Noh, J. Yeom, J. Kim, J. and Nam, T. (2014) Martensitic transformation behaviour of Ti-Ni-Ag alloys, *Intermetallics* **46**, pp.91-96.
- Clayton, J. (2014) Optimising metal powders for additive manufacturing, Metal Powder Report, September-October 2014, Vol.69 (5), pp.14-17. [info@freemantech.co.uk](mailto:info@freemantech.co.uk)
- Cordova, S. Campos, M. Tinga, T. (2017) Assessment of moisture content and its influences on laser beam melting feedstock.
- Dadbakhsh, S. and Hao, L. (2014) Effect of layer thickness in selective laser melting on microstructure of Al/5 wt.%Fe<sub>2</sub>O<sub>3</sub> powder consolidated parts, *The scientific world journal*, Volume 2014 Article ID 106129.
- Deshpande, A. Manda, P. Vanitha, C. and Singh, A. K. (2018) Microstructural Characterization of Metastable Beta Titanium Alloys in Hot Rolled and Solution Treated condition, *Materials Today: Proceedings* **5**, pp.3657-3663
- Dickens, P. Minshall, T. (2015) UK National strategy for additive manufacturing; Update report 2. [www.amnationalstrategy.uk](http://www.amnationalstrategy.uk)
- <http://www.differencebetween.net>

- Dimitrov, D. Becker, T.H. Yadroitsev, I. and Booyesen, G (2016) On the impact of different system strategies on the material performance of selective laser melting – manufacturing Ti6Al4V components, *South African journal of industrial engineering* **27**(3), pp.184-191.
- Dingal, S. Pradhan, T.R. Sarin Sunder, J.K. Roy Choudhury, A. and Roy, S.K. (2008) The application of Taguchi's method in the experimental investigation of the laser sintering process, *International journal of advanced manufacturing technology* **38**, pp.904-914.
- Dolinsek, S. (2005) Wear Characteristics of laser sintered moulding tools, *Wear* **259**, pp.1241-1247.
- Dynamic Ceramic, Crewe Hall Enterprise Park, Weston Road, Crewe, CW1 6UA, England +44(0)1270 501000, info\_crewe@coorstek.com
- El-Raghy, T. Barsoum, W. (1999) Processing and mechanical properties of Ti<sub>3</sub>SiC<sub>2</sub>: Reaction path and microstructure evaluation, *Journal of American ceramic society* **82**(10), pp.2849-2854.
- EOS GmbH (2016) Material data sheet, EOS Titanium Ti64, EOS GmbH Electro optical systems, Robert Stirling Ring 1, D-82152 Krailling Munchen.
- Eriksson, J. (2010) Transport properties at 3C-SiC interfaces PhD in Nanoscience, Scuola Superiore of the University of Catania, 2010
- European additive manufacturing group (EAMG)
- European powder metallurgy association (EPMA), epma.com
- Eustathopoulos, N. Voytovych, R. (2016), The role of reactivity in wetting by liquid metals: a review, *J Mater Sci* 51, pp. 425-437.
- Fiore, M. Neto, F.B. Azevedo, C. R. (2016) Assessment of the Ti-Rich corner of the Ti-Si phase diagram: the recent dispute about the eutectoid reaction. *Materials Research*. **19** (4), pp.942-653.
- FSLMbigl, M. Romaka, V.V. Grytsiv, A and Rogl, P. (2014) Formation and stability of the clathrate-I structure in the systems Sr-(Ni,Cu,Zn)-Ge based on experimental and DFT studies, *Intermetallics* **46**, pp.185-189.
- Fogagnolo, J.B. Ruiz-Navas, E.M. Robert, M.H and Torralbs, J.M. (2003) The effects of mechanical alloying on the compressibility of aluminium matrix composite powder, *Materials science and engineering* **355**(A), pp.50-55.
- Foratirad, H. Baharvandi, H and Maraghe, M.G. (2017) Effect of excess silicone content on the formation of nano-layered Ti<sub>3</sub>SiC<sub>2</sub> ceramic via infiltration of TiC preforms, *Journal of the European ceramic society* **37**, pp.451-457.
- Fukuda, A. Yoshikawa, T. Tanaka, T. (2009) A fundamental approach for the measurement of solid-liquid interfacial energy, *Journal of Physics: Conference Series* **165**.
- Gharbi, M Peyre, P. Gorny, C Carin, M. Morville, S. Le Masson, P. Carron, D and Fabbro, R (2013) Influence of various process conditions on surface finishes induced by the direct

- metal deposition laser technique on a Ti-6AL-4V alloy, *Journal of materials processing technology* **213**, pp.791-800.
- Griggs, J. Lang, A.C. Gruber, J. Tucker, G.j. Taheri, M.L and Barsoum, M.W. (2017) Spherical Nanoindentation, modelling and transmission electron microscopy evidence of ripplocations in Ti<sub>3</sub>SiC<sub>2</sub>, *Acta Materialia* **131**, pp.141-155.
- Gu, D. Chen, H. (2018) Selective laser melting of high strength and toughness stainless steel parts: The roles of laser hatch style and part placement strategy, *Materials Science & Engineering A* **725**, pp.419-427.
- Gu, D. Hagedorn, Y. Meiners, W. Meng, G. Batista, R.J.S. Wissenbach, K and Poprawe, R (2012) Densification behaviour, microstructure evolution, and wear performance of selective laser melting processed commercially pure titanium, *Acta Materialia* **60**, pp.3849-3860.
- Gu, D and Ma, C (2018) In-situ formation of Ni<sub>4</sub>Ti<sub>3</sub> precipitate and its effect on pseudoelasticity in selective laser melting additive manufactured NiTi-based composites, *Applied surface science* **441**, pp.862-870.
- Gu, D. Meiners, W. Li, C and Shen, Y. (2010) In situ synthesized TiC/Ti<sub>5</sub>Si<sub>3</sub> nanocomposites by high-energy mechanical alloying: microstructural development and its mechanism, *Materials Science and Engineering A* **527**, pp.6340-6345.
- Gu, D.D. Meiners, W. Wissenbach, K and Roprawe, R. (2012) Laser additive manufacturing of metallic components: materials, processes and mechanisms, *International materials review* **57**(3), pp.133-164.
- Gu, D. Shen, Y and Xiao, J (2008) Influence of processing parameters on particulate dispersion in direct laser sintered WC-Cop/Cu MMCs, *International journal of refractory metals and hard materials* **26**, pp.411-422.
- Gu, D. Wang, Z. Shen, Y. Li, Q and Li, Y. (2009) In-situ TiC particle reinforced Ti-Al matrix composites: powder preparation by mechanical alloying and selective laser melting behaviour. *Applied surface Science* **255**, pp.9230-9240.
- Gu, H. Gong, H. Pal, D. Rafi, K. Starr, T and Stucker, B (2013) Influence of energy density on porosity and microstructure of selective laser melted 17-4PH stainless steel, 24TH Annual international solid freeform fabrication symposium, University of Texas, Austin, Texas, 12-14 August. pp.474-489.
- Gupta, M. (2017) 3D printing of metals, (editorial) *Journal of Metals* **7**, Department of mechanical engineering, national university of Singapore, 9 engineering drive 1, Singapore 117576, Singapore: mpegm@nus.edu.sg pp.402-403.
- Hanzel, P. Zetek, M. Baksa, T and Kroupa, T (2015) The influence of process parameters on the mechanical properties of SLM Parts, *Procedia engineering* **100**, pp.1405-1413.
- Hentschel, M.L and Page, N.W (2003) Selection of descriptors for particle shape characterization. *Particle & Particle Systems Characterization*, **20**(1), pp.25-38.

- Hidnert, P. (1943) Thermal expansion of titanium, *Journal of research of the national bureau of standards*, Volume **30**, pp.101-105, National bureau of standards.
- Ho-Duc, L.H. (2002) Synthesis and characterisation of the properties of Ti<sub>3</sub>SiC<sub>2</sub>/SiC and Ti<sub>3</sub>SiC<sub>2</sub>/TiC composites. Master of science thesis, Drexel University.
- Holt John M. (Tim), Technical Ed; C. Y. Ho, Ed. *Structural Alloys Handbook*, 1996 edition, CINDAS/Purdue University, West Lafayette, IN.
- Hu, B and Richardson, I.M (2006) Mechanism and possible solution for transverse solidification cracking in laser welding of high strength aluminium alloys, *materials science and engineering A* **429**, pp.287-294.
- Hu, L. Kothalkar, A. Proust, G. Karaman, I and Radovic, M (2014) Fabrication and characterisation of NiTi/Ti<sub>3</sub>SiC<sub>2</sub> and NiTi/Ti<sub>2</sub>AlC composites, *Journal of alloys and compounds* **610**, pp.635-644.
- Hung, Y.C and Withers, P.J (2012) Fibre bridging during high temperature fatigue crack growth in Ti/SiC composites, *Acta Materialia* **60**, pp.958-971.
- [http://www.lindegas.ru/en/applications/laser\\_technologies/gases\\_for\\_laser\\_welding](http://www.lindegas.ru/en/applications/laser_technologies/gases_for_laser_welding).
- Innovate UK-NEDO Meeting (2016) New manufacturing technology – metal additive manufacturing.
- Izhevskiy, V.A. Genova, L.A. Bressiani, J.C & Bressiani, A.H.A. (2000) Review article: Silicon Carbide. Structure, properties and processing. *Ceramics* **46**(297) pp.4-13.
- Jabbar, H. Monchoux, J.P. Thomas, M. Pyczak, F and Couret, A. (2014) Improvement of creep properties of TiAl alloys defined by spark plasma sintering. *Intermetallics* **46** pp.1-3.
- Jandl, I. Boero, F. Ipser, H and Richter, K.W. (2014) Phase equilibria and structural investigations of the general NiAs-type in the ternary systems Ni-Sn-Te, *Intermetallics* **46**, pp.199-210.
- Jing, S. Lian, G. (2001) Dispersing SiC Powder and improving its Rheological behaviour, *Journal of the European Ceramic Society* **21**, pp.2447-2451.
- Jing, W. Peijie, L. Guangbao, M. Yuexian, Z. (2010) Microstructural evaluation caused by electromagnetic stirring in superheated AlSi7Mg alloys, *Journal of materials processing technology* **210**, pp.1652-1659.
- Jordan, J.L. Sekine, T. Kobayashi, T. Li, X. Thadhani, N.N. El-Raghy, T. and Barsoum, M.W. (2003) High pressure behaviour of Titanium-Silicon Carbide (Ti<sub>3</sub>SiC<sub>2</sub>), *Journal of applied physics* **93**, pp.9639-9643.
- Jung, Y.I. Parl, J.H. Kim, H.G. Park, D.J. Park, J.Y and Kim, W.J. (2016) Effect of Ti and Si interlayer materials on the joining of SiC ceramics, *Nuclear engineering and technology* **48**, pp.1009-1014.
- Kainer, K.U. (2006) *Basics of metal matrix composites*. Germany: Wiley-VCH Verlag GmbH & Co.

- Khaing, M.W. Fuh, J.Y.H and Lu, L (2001) Direct metal laser sintering for rapid tooling: processing and characterisation of EOS parts, *Journal of materials processing technology* **113**, pp.269-272.
- Klicpera, M. Javorsky, P. Cermak, P. Rudajevova, A. Denis, S. Brunatova, T. Cisarova, I (2014) Crystal Structure and its Stability in CeCuAl<sub>3</sub> Single crystal, *Intermetallics* **46**, pp.126-130.
- Knowles, C.R. Becker, T.H and Tait, R.B (2012) Residual stress measurements and structural integrity implications for selective laser melted Ti-6Al-4V, *South African journal of industrial engineering* **23**(3), pp.119-129.
- Krakhmalev, P. Yadroitsev, I. Yadroitsava, I. and de Smidt, O. (2017) Functionalization of Biomedical Ti6Al4V via In Situ Alloying by Cu during Laser Powder Bed Fusion Manufacturing, *Materials* **10**, 1154
- Krinitcyn, M. Fu, Z. Harrsi, J. Kostikov, K. Pribytkov, G.A. Greil, P and Travitzky, N (2017) Laminated object manufacture of in-situ synthesized MAX-phase composites, *Ceramics international* **43**, pp.9241-9245.
- Kruth, J.P. Froyen, L. Van Vaerenbergh, J. Mercelis, P. Rombouts, M and Lauwers, B. (2004) Selective laser melting of iron-based powder, *Journal of materials processing technology* **149**, pp.616-622.
- Kruth, J.P. Leu, M.C. Nakagawa, T (1998) Process in additive manufacturing and rapid prototyping, Keynote paper Annals of the CIRP **47**(2), pp.525-540.
- Kruth, J. P. Levy, G. Klocke, F. Childs, T. H. C. (2007) Consolidation phenomena in laser and powder-bed based layered manufacturing. Annals of the CIRP **56**(2), pp.730-759.
- Kumar Ghosh, S and Saha, P (2011) Crack and wear behaviour of SiC particulate reinforced aluminium based metal matrix composite fabricated by direct metal laser sintering process, *Materials and design* **32**, pp.139-145.
- Kumar Ghosh, S. Saha, P and Kishore, S (2010) Influence of size and volume fraction of SiC particulates on properties of ex situ reinforced Al-4.5Cu-3Mg metal matrix composite prepared by direct metal laser sintering process, *Materials science and engineering A* **527**, pp.4694-4701.
- Kumar, V. Fang, Z. Z. Wang, H and Shetty, D. K. (2016) Geometric model of sintering of unequal-sized particles. *Powder metallurgy* **59**(3), pp.170-181.
- Kurzynowski, T. Chlebus, E. Kuźnicka, B. Reiner, J. (2012) Parameters in Selective Laser Melting for processing metallic powders. SPIE 8239, High Power Laser Materials Processing: Lasers, Beam Delivery, Diagnostics, and Applications, San Francisco, California, USA
- Kusuma, C. (2014) The Effect of Laser Power and Scan Speed on Melt Pool Characteristics of Pure Titanium and Ti-6Al-4V alloy for Selective Laser Melting, Kakatiya University.
- Lecoanet, A. Ivey, D.G. and Henein, H. (2014) Simulation of the temperature profile during welding with COMSOL Multiphysics® software using Rosenthal's approach. COMSOL Conference in Boston.

- Leuders, S. Thone, M. Riemer, A. Niendorf, T. Troster, T. Richard, H.A. and Maier, H.J (2013) On the mechanical behaviour of titanium alloy TiAl6V4 manufactured by selective laser melting: fatigue resistance and crack growth performance, *International journal of fatigue* **48**, pp.300-307.
- Li, J.F. Matsuki, T. and Watanabe, R. (2002) Mechanical-alloying-assisted synthesis of Ti<sub>3</sub>SiC<sub>2</sub> powder, *Communications of the American ceramic society* **85**(4), pp.1004-1006.
- Li, H.T. Xia, M. Jarry, P.H. Scamans, G.M and Fan, Z (2011) Grain reinforcement in a AlZnMgCuTi alloy by intensive melt shearing: a multi-step nucleation mechanism, *Journal of crystal growth* **314**, pp.285-292.
- Liang, B. Han, X. Zou, Q. Zhao, Y. and Wang, M. (2009) TiC/Ti<sub>3</sub>SiC<sub>2</sub> Composite prepared by mechanical alloying. *Int. Journal of refractory metals and hard materials* **27** pp.664-666.
- Lin, Z.J. Zhuo, M.J. Zhou, Y.C. Li, M.S. and Wang, J.Y. (2006) Microstructural Relationship between compounds in the Ti-Si-C system, *Scripta Materialia* **55**, pp.445-448.
- Linde Group, The. info@linde.com. Additive manufacturing and powder metallurgy
- Liu, D. Hu, P. and Min, G. (2015) Interfacial reaction of cast Wu particulate reinforced titanium metal matrix composites coated by laser processing, *Optics and laser technology* **69** pp.180-186.
- Z. Liu, Z. Welsch, G. (1988) Literature Survey on Diffusivities of Oxygen, Aluminum, and Vanadium in Alpha Titanium, Beta Titanium, and in Rutile, *Metallurgical Transactions A*, **19**(4), pp.1121-1125
- Locker. Metal 3D Printer Guide – All About Metal 3D Printing, 2018.
- Lu, X.H. Yang, Y.Q. Huang, B. Luo, X and Liu, Y.C. (2006) Reaction diffusion in continuous SiC fibre reinforced Ti matrix composites, *Transactions of nonferrous metals society of China* **17**, pp.27-34.
- Maeda, K and Childs, T.H.C. (2004) Laser sintering (SLS) of hard metal powders for abrasion resistant coatings, *Journal of materials processing technology* **149**, pp.609-615.
- Makoana, N.W. Moller, H. Burger, H. Tlotleng, M. Yadroitsev, I. (2016) Evaluation of single tracks of 17-4PH Steel manufactured at different power densities and scanning speeds by selective laser melting. *South African Journal of industrial engineering* **27**(3), pp.210-218.
- Malvern instruments worldwide (2012) A basic guide to particle characterisation.
- Manickavasagam, K. Atzeni, E. Riccardo, C. Calignano, F. Diego, M. Ambrosio, E. P. and Iuliano, L. (2014). On the effect of process parameters on properties of AlSi10Mg parts produced by DMLS. *Rapid Prototyping Journal*, Vol. **20**(6), pp.449-458.
- Mattern, A. Huchler, B. Staudenecker, D. Oberacker, R. Nagel, A and Hoffmann, M.J (2004) Preparation of interpenetrating ceramic-metal composites, *Journal of European ceramic society* **24**, pp.3399-3408.



- Melendez, I.M Neubauer, E. Angerer, P. Danninger, H and Torralba, J.M (2011) Influence of nano-reinforcements on the mechanical properties and microstructure of titanium matrix composites, *Composites science and technology* **71**, pp.1154-1162.
- Mikli, V. Kaerdi, H. Kulu, P and Besterci, M. (2001) Characterization of powder particle morphology. *Proceedings of the Estonian Academy of Sciences: Engineering (Estonia)*, **7**(1), pp.22-34.
- Miracle, D.B. (2005) Metal Matrix Composites – From Science to technological significance, *Composite Science and Technology* **65**, pp.2526-2540
- Montealegre, I. Melendez. Neubauer, E. Angerer, P. Danninger, H and Torralba, J.M (2011) Influence of nano-reinforcements on the mechanical properties and microstructure of titanium matrix composites, *Composites Science and Technology* **71**, (2011) pp.1154–1162.
- Morgan, R. Papworth, A. Sutcliffe, C. Fox, P and O’Neill, B (2001) Direct Metal Laser Re-Melting of 316L Stainless Steel Powder Part 2: Analysis of Cubic Primitives, Solid freeform fabrication symposium, Austin Texas USA.
- Murr, L.E. Gaytan, S.M. Ceylan, A. Martinez, E. Martinez, J.L. Hernandez, D.H. Machado, B.I. Ramirez, D.A. Medina, F. Collins, S and Wicker, R.B (2010) Characterization of titanium aluminide alloy components fabricated by additive manufacturing using electron beam melting, *Acta Materialia* **58**, pp.1887-1894.
- Murray, K. (2016) Developments in metal powders for additive manufacturing (Presentation) Sales and marketing manager – EMEA,
- Negi, S. Dhiman, S and Sharma, R.K (2013) Basics, Applications and Future of Additive Manufacturing Technologies: A Review, *Journal of manufacturing technology research* **5**(1/2), pp.75-97.
- Nelson, M. Agne, M.T. Anasori, B. Yang, J and Barsoum, M.W (2017) Synthesis and characterisation of the mechanical properties of Ti<sub>3</sub>SiC<sub>2</sub>/Mg and Cr<sub>2</sub>AlC/Mg alloy composites, *Materials science and engineering A* **706**, pp.182-188.
- Olowofela, H.O. Lyall, I. Stanford, m. Zhang, L. and Obuoza, C. (2013) Mechanical alloying (MA) of composite materials for the laser melting (LM) process, Faim 2013,
- Pavlov, M. Doubenskaia, M and Smurov, I (2010) Pyrometric analysis of thermal processes in SLM technology, *Physics procedia* **5**, pp.523-531.
- Pilling, J. Professor of Materials Science and Engineering, Michigan Technological University, 1400 Townsend Dr, Houghton, MI 49931, USA.
- Prashanth, K. G. Scudino, S. Maity, T. Das, J. & Eckert, J. (2017), Is the energy density a reliable parameter for materials synthesis by selective laser melting? *Materials Research Letters*, **5:6**, pp.386-390.
- Primes GmbH, Max-Planck-Str. 2, 64319 Pfungstadt, Germany, T +49 6157 9878 0
- PyroGenesis 1744, William St., Suite 200, Montréal, Qc H3J 1R4, CANADA T +1 514 937 0002

- Rausch, A. M. Küng, V.E. Pobel, C. Markl, M and Körner, C (2017) Predictive Simulation of Process Windows for Powder Bed Fusion Additive Manufacturing: Influence of the Powder Bulk Density, *Materials Basel, Switzerland*, Vol.10 (10)
- Renishaw PLC. Industrial applications of Renishaw metal additive manufacturing technology.
- Rosso, M. (2006) Ceramic and metal matrix composites: Routs and properties, *Journal of materials processing technology* **175**, pp.364-375.
- Ruiz-Navas, E.M. Fogagnolo, J.B. Velasco, F. Ruiz-Prieto, J.M and Froyen, L. (2006) One step production of aluminium matrix composite powders by mechanically alloying, *Composites part A* **37**, pp.2114-2120.
- Rutkowski, P. Huebner, J. Kata, D. Lis, J. Grabos, A and Chlubny, L (2018) Lasert initiated Ti<sub>3</sub>SiC<sub>2</sub> Powder and coating synthesis, *Ceramics international* **44**, pp.10883-10890.
- Savalani, M. M., Chung, C. C., Poon, C. and Yeung, W. (2011) Selective laser melting of Aluminium and its alloys. New Zealand Rapid Product Development Conference. Auckland University of Technology, Auckland 7 - 8 February.
- SSLMinen, A. Piili, H and Purtonen, T (2010) The characteristics of high power fibre laser welding, *Journal of mechanical engineering science* **224**, pp.1019-1029.
- Salazar, A. Rico, A. Rodríguez, Segurado Escudero, J. Seltzer, R. Martin de la Escalera Cutillas, F (2014) Fatigue crack growth of SLS polyamide 12: Effect of reinforcement and temperature, *Composites: Part B* **59**, pp.285-292
- Sampedro, J. Perez, I. Carcel, B. Ramos, J.A and Amigo, V (2011) Laser cladding of TiC for better titanium components, *Physics procedia* **12**, pp.313-322.
- Saunders, N. (1996) Modelling of phase equilibria in Ti-alloys, *Titanium 95: science and technology*.
- Sevcik, S. How 3D Printing Is Shaping the Future of Manufacturing. VP of Manufacturing Solutions at Stratasys.
- Sculpteo. (2015) The state of 3d printing.
- Sculpteo. (2017) The complete metal 3d printing guide.
- Shannahan, L. Barsoum, M.W and Lamberson, L (2017) Dynamic fracture behaviour of a MAX phase Ti<sub>3</sub>SiC<sub>2</sub>, *Engineering fracture mechanics* **169**, pp.54-66.
- Sharfrin, E.; Zisman, William A. (1960). Constitutive relations in the wetting of low energy surfaces and the theory of the retraction method of preparing monolayers. *The Journal of Physical Chemistry*, **64**(5), pp.519-524.
- Shi, S.L. Pan, W. (2007) Toughening of Ti<sub>3</sub>SiC<sub>2</sub> with 3Y-TZP addition by spark plasma sintering, *Materials science and engineering A* **447**, pp.303-306.
- Simchi, A. Petzoldt, F and Pohl, H. (2003) On the development of direct metal laser sintering of rapid tooling, *Journal of materials processing technology* **141**, pp.319-328.

- Simchi, A. (2006) Direct metal laser sintering of metal powders: mechanism, kinetics and microstructural features, *Materials science and engineering A* **428**, pp.148-158.
- Simonelli, M. Aboulkhair, N. T. Cohen, P. Murray, J. W. Clare, A.T. Tuck, C. Hague, R. J. M. (2018), A comparison of Ti-6Al-4V in-situ alloying in Selective Laser Melting using simply-mixed and satellited powder blend feedstocks, *Materials Characterization* **143**, pp.118-126.
- Singerman, S.A. Jackson, J.J. (1996) Titanium metal matrix composites for aerospace applications, *The minerals, metals and materials society*, pp.579-586.
- Sivakumar, G. Ananthi, V and Ramanathan, S. (2016) Production and mechanical properties of nano SiC particle reinforced Ti-6Al-4V matrix composite, *Transactions of nonferrous metals society of china* **27**, pp.82-90.
- Slipenyuk, A. Kuprin, V. Milman, Y. Goncharuk, V. Eckert, J. (2006) Properties of P/M processed particle reinforced metal matrix composites specified by reinforcement concentration and matrix-to-reinforcement particle size ratio, *Acta Materialia* **54**, pp.157-166
- Sobczak, N. Singh, M and Asthana, R. (2005) High-temperature wettability measurements in metal/ceramic systems – some methodical issues, *Current opinion in solid state and materials Science* **9**, pp.241-253.
- Song, B. Dong, S. Zhang, B. Liao, H and Coddet, C (2012) Effects of processing parameters on microstructure and mechanical property of selective laser melted Ti6Al4V, *Materials and design* **35**, pp.120-125.
- Spierings, A B; Herres, N; Levy, G (2011). Influence of the particle size distribution on surface quality and mechanical properties in AM steel parts. *Rapid Prototyping Journal* Vol. 17 (3), pp.195-202.
- Srinivasa, C. K. Ramesh, C. S. Prabhakar, S. K. (2009) Blending of iron and silicon carbide powders for producing metal matrix composites by laser sintering process. Central manufacturing technology institute, Bangalore, India.
- Sustarsic, B. Godec, M. Jenko, M. Drglin, T and Dolinsek, S. (2005) Bulk and surface characterisation of metal powders for direct laser sintering. *Vacuum* **80**, pp.29-34.
- Suarez, A. Tobar, M.J. Yanez, A. Perez, I. Sampedro, J. Amigo, V and Candell, J.J. (2011) Modeling of phase transformations in Ti6Al4V during laser metal deposition, *Physics procedia* **12**, pp.666-673.
- Sun, J and Gao, L. (2001) Dispersing SiC powder and improving its rheological behaviour, *Journal of the European ceramic society* **21**, pp.2447-2451.
- Sun, P. fang, Z. Z. zhang, Y and xia, Y (2017) Review of the Methods for Production of Spherical Ti and Ti Alloy Powder, *The Minerals, Metals & Materials Society, JOM*, Vol. 69, No. 10, pp.1853-1860.
- Suryanarayana, C. (2001) Mechanical alloying and milling, *Process in materials Science* **46**, pp.1-184.

- Sustarsic, B. Godec, M. Jenko, M. Drglin, T and Dolinsek, S. (2005) Bulk and surface characterisation of metal powders for direct laser sintering, *Vacuum* **80**, pp.29-34.
- Tatarko, P. Chlup, Z. Mahajan, A. Casalegno, V. Saunders, T. G. Dlouhy, I. and Reece, M. J. (2017) High temperature properties of the monolithic CVD  $\beta$ -SiC materials joined with a pre-sintered MAX phase Ti<sub>3</sub>SiC<sub>2</sub> interlayer via solid-state diffusion bonding, *Journal of the European ceramic society* **37**, pp.1205-1216.
- Theodore, L. Kunz, R.G. (2005) Nanotechnology: Environmental implications and solutions, John Wiley & Sons.
- Tjong, S. C. Mai, Y. (2008) Processing-Structure-property aspects of particulate and whisker-reinforced titanium matrix composites. *Composites Science and technology* **68**, pp.583-601.
- Tolochko, N. K. Mozzharov, S. E. Yadroitsev, I. A. Laoui, T. Froyen, L. Titou, V. I. and Ignatieu, M. B. (2004) Balling processes during selective laser treatment of powders, *Rapid prototype journal* **10**(2), pp.78-87.
- Vrancken, B. Thijs, L. Kruth, J.-P. and Van Humbeeck, J. (2014) Microstructure and mechanical properties of novel  $\beta$  titanium metallic composite by selective laser melting. *Acta Materialia* **68**, pp.150-158.
- Vlutters, N. (2016) The absorption of moisture by metal powder in a humid environment and the effects on its composition. University of Twente, Drienerlolaan 5, 7522 NB Enschede, The Netherlands.
- Tucho, W. M. Lysne, V. H. Austbø, H. Sjolyst-Kverneland, A. Hansen, V. (2018) Investigation of effects of process parameters on microstructure and hardness of SLM manufactured SS316L, *Journal of Alloys and Compounds* **740**, pp.910-925.
- Wan, G.U. Yan-Chun, Z. (2006) Reactions between Ti and Ti<sub>3</sub>SiC<sub>2</sub> in a temperature range of 1273-1573 K, *Trans. Nonferrous Met. Soc. China* **16**, pp.1281-1288.
- Wang, Z. Song, M. Sun, C. He, Y. (2011) Effects of particle size and distribution on the mechanical properties of SiC reinforced Al-Cu alloy composites, *Materials Science and Engineering A* **528**, pp.1131-1137
- Wang, Z. Zhang, H. Liu, X. Jiang, Y. Gao, H and He, Y. (2018) Reactive synthesis of porous nanolaminates Ti<sub>3</sub>(Si,Al)C<sub>2</sub> intermetallic compound, *Materials chemistry and physics* **208**, pp.85-90.
- Ward, J. Middleburgh, S. Topping, M. Garner, A. Stewart, D. Barsoum, M. W. Preuss, M. and Frankel, P. (2018) Crystallographic evolution of MAX phase in proton irradiating environments, *Journal of nuclear materials* **502**, pp.220-227.
- Wdowik, U. D. Twardowska, A. and Medala-Wasik, M. (2015) Lattice dynamics of binary and ternary phases in Ti-Si-C system: A combined Raman spectroscopy and density functional theory study, *Materials chemistry and physics* **168**, pp.58-65.
- Wegner, A. Witt, G. (2012) Correlation of process parameters and part properties in laser sintering using response surface modelling. *Physics Procedia* **39**, pp.480-490.

- Watanabe, T. Shiroki, M. Yanagisawa, A. and Sasaki, T. (2010) Improvement of mechanical properties of ferritic stainless-steel weld metal by ultrasonic vibration, *Journal of materials processing technology* **210**, pp.1646-1651.
- Wilkinson, S. Rolls-Royce (2009) Productionising powder manufacture in an aerospace environment.
- Williams, J. Miller, D. Deckard, C. (1996) Selective laser sintering part strength as a function of Andrew number, scan rate and spot size. Clemson University, pp.549-559.
- Withers, P. J. Bennett, J. A. Kuroda, M. (2010) Interfacial shear strength behaviour of Ti/SiC metal matrix composites at room and elevated temperature, *Acta materialia* **58**, pp.6090-6103.
- Witsa, W.W. Bruinsb, R. Terpstra, L. Hulsb, R.A. Geijselaers, H.J.M. (2016) Single scan vector prediction in selective laser melting, *Additive Manufacturing* **9**, pp.1-6
- Yadroitsev, I. Yadroitsava, I. Bertrand, P and Smurov, I. (2012) Factor analysis of selective laser melting process parameters and geometrical characteristics of synthesized single tracks, *Rapid Prototyping Journal* **18**(3), pp.201-208
- Yadroitsev, I. Gusarov, A. Yadroitsava, I. Smurov, I. (2010) Single track formation in selective laser melting of metal powders. *Journal of materials processing technology* **210**, pp.1624-1631.
- Yadroitsev, I. Krakhmalev, P. Yadroitsava, I. Johansson, S. Smurov, I. (2013) Energy input effect on morphology and microstructure of selective laser melting single track from metallic powder. *Journal of materials processing technology* **213**, pp.606-613.
- Yadroitsev, I. Krakhmalev, P. Yadroitsava, I. (2014) Selective laser melting of Ti6Al4V alloy for biomedical applications: temperature monitoring and microstructural evolution. *Journal of alloys and compounds* **583**, pp.404-409.
- Yadroitsev, I. Smurov, I. (2010) Selective laser melting technology: from single laser melted track stability to 3D parts of complex shape. *Physics Procedia* **5**, pp.551-560.
- Yadroitsev, I. Smurov, I. (2011) Surface morphology in selective laser melting of metal powders. *Physics Procedia* **12**, pp.264-270.
- Yadroitsev, I. Thivillon, L. Bertrand, P. H. Smurov, I. (2007) Strategy of manufacturing components with designed internal structure by selective laser melting of metal powders. *Applied surface science* **254**, pp.980-983.
- Yamada K., Mohri M. (1991) Properties and Applications of Silicon Carbide Ceramics. In: Sömiya S., Inomata Y. (eds) *Silicon Carbide Ceramics -1*, pp. 13-44 Springer, Dordrecht.
- Yin, Y.F. Xu, W. Sun, Q.Y. Xiao, L and Sun, J. (2015) Deformation and fracture behaviour of commercially pure titanium with gradient nano-to-micro-grained surface layer, *Transactions of nonferrous metals society of china* **25**(3), pp.738-747.
- Zadra, M. Girardini, L. (2014) High Performance, Low cost Titanium metal matrix composites, *Materials Science and Engineering A*, **608**, pp.155-163.

- Zhang, B. n, Dembinski, L. Coddet, C. (2013) The study of the laser parameters and environment variables effect on mechanical properties of high compact parts elaborated by selective laser melting 316L powder, *Materials Science & Engineering A* **584**, pp.21-31
- Zhang. Z, Luo. Y, Xu. C. (2012) Phase and morphology evaluation of TiC in the Ti-Si-C System. *International Journal of Refractory Metals and Hard Materials*.
- Zhao, X. Fan, Y. Wang, H. Liu, Y. (2015) Revealing the surface nano-enhancing mechanism of  $\alpha$ -titanium alloy by microstructure evolution, *Materials Letters* **160** pp.51-54
- Zoz, H. (2008) Simoloyer ®: major characteristics and features. Zoz GmbH, Germany.
- Zoz, H. Ernst, D. SLM, I. S. Kwon, W. H. (2008) Mechanical alloying of Ti-Ni based materials using the Simoloyer® Zoz GmbH, Germany.
- Zoz, H. Ernst, Weiss, H. Magini, M. Powell, C. Suryanarayana, C. Froes, F. H. (2008) Mechanical alloying of Ti-24Al-11Nb (AT%) using the Simoloyer® Zoz GmbH, Germany.
- Zoz, R.H. Kaupp, H. Naimi-Jamal, G. (2008) Environmentally protecting reactive milling. Zoz GmbH, Germany.
- Zoz, H. Ren, H. (2008) Processing of ceramic powder using high energy milling. Zoz GmbH, Germany.
- Zoz, H. Ren, H. Reichardt, R. Benz, H. U. (2012) High energy milling / mechanical alloying / reactive milling, Part 1. Zoz GmbH, Germany.

# Chapter Ten

## 10.0 Appendices

### Appendix 1, Zoz Maltoz 3.2.1 software configuration.



## Appendix 2, Struers, Titanium Alloys (DiaPro, Application Notes)

### Titanium Alloys (DiaPro, Application Note)

Select equipment disc size 300 mm ▼

**Method details**

Method number: 1417

Download documents: [Print method](#)

**These methods are meant as a guide**

All methods are generic methods. This means that the methods have been developed according to the following standard: 8 specimens of 30 mm diameter clamped in a specimen holder of 160 mm diameter (MAXCY).

**Grinding**

| Step                 | PG                        | FG       |
|----------------------|---------------------------|----------|
| Surface              | MD-Mezzo 220              | MD-Largo |
| Abrasive Type        | DiaPro Allegro/Largo 9 µm |          |
| Lubricant Type       | Water                     |          |
| Speed (rpm)          | 300                       | 150      |
| Force (N) / Specimen | 40                        | 30       |
| Holder direction     | >>                        |          |
| Time (min)           | 01:00                     | 04:00    |

**Polishing**

| Step                 | OP            |
|----------------------|---------------|
| Surface              | MD-Chem       |
| Abrasive Type        | OP-S, 0.04 µm |
| Lubricant Type       |               |
| Speed (rpm)          | 150           |
| Force (N) / Specimen | 30            |
| Holder direction     | ><            |
| Time (min)           | 05:00         |

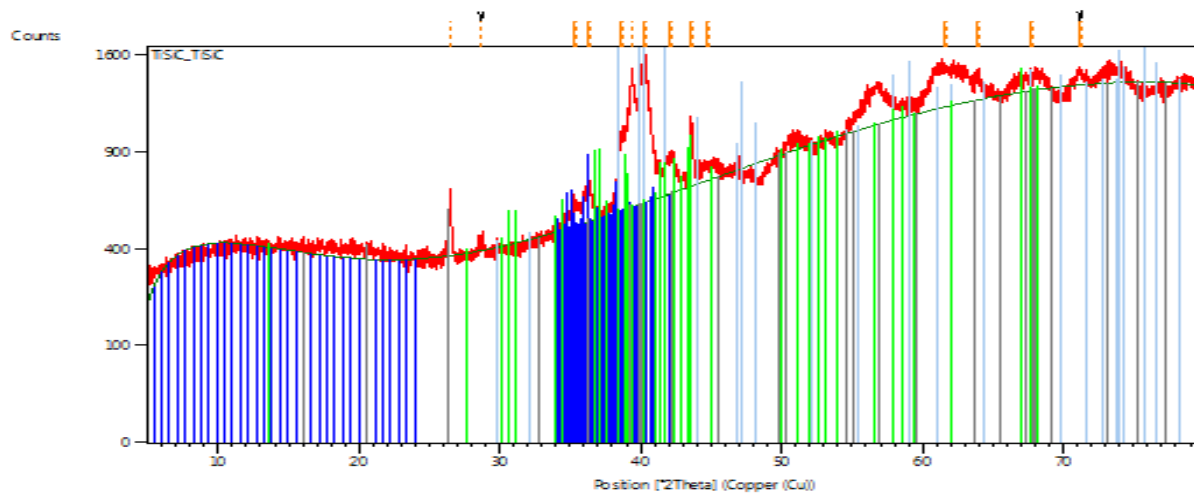


## Appendix 3, XRD Analysis Results

### Anchor Scan Parameters

|                                |                                                                                                                                                                                                                                                                                                                                                                                                                                                                                                                                                                                   |
|--------------------------------|-----------------------------------------------------------------------------------------------------------------------------------------------------------------------------------------------------------------------------------------------------------------------------------------------------------------------------------------------------------------------------------------------------------------------------------------------------------------------------------------------------------------------------------------------------------------------------------|
| Dataset Name:                  | TiSiC                                                                                                                                                                                                                                                                                                                                                                                                                                                                                                                                                                             |
| File name:                     | C:\XRD Data\TiSiC_TiSiC.xrdml                                                                                                                                                                                                                                                                                                                                                                                                                                                                                                                                                     |
| Sample Identification:         | TiSiC                                                                                                                                                                                                                                                                                                                                                                                                                                                                                                                                                                             |
| Comment:                       | Configuration=Reflection-transmission spinner, Owner=User-1, Creation date=6/28/2012 10:39:29 AM<br>Goniometer=Theta/Theta; Minimum step size 2Theta:0.0001; Minimum step size Omega:0.0001<br>Sample stage=Reflection-transmission spinner; Minimum step size Phi:0.1<br>Diffractometer system=EMPYREAN<br>Measurement program=C:\PANalytical\Data Collector\Programs\powder 15mm PDS.xrdmp, Identifier={69CD223E-1BDD-4632-83DC-936429B8747A}<br>Batch program=C:\PANalytical\Data Collector\Programs\Changer 1 sample.xrdmp, Identifier={80E5EB34-F8D8-417D-BE8A-B1D9D16B193E} |
| Measurement Date / Time:       | 1/29/2020 2:43:27 PM                                                                                                                                                                                                                                                                                                                                                                                                                                                                                                                                                              |
| Operator:                      | Univ Wolverhampton                                                                                                                                                                                                                                                                                                                                                                                                                                                                                                                                                                |
| Raw Data Origin:               | XRD measurement (*.XRDML)                                                                                                                                                                                                                                                                                                                                                                                                                                                                                                                                                         |
| Scan Axis:                     | Gonio                                                                                                                                                                                                                                                                                                                                                                                                                                                                                                                                                                             |
| Start Position [°2Th.]:        | 5.0064                                                                                                                                                                                                                                                                                                                                                                                                                                                                                                                                                                            |
| End Position [°2Th.]:          | 79.9904                                                                                                                                                                                                                                                                                                                                                                                                                                                                                                                                                                           |
| Step Size [°2Th.]:             | 0.0130                                                                                                                                                                                                                                                                                                                                                                                                                                                                                                                                                                            |
| Scan Step Time [s]:            | 8.6700                                                                                                                                                                                                                                                                                                                                                                                                                                                                                                                                                                            |
| Scan Type:                     | Continuous                                                                                                                                                                                                                                                                                                                                                                                                                                                                                                                                                                        |
| PSD Mode:                      | Scanning                                                                                                                                                                                                                                                                                                                                                                                                                                                                                                                                                                          |
| PSD Length [°2Th.]:            | 3.35                                                                                                                                                                                                                                                                                                                                                                                                                                                                                                                                                                              |
| Offset [°2Th.]:                | 0.0000                                                                                                                                                                                                                                                                                                                                                                                                                                                                                                                                                                            |
| Divergence Slit Type:          | Automatic                                                                                                                                                                                                                                                                                                                                                                                                                                                                                                                                                                         |
| Irradiated Length [mm]:        | 15.00                                                                                                                                                                                                                                                                                                                                                                                                                                                                                                                                                                             |
| Specimen Length [mm]:          | 10.00                                                                                                                                                                                                                                                                                                                                                                                                                                                                                                                                                                             |
| Measurement Temperature [°C]:  | 25.00                                                                                                                                                                                                                                                                                                                                                                                                                                                                                                                                                                             |
| Anode Material:                | Cu                                                                                                                                                                                                                                                                                                                                                                                                                                                                                                                                                                                |
| K-Alpha1 [Å]:                  | 1.54060                                                                                                                                                                                                                                                                                                                                                                                                                                                                                                                                                                           |
| K-Alpha2 [Å]:                  | 1.54443                                                                                                                                                                                                                                                                                                                                                                                                                                                                                                                                                                           |
| K-Beta [Å]:                    | 1.39225                                                                                                                                                                                                                                                                                                                                                                                                                                                                                                                                                                           |
| K-A2 / K-A1 Ratio:             | 0.50000                                                                                                                                                                                                                                                                                                                                                                                                                                                                                                                                                                           |
| Generator Settings:            | 40 mA, 40 kV                                                                                                                                                                                                                                                                                                                                                                                                                                                                                                                                                                      |
| Diffractometer Type:           | 0000000001126545                                                                                                                                                                                                                                                                                                                                                                                                                                                                                                                                                                  |
| Diffractometer Number:         | 0                                                                                                                                                                                                                                                                                                                                                                                                                                                                                                                                                                                 |
| Goniometer Radius [mm]:        | 240.00                                                                                                                                                                                                                                                                                                                                                                                                                                                                                                                                                                            |
| Dist. Focus-Diverg. Slit [mm]: | 100.00                                                                                                                                                                                                                                                                                                                                                                                                                                                                                                                                                                            |
| Incident Beam Monochromator:   | No                                                                                                                                                                                                                                                                                                                                                                                                                                                                                                                                                                                |
| Spinning:                      | Yes                                                                                                                                                                                                                                                                                                                                                                                                                                                                                                                                                                               |

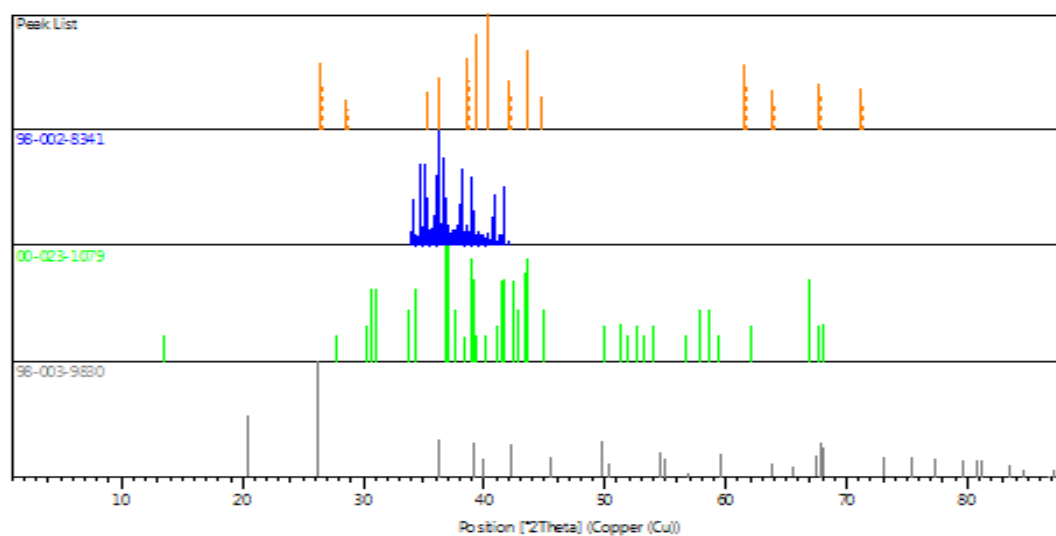
### Graphics



### Pattern List

| Visible | Ref.Code    | Score | Compound Name        | Displ. [°2Th] | Scale Fac. | Chem. Formula |
|---------|-------------|-------|----------------------|---------------|------------|---------------|
| *       | 98-002-8341 | 45    | Silicon Carbide      | 0.447         | 0.222      | C1 Si1        |
| *       | 00-023-1079 | 32    | Titanium Silicide    | -0.313        | 0.234      | Ti5 Si4       |
| *       | 98-003-9830 | 37    | Silicon Oxide - Al.. | -0.283        | 0.127      | O2 Si1        |

### Graphics



### Name and formula

Reference code: 98-002-8341

Compound name: Silicon Carbide  
Common name: Silicon Carbide

Chemical formula: C<sub>1</sub>Si<sub>1</sub>

## **Crystallographic parameters**

Crystal system: Hexagonal  
Space group: R 3 m  
Space group number: 160

a (Å): 3.0790  
b (Å): 3.0790  
c (Å): 475.9780  
Alpha (°): 90.0000  
Beta (°): 90.0000  
Gamma (°): 120.0000

Calculated density (g/cm<sup>3</sup>): 3.22  
Volume of cell (10<sup>6</sup> pm<sup>3</sup>): 3907.84  
Z: 189.00

RIR: 0.54

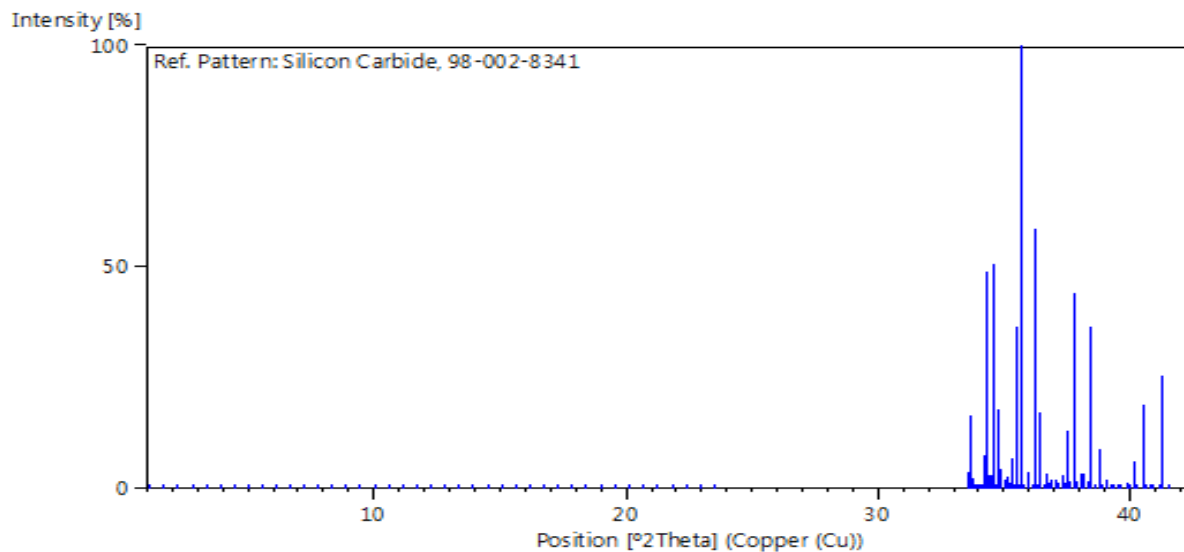
## **Subfiles and quality**

Subfiles: User Inorganic  
Quality: User from Structure (=)

## **Comments**

Creation Date: 1/1/1980  
Modification Date: 7/15/2000  
Original ICSD space group: R3MH  
Zhdanov-symbol: ((34)8 43)3. At least one temperature factor missing in the paper. No R value given in the paper. Standard deviation missing in cell constants. Polytype structure 189R  
Recording date: 1/1/1980  
Modification date: 7/15/2000  
ANX formula: NO  
Z: 189  
Calculated density: 3.22  
Pearson code: hR126  
Wyckoff code: a126  
Structure TIDY: TRANS -x,-y,-z origin 0 0 .47752  
Publication title: A new polytype of silicon carbide, 189R  
ICSD collection code: 28341  
Chemical Name: Silicon Carbide  
Second Chemical Formula: Si C

## **Stick Pattern**



## **Name and formula**

Reference code: 00-023-1079  
 Compound name: Titanium Silicide  
 PDF index name: Titanium Silicide  
 Empirical formula:  $\text{Si}_4\text{Ti}_5$   
 Chemical formula:  $\text{Ti}_5\text{Si}_4$

## **Crystallographic parameters**

Crystal system: Orthorhombic  
 Space group: Pbnm  
 Space group number: 62  
 a (Å): 6.6450  
 b (Å): 6.5060  
 c (Å): 12.6900  
 Alpha (°): 90.0000  
 Beta (°): 90.0000  
 Gamma (°): 90.0000  
 Volume of cell ( $10^6 \text{ pm}^3$ ): 548.62  
 Z: 4.00  
 RIR: -

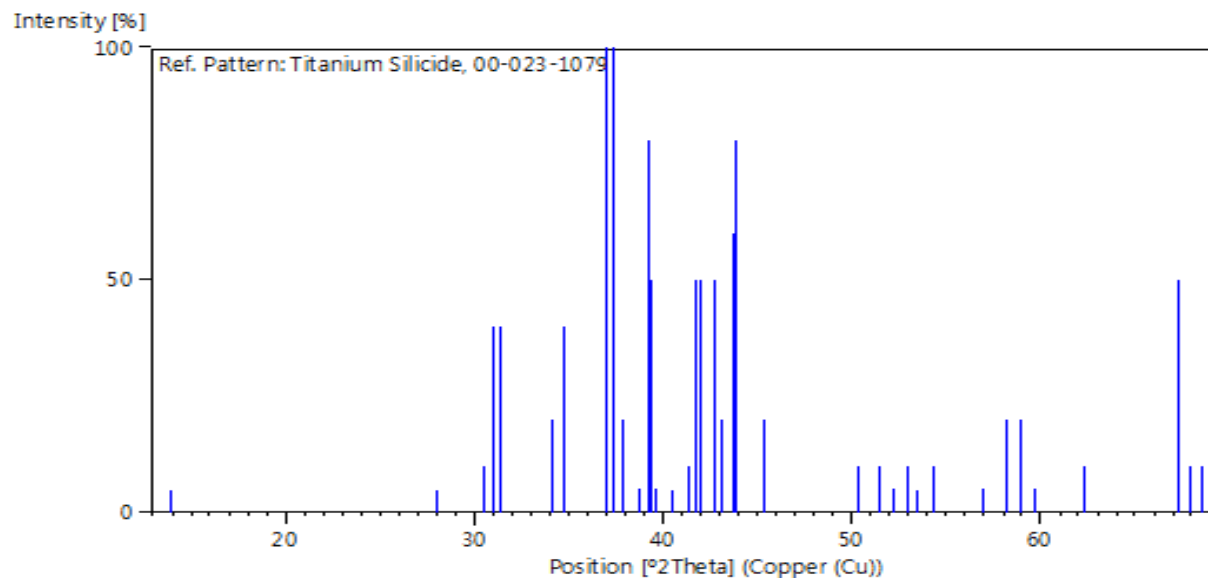
## **Subfiles and quality**

Subfiles: Alloy, metal or intermetallic Inorganic  
 Quality: Indexed (I)

## **Comments**

Creation Date: 1/1/1970  
Modification Date: 1/1/1970  
Comment: High temperature modification of Ti<sub>5</sub>Si<sub>4</sub>.

## **Stick Pattern**



## **Name and formula**

Reference code: 98-003-9830  
Compound name: Silicon Oxide - Alpha  
Common name: Silicon Oxide - Alpha  
Chemical formula: O<sub>2</sub>Si<sub>1</sub>

## **Crystallographic parameters**

Crystal system: Anorthic  
Space group: P 1  
Space group number: 1  
a (Å): 4.9160  
b (Å): 4.9165  
c (Å): 5.4070  
Alpha (°): 90.0000  
Beta (°): 90.0000  
Gamma (°): 119.9900  
Calculated density (g/cm<sup>3</sup>): 2.64  
Volume of cell (10<sup>6</sup> pm<sup>3</sup>): 113.19  
Z: 3.00  
RIR: 1.06

## Subfiles and quality

Subfiles: User Inorganic  
Quality: User from Structure (=)

## Comments

Creation Date: 10/17/1995  
Modification Date: 2/1/2012  
Original ICSD space group: P1  
AE: Si1-3: O4; O1-6: Si2; mean T-O: 1.61; mean Si-O-Si: 143,5 degree.  
At least one temperature factor is implausible or meaningless but agrees with the value given in the paper. No R value given in the paper. X-ray diffraction from single crystal. Structure type: SiO<sub>2</sub>(aP9). Temperature factors available. Structure type prototype: SiO<sub>2</sub>(aP9). The structure has been assigned a PDF number (experimental powder diffraction data): 77-1060.

Structure type: SiO<sub>2</sub>(aP9).  
Recording date: 10/17/1995.  
Modification date: 2/1/2012.  
ANX formula: AX<sub>2</sub>. Z: 3.  
Calculated density: 2.64.  
R value: 0.046.  
Pearson code: aP9.  
Wyckoff code: a9.  
PDF code: 01-077-1060  
Structure TIDY: TRANS -a,a+b,-c -x,-y,-z origin .41510 .26740 .45320  
Publication title: On the structure of alpha-Si O<sub>2</sub> crystals doped with Fe<sup>3+</sup>  
ICSD collection code: 39830  
Structure: SiO<sub>2</sub>(aP9)  
Chemical Name: Silicon Oxide - Alpha  
Second Chemical Formula: Si O<sub>2</sub>

## Stick Pattern

